



# City Research Online

## City, University of London Institutional Repository

---

**Citation:** Stasiek, J. (1992). Liquid crystal thermography and image processing in heat and fluid flow experiments. (Unpublished Doctoral thesis, City University London)

This is the accepted version of the paper.

This version of the publication may differ from the final published version.

---

**Permanent repository link:** <https://openaccess.city.ac.uk/id/eprint/7550/>

**Link to published version:**

**Copyright:** City Research Online aims to make research outputs of City, University of London available to a wider audience. Copyright and Moral Rights remain with the author(s) and/or copyright holders. URLs from City Research Online may be freely distributed and linked to.

**Reuse:** Copies of full items can be used for personal research or study, educational, or not-for-profit purposes without prior permission or charge. Provided that the authors, title and full bibliographic details are credited, a hyperlink and/or URL is given for the original metadata page and the content is not changed in any way.

LIQUID CRYSTAL THERMOGRAPHY AND IMAGE PROCESSING  
IN HEAT AND FLUID FLOW EXPERIMENTS

BY

JAN STASIEK

A THESIS SUBMITTED FOR THE AWARD OF THE DEGREE OF  
DOCTOR OF PHILOSOPHY IN ENGINEERING

CITY UNIVERSITY  
DEPARTMENT OF MECHANICAL ENGINEERING AND AERONAUTICS

JUNE 1992

## **TABLE OF CONTENTS**

---

**Title Page**

**Table of Contents**

**Abstract**

**Acknowledgements**

**Declaration**

**List of Contents**

**List of Figures**

**List of Tables**

**Nomenclature**

**Thesis**

## **ABSTRACT**

.... ALL'S WELL THAT ENDS WELL ....

William Shakespeare

Liquid crystal techniques, combined with sophisticated software in increasingly powerful personal computers, are now permitting fairly comprehensive full-field studies of velocity, temperature and heat transfer coefficient-distributions, with their accompanying automatic analysis.

Liquid crystals and true-colour image processing have opened some new approaches for heat transfer research and offer satisfactory accuracy and resolution. New and more incisive experiments are being designed for conventional situations, and other problems can now be studied which were previously not practical to consider.

The history of these techniques is reviewed and the principal methods are described using illustrative examples from the literature and work of the author.

A new liquid crystal thermometry method is described to determine quantitatively two-dimensional temperature distributions on a surface and in a fluid, from colour records obtained using a thermosensitive chiral-nematic material combined with image processing. Application-type experiments have been carried out both to visualise the complex distribution of temperature and local heat transfer coefficient over a cooled surface disturbed by different solid obstacles, and also to investigate temperature and flow patterns in a rectangular cavity for natural convection.

A new experimental method (optical and non-invasive) has been established to measure simultaneously both flow and thermal fields - this method may be described as particle image velocimetry and thermometry (PIVT).

Some of the experimental results presented are applied to an important industrial improvement in heat exchanger design and could result in substantial reductions in energy costs.

## **ACKNOWLEDGEMENTS**

---

Much of the work reported here was sponsored by the Central Electricity Generating Board and PowerGen plc, Ratcliffe Technology Centre, United Kingdom.

I should like to express my very warm gratitude to Professor Michael W. Collins for his considerable help during my stay at City University.

I wish to acknowledge also the help given to me by Mr. P. Chew, Dr. M. Ciofalo, Dr. X. Zhang and many others with whom I have been privileged to be in contact over the last three years.

I should like to express my special thanks to Mrs. E. Da Silva and Ms D. A. King for their generous efforts in the preparation and linguistic correction of this thesis.

Lastly, and by no means least, I acknowledge the assistance of my wife, Jadwiga, and my son, Adam, who have been the inspiration for my efforts. Without their loving support none of this would have been possible.

**DECLARATION**

The circulation of this thesis is restricted until June 1995 and shall not be reproduced or used without the author's written consent.

## LIST OF CONTENTS

	Page
TITLE PAGE	1
TABLE OF CONTENTS	2
ABSTRACT	3
ACKNOWLEDGEMENTS	4
DECLARATION	5
LIST OF CONTENTS	6
LIST OF FIGURES	8
LIST OF TABLES	17
NOMENCLATURE	18
1. INTRODUCTION	20
2. PHYSICAL AND THERMAL CHARACTERISTICS OF LIQUID CRYSTALS	25
2.1 Classification	26
2.2 Compensated Mixtures and Textures	30
2.3 Structure of the Chiral Nematic Mesophase	30
2.4 Optical Properties	32
2.5 Colour-Play Properties	37
2.6 Use of the Materials	38
2.6.1 Unsealed Liquids	42
2.6.2 Microencapsulated (Slurries and Coatings)	43
2.6.3 Coated (Printed) Sheets	44
APPENDIX 2.1 A Glossary of Terms Associated with TLC [118]	46

## LIST OF CONTENTS

	<b>Page</b>
<b>3. LITERATURE REVIEW - THE USE OF LIQUID CRYSTALS</b>	<b>48</b>
<b>3.1 Visualisation of Boundary Layer Transitions</b>	<b>48</b>
<b>3.2 Surface Temperature and Heat Transfer Measurements</b>	<b>49</b>
<b>3.3 Flow Visualisation in Fluids</b>	<b>54</b>
<b>3.4 Flow Visualisation using Shear-Induced Colour Changes</b>	<b>56</b>
<b>4. LIQUID CRYSTALS AND IMAGE PROCESSING TECHNIQUES</b>	<b>63</b>
<b>5. CALIBRATION OF LIQUID CRYSTALS AND TRUE-COLOUR IMAGE PROCESSING</b>	<b>75</b>
<b>5.1 Calibration Tests</b>	<b>75</b>
<b>5.2 True-Colour Image Processing</b>	<b>78</b>
<b>6. EXPERIMENTAL APPARATUS AND PROCEDURE</b>	<b>85</b>
<b>6.1 Design and Construction of the Wind Tunnel</b>	<b>85</b>
<b>6.1.1 Entrance Section</b>	<b>87</b>
<b>6.1.2 Mapping Section</b>	<b>87</b>
<b>6.1.3 Working Section</b>	<b>89</b>
<b>6.1.4 Measurements of Velocity and Static Pressure in the Corrugated Working Section</b>	<b>95</b>
<b>6.1.5 Cooling Water System</b>	<b>96</b>
<b>6.2 Experimental Setup for Flow Visualisation in a Rectangular Cavity</b>	<b>101</b>
<b>7. EXPERIMENTAL RESULTS</b>	<b>105</b>
<b>7.1 Heat Transfer and Friction Factor - Results for Flat-Plate Working Section</b>	<b>106</b>
<b>7.2 Heat Transfer and Friction Factor - Results for Corrugated Working Section</b>	<b>123</b>
<b>7.3 Heat Transfer in a Parallel Plate Channel with Obstructions of Different Geometrical Shapes</b>	<b>126</b>
<b>7.4 Temperature and Flow Visualisation in a Glycerol-Filled Cavity</b>	<b>148</b>
<b>8. UNCERTAINTY ANALYSIS</b>	<b>155</b>
<b>9. CONCLUSIONS</b>	<b>160</b>
<b>REFERENCES</b>	<b>161</b>

## LIST OF FIGURES

**Fig. 1** The liquid crystalline phase on the temperature scale

**Fig. 2** The Smectic liquid crystal structure (from [118])

**Fig. 3** The Nematic liquid crystal structure (from [118])

**Fig. 4** The Chiral Nematic (cholesteric) liquid crystal structure. The director (arrow) traces out a helical path within the medium (from [118])

**Fig. 5** Left- and right-handed helical structures showing pitch P and displacement angle (from [118])

**Fig. 6** Orientations of helical (long lines) and molecular axes (short lines) relative to observer for a) focal conic texture and b) Grandjean texture (from [118])

**Fig. 7** Optical properties of a hypothetical chiral nematic liquid crystal with right-handed helical structure and pitch corresponding to a reflective wavelength  $\lambda_0 = 500$  nm;

- a) birefringence-definition of negative optic axis,
- b) rotation of plane polarised incident light,
- c) circular dichroism,
- d) Bragg-type scattering of non-normal incident light (from [118])

**Fig. 8** The wavelength of dependence of:

- a) rotation of plane of polarisation and
- b) reflection coefficient in hypothetical chiral nematic liquid crystal with a pitch corresponding to a reflective wavelength  $\lambda_0 = 500$  nm (from [118])

**Fig. 9** Typical pitch vs temperature response of thermochromic liquid crystal (from [118])

**Fig. 10a** Phase diagram for mixtures of TM74A and TM75A (from [118])

**Fig. 10b** Colour play range for mixtures of TM74A and TM75A (from [118])

**Fig. 11** Liquid crystal thermogram of human hand (from [118])

**Fig. 12** Liquid crystal show colour: in this case turbulent areas appear blue (B) and laminar regions orange (O) (from [73])

**Fig. 13** Schematic of a typical liquid crystal display. The conditions depicted are representative of subcritical flow. The shaded region represents colour (from [29])

**Fig. 14** Schematic of a typical liquid crystal display. The conditions depicted are representative of critical flow. The shaded region represents colour (from [29])

**Fig. 15** Single jet impingement. Photographs of blue-green line isotherm  $t = 33.3^{\circ}\text{C}$  on liquid crystal sheet at different heat fluxes (Nusselt numbers) (from [53])

**Fig. 16** Photograph of a contour of the heat transfer coefficient on the endwall of a cylinder held perpendicular to the wall. The flow is from left to right.  $\text{Re} = 3390$ ,  $h = 893 \text{ W/m}^2\text{K}$  (from [90])

**Fig. 17** A - Vane endwall cascade  
B - Film injection from a cylinder in cross flow (from [62])

**Fig. 18** Photographs of transient liquid crystal patterns on duct floor.  
a) higher temperature liquid crystal-early in test run,  
b) lower temperature liquid crystal-later in test run (from [69])

**Fig. 19** Photograph of steady-state liquid crystal pattern on duct floor (from [69])

**Fig. 20** Temperature and velocity visualisation in glycerol-filled cavity under free convection, using unencapsulated chiral nematic liquid crystals (from [60])

**Fig. 21** Marangoni convection and centrifugal-buoyancy driven motion visualisation in a rotating cylinder using microencapsulated liquid crystals suspended in glycerol (from [105])

**Fig. 22** Flow visualisation and shear-stress indication of horse-shoe vortex using chiral nematic mixture-flow velocity 40 m/s (from [9])

**Fig. 23** Chameleon clothing: liquid crystal dye changes colour as the dress becomes warmer (from [26])

**Fig. 24** Spectral reflectance of the used liquid crystal layer measured by monochrometer at various temperatures (from [3])

**Fig. 25** Light intensity distribution along the test plate (from [2])

**Fig. 26** Monochromatic TV images of the liquid crystal layer on the test plate without pass filters (from [2])

**Fig. 27** Isothermal lines obtained by the multiple narrow-band spectral intensity image processing system for two Reynolds numbers of 4000 and 10000 (from [2])

**Fig. 28** Measured temperature distribution processed using the method of multiple linear regression for the case of linear temperature distribution with intermediate temperature gradient (from [3])

**Fig. 29** Temperature and Nusselt number distributions around two cylinders (from [1])

**Fig. 30** The electromagnetic spectrum ranges from cosmic rays to electric power; the visible portion makes up only a small portion of the spectrum. As can be seen, the visible portion can be roughly divided into red, green and blue sections (from [112])

**Fig. 31** HSI triangle model and RGB colour cube (from [118])

**Fig. 32** The 1976 chromaticity diagram (from [108])

**Fig. 33** Experimental apparatus for the calibration experiment. Linear temperature distribution was obtained along the calibration plate on which colour of liquid crystal on calibration plate was observed and measured

**Fig. 34** Schematic drawing of calibration (brass) plate circuit diagram.  
1. Brass plate 2. Thermocouples-type T 3. Heater-200 W  
4. Autotransformer 5. Digital voltmeter 6. Dewar flask  
with melting ice 7. Cooler 8. Water pump 9. TE-8A  
constant temperature water baths

**Fig. 35** Colour distribution of liquid crystal visualising temperature distribution along test plate ( $\Delta t / \Delta X = 94 \text{ K/m}$ ) (Dashed line - temperature distribution without lamp)

**Fig. 36** Hue and temperature distribution along the test plate ( $\Delta t/\Delta X = 94 \text{ K/m}$ )  
a) temperature range  $29.73 - 26.8^\circ\text{C}$   
b) temperature range  $28.45 - 26.8^\circ\text{C}$   
c) Hue value as a function of surface temperature

**Fig. 37** The information flow chart for True Colour Image Processing interpreter system

**Fig. 38** DT 2871 (HSI) Colour Frame Grabber block diagram (from [119])

**Fig. 39** DT-Connect Image Processing overview block diagram (from [119])

**Fig. 40** Open low-speed wind tunnel

**Fig. 41** Mapping section geometry and liquid crystal package with component thickness

**Fig. 42** Scheme of three different end walls of cascade

**Fig. 43** a) A schematic diagram of the flat-plate working section  
b) Three-dimensional corrugated geometry passage  
c) Cross-corrugated heat transfer element

**Fig. 44** Schematic diagram of the working section and position of pressure tappings; R -reference pressure tapping, PT -pitot mounting plane, L -length of duct

**Fig. 45** Extension of the wind tunnel with new corrugated working section and an upper constant-temperature water bath

**Fig. 46** A schematic diagram of the corrugated working section - inclination angle  $\varphi = 36^\circ$

**Fig. 47** General view of the three-dimensional diamond geometry

**Fig. 48** General view of the location of pressure tappings along flow ducts Nos. II and IV - arrangement for flat-plate working section

**Fig. 49** Schematic illustration for pressure drop and velocity measurements using tappings and Pitot tube-arrangement for corrugated working section

**Fig. 50** Schematic drawing of the TE-8A water circuit diagram

**Fig. 51 Schematic of rectangular cavity**  
1. Copper plate 2. Thermocouples 3. Blanket 30 W heater 4. Wool insulation 5. Polystyrene 6. Cooling water 7. Perspex top cover

**Fig. 52 Schematic of experimental facility**  
1. Cavity 2. Power flash lamp 3. Light slots  
4. Programmable generator trigger 5. Camera  
6. Water bath 7. Blanket 30 W heater 8. Transformer

**Fig. 53 Local heat transfer coefficient and Nusselt number distributions on the bottom wall of the measurement diamond;**  
 $\varphi = 36^\circ$ ;  $Re = 5506$ ;  $P/H_i = 3.67$

**Fig. 54 Local heat transfer coefficient and Nusselt number distributions on the bottom wall of the measurement diamond;**  
 $\varphi = 36^\circ$ ;  $Re = 4540$ ;  $P/H_i = 3.67$

**Fig. 55 Local heat transfer coefficient and Nusselt number distributions on the bottom wall of the measurement diamond;**  
 $\varphi = 36^\circ$ ;  $Re = 3900$ ;  $P/H_i = 3.67$

**Fig. 56 Local heat transfer coefficient and Nusselt number distributions on the bottom wall of the measurement diamond;**  
 $\varphi = 36^\circ$ ;  $Re = 3394$ ;  $P/H_i = 3.67$

**Fig. 56a Reproduction of colour transparency representing wall temperature contours at  $Re = 3394$  (Photo 1 - Exp.3,  
Photo 2 - Exp.7, Photo 3 - Exp.9, Photo 4 - Exp.12)**

**Fig. 57 Local heat transfer coefficient and Nusselt number distributions on the bottom wall of the measurement diamond;**  
 $\varphi = 36^\circ$ ;  $Re = 2850$ ;  $P/H_i = 3.67$

**Fig. 58 Local heat transfer coefficient and Nusselt number distributions on the bottom wall of the measurement diamond;**  
 $\varphi = 36^\circ$ ;  $Re = 2390$ ;  $P/H_i = 3.67$

**Fig. 59 Local heat transfer coefficient and Nusselt number distributions on the bottom wall of the measurement diamond;**  
 $\varphi = 36^\circ$ ;  $Re = 1796$ ;  $P/H_i = 3.67$

**Fig. 60** Three-dimensional Nusselt number distributions for  
 $Re = 1796; 2390$  and  $5506$ ;  
 $\varphi = 36^\circ$ ;  $P/H_i = 3.67$

**Fig. 61** Experimental; maximum, minimum and average Nusselt number distribution for uniform wall temperature  $t_R = 27.7^\circ C$ ;  
 $\varphi = 36^\circ$ ;  $P/H_i = 3.67$

**Fig. 62** Outlet velocity profiles (red colour - upper wall, green colour - lower wall).  $V_i = 3.72, 2.44$  and  $2.07 \text{ m/s}$   
 $\varphi = 36^\circ$ ;  $P/H_i = 3.67$

**Fig. 63** Wall static pressure distribution along the flow ducts Nos. II and IV for  $V_i = 15.52, 11.13, 8.54$  and  $5.0 \text{ m/s}$   
 $\varphi = 36^\circ$ ;  $P/H_i = 3.67$

**Fig. 64** Wall static pressure distribution along the flow ducts Nos. II and IV for  $V_i = 3.72, 2.44$ , and  $2.07 \text{ m/s}$   
 $\varphi = 36^\circ$ ;  $P/H_i = 3.67$

**Fig. 65** Friction coefficient as functions of the Reynolds number in "cell 2" of corrugated upstream passages ( $f$  - the peak friction coefficient;  $f_t$  - the trough friction coefficient)

**Fig. 66 a)** Photographs of the colour distributions of the liquid crystal layer on a corrugated geometry  
**b)** Images of the computer display after segmentation processing (Hue:  $55.70$ , Saturation:  $0.255$ , Intensity:  $0.255$ ).  $t_G = 28.3^\circ C$   
**c)** Images on the computer display after chromaticity processing (adjust saturation)  
 $Re = 5100$ ;  $\varphi = 60^\circ$ ;  $P/H_i = 4.0$ ;  $t_a = 45.33^\circ C$ ;  $t_b = 22.2^\circ C$

**Fig. 67 a)** Photographs of the colour distributions of the liquid crystal layer on a corrugated geometry  
**b)** Images of the computer display after segmentation processing (Hue:  $55.70$ , Saturation:  $0.255$ , Intensity:  $0.255$ ).  $t_G = 28.3^\circ C$   
**c)** Images on the computer display after chromaticity processing (adjust saturation)  
 $Re = 2670$ ;  $\varphi = 48^\circ$ ;  $P/H_i = 4.0$ ;  $t_a = 45.33^\circ C$ ;  $t_b = 26.29^\circ C$

**Fig. 68** Experimental; average Nusselt number distributions developed from True-colour image processing system for uniform wall temperature  $t_w = 28.3^\circ\text{C}$ .  $P/H_i = 4.0$  and  $\varphi = 30^\circ; 36^\circ; 48^\circ; 60^\circ$  and  $75^\circ$

**Fig. 69** Experimental friction coefficient of open downstream corrugated passages measured by the wall pressure tappings

**Fig. 70** Experimental friction coefficient of closed downstream corrugated passages measured by the wall pressure tappings

**Fig. 71** Predicted vs. experimental average Nusselt number for  $\varphi = 36^\circ$  and  $P/H_i = 4.0$

**Fig. 72** Predicted vs. experimental friction factor for  $\varphi = 36^\circ$  and  $P/H_i = 4.0$

**Fig. 73** Average Nusselt number of corrugated passages for  $Re_m = 2000$ ; where  $\theta = 90 - \varphi/2$

**Fig. 74** Friction factors of corrugated passages for  $Re_m = 2000$ ; where  $\theta = 90 - \varphi/2$

**Fig. 75** Contours of constant Nusselt number distribution around single square column at  
 $Re = 10000$ ;  $q = 228 \text{ W/m}^2$ ;  $D_h = 0.009 \text{ m}$

**Fig. 76** Contours of constant Nusselt number distribution around double square column at  
 $Re = 10000$ ;  $q = 228 \text{ W/m}^2$ ;  $D_h = 0.009 \text{ m}$

**Fig. 77** Reproduction of colour transparency representing wall temperature contours at  $Re = 10000$ ;  $q = 228 \text{ W/m}^2$   
Photo 1 -  $t_a = 37.1^\circ\text{C}$ , Photo 2 -  $t_a = 38.5^\circ\text{C}$ ,  
Photo 3 -  $t_a = 40.0^\circ\text{C}$ , Photo 4 -  $t_a = 41.4^\circ\text{C}$ .

**Fig. 78** Reproduction of colour transparency representing wall temperature contours at  $Re = 10000$ ;  $q = 228 \text{ W/m}^2$

Photo 1 -  $t_a = 35.7^\circ\text{C}$ , Photo 2 -  $t_a = 37.5^\circ\text{C}$ ,

Photo 3 -  $t_a = 40.0^\circ\text{C}$ , Photo 4 -  $t_a = 41.4^\circ\text{C}$ .

**Fig. 79** Contours of constant Nusselt number distribution around single cylinder at  $Re = 10000$ ;  $q = 228 \text{ W/m}^2$ ;  $D_h = 0.015 \text{ m}$

**Fig. 80** Contours of constant Nusselt number distribution around double cylinder at  $Re = 10000$ ;  $q = 228 \text{ W/m}^2$ ;  $D_h = 0.015 \text{ m}$

**Fig. 81** Reproduction of colour transparency representing wall temperature contours at  $Re = 10000$ ;  $q = 228 \text{ W/m}^2$

Photo 1 -  $t_a = 38.3^\circ\text{C}$ , Photo 2 -  $t_a = 39.4^\circ\text{C}$ ,

Photo 3 -  $t_a = 40.3^\circ\text{C}$ , Photo 4 -  $t_a = 42.0^\circ\text{C}$ .

**Fig. 82** Reproduction of colour transparency representing wall temperature contours at  $Re = 10000$ ;  $q = 228 \text{ W/m}^2$

Photo 1 -  $t_a = 38.3^\circ\text{C}$ , Photo 2 -  $t_a = 39.4^\circ\text{C}$ ,

Photo 3 -  $t_a = 40.3^\circ\text{C}$ , Photo 4 -  $t_a = 42.0^\circ\text{C}$ .

**Fig. 83** Contours of constant Nusselt number distribution around roughness plate at  $Re = 10000$ ;  $q = 228 \text{ W/m}^2$ ;  $D_h = 0.009 \text{ m}$

**Fig. 84** Reproduction of colour transparency representing wall temperature contours at  $Re = 10000$ ;  $q = 228 \text{ W/m}^2$

Photo 1 -  $t_a = 38.3^\circ\text{C}$ , Photo 2 -  $t_a = 40.3^\circ\text{C}$ ,

Photo 3 -  $t_a = 42.0^\circ\text{C}$ , Photo 4 -  $t_a = 44.7^\circ\text{C}$ .

**Fig. 85** Distribution of the local Nusselt number determined by the method employing human colour sensation and True-colour image processing, along a radius directly upstream and downstream of the cylinder (horizontal line represents channel base Nusselt number)

**Fig. 86** Colour TV images of the liquid crystal layer on a cooled plate disturbed by a cylinder

a) Image from RGB-camera

b) Image through a segmentation-monochrome line show  $27.7^\circ\text{C}$  isochrone

c) Image through chromaticity-adjust hue map

**Fig. 87** Local Nusselt number around root of double square determined by human colour sensation (horizontal line represents channel base Nusselt number)

**Fig. 88** Local Nusselt number around root of single square determined by human colour sensation and numerical simulation using Harwell-FLOW3D code

**Fig. 89** Numerical simulation of isothermal map around root of single square using Harwell-FLOW3D code for Reynolds number of 10000 and constant heat flux  $q = \text{const} = 228 \text{ W/m}^2$

A)  $t_a = 38^\circ\text{C}$  B)  $t_a = 39^\circ\text{C}$  C)  $t_a = 40^\circ\text{C}$  D)  $t_a = 41^\circ\text{C}$  E)  $t_a = 42^\circ\text{C}$

**Fig. 90** Temperature and velocity visualisation in a glycerol-filled cavity under free convection using neat chiral nematic liquid crystal;  
 $\text{Ra} = 1 \cdot 2 \cdot 10^4$  and  $\text{Pr} = 12 \cdot 5 \cdot 10^3$   
a) the horizontal position -  $\theta = 0^\circ$  showing the Bernard cells  
b) the vertical position -  $\theta = 90^\circ$

**Fig. 91** Temperature and velocity visualisation in a glycerol-filled cavity under free convection using neat chiral nematic liquid crystal;  
 $\text{Ra} = 1 \cdot 2 \cdot 10^4$  and  $\text{Pr} = 12 \cdot 5 \cdot 10^3$   
a) the inclination position -  $\theta = 30^\circ$   
b) the inclination position -  $\theta = 60^\circ$

**Fig. 92** Vertical velocity profiles at different heights in the vertical position of cavity;  
 $\text{Ra} = 1 \cdot 2 \cdot 10^4$  and  $\text{Pr} = 12 \cdot 5 \cdot 10^3$

**Fig. 93** Segmentation transform of the cavity image shown in framed region of Figure 86a  
1. Photo a - Hue: 40-60 2. Photo b - Hue: 100-120  
3. Photo c - Hue: 120-140 4. Photo d - Hue: 140-150

**LIST OF TABLES**

---

**Table 1. Some Temperature Sensing of TLC [118]**

**Table 2. Uncertainty Analysis**

## NOMENCLATURE

A	area
$C(\lambda)$	spectral sensitivity of the light intensity sensor
$c_p$	specific heat capacity
D	hydraulic diameter
d	diameter
F	function of colour components (Eqn.5)
$F_n(\lambda)$	spectral transmittance function
$f_n(\lambda)$	n-th band-pass filter transmittance
f	friction factor
g	gravitational acceleration
H	hue, corrugation height, cavity wall height
$H_i$	internal height
h	heat transfer coefficient
I	intensity
$I_n(T)$	intensity of colour components
$i(\lambda)$	spectral intensity of incident light
K	parameter of diamond geometry
k	thermal conductivity
L	corrugation cell length in the main flow direction
$\ell$	length of the structure in the main flow direction
n	refractive index
Nu	Nusselt number
P	helical or corrugation pitch, static pressure
Pr	Prandtl number
q	heat flux
R,G,B	intensities of colour components
Ra	Rayleigh number
Re	Reynolds number
S	parameter length of corrugation geometry, saturation
$S(\lambda,T)$	spectral reflectance of liquid crystals
s	wall thickness
T	absolute temperature

## NOMENCLATURE

t	temperature
v	velocity
X,Y,Z	co-ordinates
X	measured quantity

### Greek Letters

$\alpha$	thermal diffusity
$\alpha, \beta, \gamma, \delta$	regression constants
$\beta$	volume coefficient of thermal expansion
$\delta$	total thickness of liquid crystals components
$\epsilon$	uncertainty
$\lambda_0$	reflective wavelength
$\nu$	kinematic viscosity
$\rho$	density
$\varphi$	inclination angle
$\theta$	cavity angle of inclination, inclination angle

### Subscripts

a	air
av	average
b	water
c	cold
f	fluid
G	green
h	hydraulic
i	inlet, number of images
l	local value
m	mean
p	peak value
R	red
s	solid
t	trough value
w	water, wall

## 1. INTRODUCTION

### General

The theoretical equations for fluid flow and convective heat transfer are complex, non-linear partial differential equations, requiring the simultaneous satisfaction of continuity, momentum and energy principles. Current standard CFD (computational fluid dynamics) codes can now deal with three-dimensional transient problems associated with irregular geometries. Using the largest current computers it is now possible directly to treat not only 3-dimensional laminar transient flows, but also transitional and low-turbulent flows. For the two latter, the procedure is termed "direct simulation". For higher turbulence, however, the movement of the larger slower eddies may be resolved (large eddy simulation or LES) while the unresolved smaller eddies require a sub-grid model.

The whole-field nature of such numerical treatments and the broader question of general code validation, demand corresponding experimental methods. Laser doppler anemometry and, more recently, particle image velocimetry (PIV) have been established and are extensively used for obtaining point velocities and planar velocity field measurements respectively in wide ranging laboratory and industrial situations. For fluid temperature measurement, current techniques are usually invasive and difficult near the wall. Holographic interferometry, on the other hand, one of the number of new non-invasive optical methods, gives whole-field instantaneous temperature data on a par with LES. It can be applied qualitatively for thermal structure visualisation and also quantitatively. Another whole-field and surface method for heat transfer is the use of thermochromic liquid crystals (TLC). Due to a synergistic combination of TLC techniques and small, powerful computers, we are seeing a revolution in heat transfer and fluid flow research. Also, image processing of liquid crystal records has been established during the past several

years. The use of TLC now stands as a powerful technique, which will make possible new areas for research and new ways to think about heat transfer and fluid flow (Jones et al. 1992, Collins. 1991 and Moffat. 1990).

### Objectives of Research

The main purpose of the present study is to demonstrate the feasibility of liquid crystal and true-colour image processing in practical heat transfer and fluid flow contexts. Subsidiary aims are:

- (1) To introduce colour digital processing of liquid crystal images to yield full-field measurements of temperature and surface distribution heat transfer coefficients.
- (2) To establish a new experimental method (optical and non-invasive) to measure simultaneously both flow and thermal fields - this method may be described as particle image velocimetry and thermometry (PIVT).
- (3) To investigate temperature and heat transfer coefficient distributions on a cooled surface heated by an air flow and disturbed by a number of complex geometrical configurations, namely:-
  - crossed-corrugated geometrical elements as used in rotary heat exchangers (regenerators) for fossil-fuelled power stations,
  - circular (both single and double) and a square section column, and
  - square roughness elements.
- (4) Flow structure and temperature visualisation in a glycerol-filled rectangular cavity under free convection.

### Engineering Background

The engineering rationale for and description of the specific experiments are as given below.

#### i) Corrugated heat transfer

Rotary air heat exchangers used in power stations are large items of plant composed of very large numbers of nominally identical elements. Improvements in heat transfer performance could result in substantial reductions in energy costs. Using the latest experimental and predictive methods (developed in parallel at City University) the detailed flow and heat transfer characteristics for a common design of corrugated geometry (CG) heater element were investigated. How these characteristics depend on inclination angle, amplitude and pitch and Reynolds numbers was also obtained. This work is part of a comprehensive experimental and theoretical research programme, aimed at optimizing the geometry and the operating conditions of rotary regenerators.

#### ii) Heat transfer effects of obstructions

Circular and square columns, square roughness elements and more complex geometries exist in a wide range of environments involving heat transfer and fluid flow. They can be found in conventional heat exchangers used in cars, air conditioning industries and gas turbine internal cooling passages, as well as in high temperature gas-cooled nuclear reactors as spacer ribs. The induced flow around the geometries could enhance the convective heat transfer. The current work has investigated the variation of these heat transfer distributions within all the above geometries and at a Reynolds number of 10000. The experimental technique employed is a steady-state method which makes use of TLC and image processing to furnish a complete map of heat transfer coefficients or Nusselt numbers.

An experimental study using a circular cylinder attached to a heated plate was reported by Akino et al [2]. While their experiment used cool air, the present study uses heated air and the heat flux is in the opposite direction. Heat transfer measurements on and around a pedestal were performed by Ireland and Jones [66], however, they used liquid crystals for the surface temperature indicator in the transient inverse technique. The present experiments use TLC's to visualise the temperature distributions and measure the heat transfer coefficients on a cooled plate heated by air under forced convection. To evaluate heat transfer coefficient distributions quantitatively, only one temperature is used, corresponding to the red colour for the human observed method (HOM) and the yellow-green colour for true-colour image processing method (TIPM), respectively. With the temperature difference between the hot air and liquid isotherm fixed, different Nusselt number contours are determined by varying the heat flux. By these methods, the isothermals are determined almost independently either with (for HOM) or without (for TIPM) human colour sensation. While the overall procedure requires long waiting times before steady conditions are reached, the accuracy of the temperature determination is better than  $\pm 0.1^{\circ}\text{C}$ .

### iii) Heat transfer in cavities

Free convection is the dominant mode of heat transfer in many industrial applications, including nuclear reactor systems, electronic packaging, material processing and solar energy. Typical examples of enclosed spaces are window glazing and flat plate solar collectors. Free convection is preferred to forced convection because of its high reliability. It is evident that convective flows, as well as fluid motion in general, are specifically three-dimensional in nature. However, the limitations of mathematical analyses and experimental techniques have led to a very common trend of approximating convective flows by two-dimensional models. The experimental simulation and

mathematical modelling of two-dimensional convective flows have thus created many flow structures which do not appear to be comparable with real three-dimensional flows. Therefore, the aim of the present experiments in a glycerol-filled rectangular cavity is to create new techniques to determine three-dimensional temperature and velocity distributions in the fluid. Such is intended to provide either qualitative data for flow visualisation, or quantitative data for performance purposes, and comparison with theory.

## 2. PHYSICAL AND THERMAL CHARACTERISTICS OF LIQUID CRYSTAL

Liquid crystals constitute a class of matter unique in exhibiting mechanical properties of liquids (fluidity and surface tension) and optical properties of solids (anisotropy to light, birefringence). In the liquid crystal state constituent molecules are neither fixed firmly in three-dimensional array as in ideal solids, nor free to form random patterns as in ideal liquids. They are formed instead into structured layers which are free to slide over one another or to revolve about a fixed axis [83][118].

Liquid crystals are temperature indicators that modify incident white light and display colour whose wavelength is temperature. They can be painted on a surface or suspended in a fluid and used to make visible the distribution of temperature. Normally clear, or slightly milky in appearance, liquid crystals change in appearance over a narrow range of temperature called the "colour-play interval" (the temperature interval between first red and last blue), centred around the nominal "event temperature". The displayed colour is red at the low temperature margin of the colour-play interval and blue at the high end. Within the colour-play interval, the colours range smoothly from red to blue as a function of temperature [78].

Liquid crystal films exhibit another optical property known as circular dichroism, the selective scattering of right- or left-handed polarised light. When white light is directed at these substances the light is separated into two components, one with the electric vector rotating clockwise, the other counter-clockwise. One component is transmitted, one scattered. The wavelengths scattered depend on the nature of the substance, the temperature and the angles of incidence and view [36].

## **2.1 Classification**

In 1888 an Austrian botanist, Friedrich Reinitzer, observed that certain organic compounds appeared to possess two melting points (m.p.'s), an initial m.p. at which the solid phase turned to a cloudy liquid and a second m.p. at which the cloudy liquid turned clear (clearing point, Figure 1).

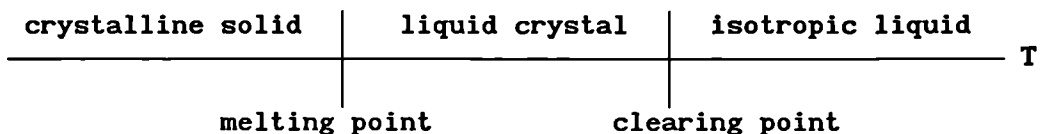


**Fig.1 The liquid crystalline phase on the temperature scale**

Further research revealed that an intermediate phase, or "mesophase", did indeed exist between the pure solid and pure liquid phases of some organic compounds. Reinitzer termed this phase as "liquid crystal", an appropriate designation when one considers that the material exhibits the fluidity of a liquid while at the same time maintaining a degree of the anisotropic, ordered structure of a crystalline solid. Since Reinitzer's original work, a great deal of research concerning the structure of liquid crystals has been carried out resulting in their classification into two categories: lyotropic and thermotropic.

**LYOTROPIC** liquid crystals result from the action of a solvent and hence are multi-component systems. A lyotropic liquid crystal can be destroyed or converted into an isotropic fluid at sufficiently high temperatures.

**THERMOTROPIC** liquid crystals, which also may be mixtures of compounds, result from the melting of mesogenic (liquid crystal-forming) solids and hence are thermally activated mesophases.

Excellent papers on this aspect of liquid crystal technology have been published by Brown and Shaw [11], Fergason and Brown [45,46], Dreher, Meier and Saupe [41], Stephen and Straley [104] & De Jeu [42]. Of particular interest in the present investigation is the use of thermochromic liquid crystals (TLC).

TLC's are "Thermotropic" in origin and have a chiral (twisted) structure. It is possible to classify liquid crystals according to the optical properties of their structures. Three classes can be distinguished from their differing optical properties and are called nematic, cholesteric and smectic. However, from a structural viewpoint, it can be argued that there are only two basic types of liquid, chiral-nematic and smectic, with cholesteric being regarded as a special kind of nematic.

The difference between nematic and smectic is certainly the major distinction among thermotropic liquid crystals. The structures are related to the dimensionality and packing aspects of the residual molecular order. Liquid crystal molecules are generally elongated, relatively rigid and rod-shaped. However, discotic liquid crystalline structures composed of large plate-like molecules also occur. Discussion here is limited to rod-like molecules.

The classes of liquid crystals are described briefly as follows:-  
**SMECTIC PHASE:** these liquid crystals are characterised by molecules that lie in planes with the long axes orientated perpendicular to the planes as shown in Fig.2. The structure displayed is one of many smectic phases. This variation of liquid crystal is the most solid like.

**NEMATIC PHASE:** it can be recognised from Fig.3 that in this phase the extent of randomness is greater than in the smectic phase. The molecules have the same long axis alignment but their positions are more unsystematic than in smectics.

**CHIRAL NEMATIC or CHOLESTERICS:** these can be classified as twisted nematics. This structure enables the liquid crystal to be exceptionally active optically.

The helical structures which the chiral nematics exhibit, as shown in Fig.4, are as a result of the long molecular axis being twisted from one layer to the other. Because of the impediment caused by the twist the chiral nematics are not as free flowing as nematics but are more so than smectics. As well as chiral nematics showing optical properties of iridescent colours, a chiral-smectics phase also exists and is used in TLC mixtures.

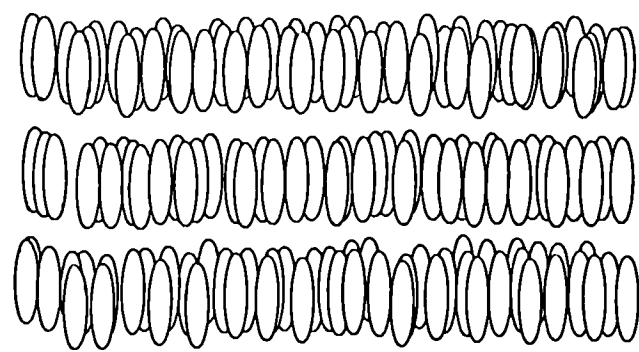


Fig. 2 The Smectic liquid crystal structure (from [118])

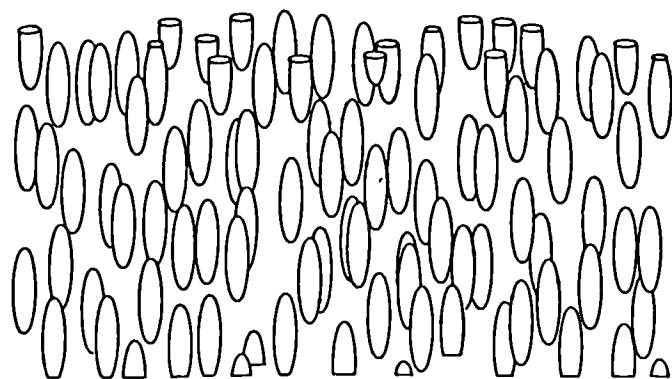


Fig. 3 The Nematic liquid crystal structure (from [118])

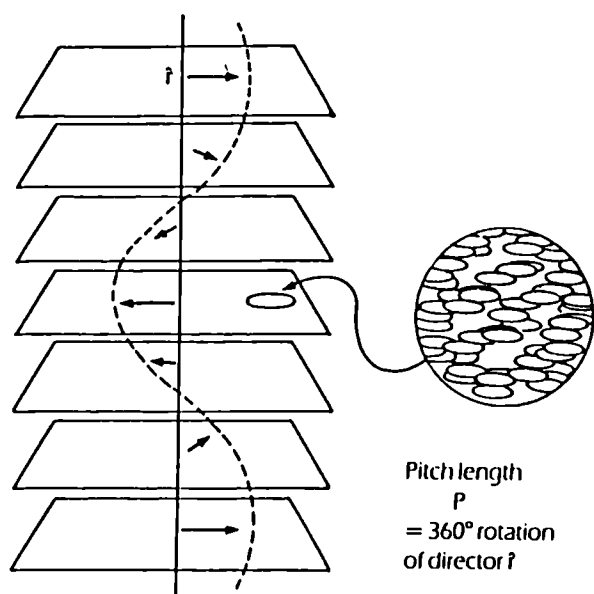


Fig. 4 The Chiral Nematic (cholesteric) liquid crystal structure. The director (arrow) traces out a helical path within the medium (from [118])

## **2.2 Compensated Mixtures and Textures**

Compensated chiral nematics are the product of left- and right-handed helically structured mixtures so as to derive a mixture with no handedness at a specific temperature.

The chiral nematics have three different characteristic appearances. These different textures are as a result of the orientation of the molecular and helical axis (Figure 5).

The FOCAL CONIC texture results if the orientation of the helical structure is perpendicular to the incident light source. This undisturbed form is optically inactive and has a milky white appearance.

The GRANDJEAN texture is an optically active mesophase. This disturbed form has a structure in which the helices are arranged with their axes parallel to the incident light and selective reflection of white light to show brilliant colours.

There also exists a third texture, HEMEOTROPIC, which is optically inactive,- the orientation of this structure is not well understood. The orientation of the Grandjean and focal conic textures is shown in Figure 6.

## **2.3 Structure of the Chiral Nematic Mesophase**

The chiral mesophase has a structure that is an accumulation of sheets of molecules. Each sheet direction varies in a regular way and this is defined by a unit director  $\hat{r}$ , as shown in Fig.4. This configuration form has a helical arrangement. The degree of twist called the pitch is the distance measured as the director completes a full circle. The helix configuration can be either left- or right-handed, but the liquid crystals are classified according to the sense of reflected light, so a right-handed helix will reflect left circularity light and therefore the liquid crystal is defined as left-handed.

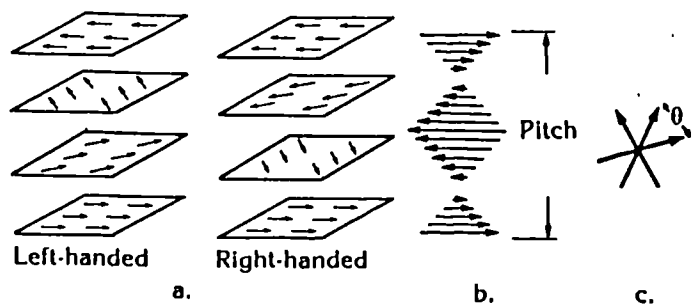


**Fig. 5 Left- and right-handed helical structures showing pitch  $P$  and displacement angle (from [118])**

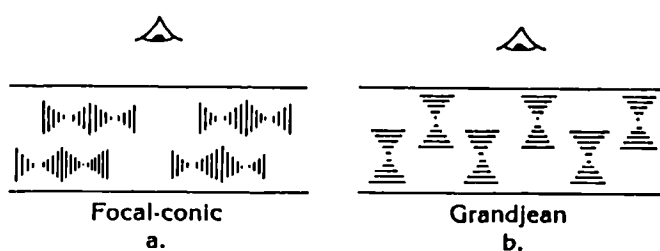


**Fig. 6 Orientations of helical (long lines) and molecular axes (short lines) relative to observer for a) focal conic texture and b) Grandjean texture (from [118])**

## 2.4 Optical Properties

The chiral nematics phase exhibits a number of properties being classed according to how it deals with white light changes as it passes through the structure.

The first basic property is BIREFRINGENCE. As the chiral nematic is an anisotropic material then light passes through only in certain directions at right angles. The structure will be different in each direction so therefore the refractive index will also be different. Hence, the effect shown in Fig.7a will be for unpolarised light entering and the chiral nematic structure. The initial beam will be split at different velocities. This phenomenon of double refraction is known as birefringence.

Chiral nematic liquid crystals are optically negative. This means that light travels with a slower velocity along the optic axis than it does at right angles to it.

A second optical property, shown in Fig.7b, is the chiral nematic HIGH OPTICAL ACTIVITY, giving rise to one plane of light being rotated several thousand degrees per mm (as indicated in the BDH brochure [118]).

The third property of relevance here is CIRCULAR DICHROISM. An incident light source, with both right and left circularity polarised light, will have one handedness transmitted and the other reflected at a particular wavelength. This wavelength depends on the angle of the incident light and the helical pitch of the liquid crystal (Fig.7c). The relationship of this wavelength is given by the equation:

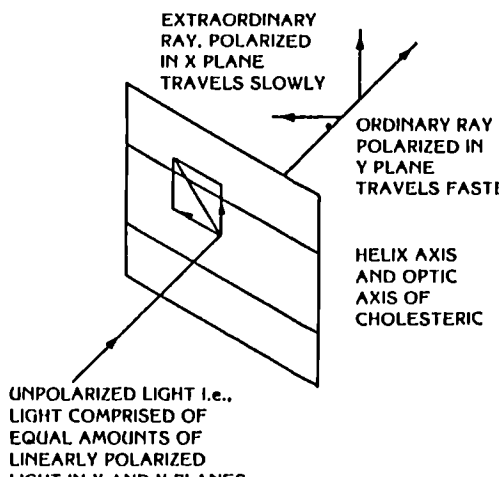
$$\lambda_0 = \bar{n} P \quad (1)$$

where

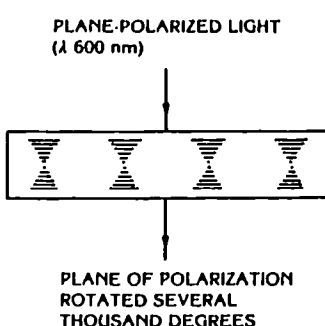
$\lambda_0$  = is the reflective wavelength,

$\bar{n}$  = is the mean refractive index, and

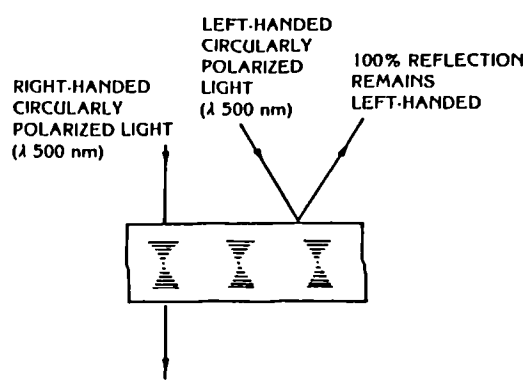
P = is the helical pitch.



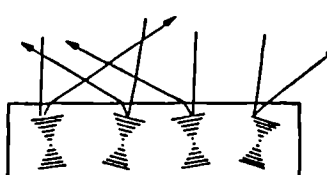
(a)



(b)



(c)



(d)

**Fig. 7 Optical properties of a hypothetical chiral nematic liquid crystal with right-handed helical structure and pitch corresponding to a reflective wavelength  $\lambda_0 = 500 \text{ nm}$ ;**

- birefringence-definition of negative optic axis,
- rotation of plane polarised incident light,
- circular dichroism,
- Bragg-type scattering of non-normal incident light (from [118])

A certain type of BRAGG SCATTERING also occurs and is similar to that which occurs with crystalline solids and X-rays. The liquid crystal acts as a three-dimensional grating and results in iridescent colours being produced. The colours are dependent on the temperature and angle of incident light, this effect being shown in Figure 7d.

The wavelength dependence of rotation of plane of polarisation and reflection coefficient in a hypothetical chiral nematic liquid crystal with a pitch corresponding to a reflective wavelength  $\lambda_0 = 500$  nm is shown in Figures 8a and 8b.

The structure of liquid crystals also changes with temperature variations. The response in this case is that the molecular distance along the helical axis grows and this in turn increases both the pitch and the displacement angle between adjacent molecules in the helical stack. This tends to decrease but the degree is much smaller than the effect increasing the pitch, therefore, in most cases, the pitch always decreases, increasing pitch being exceptional. Typical pitch vs temperature response of thermochromic liquid crystal is shown in Figure 9.

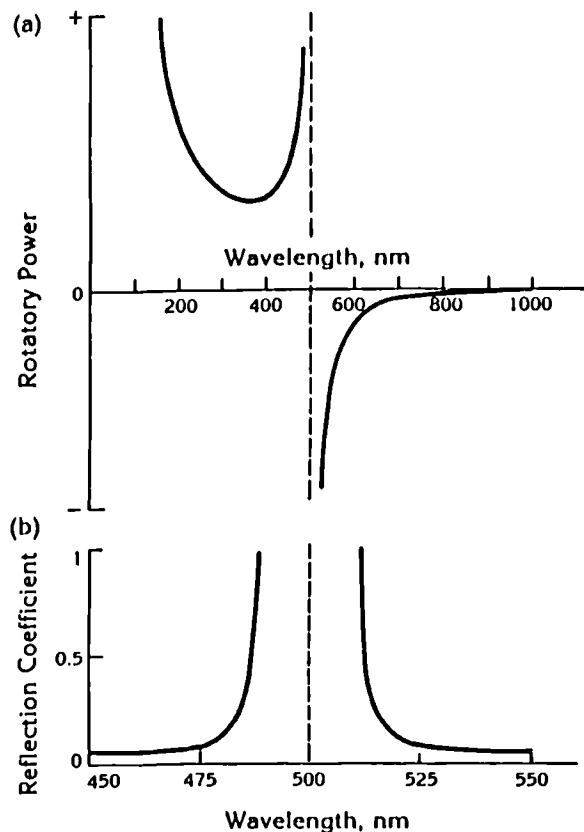


**Fig. 8** The wavelength of dependence of:  
 a) rotation of plane of polarisation and  
 b) reflection coefficient in hypothetical chiral nematic liquid crystal with a pitch corresponding to a reflective wavelength  $\lambda_0 = 500$  nm (from [118])

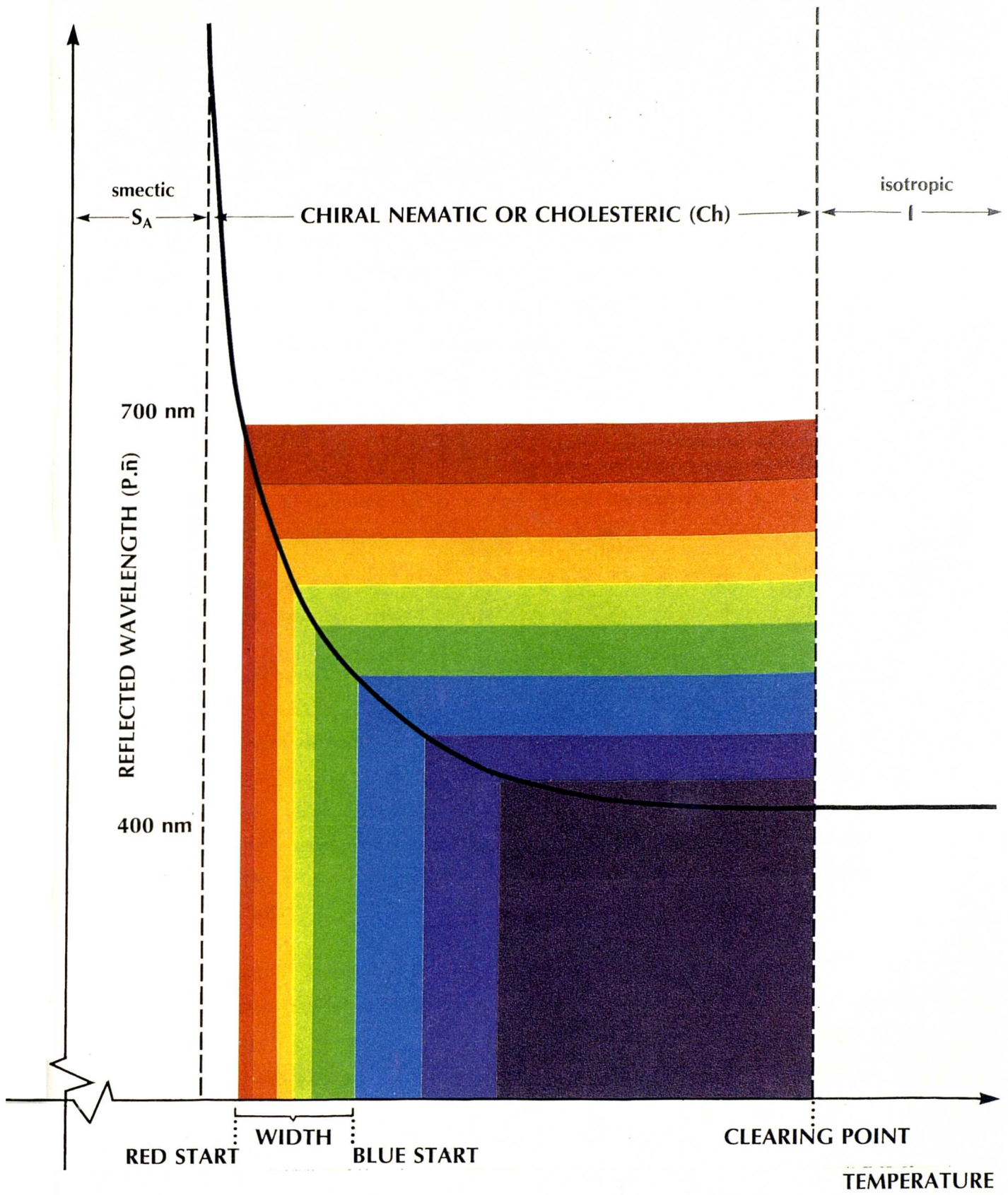


Fig. 9 Typical pitch vs temperature response of thermochromic liquid crystal (from [118])

## 2.5 Colour Play Properties

TLC mixtures, and products made from them, all have a characteristic red start or mid-green temperature and colour play bandwidth. The bandwidth is defined as the blue start temperature minus the red start temperature. The colour play of TLC is defined by specifying the red start or mid-green temperature and the bandwidth. Mixtures are identified by a code which gives the red start (R) or mid-green (G) temperature, the temperature scale (C or F) and the colour play bandwidth (W).

Some examples are given below:-

1. R27C2W is a mixture with a red start temperature at 27°C and a blue start temperature 2°C higher, at 29°C.
2. G97F1W is a mixture with a mid-green temperature at 97°F and a red start to blue start bandwidth of 1°F.

Each different thermochromic formulation is identified by a number, for example, R30C6W is 100 and R27C6W is 107. For chiral-nematic mixtures which are not microencapsulated this identity number is prefixed by the letters TM, and for microencapsulated mixtures the prefix is TCC. For example, TM100 is a non-microencapsulated (neat liquid crystal) mixture having a colour profile described by R30C6W and TCC107 is a microencapsulated mixture having a colour profile described by R27C6W.

Temperature insensitive (also called shear-sensitive) TLC are defined by specifying colour and clearing point. The clearing point is defined as the temperature above which the colour disappears (the cholesteric liquid crystal to isotropic liquid transition temperature).

Formulations of TLC are available which show colour plays varying from 0.5°C to in excess of 20°C over the temperature range -30°C to 115°C depending on the particular range required. Figure 10 shows one example of a composition diagram giving both colour play range and

temperature for TLC mixtures TM74A plus 70wt% TM75A. The example shown gives a colour play beginning at 21°C and colour play 0.7°C.

Single colour liquid crystals are also available; the colour can be any colour of the spectrum but, for maximum apparent intensity to the eye, green is suggested. Apart from a very slight colour change as the temperature rises (less than 2 nm per °C), there is a sudden loss of colour as the liquid crystal melts to become a transparent liquid. This melting will normally take place over a range of about 0.5°C. Single colour liquid crystals can thus be used to show if a test surface is above or below a certain temperature - the melting point.

The melting point of single colour LC can be anywhere in the range -20°C to 120°C, with an accuracy of ±0.5°C, although mixtures with a melting point above 60°C are liable to crystallization at normal storage temperatures and may need melting before use.

Colour plays of TLC mixtures are very sensitive and susceptible to change during any processing step to which the materials are subjected. Care must be exercised whenever the materials are handled.

## 2.6 Use of the Materials

The unique properties of TLC can only be used to advantage if they are controlled, and the materials made to behave predictably for a given period of time. For research applications, the expected duration of the experiment or study will be the obvious criterion.

The new, stable, versatile, wide temperature range thermochromic mixture made with BDH chiral-nematic materials will allow the successful development of a number of potential applications previously unobtainable with cholesteryl esters for one reason or another. Some possible applications are listed in Table 1 [118].

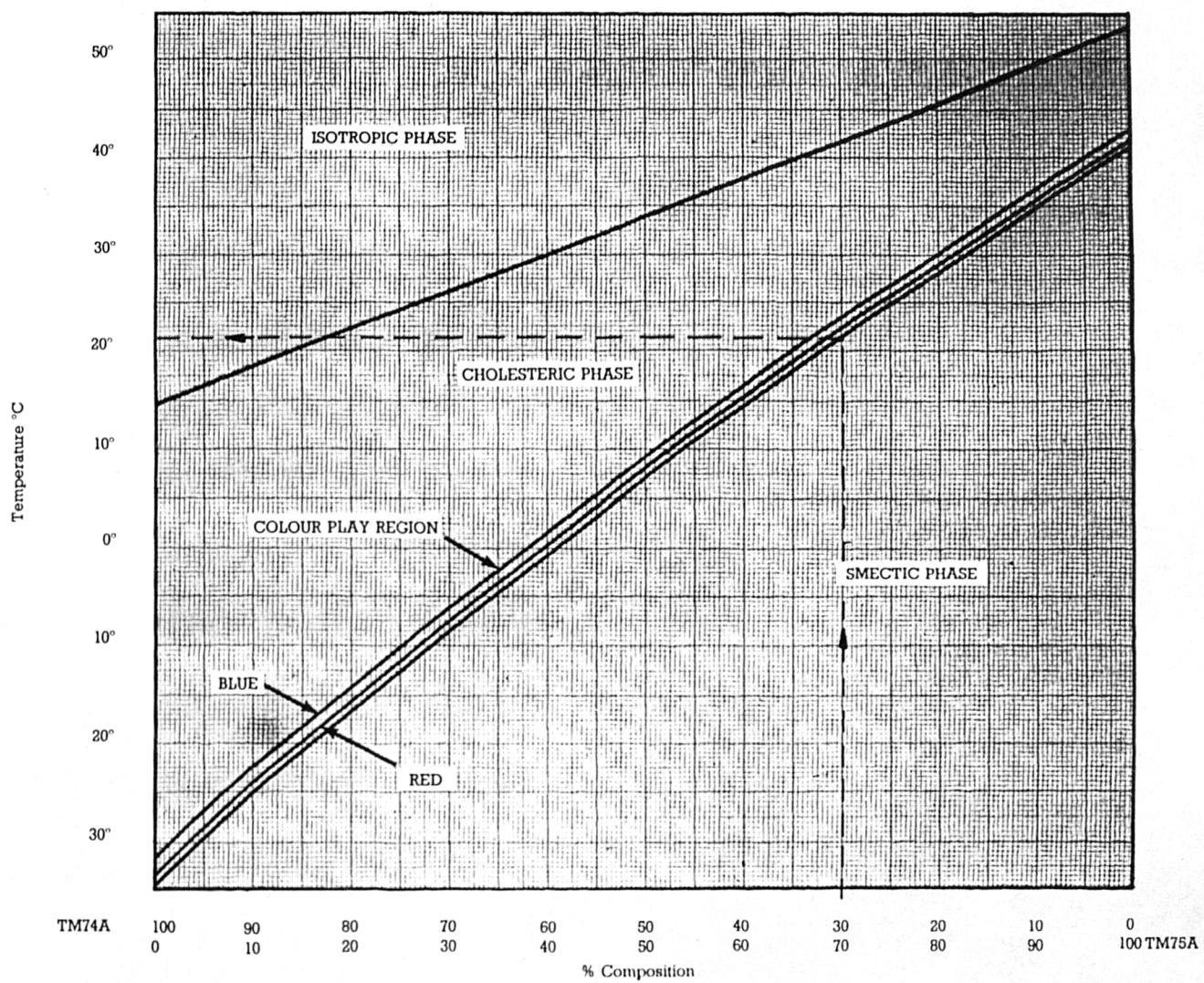


Fig. 10a Phase diagram for mixtures of TM74A and TM75A (from [118])

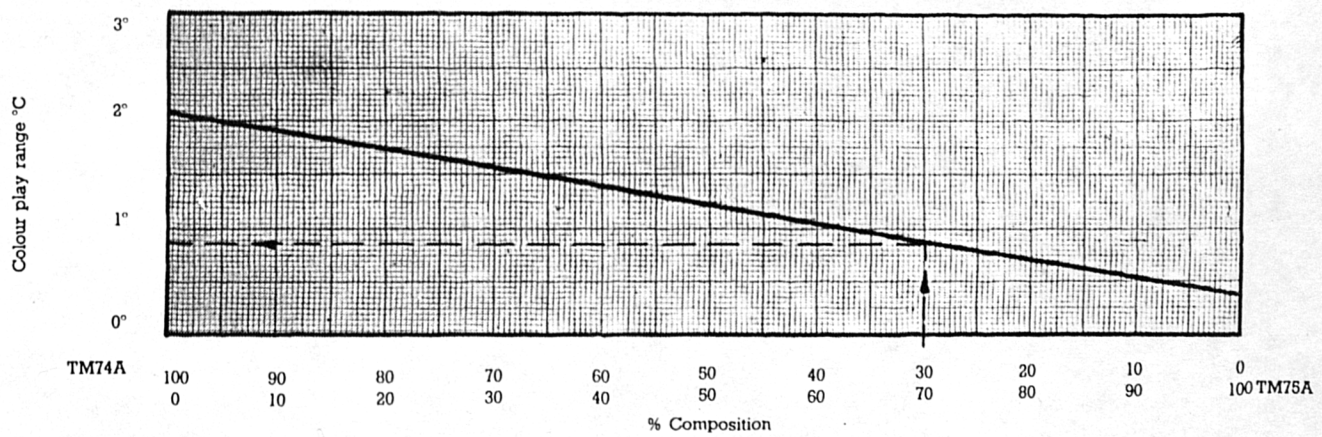


Fig. 10b Colour play range for mixtures of TM74A and TM75A (from [118])

Temperature Range/ <sup>o</sup> C	Possible Applications
-30 to -10	Freezer Food Applications Freezer-Thaw Indicators
-10 to 0	Ice Warning Indicators Blood Banks Refrigerators, etc.
0 to 20	Wine Bottle Labels Beer (Lager) Labels Food Storage Advertising (e.g. on cold drink cups)
20 to 30	Advertising (point of sale displays) Decorative (wall coverings, etc.) Thermometric (all temperatures)
25 to 45	Jewellery/Badges Medical Thermography Clothing/Fabrics Radiation Detectors Non-Destructive Testing
50 to 80	Heat Warning Indicators Domestic Cookers, Pan Handles, etc. "Do Not Touch" Applications Advertising (e.g. on coffee, tea cups)
90 to 100	Steam Point/Boiling Indicators
100 to 150	Industrial Applications: Superheating, Sterilization, Pipework Indicators, Machine Overheating, etc.

Table 1 Some temperature sensing applications of TLC [118]

The applications listed in the table rely on the variation of the reflected colour with change in temperature. This is by far the most important property of chiral-nematic liquid crystals from the applications viewpoint. Temperature sensing applications can be broadly categorised as below:-

- 1. Temperature Indication/Measurement**
  - a) Digital Thermometers
  - b) Heat Warning Indicators
  - c) Freeze/Thaw Indicators
- 2. Medical Thermography**
  - a) Breast Cancer Detection
  - b) Sub-cutaneous Cancer Detection
  - c) Diagnosis of Vascular Disease
  - d) Placental Location
  - e) Pharmacological Tests
  - f) Skin Grafting
  - g) Vein Location
  - h) Veterinary Use, etc.
- 3. Non-Destructive Testing**
  - a) Detection of surface and sub-surface flaws in metals, welded metals, bonded structures and other composite structures.
  - b) Fault detection in electric components and electronic circuits, etc.
  - c) Turbulent flow determination in aerodynamic models.
  - d) Laminar and turbulent flow visualisation.
- 4. Radiation Detectors**
  - a) Thermal Imaging
  - b) Holography of infra-red microwave and ultrasonic radiation.
- 5. Aesthetic**
  - a) Advertising, point-of-sale displays, etc.
  - b) Decoration, wall coverings, etc.
  - c) Jewellery, badges, fabrics, clothing, etc.

TLC's can be used in a number of different forms:

- a) As the unsealed liquids
  - the neat LC mixtures, or
  - in solution
- b) In the microencapsulated form
  - aqueous slurries, etc.
  - coating formulation
- c) Coated (printed) sheets

#### **2.6.1 Unsealed Liquids**

The chemicals used in TLC mixture manufacture are essentially oils and the consistency of most TLC mixtures at their working temperatures varies between that of a thick oil (motor oil) and a viscous paste (lanolin). They are difficult to use and are commonly applied as the isotropic melts, or as solutions by small brush or spray.

Unsealed TLC mixtures need to be applied in thin uniform films with thicknesses varying from 5-10 microns for chiral-nematics up to as much as 50 or more microns for cholesterics. The resulting large surface area to volume ratio gives rise to a high susceptibility to degradation, particularly from ultraviolet light and also from oxygen in the atmosphere which can diffuse into the shallow film easily. Films of unsealed TLC are also very sensitive to certain chemicals, particularly fats, greases and common solvents. The presence of small amounts (as little as a few ppm) of these chemicals can change the accurately calibrated colour play response of mixtures. In addition, dust and fibre particles are readily trapped by viscous films of unsealed TLC. These can induce changes in the film from the maximally reflecting, planar texture of the cholesteric/chiral-nematic mesophase

to the colourless focal-conic texture. High viscosity can also result in entrapment of solvent which may have been used to apply the film initially; here the volatile solvent will eventually evaporate out, changing the colour-temperature characteristic of the film as it does so.

As a result of the effects described above, the lifetime of unsealed TLC film can vary from a matter of hours to days, depending on how the materials are used. In studies involving shear-induced rather than temperature-induced colour changes, the materials must be used in the form of neat, unsealed liquids. It is possible to design experiments to take the limited lifetimes of the materials into account and chiral-nematics in particular have been used successfully in a number of recent studies.

In general, however, the degree of stability offered by the materials as the neat, unsealed liquid falls far short of that required for the successful commercial exploitation of their unique properties in the majority of temperature indicating applications.

#### 2.6.2 Microencapsulation (Slurries and Coatings)

To date, the microencapsulation process has been the most versatile, widely applicable and successful way of stabilising, packaging and protecting TLC mixtures. The TLC is isolated from the atmosphere by a protective barrier and, at the same time, converted into a comparatively easy-to-use form. In simple terms, a microcapsule is a small sphere with a uniform wall around it, and in the micro-encapsulation process tiny particles or droplets of liquid crystal are surrounded by a coating to give discrete microcapsules. Most micro-capsules have diameters ranging from a few microns (8-15 microns) and a few millimetres [118].

The product of the microencapsulation process is an aqueous slurry of discrete TLC-containing microcapsules. This can be used directly (e.g. in hydrophilic liquids as tracer particles in flow field studies) or more commonly is incorporated (as a temperature sensitive pigment, in effect) into a coating formulation optimised for a particular method of application (e.g. spraying, screen-printing, etc.), for a given surface. The coating, when dry, should ideally support the liquid crystal in a uniform film with the minimum degrading effect on the intensity and purity of the selectively reflected light. Thus, isolated to a certain extent from the deleterious effects of the atmosphere and ultraviolet light, and partially protected from solvents and impurities, microencapsulated TLC mixtures offer improved stability and versatility of use over their unsealed precursors. While initial protection against degradation can be provided by microencapsulation, further protection can be achieved by the use of materials with ultraviolet absorbing properties. Whenever possible water resistant coatings should be used.

### **2.6.3 Coated (Printed) Sheets**

The majority of commercial temperature indicating devices using TLC contain a thin film of the liquid crystal sandwiched between a transparent polyester sheet and a black absorbing background. The standard method of producing such devices, which has evolved since the late 1960's, has been to produce a coating (ink) containing preferably microencapsulated TLC and use a printing method to apply it to the supporting substrate. A black ink is then applied on top of the dry TLC coating and colour change effects are viewed from the reverse (uncoated) side of the sheet. Adhesive can be applied to the back of the sheet to facilitate adhesion to a variety of surfaces.

Optimum coating thicknesses vary with method of application, coating composition, microcapsule size and nature of the substrate. For example, good results (clear, bright colours, no shift in colour/temperature profile) are achievable on polyester sheet (application by screen-printing) with capsules having a typical diameter of 10 microns contained in an ink with a solids content of 25-30% (weight) when a wet film thickness of 40-50 microns is used. This dries to give a coating 10-15 microns thick.

The different forms of the materials are suited to various temperature and flow visualisation applications, examples of which are given in the literature review and prior work.

## APPENDIX 2.1

### A GLOSSARY OF TERMS ASSOCIATED WITH TLC [118]

TERM	DEFINITION
<b>Chiral Nematic</b>	A special kind of liquid crystal that has a natural twisted structure, exhibiting thermochromism if the pitch is of the order of wavelength of visible light. Also called cholesteric. The term "chiral nematic" is preferred by BDH as many such materials are not derivatives of cholesterol.
<b>Chiral Smectic</b>	A special kind of smectic liquid crystal that has a natural twisted structure.
<b>Cholesteric</b>	See chiral nematic. Originally used as such substances were derived from cholesterol.
<b>Cholesterol</b>	Naturally occurring organic substance from which cholesteryl esters, carbonates and halides are derived, many of which can be used in thermochromic mixtures. These are frequently difficult to purify and suffer from chemical and photochemical instability.
<b>Colour-Play Band</b>	The temperature range in which light of the visible spectrum is reflected.
<b>Electro-Optic Liquid Crystal</b>	Liquid crystal used in electro-optic display which reacts to electrical stimulus.
<b>Encapsulated Liquid Crystal</b>	See Micro-encapsulated liquid crystal.
<b>Focal-Conic Texture</b>	One of the possible textures of the chiral nematic mesophase, optically inactive and usually undesired. Forms upon cooling the isotropic liquid without disturbance.

<b>Grandjean Texture</b>	The optically active texture of the chiral nematic mesophase, exhibits iridescence and selective reflection of white light to show brilliant colours. Sometimes known as planar or disturbed.
<b>Isotropic</b>	The conventional liquid phase.
<b>LICRITHERM</b>	Trade Mark of BDH Ltd. for thermochromic liquid crystals, mixtures and coatings.
<b>Liquid Crystal</b>	Material in a state intermediate between a crystalline solid and an ordinary (isotropic) liquid, so called first by Lehmann in 1889 because it exhibits optical properties of a crystal and mechanical properties of a liquid. Many different liquid crystal structures exist.
<b>Mesophase</b>	Short for mesomorphic phase (mesomorphic-of intermediate form).
<b>Micro-Encapsulated Liquid Crystal</b>	Small droplets of liquid crystal, usually thermochromic, encased in gelatine (cross-linked with an aldehyde). Sometimes shortened to Encapsulated liquid crystal.
<b>Nematic</b>	A structure or mesophase of liquid crystal of which the chiral nematic is a special form.
<b>Planar Texture</b>	See Grandjean.
<b>Polymer Dispersion</b>	Droplets of liquid crystal dispersed in a polymer matrix to protect the liquid crystal and make a surface coating. Rarely used with thermochromics.
<b>Smectic</b>	A structure or mesophase of liquid crystal, more solid-like than nematic, occurs at temperatures below the (chiral) nematic phase.
<b>Thermochromic</b>	A material that reacts to change in temperature by changing colour.

### 3. LITERATURE REVIEW - THE USE OF LIQUID CRYSTALS

Liquid crystals were first reported in 1888 by Reinitzer, but their application has greatly increased very recently. No early reports of engineering are apparent from European literature, but liquid crystals began to play a role in non-destructive testing in the U.S.A. in the early 1960's. This review was compiled at the end of 1991 utilising, among others, the recent reviews of Parsley and Moffat in [83] and [78] respectively. It is not claimed to be exhaustive, and additional work has been published recently.

#### 3.1 Visualisation of Boundary Layer Transitions

The use of TLC's in wind tunnel experiments was first investigated by Klein [73,74] in 1968. Klein employed unencapsulated TLC's as the surface temperature sensor in determining the location of laminar and turbulent layer transitions on aircraft models. Also, the TLC's were able to show the temperature distribution on the model surface because turbulent areas appeared hotter than laminar ones on an insulated surface - a turbulent boundary layer exhibited a different colour to its laminar counterpart. The difference in colour displayed by the liquid crystals was a consequence of the slightly higher adiabatic wall temperature associated with the turbulent flow. Although Klein was able to obtain such qualitative information using the liquid crystal technique, he was unsuccessful in attempts to obtain quantitative data due to the adverse effects of surface contamination, ultraviolet light and flow induced shear stress produced on the unencapsulated liquid crystals.

In a follow-up study, Klein and Margozzi [75] attempted to develop a technique for visually measuring shear stress by utilizing the shear stress sensitivity of certain types of unencapsulated TLC's. Although they found that liquid crystals could be formulated that were

relatively sensitive to shear and insensitive to temperature, they found it difficult to interpret accurately the colour signal produced by the crystals since the liquid crystal coating tended to flow and develop a rough texture in response to the shearing effects of the flow. It was concluded that while it appeared feasible in principle to measure shear stress using unencapsulated liquid crystals, much additional research would be needed to develop liquid crystals that could exhibit high shear sensitivity combined with low temperature, angle and pressure dependence.

McElderry [77], in an investigation similar in principle to the one conducted by Klein, used microencapsulated cholesteric liquid crystals as a means of determining boundary layer transition on a flat plate placed in a supersonic air stream. McElderry found that the encapsulated liquid crystals produced colour displays unaffected by the adverse sensitivity to shear and contamination that Klein had experienced with unencapsulated crystals. McElderry also found that the colours displayed by the unencapsulated liquid crystals were relatively independent of viewing angle. Since his study, significant advances have been made on the materials side, and the use of chiral-nematic mixtures (available commercially for the first time in 1981/82) rather than cholesterics has enabled research work to overcome many of the problems encountered in the original study.

Figure 12 shows an image from a study of Klein [73] of a turbulent boundary layer on a supersonic aeroplane model.

### 3.2 Surface Temperature and Heat Transfer Measurements

TLC's have been employed in a number of interesting applications for surface temperature and heat transfer measurements over the past several years. To date, most work has involved qualitative interpretation, that is to say, observing hot and cold regions without

regard to the precise temperature levels displayed so colourfully by the liquid crystals. Liquid crystal surface temperature mapping is used in the undergraduate heat transfer laboratory at Stanford University [78]. Liquid crystals applied to high porosity, low-thermal conductivity plastic windows screens, or plastic honeycomb material, have been used to make visible the temperature distributions in stratified air flows. Most of the liquid crystal activity, over the past ten years, has been aimed at measuring surface heat transfer coefficients.

In the field of non-destructive testing, liquid crystals have been used to check for irregularities on bonded structures [39][40], to observe regions of overheating on electronics equipment [14][39][40], to check for flow blockages in heat exchangers [114], crack detectors on aircraft structures [114], and to check the effectiveness of windshield heaters [14][39][40]. These are but a few typical applications. In the medical field, TLC's have been used to observe surface blood flow patterns in humans and as a diagnostic tool for the detection of breast cancer [36,37]. Figure 11 shows a liquid crystal thermogram of the human hand [118]. LC's have also been used to study the characteristics of laser and ultrasonic beams [29].

The heat transfer coefficient is a defined quantity, calculated from the surface heat flux and the difference between the surface temperature and some agreed-upon reference temperature, usually the far field temperature, the fluid mixed mean temperature or the adiabatic surface temperature. Liquid crystals can be used to determine the distribution of surface temperature, and if the surface heat flux can be found, this allows evaluation of the heat transfer coefficient [78].

Two techniques are available for mapping the surface heat transfer coefficient using liquid crystals: steady-state and transient.

### Steady-State Methods

An electrically heated membrane painted with liquid crystals is used to create a situation in which both the surface heat flux and the surface temperature distributions are known, from which the heat transfer coefficient can be calculated, once the reference temperature is chosen. Three types of membrane have been used: (i) graphite impregnated paper, (ii) vapour deposited gold on polycarbonate, and (iii) thin stainless steel foil. The steady-state technique has been extensively reported in the literature hence only a few references will be cited here for illustration.

The first quantitative results were published by Cooper et al in 1973/75 [27,28,29]. They observed boundary layer transition and separation on a heated cylinder in cross-flow and evaluated the variation of Nusselt number around the cylinder and the temperature field produced by a cryosurgical probe. Carbon-impregnated electrically resistive paper (Themsheet) was used as the membrane in this work, two Themsheet cylinders being employed in the investigation. One cylinder was coated entirely with single homogeneous liquid crystals. The other cylinder was coated with a series of circumferential strips of crystals. Figures 13 and 14 are displays of typical liquid crystals results associated with subcritical and critical flows, respectively. The shaded region on each liquid crystal band represents colour. The liquid crystal thermographic technique developed in Cooper's investigation provides an excellent means of obtaining both qualitative and quantitative heat transfer information on heated objects placed in forced convection environments.

Goldstein et al [53,54] used liquid crystals to visualise the temperature distributions and measure the heat transfer coefficients on a heated plate cooled by impinging jets. To evaluate temperature distributions quantitatively they made use of only one temperature corresponding to the colour boundary between green and blue, which was

sharpest to (their) naked eye. In this way the isothermal line was determined almost completely besides avoiding any ambiguous judgement of colour by human sensation, Figure 15.

Kasagi et al [71], Baughn et al [8] and Simonich et al [90] improved the method (they used gold deposited on polycarbonate) in a study of film-cooling and flat plate heat transfer. A monochromatic light source [(a) a sodium lamp emitting light at 589 nm and (b) a mercury-vapour light of 546.1 nm wavelength, and photographed with high-contrast black and white film], was used selectively to illuminate the single isothermal line. By these methods, the isothermal line could be determined almost independently of human capability to judge colours, but they obtained only one line, Figure 16. Therefore, to record multiple isothermal lines for a thermal contour map, the temperature levels of the heat transfer surfaces were altered by changing the heating rate. Unfortunately, this procedure required long waiting times before steady conditions were reached.

Hippensteele et al [62], Ireland et al [66,67] and Klein et al [73,74] describe several important improvements in a new technique for measuring and mapping local heat transfer coefficients. The first development involves the use of a new encapsulated thermochromic liquid crystal which has better stability and a narrower bandwidth than the cholesteric crystals previously used. The second important improvement is in the packaging arrangement. In this new arrangement, useful for gas flow, the liquid crystal is applied directly onto the surface of an electrically conducting gold or stainless steel coating used as an electric heater, and is essentially in direct contact with the fluid. The new packaging arrangement has two advantages. First, no correction for the temperature drop across the plastic substrate is required. Second, a significant increase in the maximum detectable frequency is predicted. In order to improve the measuring and mapping

of local heat transfer coefficients the light density is measured by using a video image processor, a scanning micro-densitometer, high bandwidth photodiode detector or monochromator and photomultiplier. The steady-state technique has been used to visualise the heat transfer coefficient distributions caused by secondary flows on turbine vane end-walls by Hippensteele et al [62] with results shown in Figure 17.

More recently, this technique has been applied to study the thermal effects of Görtler vorticity in laminar boundary layers, in both a water channel with vertical curved walls and a curved test section of a wind tunnel with a horizontal test wall at the start of curvature, Crane and Sabzavari [35].

The main disadvantage of the steady-state technique lies in the requirement for applying a uniform electric heater on the surface. For all practical purposes, this seems to limit the method to specimens which can be wrapped in a sheet. The transient technique overcomes this restriction.

#### Transient Methods

The main advantage of the transient heat transfer technique using liquid crystals is that the test model need not be actively heated and high resolution measurements on surfaces with complex shapes may be obtained [69][78].

Ireland and Jones [66,67] seem to have been the first to use liquid crystals for the surface temperature indicator in the transient inverse technique.

Data from a transient test consists of a time-sequence of records (usually photographic or video) of the appearance of the surface. The

pattern of isochromes is interpreted as isotherms using the calibration of the liquid crystal, and the time temperature history of each considered point determined by curve-fitting and interpolation.

A typical picture of the liquid crystal colour lines in a transient test is shown in Fig.18 at a certain time within the run, from the work of Jones and Hippensteele [60]. They executed a comparison test, evaluating the heat transfer coefficient distributions on the same specimen by both steady-state and transient methods using a chiral-nematic liquid crystal. One such record of the steady-state method is shown in Figure 19.

The steady-state and transient methods were also compared by Baughn et al [7] who measured the local heat transfer coefficient around a circular pin-fin in a channel by both methods. Jones et al and Baughn et al [69][7] respectively encountered difficulty in comparing the results of the two techniques; this was a consequence of the effect of temperature boundary conditions on the value of  $h$ , as conventionally defined.

### **3.3 Flow Visualisation in Fluids**

Liquid crystals have been used in fluid as well as in air. Temperature distributions and velocity fields have been visualised using the materials in the unsealed (neat) and microencapsulated forms as both tracer particles in flow fields studies and as surface coatings [35][60,61,69][71][86][91].

The encapsulated forms of both chiral-nematic and cholesteric liquid crystal materials can be mixed directly into water, glycerol and silicone oils to use as thermal and hydrodynamic tracers. Very diluted mixtures are recommended, 0·01%-0·02% by weight of LC material in water being sufficient, for example. Too much LC will cause a milky

appearance, representing white light scattered from the surface of the particles, which dilutes the colour. Flow structures are visualised using photographic records of the motion of tracer particles illuminated by a sheet of white light.

Tanaka [106] reported using liquid crystals to visualise the temperature distributions in water with application to thermal storage tanks. Natural convection has more recently been studied using a liquid crystal suspension in silicone oil and glycerol by Akino et al [78], Hiller and Kowalewski [60] and Stasiak and Grygiel [91] respectively. Figure 20 shows the photograph of convection flow visualised with the help of liquid crystals in the vertical mid-plane of a cavity (from Hiller and Kowalewski [60]) where the motion is caused by natural convection between two vertical walls at different temperatures.

The influence of rotation on Marangoni convection and centrifugal-buoyancy driven motion in a rotating cylinder has more recently been studied using a microencapsulated liquid crystal suspension in glycerol by Szymczyk et al [105] -for flow visualisation a stroboscopic illumination was used. One of their images is shown in Figure 21.

In addition, coatings containing microencapsulated TLC mixtures, insensitive to the effects of shear stress, have been used to obtain quantitative surface temperature measurements on water tunnel models [80]. Furthermore, shear sensitive unsealed TLC mixtures have been used successfully in hydrodynamic flow visualisation on surfaces producing high resolution observations of both steady and unsteady boundary layer separation and transition characteristics [86].

### 3.4 Flow Visualisation Using Shear-Induced Colour Changes

More recently, a new technique for visualising flow and interpreting local measurements of shear stress has been reported by Holmes and Obara [63] and Bonnett, Jones and McDonnell [9]. They were examining in detail the selective reflection from chiral-nematic liquid crystal as a function of illumination and viewing angles under precise shearing conditions in a wind tunnel as well as between rotating parallel disks. All results are discussed in relation to their application for flow visualisation and shear measurement in aerodynamic testing. Also, they present an improved method for detecting laminar-to-turbulent boundary-layer transitions that utilizes a flow-induced texture change from focal-conic to Grandjean. Figure 22 shows an example of Bonnett, Jones and McDonnell [9] experiments which employed a chiral-nematic mixture to give flow visualisation and shear-stress indication by horse-shoe vortex around a cylinder pedestal.

The use of TLC's overcomes the limitations of sublimating chemicals and oil flow techniques and provides transition visualisation capability throughout almost the entire altitude and speed ranges of virtually all subsonic aircraft flight envelopes [73,74,75][63,64]. The methods are also widely applicable to supersonic transition in flight and for general use in wind tunnel research over wide subsonic and supersonic speed ranges.

The unique colour-change properties of the materials coupled with the versatility of use afforded by their availability in a number of different forms makes TLC's a very attractive and interesting tool not only for the researcher. Chemists have added a new dimension to the revival in sixties "psychedelia" by developing materials that change colour when they change temperature. Chemists at Merck, a chemicals company based at Poole, Dorset, tailored the materials so that they alter hue at temperatures between 28°C, when the material is red, and 33°C when it turns blue. Figure 23 shows chameleon clothing recently developed by Merck and the London School of Fashion [26].

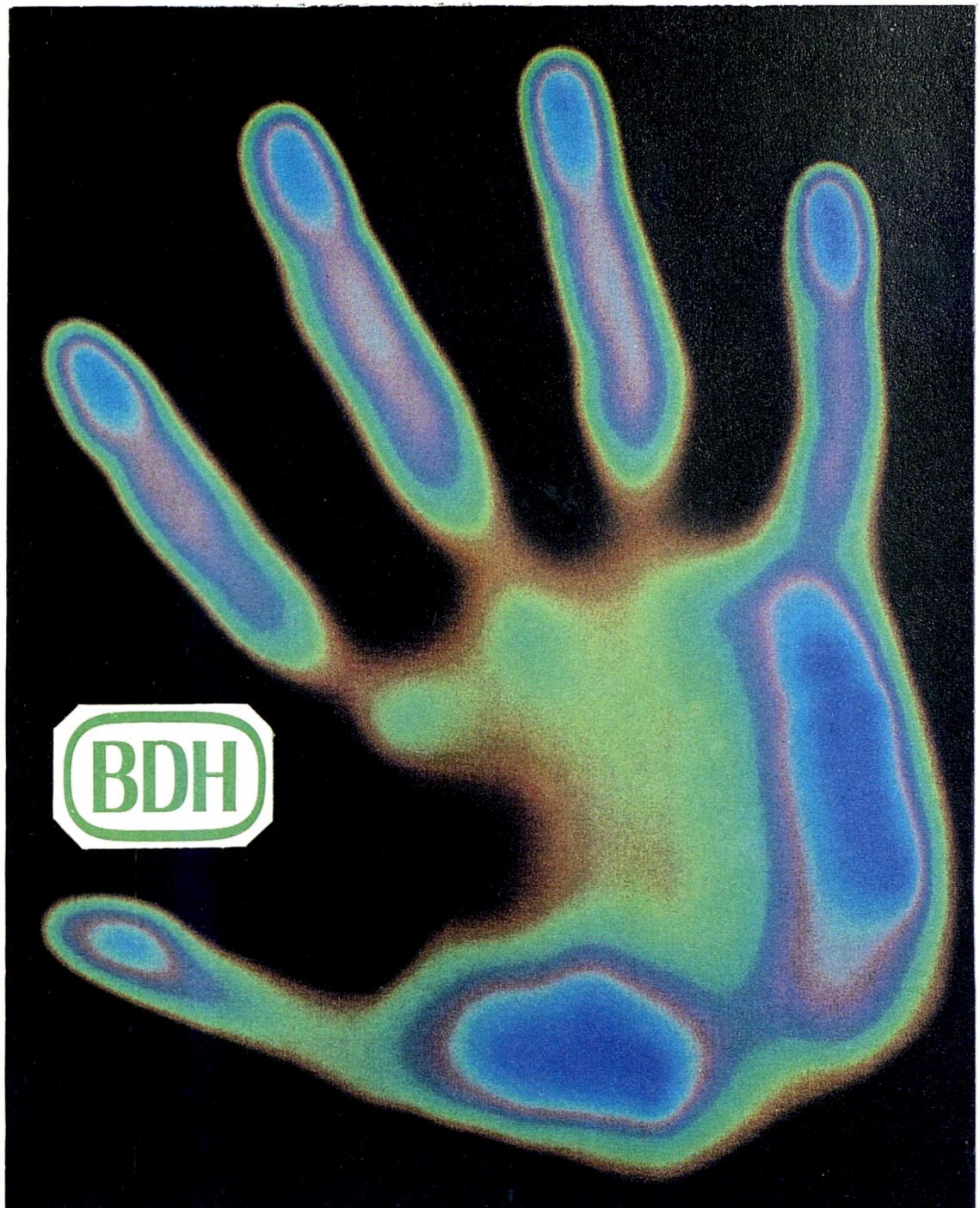
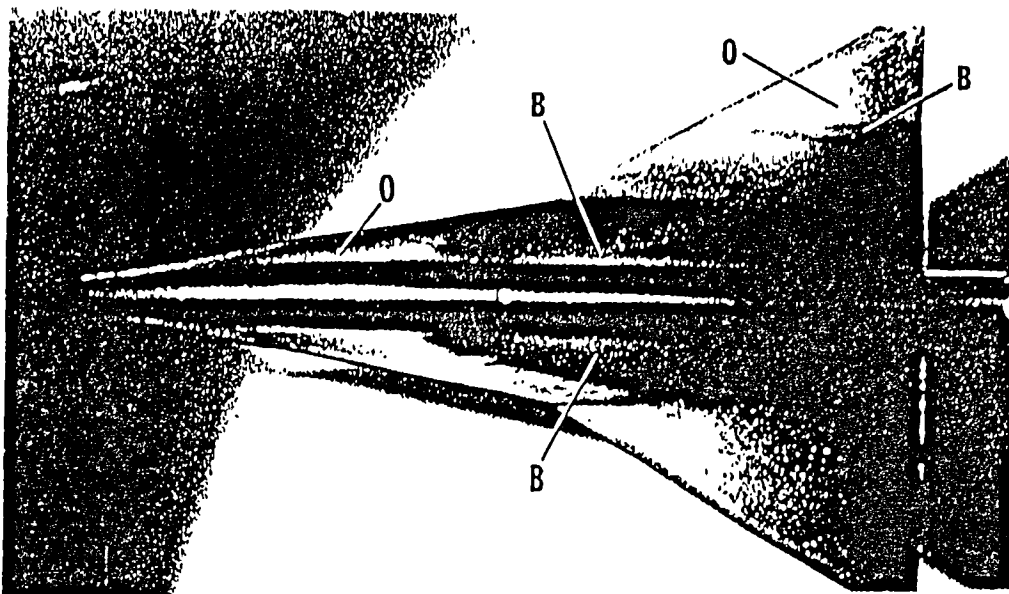
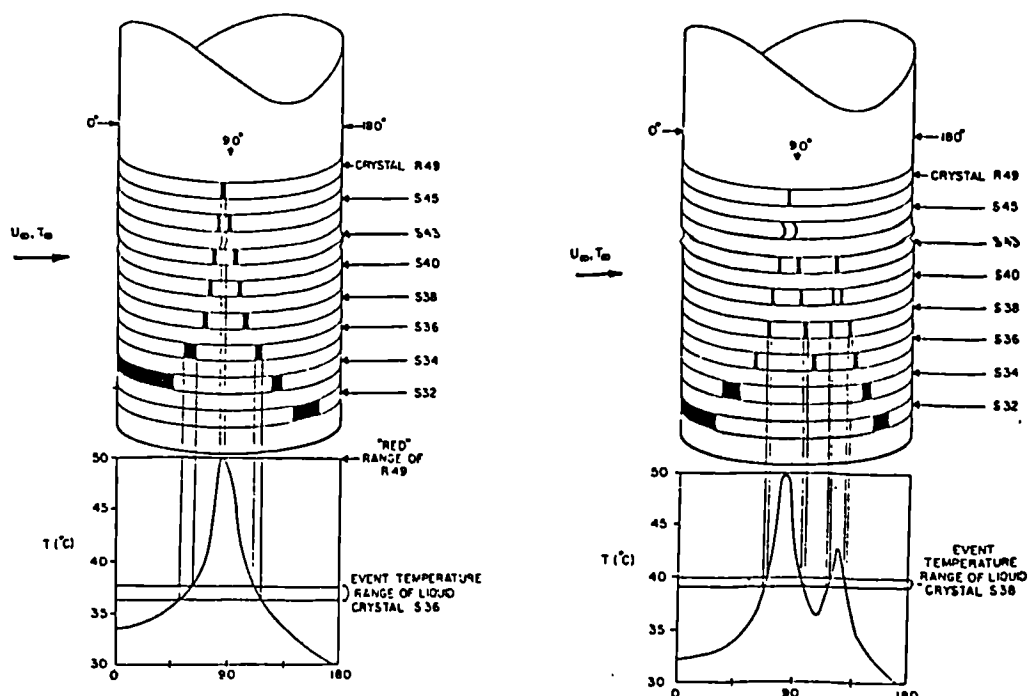


Fig. 11 Liquid crystal thermogram of human hand (from [118])



**Fig. 12** Liquid crystal show colour: in this case turbulent areas appear blue (B) and laminar regions orange (O) (from [73])



**Fig. 13** Schematic of a typical liquid crystal display. The conditions depicted are representative of subcritical flow. The shaded region represents colour (from [29])

**Fig. 14** Schematic of a typical liquid crystal display. The conditions depicted are representative of critical flow. The shaded region represents colour (from [29])

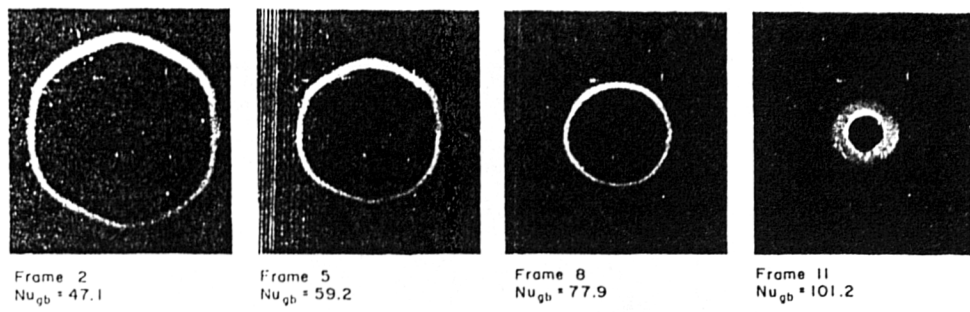


Fig. 15 Single jet impingement. Photographs of blue-green line isotherm  $t = 33.3^\circ\text{C}$  on liquid crystal sheet at different heat fluxes (Nusselt numbers) (from [53])

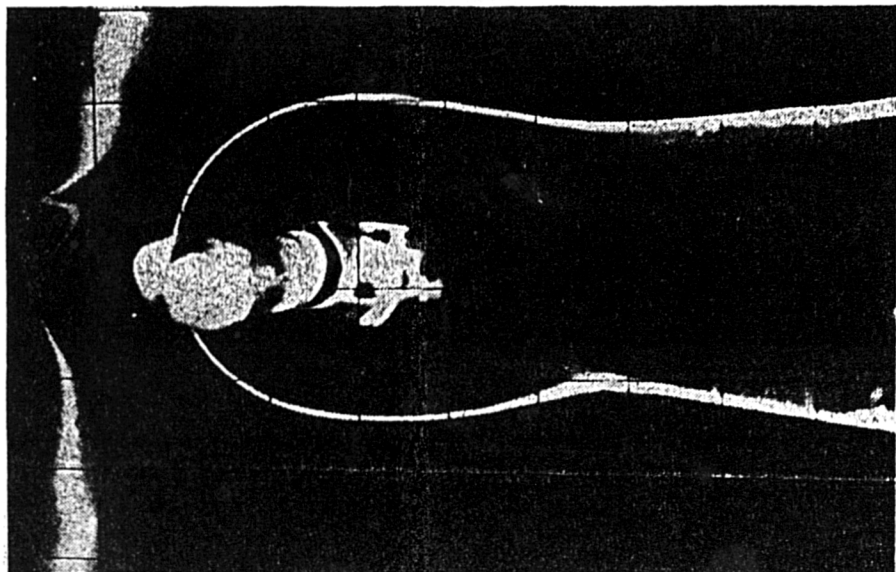


Fig. 16 Photograph of a contour of the heat transfer coefficient on the endwall of a cylinder held perpendicular to the wall. The flow is from left to right.  $Re = 3390$ ,  $h = 893 \text{ W/m}^2\text{K}$  (from [90])

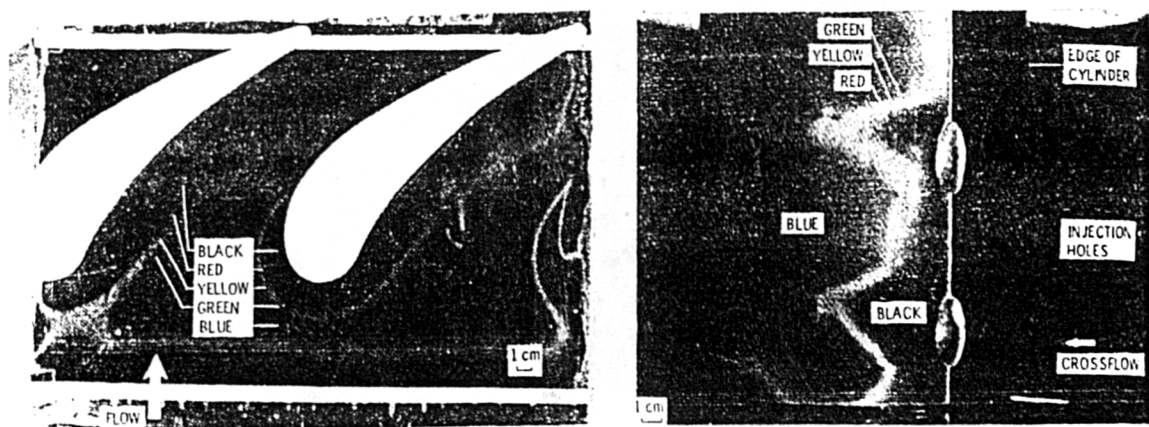


Fig. 17 A - Vane endwall cascade  
B - Film injection from a cylinder in cross flow (from [62])

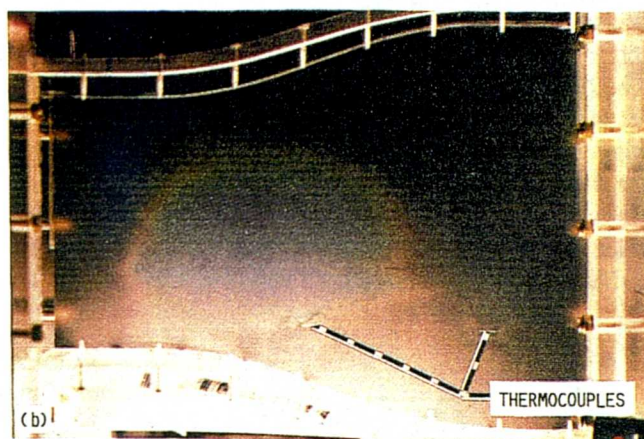
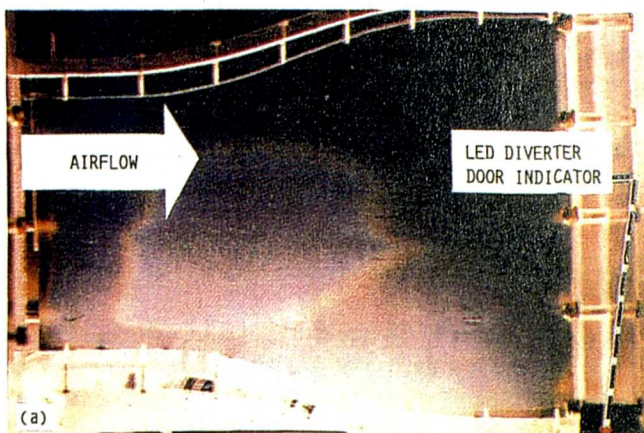


Fig. 18 Photographs of transient liquid crystal patterns on duct floor.  
a) higher temperature liquid crystal - early in test run,  
b) lower temperature liquid crystal - later in test run (from [69])

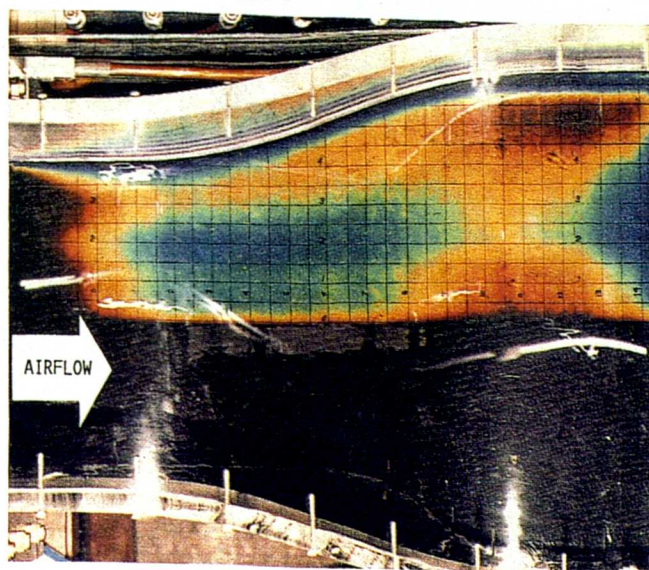


Fig. 19 Photograph of steady-state liquid crystal pattern on duct floor  
(from [69])

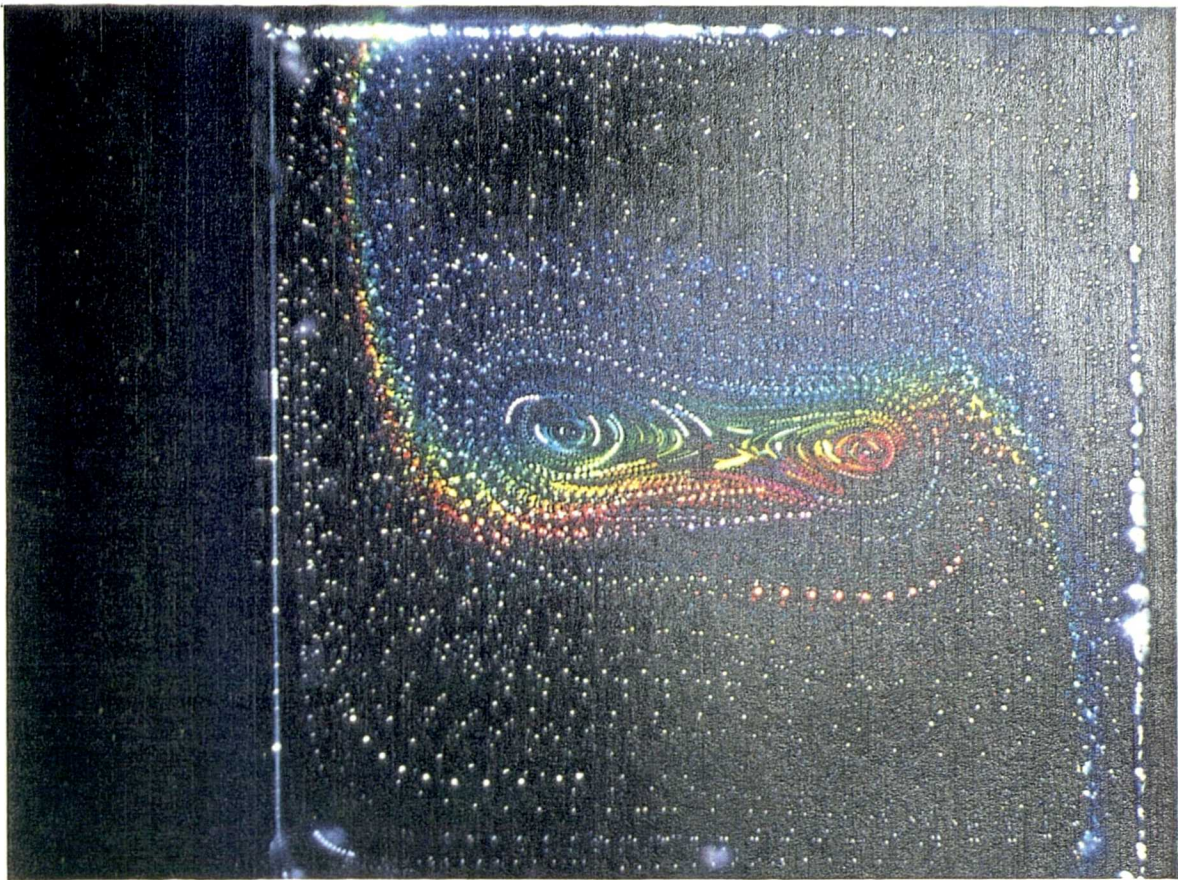


Fig. 20 Temperature and velocity visualisation in glycerol-filled cavity under free convection, using unencapsulated chiral-nematic liquid crystals (from [60])

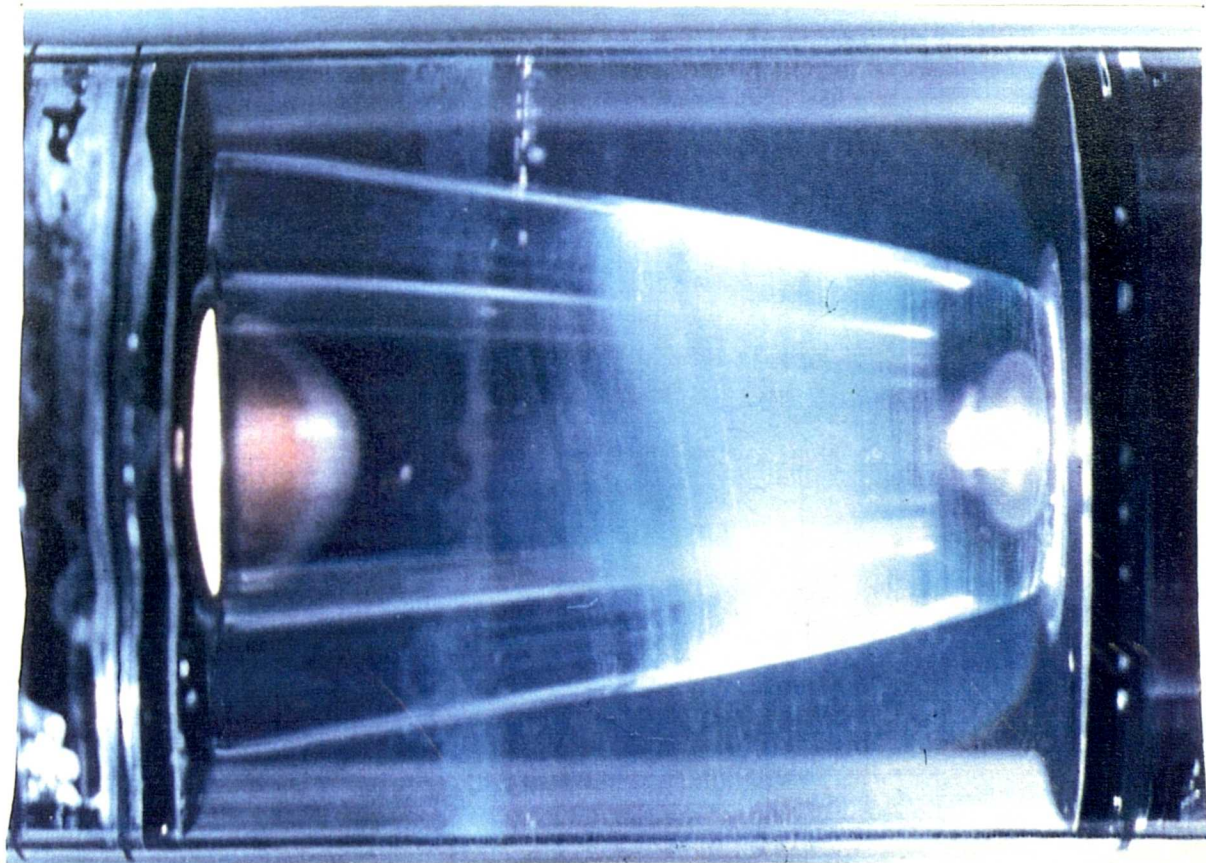


Fig. 21 Marangoni convection and centrifugal-buoyancy driven motion visualisation in a rotating cylinder using microencapsulated liquid crystals suspended in glycerol (from [105])

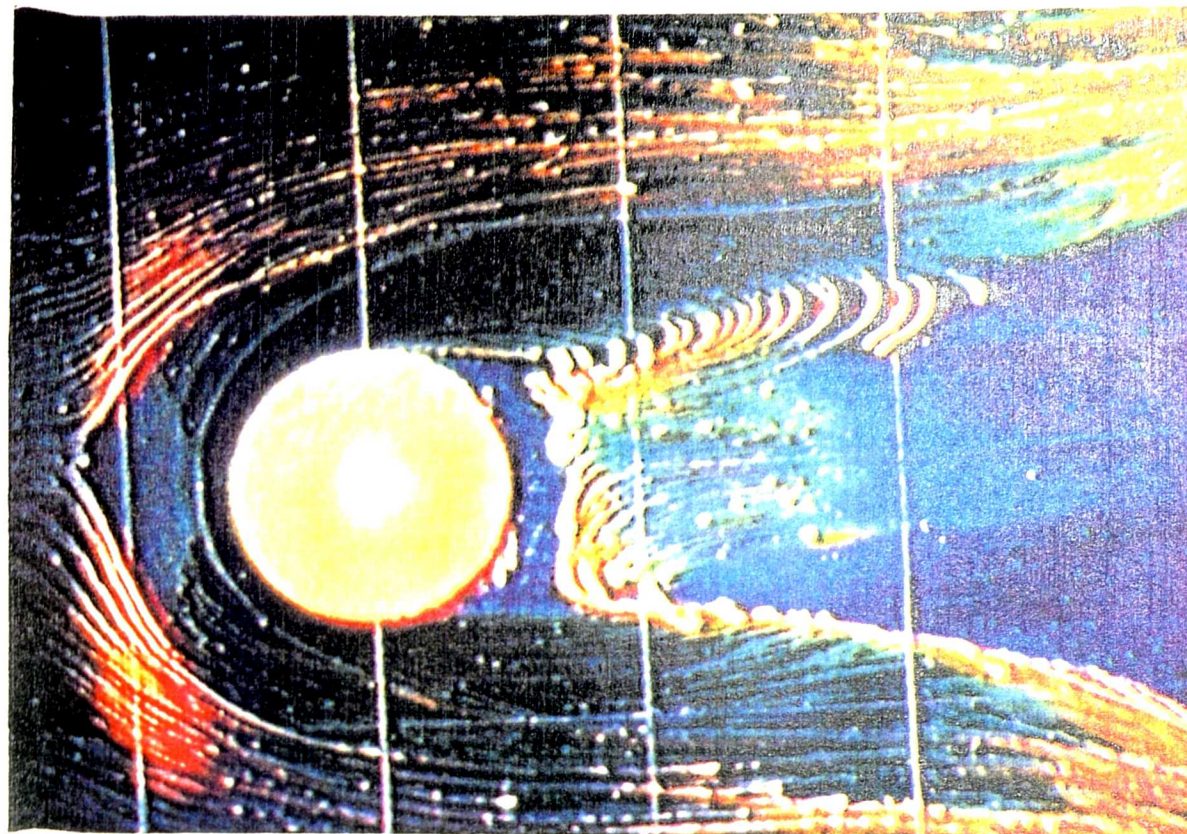


Fig. 22 Flow visualisation and shear-stress indication of horse-shoe vortex using chiral nematic mixture-flow velocity 40 m/s (from [9])

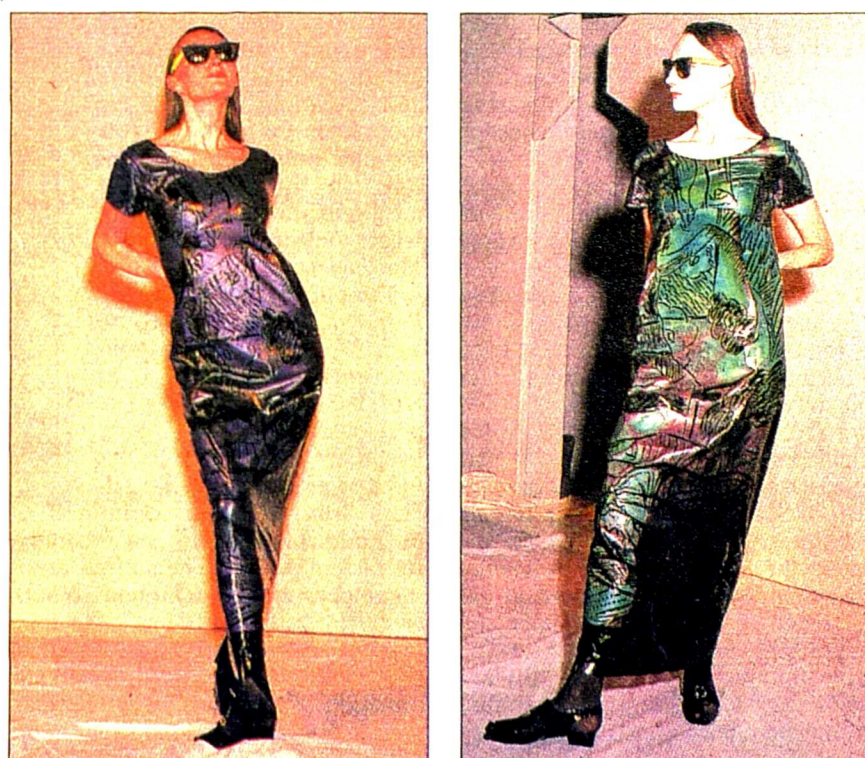


Fig. 23 Chameleon clothing: liquid-crystal dye changes colour as the dress becomes warmer (from [26])

#### 4. LIQUID CRYSTALS AND IMAGE PROCESSING TECHNIQUES

In the early days of image processing, only monochrome systems were available. Soon after, colour image processing was introduced, but monochrome continued to dominate because it was easier and less costly to manufacture and less complicated to use. However, in the last four years or so, colour image processing has gone from being used mainly by highly technical users on expensive image-processing systems to being available to virtually anyone who can use a desktop computer.

There are several commercial packages of hardware and software available which will digitize a video image from either black-and-white or colour cameras and store individual frames pixel by pixel in arrays. Three separate arrays are used to store a colour image, one each for the red, green and blue signal components. Also, three styles of cameras were used: NTSC composite (the usual home video camera), CCD (charge-coupled device) and CID (charge injected device).

There are four broad classes of image interpretation techniques available:

- human observer,
- multiple narrow-band spectral intensity image processing system,
- multiple linear regression method, and
- true-colour image processing system.

##### Human observer

A human observer can interpret liquid crystal images by direct visual inspection of colour photographs or tape recorded video images, usually using narrow-band paints. Calibration for such use is generally limited to identifying the temperature associated with a particular colour, often the red or the yellow-green colour near the centre of the colour-play band. The uncertainty associated with direct visual inspection is about 1/3 the colour-band width, given an

observer with normal colour vision and little experience, or about  $\pm 0.2$  to  $0.5^\circ\text{C}$  depending on the band-width and individual difference and non-constancy of human sense [2,3][78][90]. The uncertainty can be reduced by adaptation of monochromatic light sources (especially sodium lamps), although infra-red filters are required to protect the specimen from the heat from the lamps [2][71][90].

#### Method of narrow band-pass filter

A drawback of the studies discussed above is that the liquid crystal method seems to have been applied mainly for qualitative visualisation in order to recognise global views of thermal phenomena. Further, unaided human eyesight was employed as a sensor to evaluate colours and to determine temperatures. This may cause errors because of individual differences and unconstancy of human sensation. To decrease the possible error caused by human colour sensation the concept of determination of only one isothermal line was introduced corresponding to the clearest colour, and using a monochromatic light lamp or densitometer. Recently, Akino et al [1,2,3] have developed two new crystal thermometry methods to determine an isothermal map on a heated surface coated with a cholesteric liquid-crystal layer that changes colour according to temperature.

The first method, that of narrow band-pass filter, uses a set of 18 such filters. For a given liquid crystal material, the wavelength of peak intensity is a function of temperature (Fig.24) and that function can be determined by calibration. The intensity  $I_n(T)$  of the light filtered by the  $n$ -th band-pass filter with a transmittance function  $F_n(\lambda)$ , is represented by

$$\begin{aligned} I_n(T) &= \int_0^{\infty} S(\lambda, T) i(\lambda) f_n(\lambda) C(\lambda) d\lambda = \\ &= \int_0^{\infty} S(\lambda, T) F_n(\lambda) d\lambda \end{aligned} \quad (2)$$

where:  $S(\lambda, T)$  - spectral reflectance of liquid crystals,  
 $i(\lambda)$  - spectral intensity of incident light,  
 $C(\lambda)$  - spectral sensitivity of the light intensity sensor,  
 $f_n(\lambda)$  - n-th band-pass filter transmittance.

That is, the light intensity depends on both the temperature and the filter.

The 18 narrow band-pass filters were chosen, to have central wave-lengths from 400 to 750 nm, and the full width of the half maximum (FWHM) of the filters is then less than 10 nm. Figure 25 shows the brightness distribution through two filters along the centre line of the plate subject to a temperature variation. The peak brightness is observed, where the maximum transmittance of a filter coincides with colour of the liquid crystal. Therefore, one peak brightness temperature is determined uniquely by one filter. Unfortunately, as shown in Fig.25, the brightness curve is too broad to draw an isothermal directly at high temperature. In practise, the authors reported that the locus of points of maximum brightness was not very well defined except in regions of high temperature gradient, and image processing techniques had to be used to locate the most likely centroids of areas of equal brightness.

The characteristics of this method are illustrated in Fig.26 a-d, which show a calibration image viewed without a filter, and through three narrow band-pass filters; red, green and blue respectively. When the isothermal region is broad, as in Fig.26d, image processing techniques are needed to identify the position of the isotherm. The colour image was converted into an electrical signal by a black-and-white CCD video-camera and the output from the camera was recorded by video-recorder. The image signals were digitized with 8-bit gradations (i.e. 0 to 255) with  $256 \times 256$  pixels per frame. Using a small computer peak intensity was determined from each digital image for

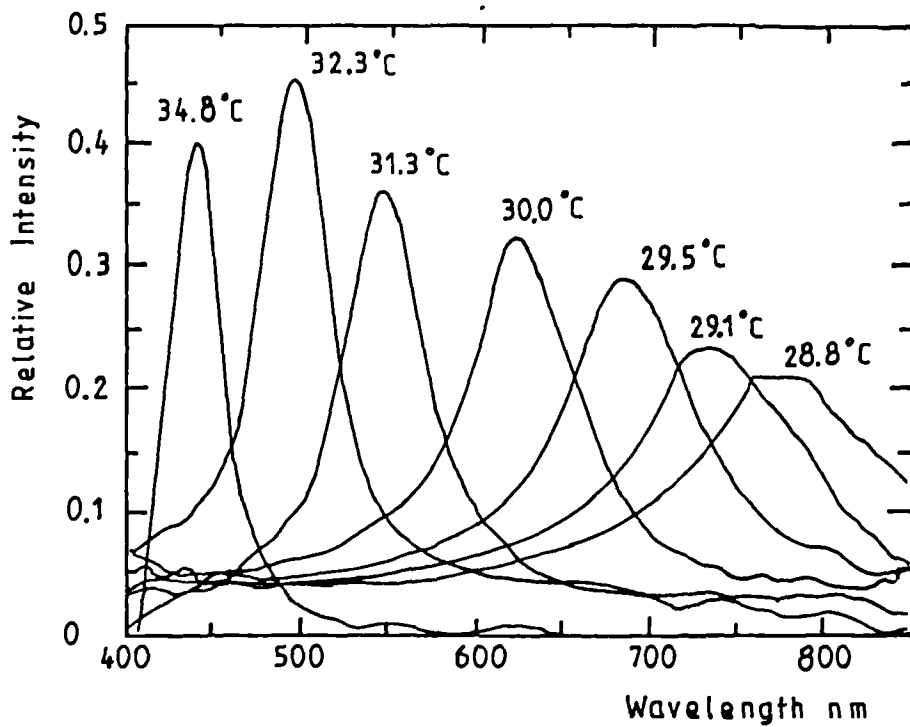


Fig. 24 Spectral reflectance of the used liquid crystal layer measured by monochromometer at various temperatures (from [3])

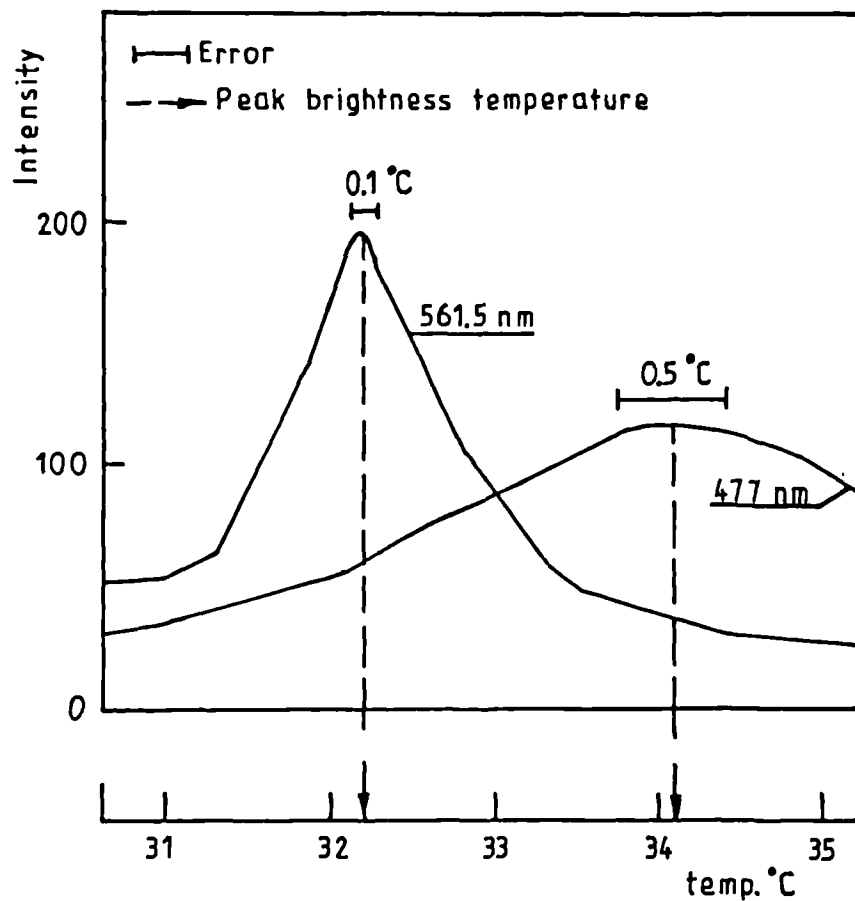
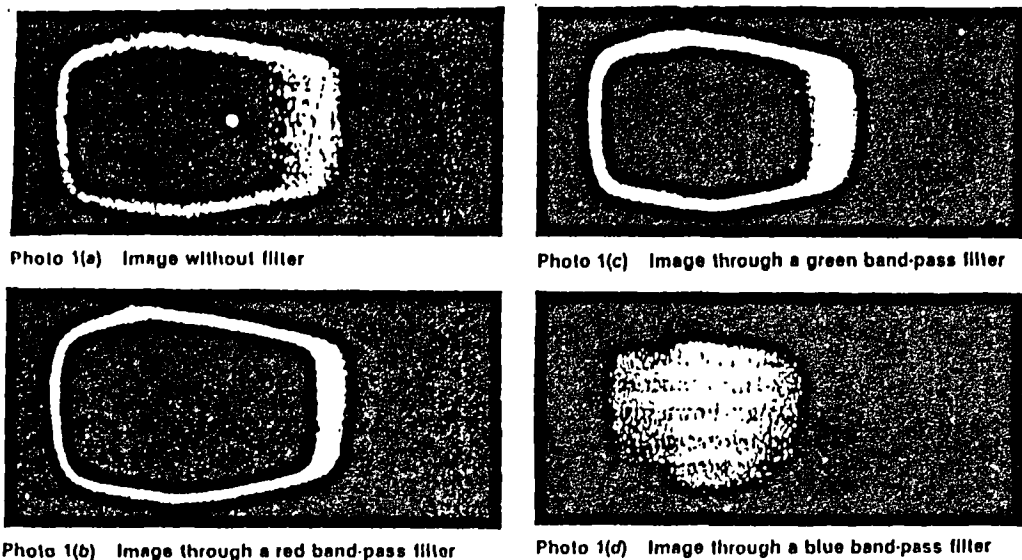
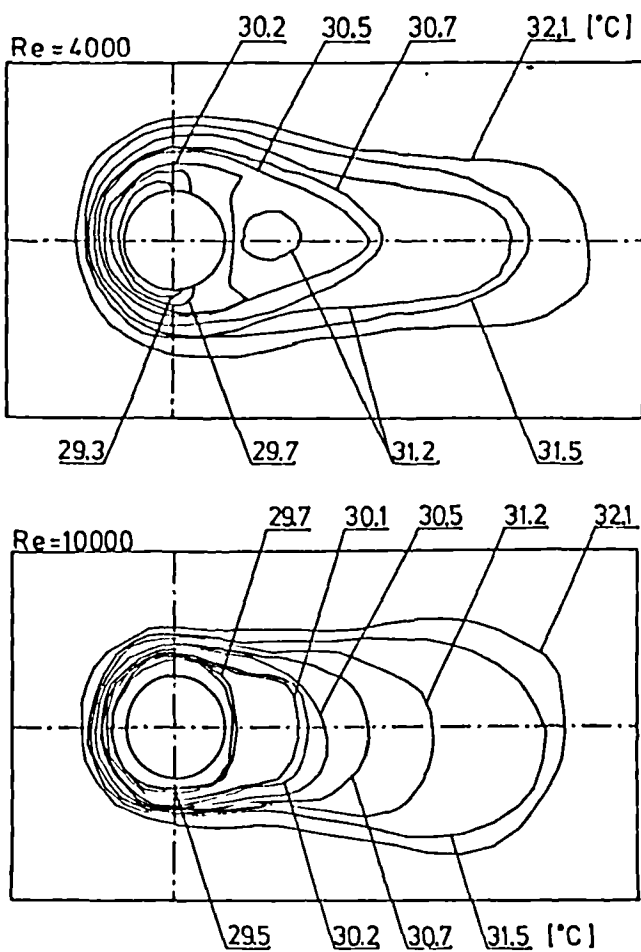


Fig. 25 Light intensity distribution along the test plate (from [2])



**Fig. 26 Monochromatic TV images of the liquid-crystal layer on the test plate without pass filters (from [2])**



**Fig. 27 Isothermal lines obtained by the multiple narrow-band spectral intensity image processing system for two Reynolds numbers of 4000 and 10000 (from [2])**

each filter. Consequently, the accuracy of this method was  $\pm 0.1^\circ\text{C}$  between  $29^\circ\text{C}$  and  $32^\circ\text{C}$ . Figure 27 shows an example of the wall temperature distributions around the base of a cylinder set vertically on the test plate obtained using the narrow band-pass filter method by Akino et al [2].

#### Multiple regression method

Akino et al [1,3] have also developed the alternative multiple regression method, again based on intensity. This involves a sparse set of broad-band filters (three) instead of direct isotherm identification using the dense (18) set of the previous method. Temperature was expressed as a linear function of the intensities passed by three filters for red, green and blue individually. The colour distribution can be measured by video-camera by changing the filter, and the three colour components ( $x, y, z$ ) are digitized by the image-processor, and fitted to the measured temperatures ( $T$ ) by the following linear multiple regression equation [1]:

$$T = \alpha + \beta x + \gamma y + \delta z \quad (3)$$

where:  $\alpha, \beta, \gamma$  and  $\delta$  are the regression constants.

Figure 28 shows a comparison of the estimated temperature using Equation (3) with the measured temperature. The accuracy of this method was  $\pm 0.2^\circ\text{C}$  between  $27^\circ\text{C}$  and  $31^\circ\text{C}$ . Further, Fig.29 shows the isotherm and Nusselt number distribution derived from it using the same method. The geometry consists of two short cylinders standing on a base-plate, in line with the flow. The base-plate was electrically heated and covered with liquid crystals.

#### True-colour image processing systems

In the true-colour image processing method, colour video information is displayed as a unique brightness combination of red, green and blue (RGB) light. A displayed RGB image is immediately perceived by a user as exhibiting three distinct attributes termed as HSI:

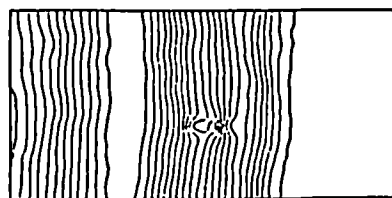
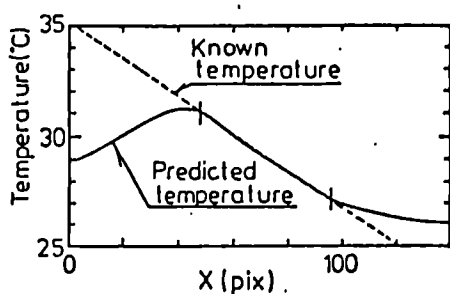


**Fig. 28** Measured temperature distribution processed using the method of multiple linear regression for the case of linear temperature distribution with intermediate temperature gradient (from [3])

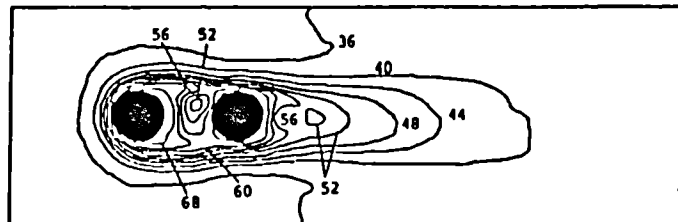
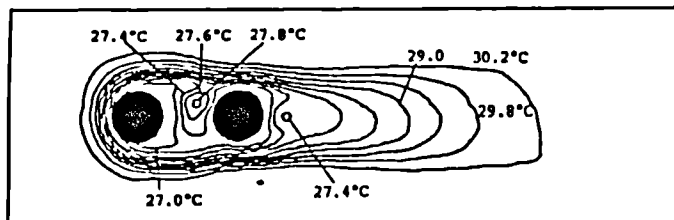


**Fig. 29** Temperature and Nusselt number distributions around two cylinders (from [1])

- HSI: 1. Hue - the spectral colours present,  
2. Saturation - how deep or faded the colour appears to be, and  
3. Intensity - the edge information or what would be seen  
if a black-and-white version of the image  
were displayed.

Unlike colour images represented in the RGB colour space, images composed of hue, saturation and intensity values can be analysed simply because the HSI values themselves can be processed individually and independently. Convolution, for example, can be performed on a colour image using just the intensity component of an HSI colour image.

Similarly, a histogram can be generated based solely on hue data in order to learn about the frequency distribution of hues. Performing similar operations on direct RGB images is more complicated, requiring at least three times as many computations since RGB values must all be manipulated. Unlike the RGB model, HSI provides direct (integrated) perceptual attributes of a colour image in terms of hue, saturation and intensity.

Visible light only forms a small part of the total electromagnetic spectrum, which ranges from cosmic rays to electric power. Figure 30 shows the electromagnetic spectrum with the visible portion highlighted. As can be seen, the visible spectrum roughly divides into three parts; red, green and blue. Red, green and blue are called additive primary colours because adding various amounts of each colour produces a single perceived colour in any part of the visible spectrum. The RGB primaries have been used to produce an equilaterally triangular colour map. The triangle, with the three primary colours as its vertices, maps out the largest range of reproducible colours in the visual spectrum (Fig.31 a-b). Further work extended this to the development of a standardised colour chart, which quantified the

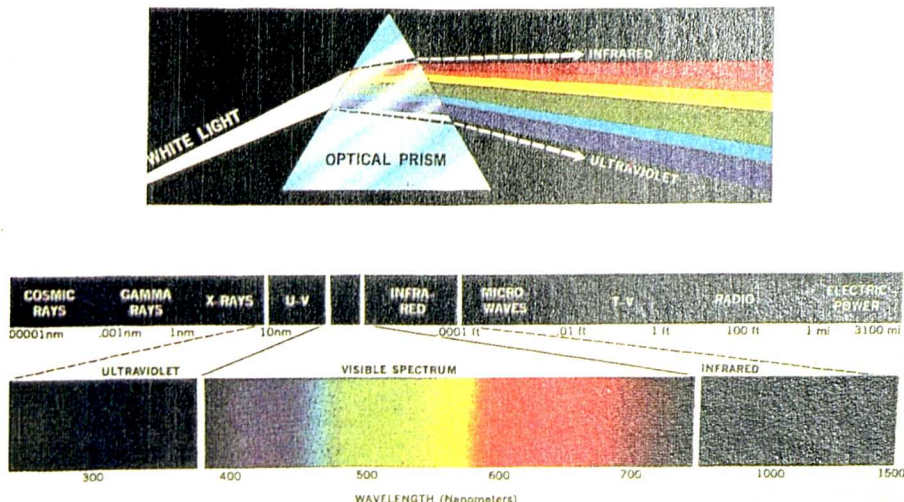


Fig. 30 The electromagnetic spectrum ranges from cosmic rays to electric power; the visible portion makes up only a small portion of the spectrum. As can be seen, the visible portion can be roughly divided into red, green and blue sections (from [112])

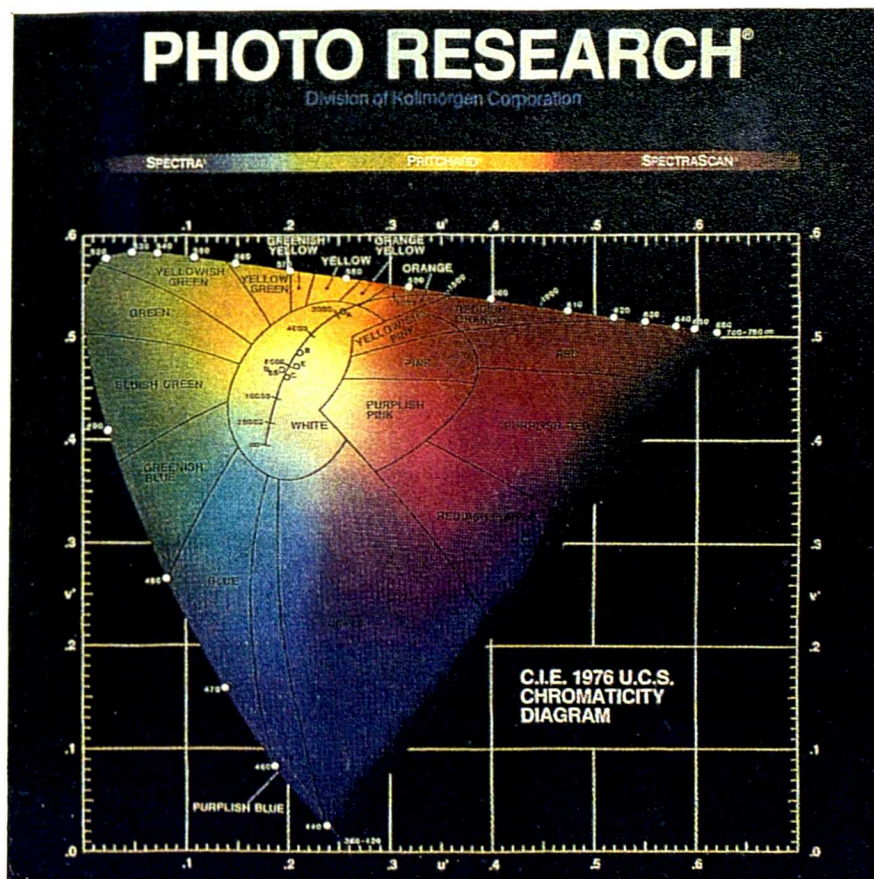
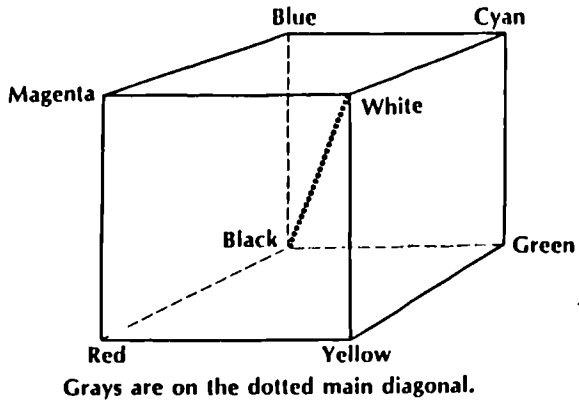
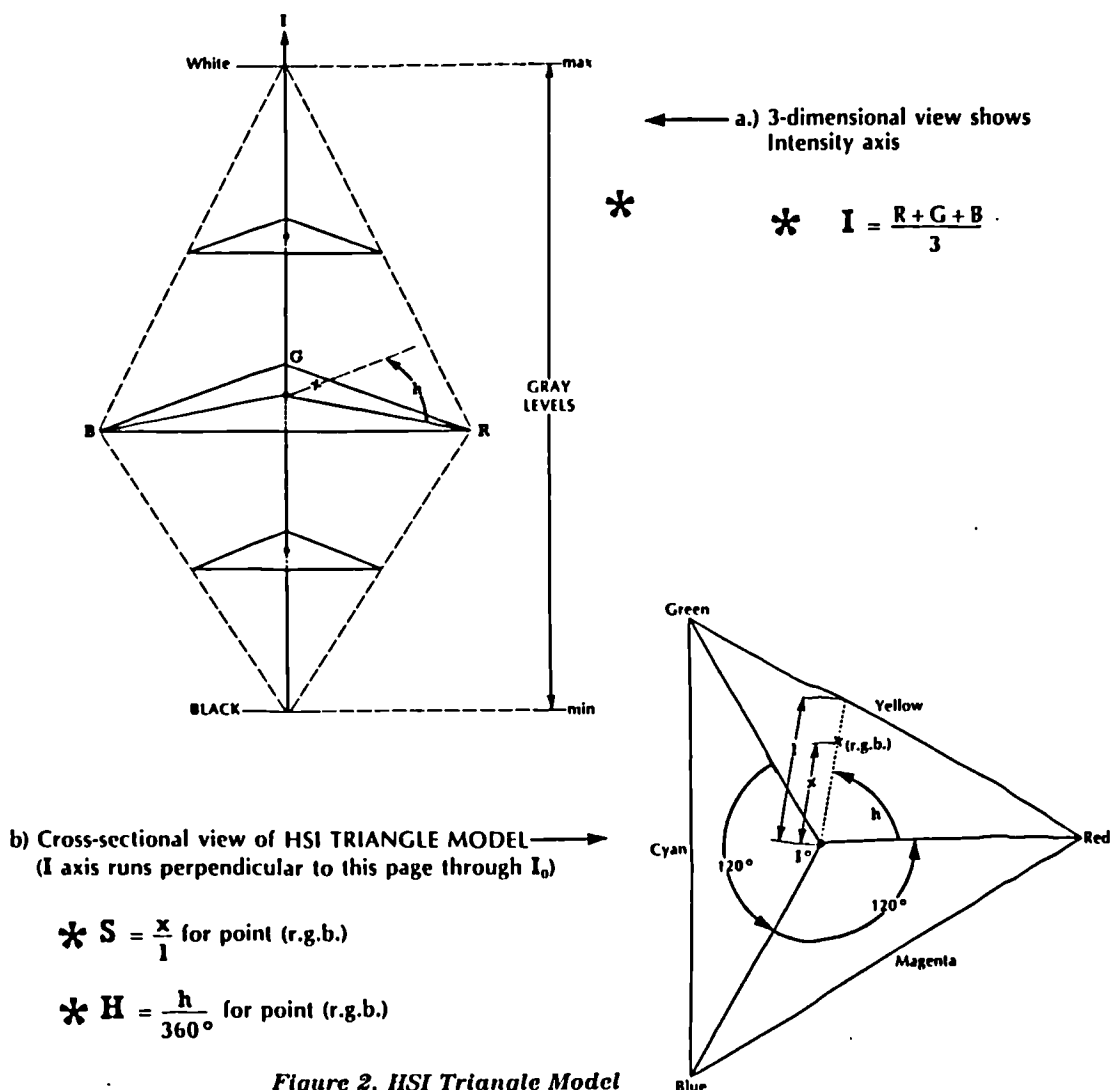


Fig. 32 The 1976 chromaticity diagram (from [108])



**Figure 1. RGB Color Cube**

**RGB to HSI Conversion Theory:**  
 Mathematically, the RGB color cube (Figure 1) is converted to the HSI triangle model (Figure 2). In HSI space, the Intensity is perpendicular through the center of the triangle. The Hue is the angle rotating around the Intensity axis with 0 degrees at R, 120 degrees at G, and 240 degrees at B.



**Fig. 31 HSI triangle model and RGB colour cube (from [118])**

perception of colours by assigning numbers to them. The chart, still in wide use, is known as the 1931 chromaticity diagram. A variation of this diagram, produced in 1976, is called the Uniform Colour Space (Fig.32). This map was developed principally as a means of matching the colour combination of the XYZ primaries to monochromatic light of a given wavelength. Thus, an additive mixture of any three of the primary colours can be represented as a point inside the equilateral triangle. For computational and colour-matching purposes, it is useful to know where colour lies on the diagram. Consequently, several colour sections are shown in Figure 32.

Unlike the RGB model, the HSI model represents colours perceptually, and it is therefore easier to extract colour information so that the data is useful for human analysis. In a computer system (or frame grabber), separate frame buffers hold the red, green and blue data comprising the colour image. The three buffers must be looked at together to be analysed or processed. Inefficient colour processing results because, in effect, operations must be performed three times.

HSI colour space is amenable to more efficient processing because the HSI frame buffers comprising the colour image are relatively uncorrelated with one another. These buffers individually provide useful information when interpreting a colour scene.

Mathematically, it is relatively easy to change a colour or an entire colour image from the RGB colour space to the HSI colour space. If the RGB co-ordinates in Fig.31 are thought of as being produced by an RGB camera, then the hue, saturation and intensity can be given by [112,119]:

$$I = \frac{R + B + G}{3} \quad (4)$$

$$H = \frac{1}{360} \left[ 90 - \text{Arctan} \left( \frac{F}{\sqrt{3}} \right) + \begin{cases} 0, G > B \\ 180, G < B \end{cases} \right] = \frac{h}{360} \text{ for point (r.g.b.)} \quad (5)$$

where:

$$F = \frac{2R - G - B}{G - B} , \text{ and} \quad (6)$$

$$S = 1 - \left[ \frac{\min(R, G, B)}{I} \right] = \frac{x}{l} \text{ for point (r.g.b.)} \quad (7)$$

In Equation (7) the lowest value of either R/I, G/I or B/I is subtracted from (4) to give the saturation. Thus, for the colour white R/I=G/I=B/I=1. The value of saturation becomes zero from (7).

Since all colour models are related mathematically, it is an easy task to convert from one colour space to another. Using a 24-bit RGB frame grabber, colour images can be captured in RGB format, converted to HSI, processed, reconverted to RGB and displayed. The more recent work with HSI colour image processing and liquid crystals techniques will be discussed in the Experimental section.

## 5. CALIBRATION OF LIQUID CRYSTALS AND TRUE-COLOUR IMAGE PROCESSING

Before the execution of a measurement of temperature and a visualisation experiment, we should recognise the characteristics of the combination of liquid crystals, the light source and the optics and camera system (ordinary CCD black-and-white or RGB colour cameras may be used), and make a rational plan for the measurement system.

Both the colour-play interval and the event temperature (see Part 2) for a liquid crystal can be selected by adjusting its composition, and materials are available with event temperatures from  $-30^{\circ}\text{C}$  to  $115^{\circ}\text{C}$  and with colour play band from  $0.5^{\circ}\text{C}$  to  $20^{\circ}\text{C}$ . However, not all combinations of event temperature and colour-play band widths of  $1^{\circ}\text{C}$  or less will be called "narrow band" materials. Those whose band width exceeds  $5^{\circ}\text{C}$  will be called "wide-band". The types of material specified for a given task depends on the type of image interpretation technique to be used.

### 5.1 Calibration Tests

The absolute uncertainty in surface temperature measurement appears to be about  $0.5^{\circ}\text{C}$  using liquid crystals, for both visual and image processed interpretations, hence the relative uncertainty of the measurement is determined by the working temperature difference [2][78]. In this particular experiment the uncertainty was estimated to be about  $\pm 0.1^{\circ}\text{C}$  to  $\pm 0.2^{\circ}\text{C}$  because the specimen was calibrated in situ with the lighting system arranged just as it was during the application.

Figures 33 and 34 show the apparatus of the calibration procedure. A known temperature distribution exists on the "calibration plate" which has a liquid-crystal layer attached. This layer is sandwiched between the brass and the perspex plates ( $\delta = 8\text{mm}$ ). This allows the liquid crystal colours to be viewed from the top side through the perspex.

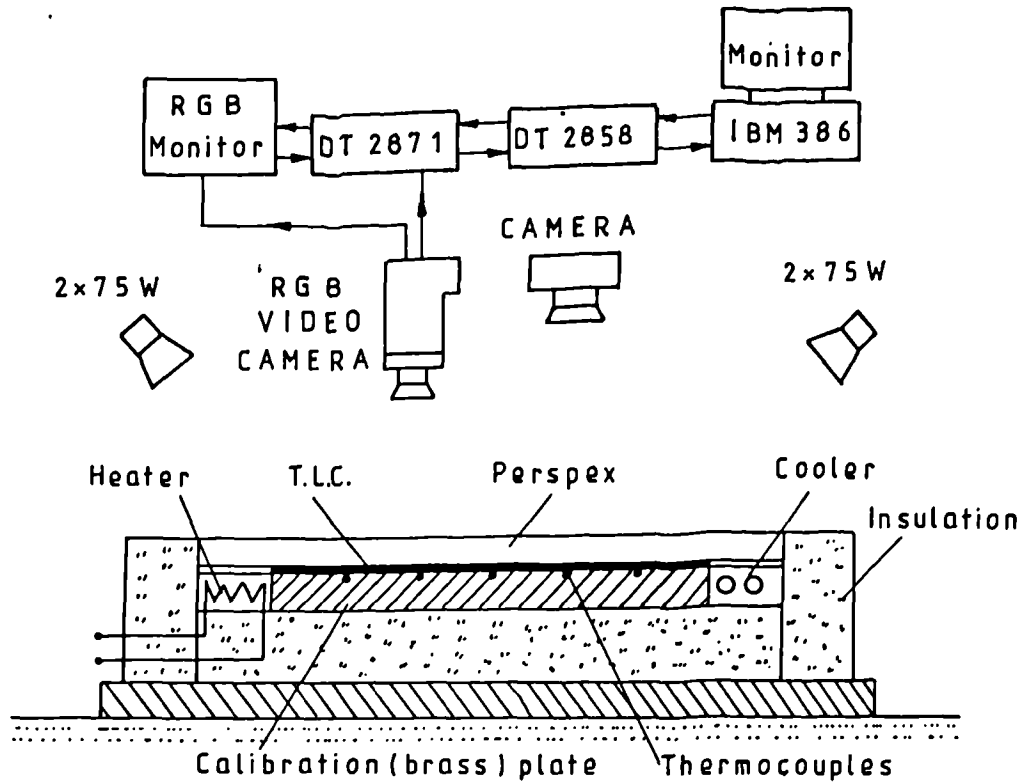


Fig. 33 Experimental apparatus for the calibration experiment. Linear temperature distribution was obtained along the calibration plate on which colour of liquid crystal on calibration plate was observed and measured

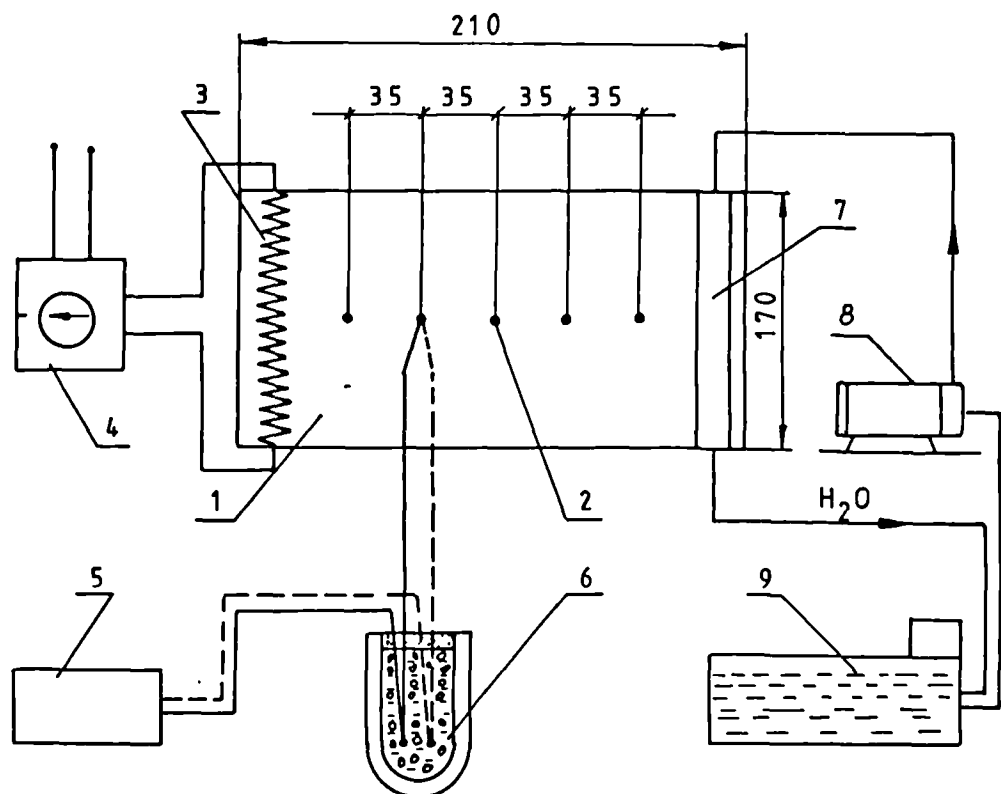


Fig. 34 Schematic drawing of calibration (brass) plate circuit diagram.  
 1. Brass plate 2. Thermocouples-type T 3. Heater-200 W  
 4. Autotransformer 5. Digital voltmeter 6. Dewar flask  
 with melting ice 7. Cooler 8. Water pump 9. TE-8A  
 constant temperature water baths

1)

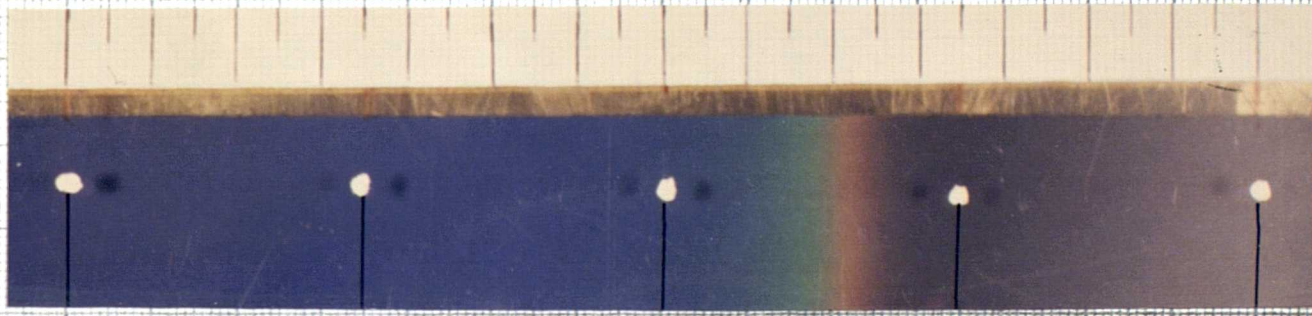
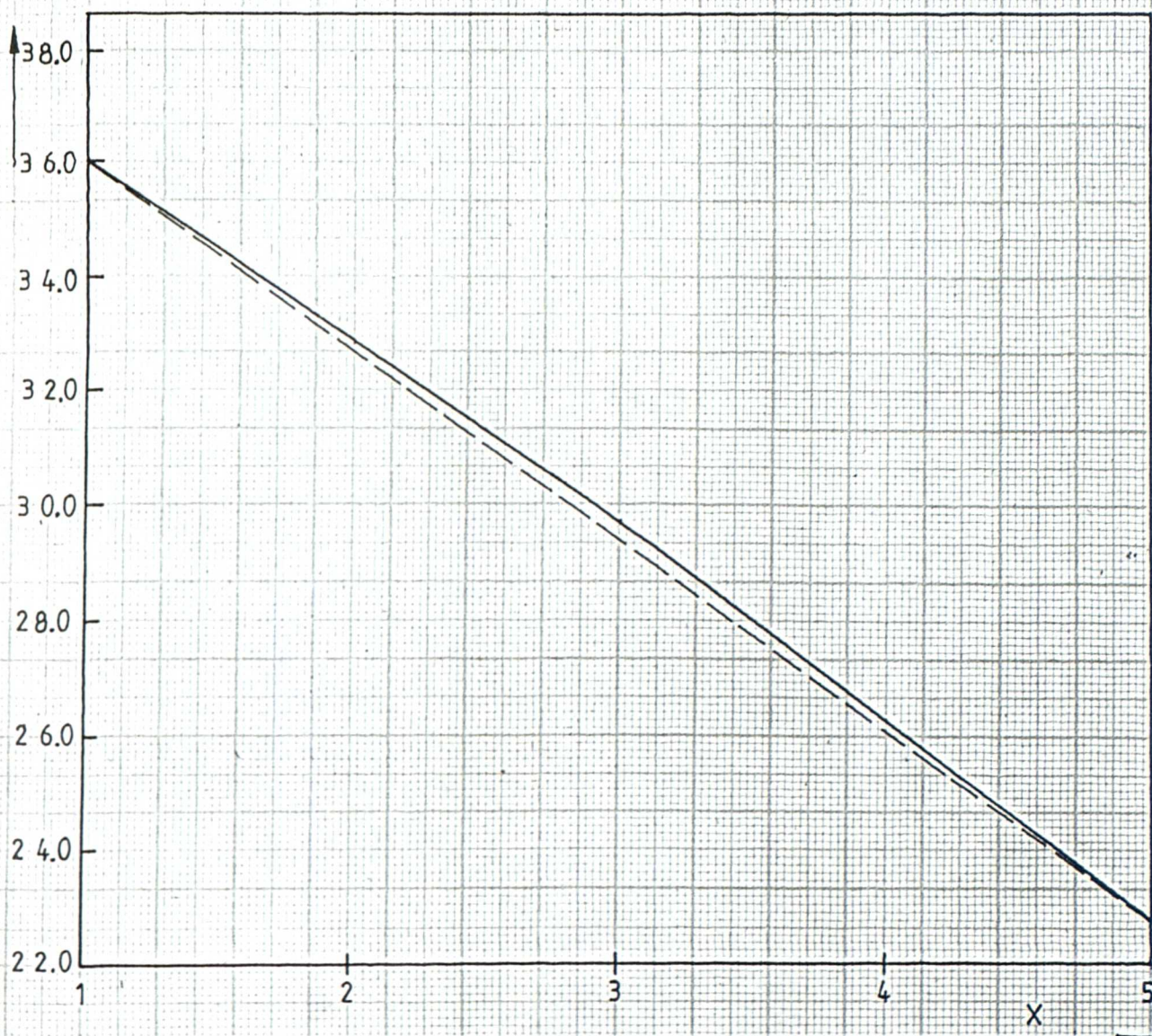
 $t$  °C

Fig. 35 Colour distribution of liquid crystal visualising temperature distribution along test plate ( $\Delta t / \Delta X = 94$  K/m) (Dashed line-temperature distribution without lamp)

The "calibration plate" is made of brass 210 mm long, 170 mm wide and 8 mm thick. In order to maintain a linear temperature distribution with desired temperature gradients, one end of the brass plate was cooled by stabilised water and the other end was controlled electrically to give a constant temperature. The temperature distribution was measured by five thermocouples (type T) imbedded in the brass plate and by a digital voltmeter with a resolution of 1mV. Both ends of the calibration plate were controlled to give a desired temperature distribution on the plate and thereby a complete colour spectrum in the longitudinal direction. The distribution of the colour component pattern on the liquid-crystal layer was measured using a photo-camera with an optical polariser filter and RGB colour-camera attached. In the present study several temperature gradients were set up. Figure 35 shows an example of the colour distribution by liquid-crystal visualisation of the temperature distribution along the test plate ( $\Delta t/\Delta X = 94 \text{ K/m}$ ) with and without illumination. Also, Fig.36 shows the relationship between Hue and temperature on R-G-B colour co-ordinates. It can be concluded that Hue correlates temperature by itself.

The liquid crystals used in this experiment are Thermochromic Liquid Crystals purchased from Liquid Crystal Devices Ltd. [120]. They have an event temperature range of  $27^\circ\text{C}$ - $29.6^\circ\text{C}$ . The isotherms of the red colour band ( $t_R = 27.7^\circ\text{C}$ ), and yellow-green band ( $t_G = 28.3^\circ\text{C}$ ), are recorded by photographing the liquid crystal through a polarised filter (to eliminate reflection from the corrugated geometry) with colour film and RGB image processing system. Examples of several of these photographs and images are illustrated in Parts 6 & 7.

## 5.2 True-Colour Image Processing

Many image processing operations routinely used to date involve the processing of grey-level (intensity) images; such methods can be readily applied to HSI colour images. These include image trans-

formations, enhancement, analysis, compression, transformations and restorations. Building on gray-scale image processing hardware and software technology, Data Translation [119] has produced a  $512 \times 512$  pixels  $\times$  8-bit (256 grey levels) colour frame-grabber board for PC/AT's. The video input section of the DT2871 (HSI) Colour Frame Grabber incorporates a 10-MHz RGB/HSI converter for transforming digitized pixel values representing weighted combinations of the primary (RGB) colours into new values representing hue, saturation and intensity (HSI). The rationale for this has already been described.

Produced in real time, these new values are colour attributes rather than actual colours. Arithmetic operations, or algorithms like convolution for edge enhancement, are performed on pixel intensities which correspond exactly to the black-and-white version of the image: all methods for processing and analysing monochrome images can be applied directly to colour images captured by the DT2871. This is an important practical property.

A schematic view of the image processing system is shown in Fig.37. The two-dimensional temperature distribution is determined using RGB video-camera, IBM Personal Computer AT, HSI Colour Frame Grabber DT2871 and Auxiliary Frame Processor DT2858. The video output section of the DT2871 incorporates a 10-MHz HSI/RGB converter for transforming HSI pixels back into RGB pixels after processing. HSI/RGB colour-space conversion is performed at 30 frames/sec for display on colour monitors. Finally, for speeding computer intensive colour processing, the DT2871 (HSI) Colour Frame Grabber connects directly to a DT-Connect processor board, which is controlled by GLOBAL LAB colour software.

Figures 38 and 39 show DT2871 HSI Colour Frame Grabber and DT-Connect Image processing overview block diagram respectively. This GLOBAL LAB colour feature includes all of the following\*:

---

\* Taken from Reference [119].

- \* Hue shifting (HSI)   \* Hue mapping (HSI)
- \* Saturation boost (HSI)
- \* Select a range of hue, saturation or intensity to work in (HSI)
- \* Quick histogram
- \* Set foreground/background colour based on hue, saturation or intensity values
- \* Set foreground/background colour based on logical combinations of hue, saturation and intensity values
- \* Set foreground/background colour automatically (based on histogram information-AOI)
- \* Select mode: direct mode (changes image) or interactive mode (view the image before change is applied-AOI)
- \* Save red-green-blue, hue, saturation or intensity component as a separate file (AOI)
- \* Load previously saved component
- \* Exchange components (RGB)
- \* Copy components (RGB)
- \* Change colour model (convert file or change display only)
- \* Point, line or AOI histogram
- \* Accumulated histogram
- \* Calculate component value range from histogram data
- \* Zoom in on histogram data and/or exclude part of histogram
- \* Move histogram display box around window
- \* Read, display or print histogram data
- \* Line profile of any component
- \* Line frequency analysis
- \* Display or save line profile or frequency analysis data
- \* Measure angle
- \* Measure length of line
- \* Calculate perimeter or area (AOI)
- \* Create or calibrate measurement units
- \* Slide/Stretch
- \* Histogram equalization (Bell,Cube,Exponential, Linear,Logarithmic)
- \* Contouring
- \* Thresholding
- \* Colour component value replacement (single colour or range of colours)

### Hue Histogram

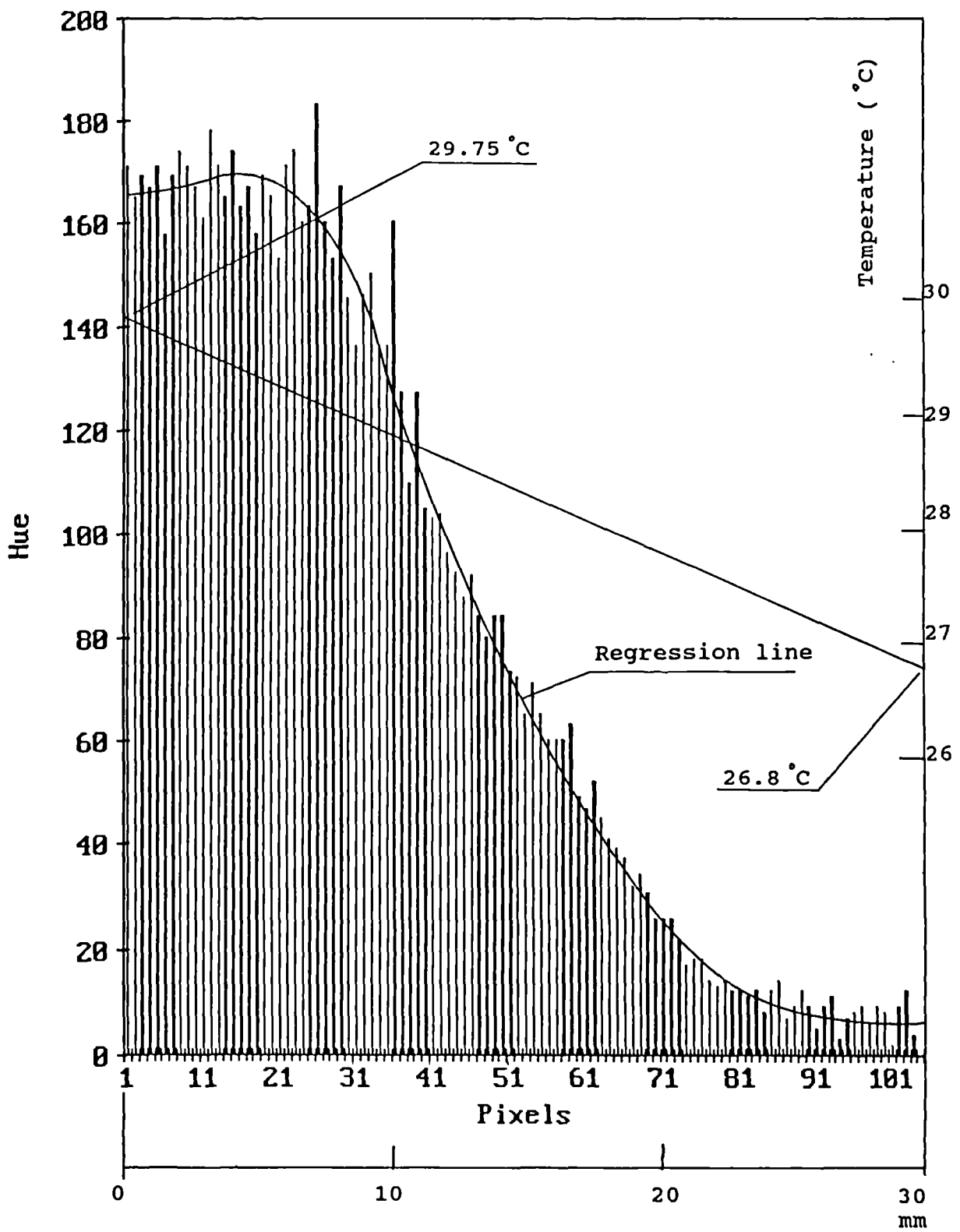


**Fig. 36** Hue and temperature distribution along the test plate ( $\Delta t/\Delta x = 94 \text{ K/m}$ )  
 a) temperature range  $29.73 - 26.8^{\circ}\text{C}$   
 b) temperature range  $28.45 - 26.8^{\circ}\text{C}$   
 c) Hue value as a function of surface temperature

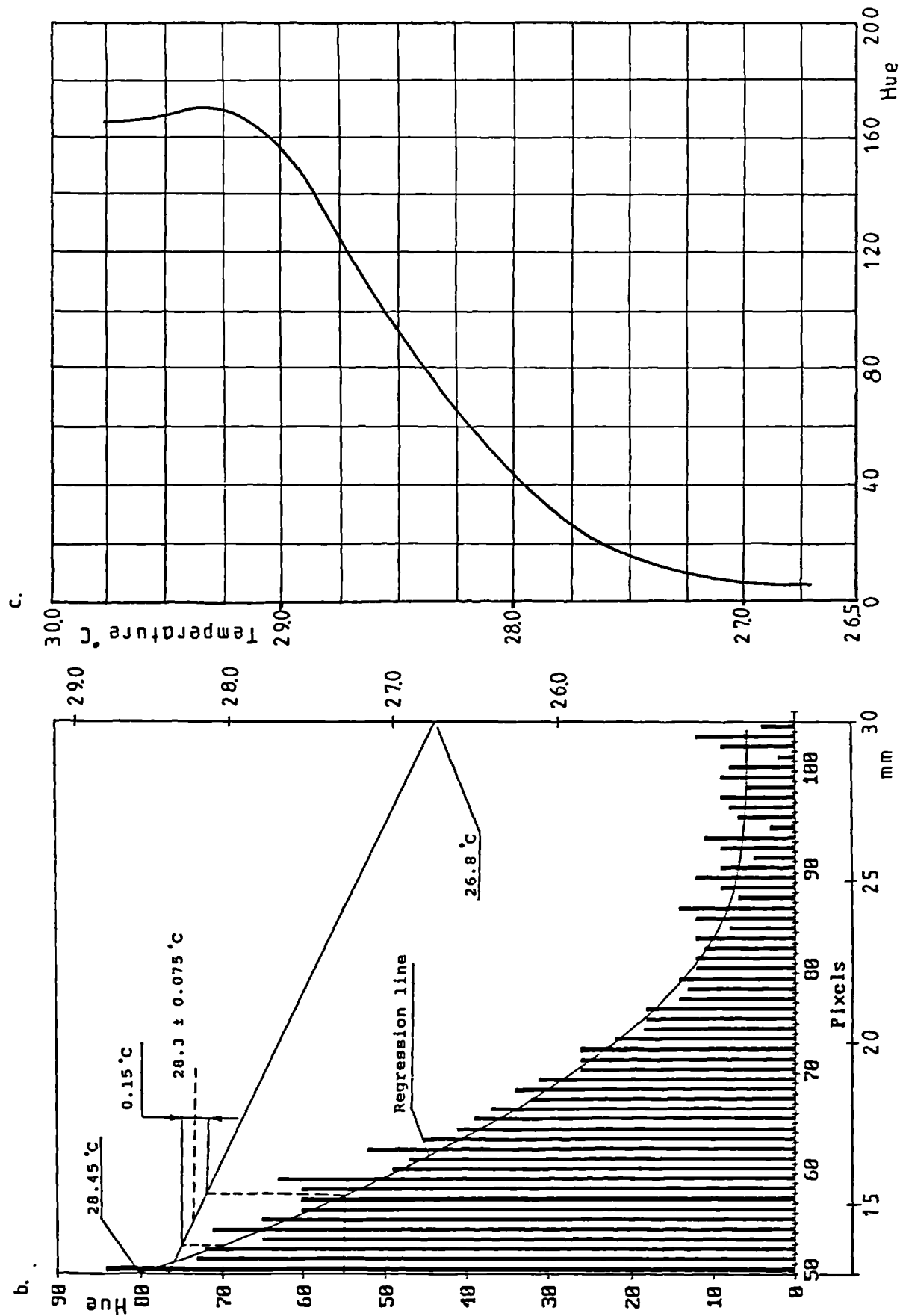


Fig. 36 Hue and temperature distribution along the test plate ( $\Delta t / \Delta x = 94 \text{ K/m}$ )  
 a) temperature range  $29.73 - 26.8^\circ\text{C}$   
 b) temperature range  $28.45 - 26.8^\circ\text{C}$   
 c) Hue value as a function of surface temperature

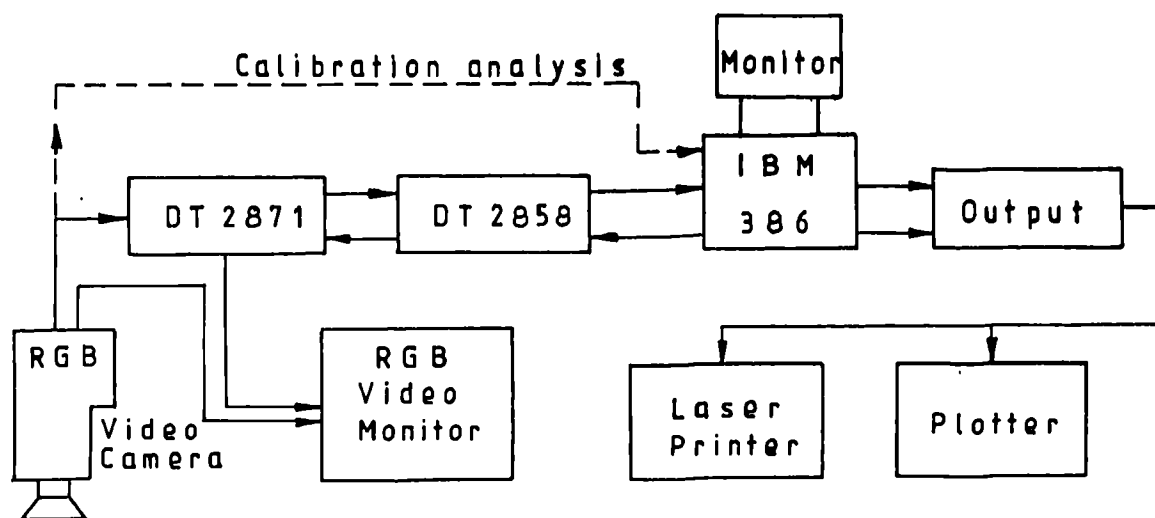


Fig. 37 The information flow chart for True Colour Image Processing interpreter system

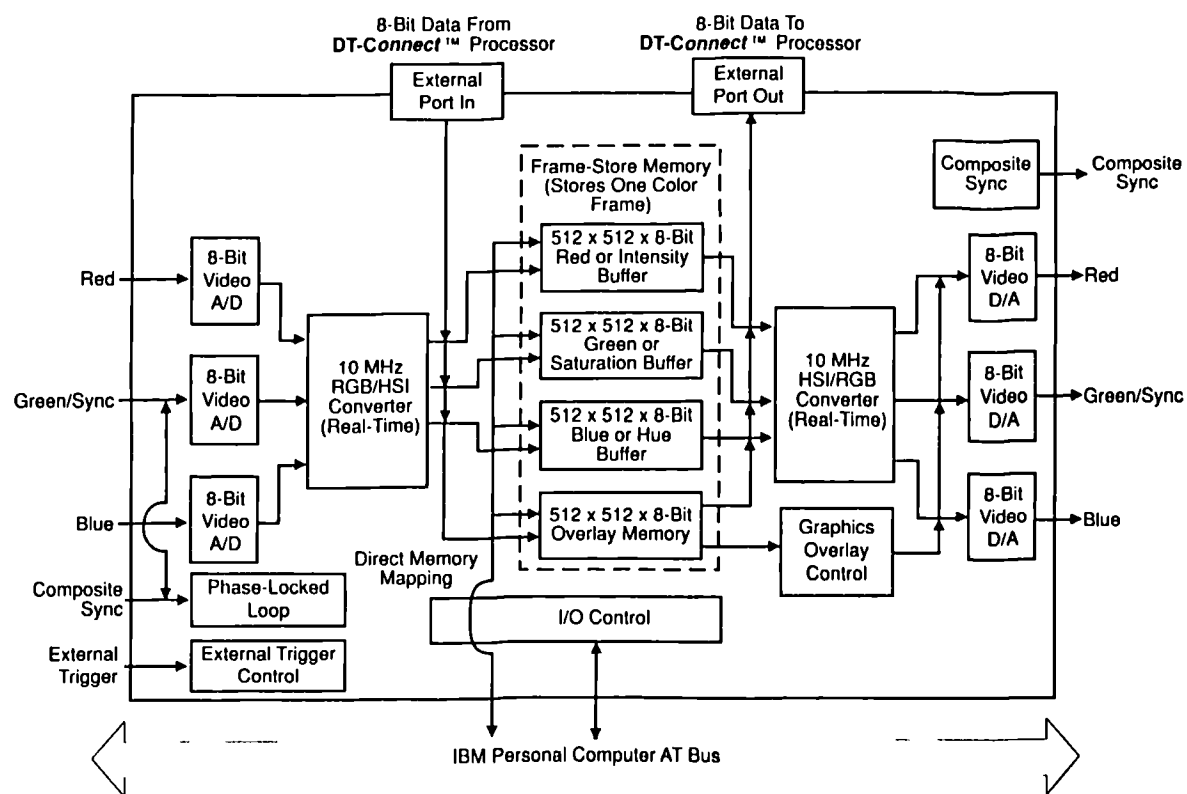


Fig. 38 DT 2871 (HSI) Colour Frame Grabber block diagram (from [119])

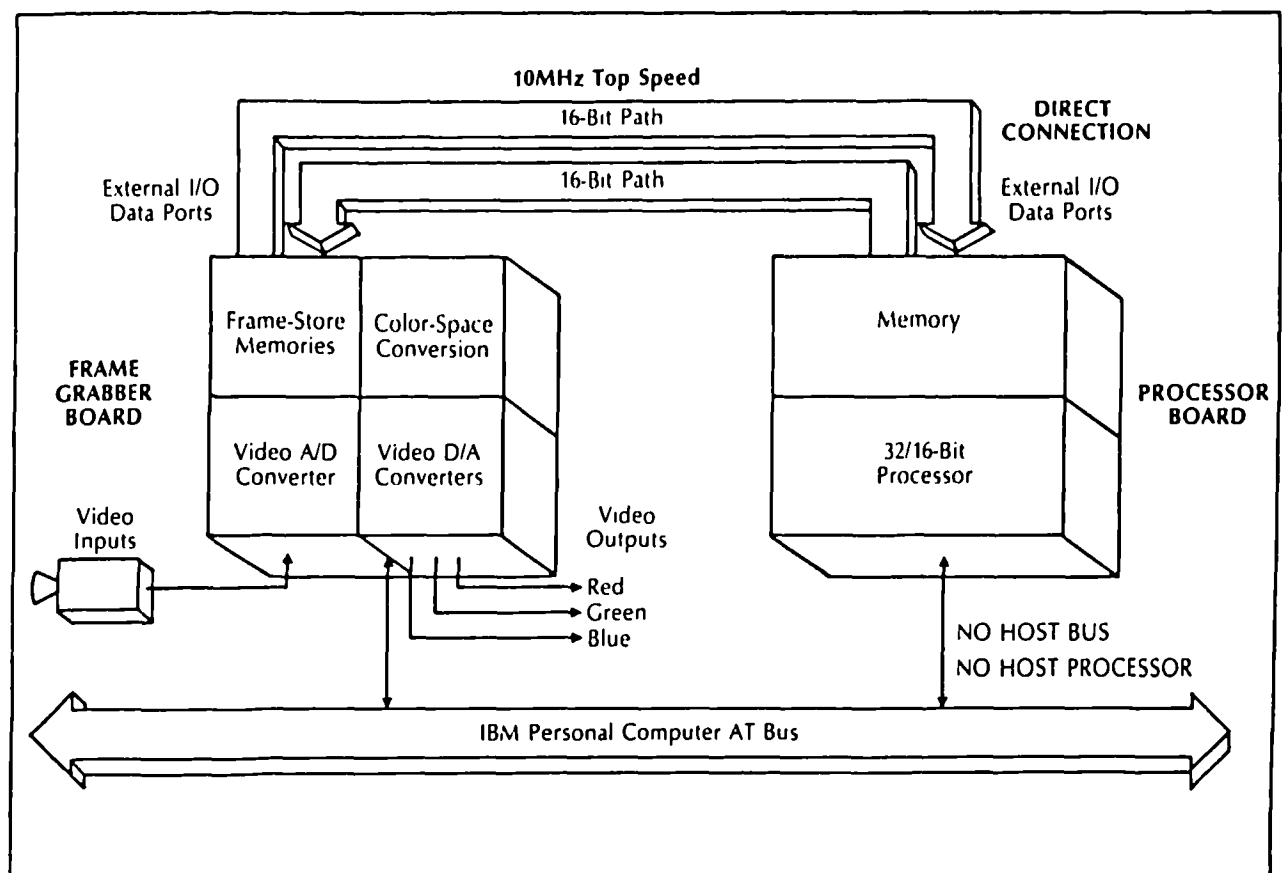


Fig. 39 DT-Connect Image Processing overview block diagram (from [119])

## 6. EXPERIMENTAL APPARATUS AND PROCEDURE

The experimental apparatus was designed, constructed and tested during the course of the present research. This chapter outlines the design criteria for the apparatus, gives a description of its construction and discusses the modifications undertaken as work progressed.

### 6.1 Design and Construction of the Wind Tunnel

The experimental study was carried out using an open low-speed wind tunnel consisting of entrance section with fan and heaters, large settling chambers with diffusing screen and honeycomb, and then mapping and working sections. Air is drawn through the tunnel using a fan able to give Reynolds numbers of between 1000 and 10000 in the working section. The working air temperatures in the rig range between 25°C to 65°C produced by the heater positioned just downstream of the inlet. The major construction material of the wind tunnel is perspex.

Mean velocity is measured using conventional Pitot tubes, and then deduced from the pressure difference between the Pitot tube and wall static pressure.

The wind tunnel is instrumented with copper-constantan (type T), thermocouples and resistance-thermometer compensation so that the surface, water bath and air temperatures can be measured and controlled by a variac control system.

In this experimental study the encapsulated thermochromic liquid-crystal layer is applied directly onto the cooled surface disturbed by the various shapes (see 6.12 and 6.13). Photographs are taken using a standard camera, RGB video-camera and True-colour image processing system. A schematic drawing of the wind tunnel is shown in Figure 40.

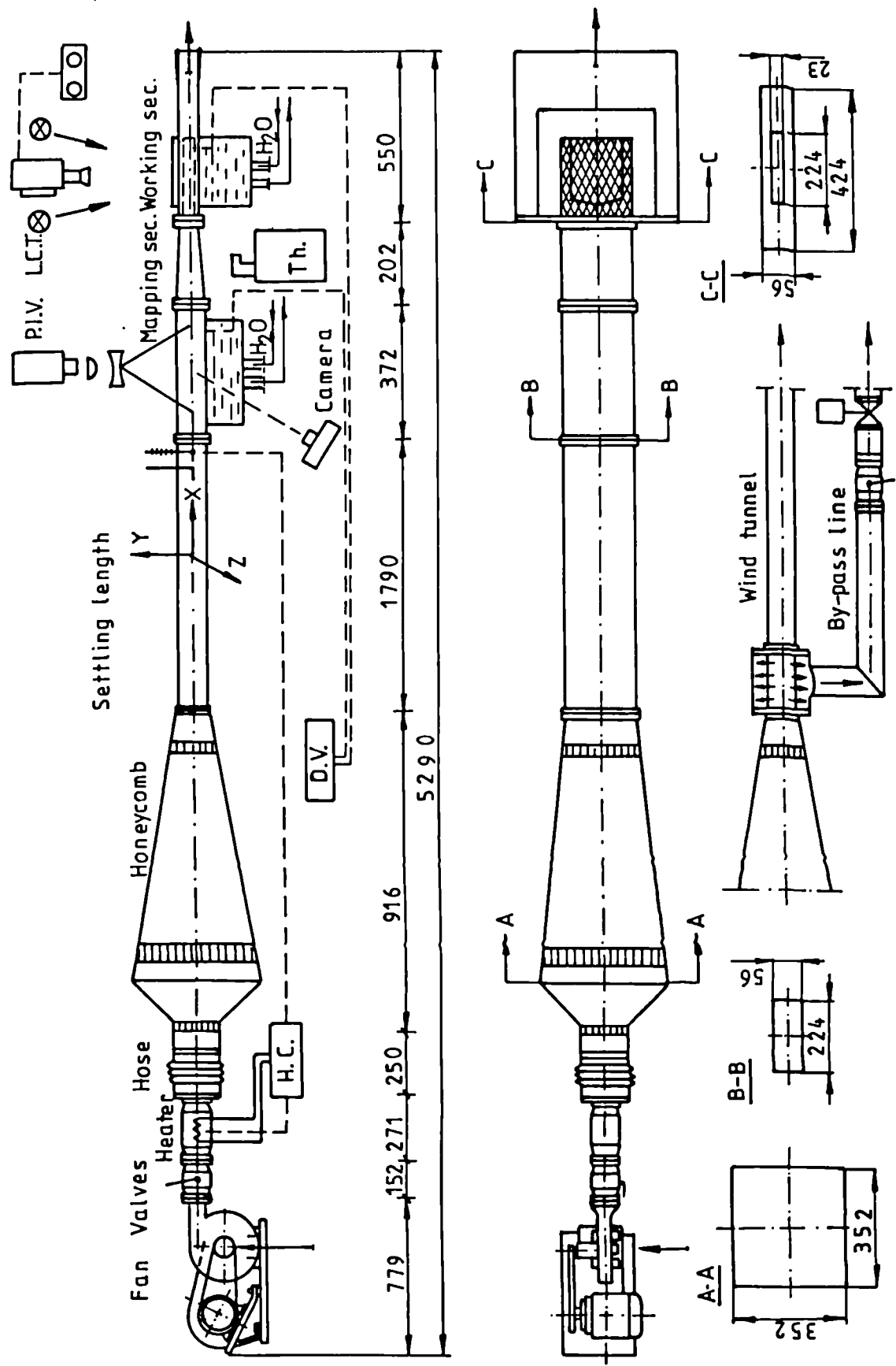


Fig. 40 Open low-speed wind tunnel

### **6.1.1 Entrance section**

According to various assumptions made and preliminary calculations the entrance section of the wind tunnel consisted of:

- (i) Secomak Centrifugal Fan Model 575/1 -  
full load duty  $312 \text{ m}^3/\text{h}$  and  $\Delta P = 333 \text{ mm H}_2\text{O}$ .
- (ii) Air Regulating Valves D11314.
- (iii) Industrial Heater Model 571 to permit 0-3 kW output.

The air flows from the large settling chamber (the combination of diffusing screens, honeycomb, diffuser and a contraction) into a channel (x-flow direction) of rectangular cross-section  $56 \times 200 \text{ mm}$  (yz-plane), i.e. an aspect ratio of 4 : 1. The settling length of 20 hydraulic diameters (1790 mm) is incorporated to ensure that the flow is fully developed before entering the final contraction and the working section.

### **6.1.2 Mapping section**

A schematic drawing of the mapping section is shown in Figure 41. The mapping section is a channel of rectangular cross-section  $56 \times 224 \text{ mm}$ , with a 280 mm long working plate surface. Between the lower and upper plate were mounted horizontally single and double cylinders, square-section column and a square rib (Fig. 42). The lower side of the mapping section is covered by the liquid-crystal sheets (Figure 41c) [120]. A perspex plate with a thickness 8mm and a thin layer ( $\delta = 0.214 \text{ mm}$ ) of liquid-crystal sheets, is cooled by water on the other side to give it a constant, uniform temperature T. The alternative effects of constant wall temperature and constant heat flux boundary conditions are obtained using a water bath, while the temperature can be controlled with a thermostat (see 6.1.5).

The experimental study, thermal mapping and surface heat transfer measurements can be carried out for two alternative inlet flow arrangements for the lower plate surface (see Figures 41a and 41b).

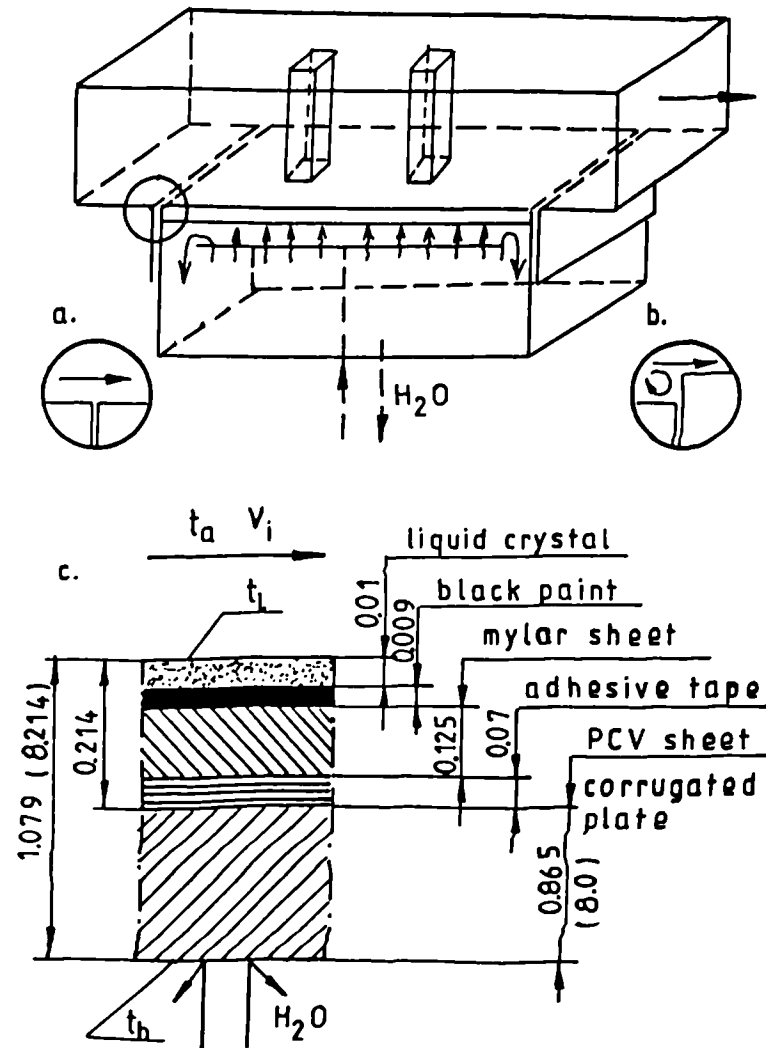


**Fig. 41** Mapping section geometry and liquid crystal package with component thickness

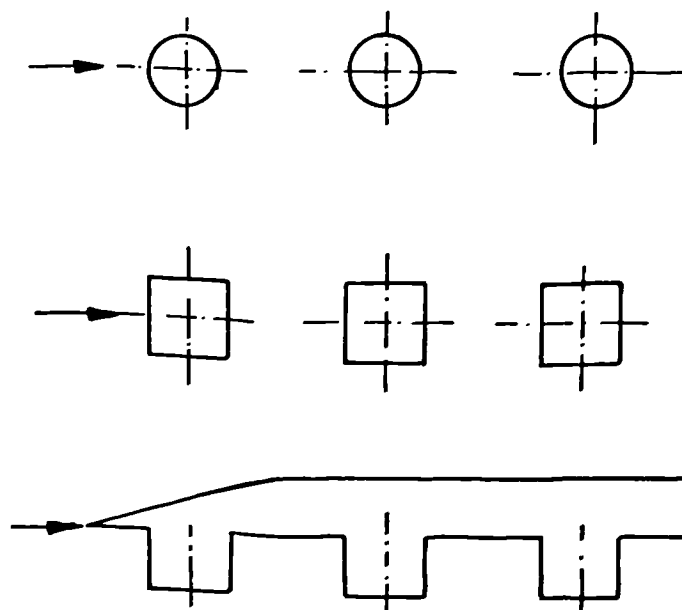


**Fig. 42** Scheme of three different end walls of cascade

### 6.1.3 Working section

It is well established that the inclination angle between plate corrugations  $\varphi$ , wavelength (pitch)  $P$ , height (amplitude)  $H$ , the shape of corrugation and the overall flow direction are major parameters in the thermohydraulic performance of plate heat exchangers. Predictions show there is a probable entrance effect, and that it would be valuable to try to take measurements on a number of "diamonds" in from the entry. This, however, has certain implications for the test section width, to ensure the approximation of a diamond-cell being in an "infinite" flow-field. In other published work, a closed side-boundary is employed, which means that the side flow is "reflected back" [51,52]. It is not absolutely certain whether this affects the performance, although it was assumed not to have an effect in that published work.

As indicated above, the heat and flow properties of the corrugated geometry are determined experimentally (for flat-plate and corrugated working sections) by the following sequence of experiments:

#### Experimental Series No.1 : flat-plate working section

A schematic diagram and engineering drawing of the flat-plate working section is shown in Figures 43 and 44. This working section consists of P.V.C.-layered corrugations twice the size of the actual corrugations. Both sides and end of the working section void into a large box of rectangular cross-section 57 x 442 mm and 550 mm length, respectively. The corrugated working section consists of seven diamonds (as shown in Fig.44), each of pitch  $P = 37.8$  mm, amplitude  $H = 9.53$  mm, cross-sectional area  $A = 145 \text{ mm}^2$ , corrugation hydraulic diameter  $D_h = 15.4$  mm and inclination angle  $\varphi = 36^\circ\text{C}$ .

The lower side of the corrugated working section is covered by the thermochromic liquid-crystal sheets. A water bath sited underneath the section provides a constant temperature side for the lower corrugations.

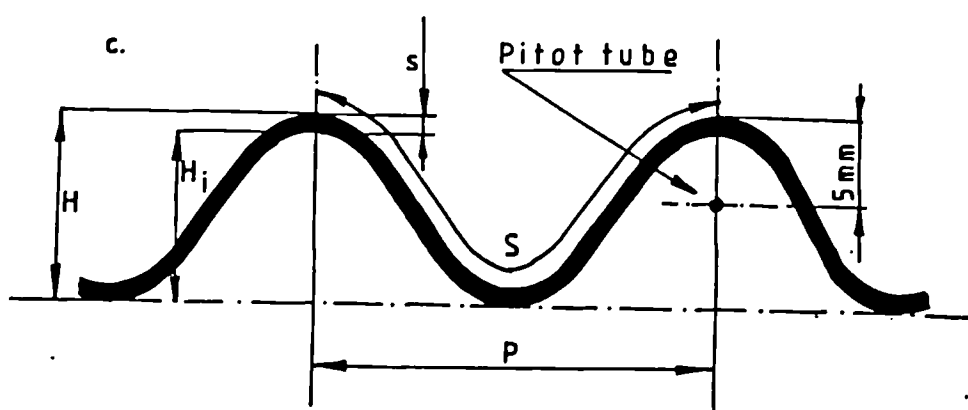
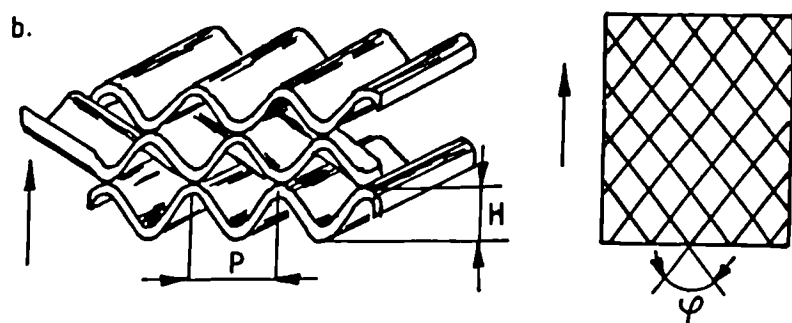
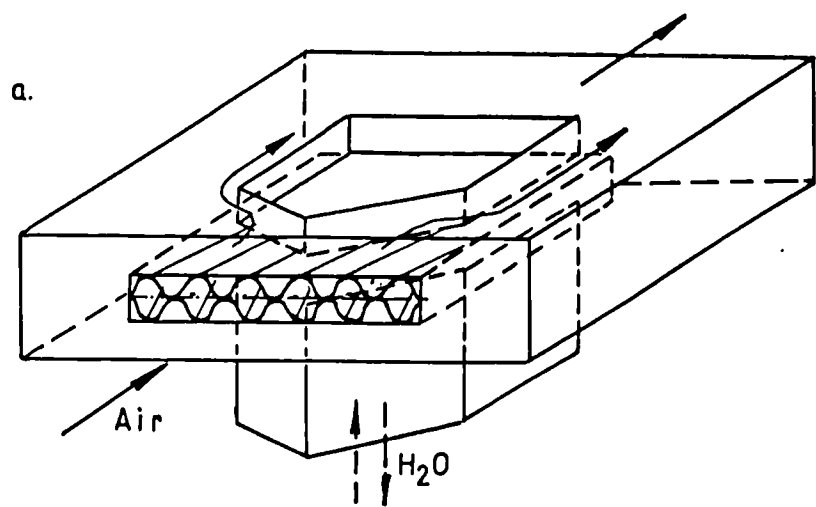


**Fig. 43**

- a) A schematic diagram of the flat-plate working section
- b) Three-dimensional corrugated geometry passage
- c) Cross-corrugated heat transfer element

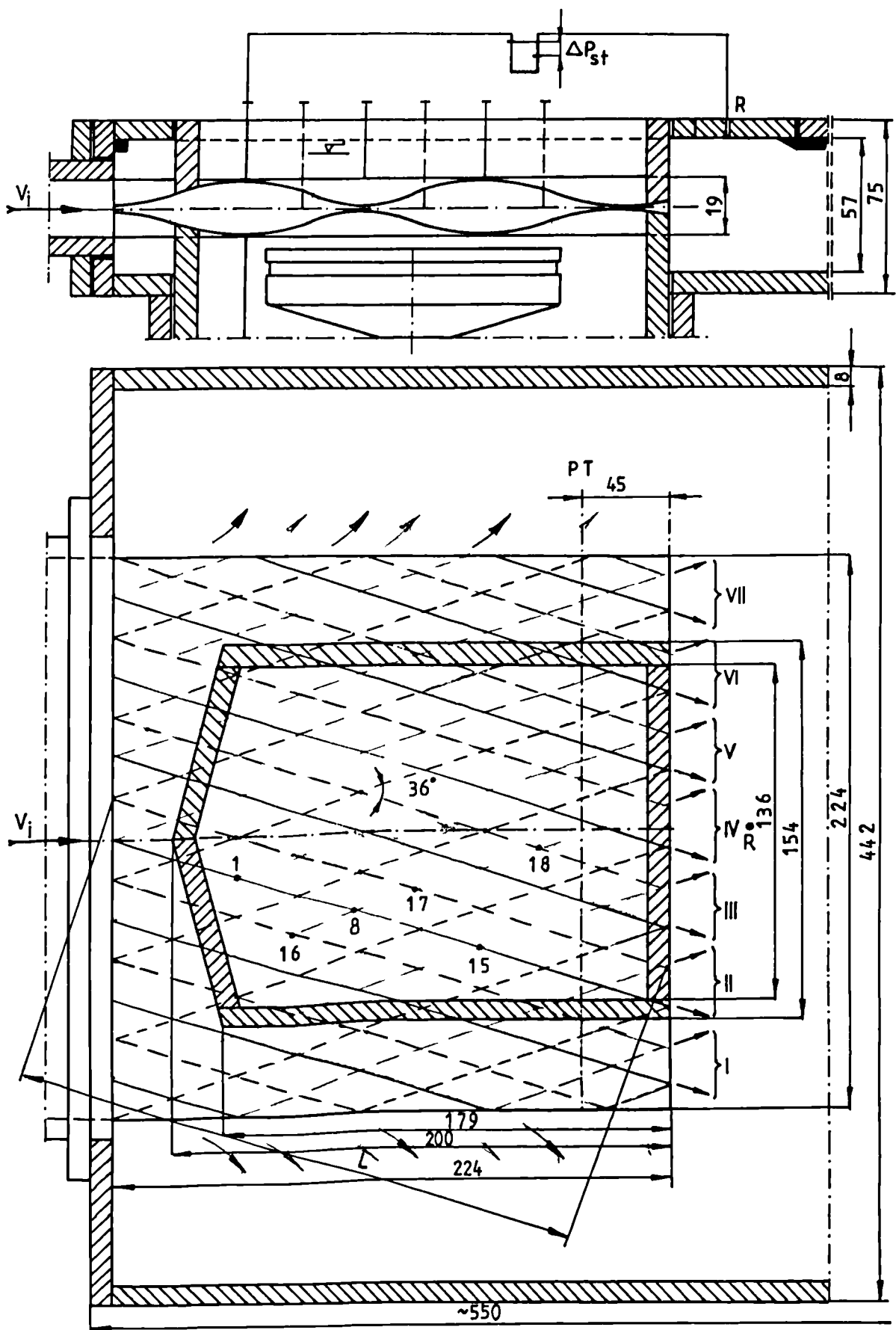


Fig. 44 Schematic diagram of the working section and position of pressure tappings; R - reference pressure tapping, PT - pitot mounting plane, L - length of duct

The working section is instrumented with copper-constantan thermocouples (type T) and thermostat, so that the constant lower surface temperature may be obtained.

#### Experimental Series No.2 : corrugated working section

Previous testing of a "diamond" in a small working section did not help the investigation of the "infinite" flow field requirement since the entrance and the end walls affected the fluid flow. Therefore, the wind tunnel was adapted by designing a larger working section. Turning to the general design, this is shown schematically in Fig.45, it can be seen that the extension of the wind tunnel comprises the following:

- (i) diffuser,
- (ii) second settling length, and
- (iii) much larger working section than before.

The purpose of the diffuser and second settling length is to make the flow more uniform and reduce the C-S area to that required for the working section. A schematic diagram of this section is shown in Figure 46. Both sides of the working section can be closed or open and void into the large box of rectangular cross-section 80 x 570 mm and 700 mm length, respectively. Plates with corrugation inclination angles of  $\varphi = 30^\circ, 36^\circ, 48^\circ, 60^\circ$  and  $75^\circ$  relative to the main flow direction were tested.

The circular test area permits for a small angle, measurements up to 6 diamonds from entry (Fig.46). Additionally, entry effects can be investigated from position 6 to 2, with no ambiguity on the side boundary condition. The corrugated working section consists of 13 diamonds each of pitch  $P = 32$  mm, amplitude  $H = 8.75$  mm, cross-sectional area of  $128.0 \text{ mm}^2$  and corrugation hydraulic diameter  $D_h = 13.84$  mm. The upper side of the corrugated P.V.C. working section is covered by the thermochromic liquid crystals in sheet form. An upper water bath provides a constant temperature side for the upper

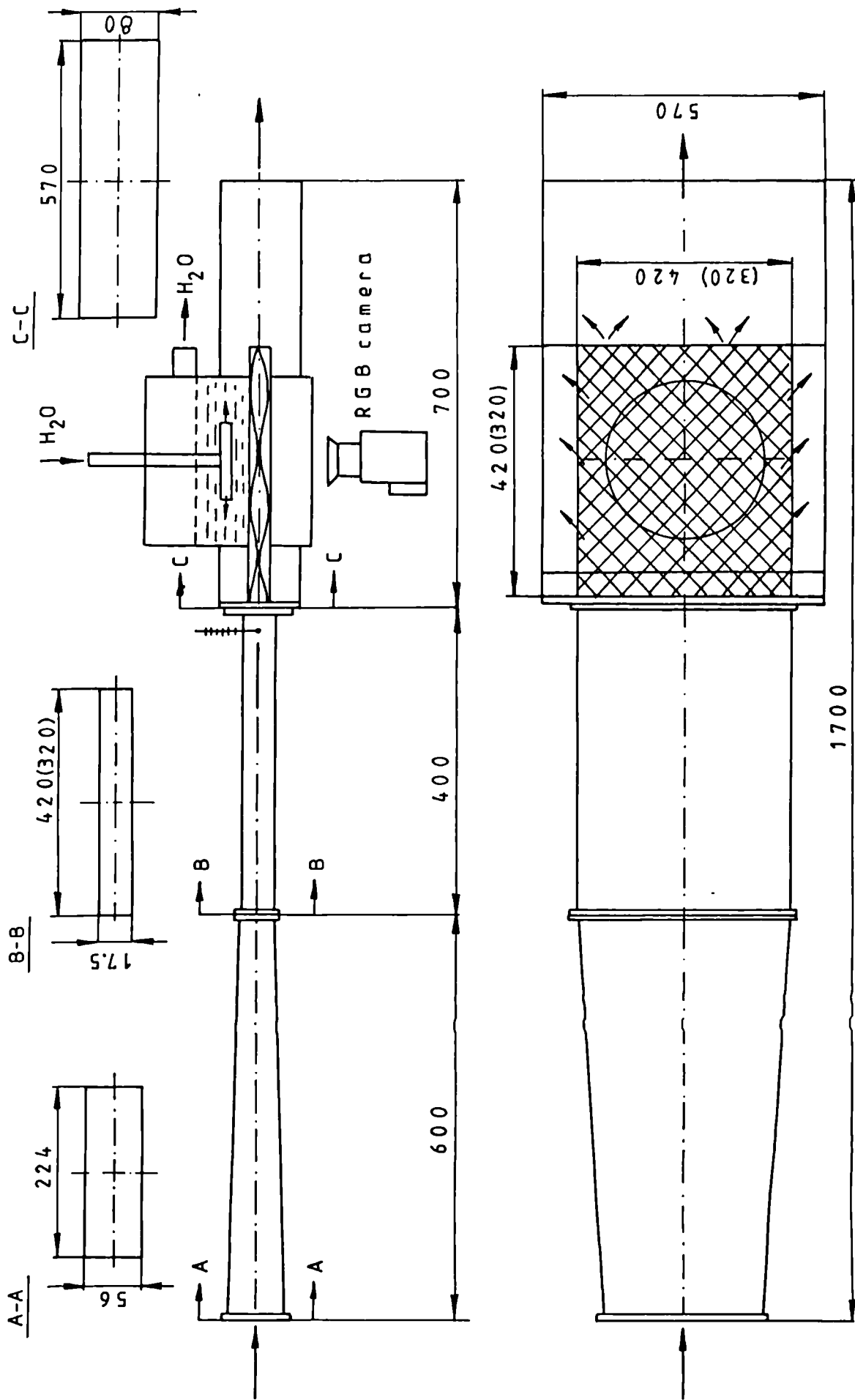


Fig. 45 Extension of the wind tunnel with new corrugated working section and an upper constant-temperature water bath

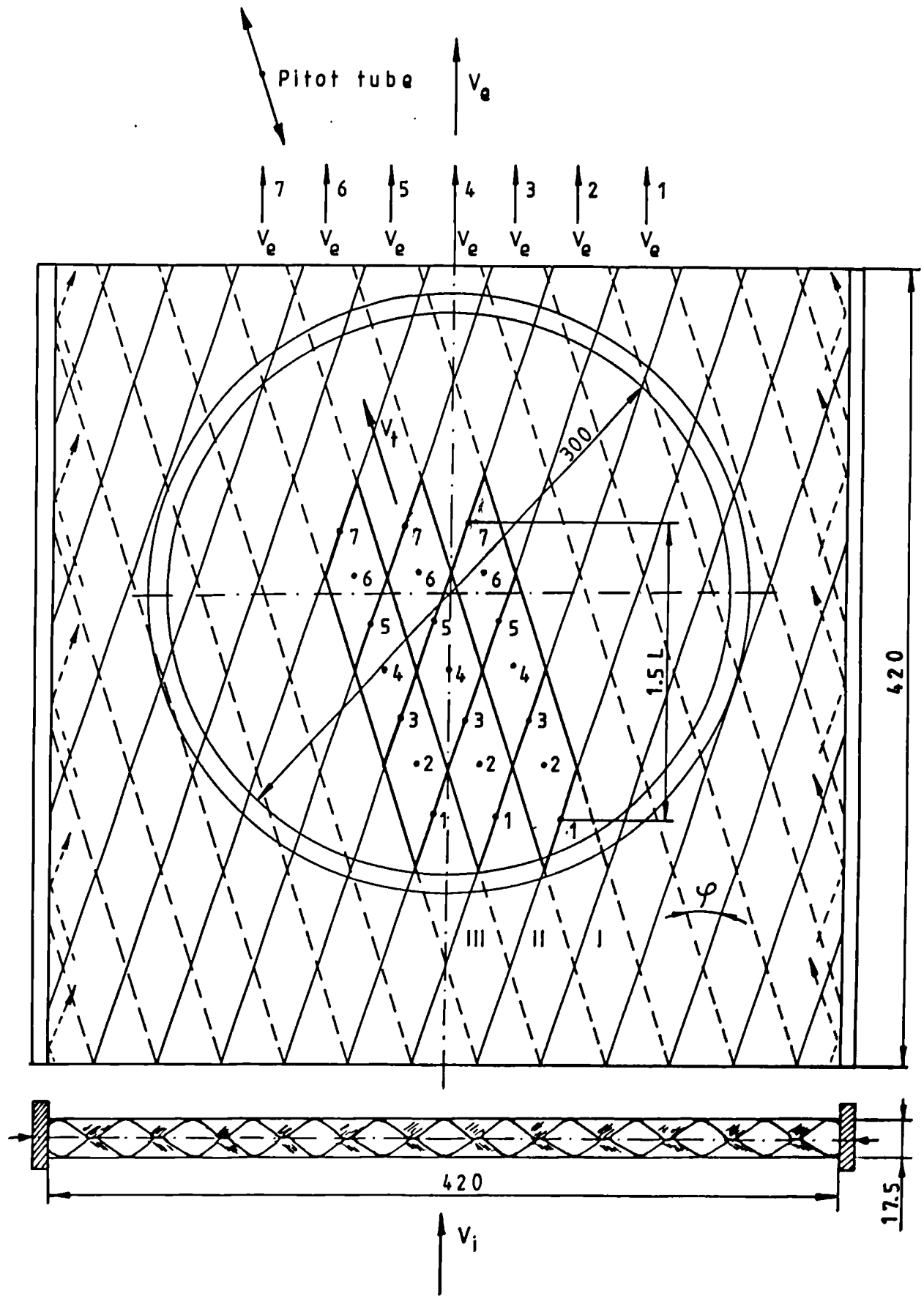


Fig. 46 A schematic diagram of the corrugated working section -  
inclination angle  $\varphi = 36^\circ$

corrugations. The perspex tube ( $D = 300$  mm) (lower and upper) is designed to facilitate fairly rapid manipulation of the corrugated plate so as to permit:

- (i) testing of a range of inclination angles,
- (ii) investigation of different diamond geometries, and
- (iii) investigation of entry and side wall effects.

#### **6.1.4 Measurements of velocity and static pressure in the corrugated working section**

Knowledge of the velocity profiles and static pressure distribution in corrugated sheets is desirable in order to enhance understanding of flow phenomena and heat transfer and to facilitate comparison with computational simulations. Therefore, the static pressure drop along the peaks and troughs of the corrugations were measured using 17 pressure tappings 1 mm in diameter with a reference tapping located in the outlet box (Figs.44,47,48). In Fig.44 the green colour corresponds to the lower side wall and the red colour to the upper wall. Solid and broken lines indicate the peaks and troughs, respectively.

Figures 47 and 48 show the general view of the location of pressure orifices (units of the diamond geometry and cross-section A and B). Wall static pressures were measured at the wall tappings by means of a micro-manometer model MDC FC002/Furness Controls Ltd., Bexhill, U.K. with two ranges:

- 1 : from 0 to  $19.999$  mm  $H_2O$ , and
- 2 : from 0 to  $1.999$  mm  $H_2O$ ,

Outlet mean velocity profiles (for seven ducts and for lower and upper corrugated plates) were measured using a Pitot pressure tube mounted 45 mm inside each duct, Figure 44.

Figure 49 shows the general arrangement of the flow and static pressure measurements in the corrugated working section. Pressure drop was measured using two methods: (i) Pitot tube and (ii) pressure taps located in the trough. Outlet mean and local velocity in the corrugated ducts was determined by a Pitot tube 2.3 mm in diameter.

#### **6.1.5 Cooling water system**

The local heat flux release from the mapping and working section (corrugated) surfaces must be known. In order to verify the technique quantitatively a testing procedure for measuring the heat release has been established.

In the present studies a Resemount constant temperature bath, capable of establishing and maintaining temperature to within  $\pm 0.01^{\circ}\text{C}$  accuracy, was used to calibrate the liquid crystals, thermocouples and to hold constant temperature in the mapping and working section.

A schematic drawing of the TE-8A circuit diagram is shown in Figure 50.

The specification of the TE-8A constant temperature water bath is as follows:

- operating temperature range	-20 to $95^{\circ}\text{C}$
- working temperature range	22 to $95^{\circ}\text{C}$
- temperature selection	analogue
- temperature stab. at $40^{\circ}\text{C}$	0.01
- set point accuracy	+2% full scale range
- method of control	proportional
- temperature sensor	thermistor
- nominal heat power	1000 W
- pump capacity	10 l/min

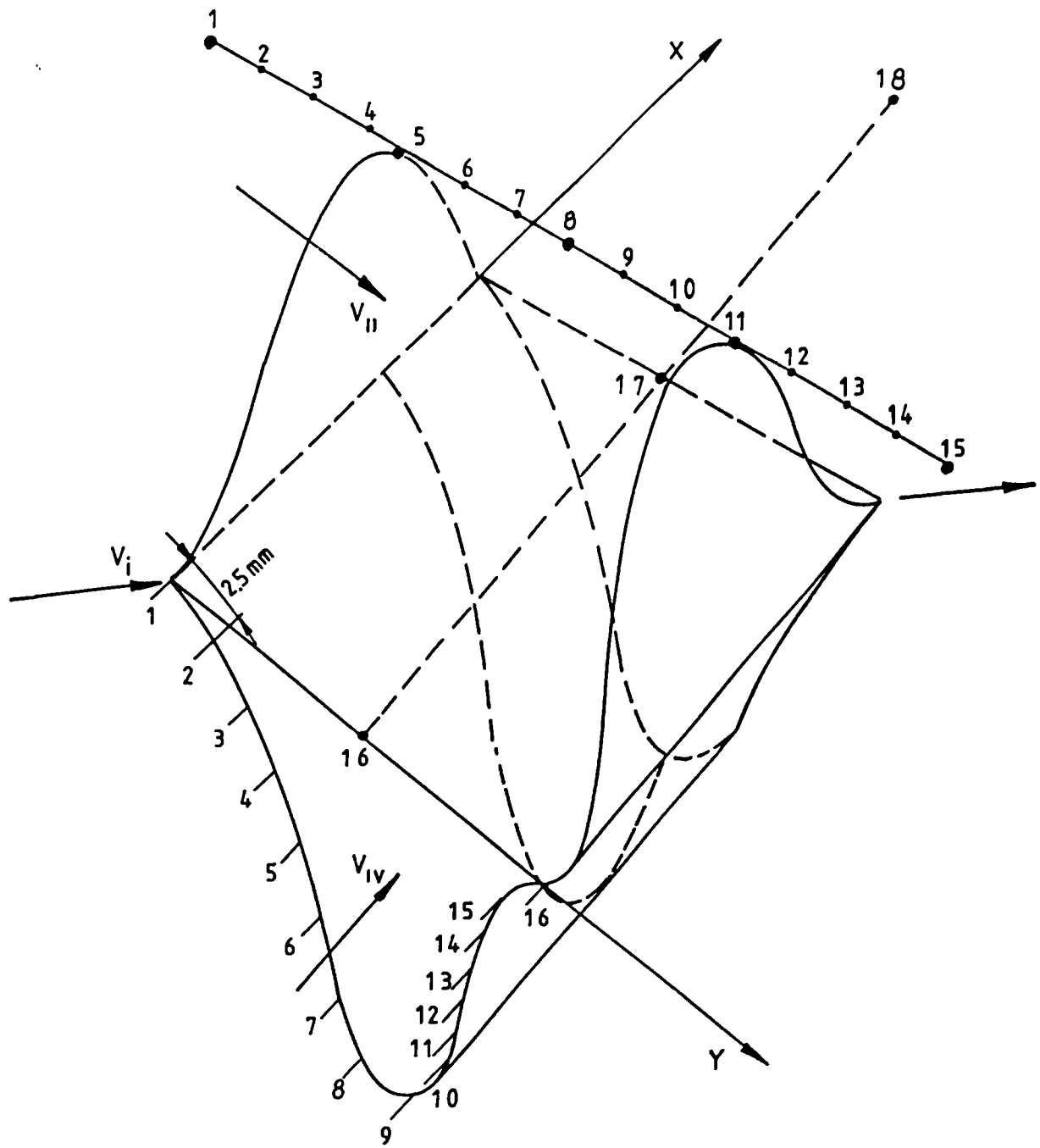


**Fig. 47 General view of the three-dimensional diamond geometry**

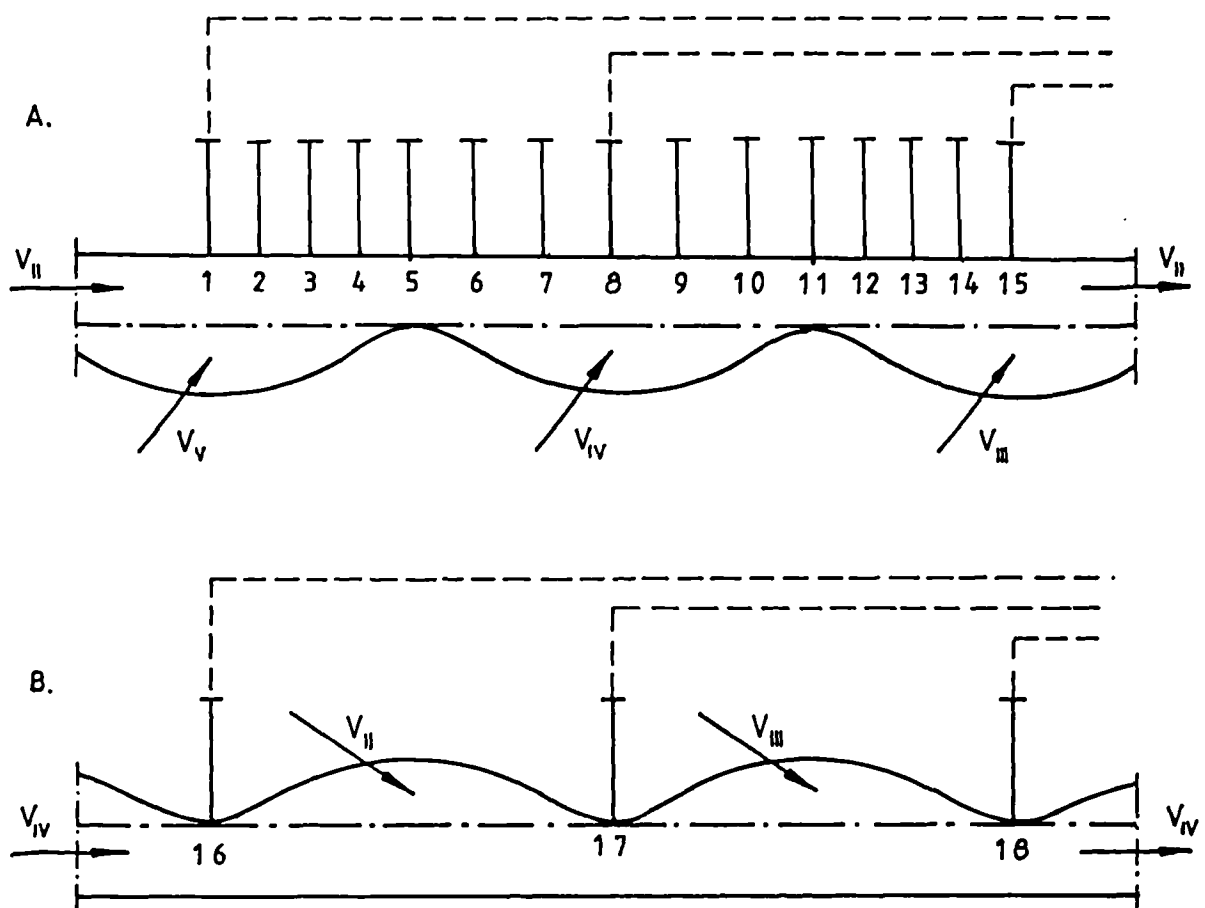


**Fig. 48 General view of the location of pressure tappings along flow ducts Nos. II and IV-arrangement for flat-plate working section**

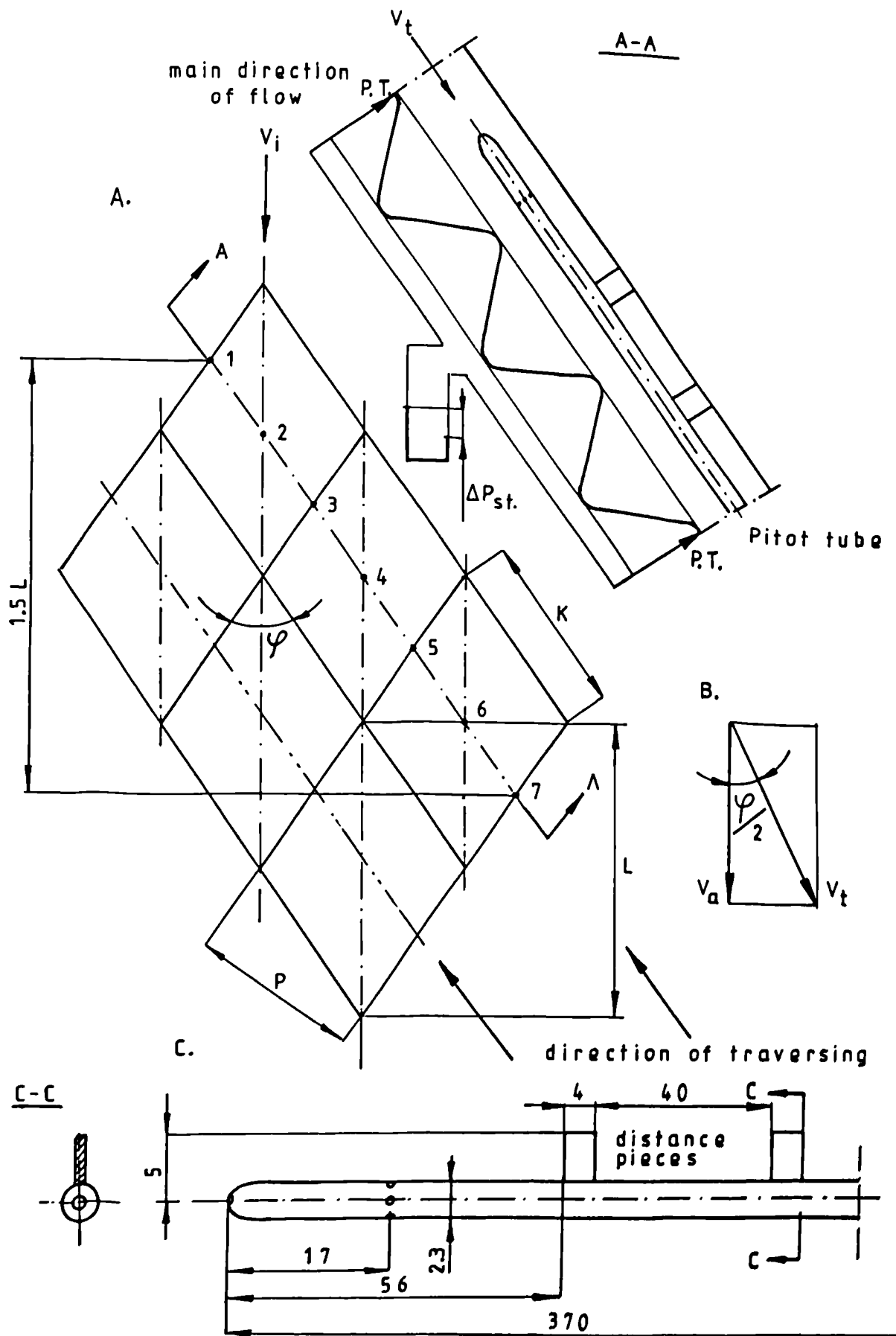


**Fig. 49 Schematic illustration for pressure drop and velocity measurements using tappings and Pitot tube-arrangement for corrugated working section**

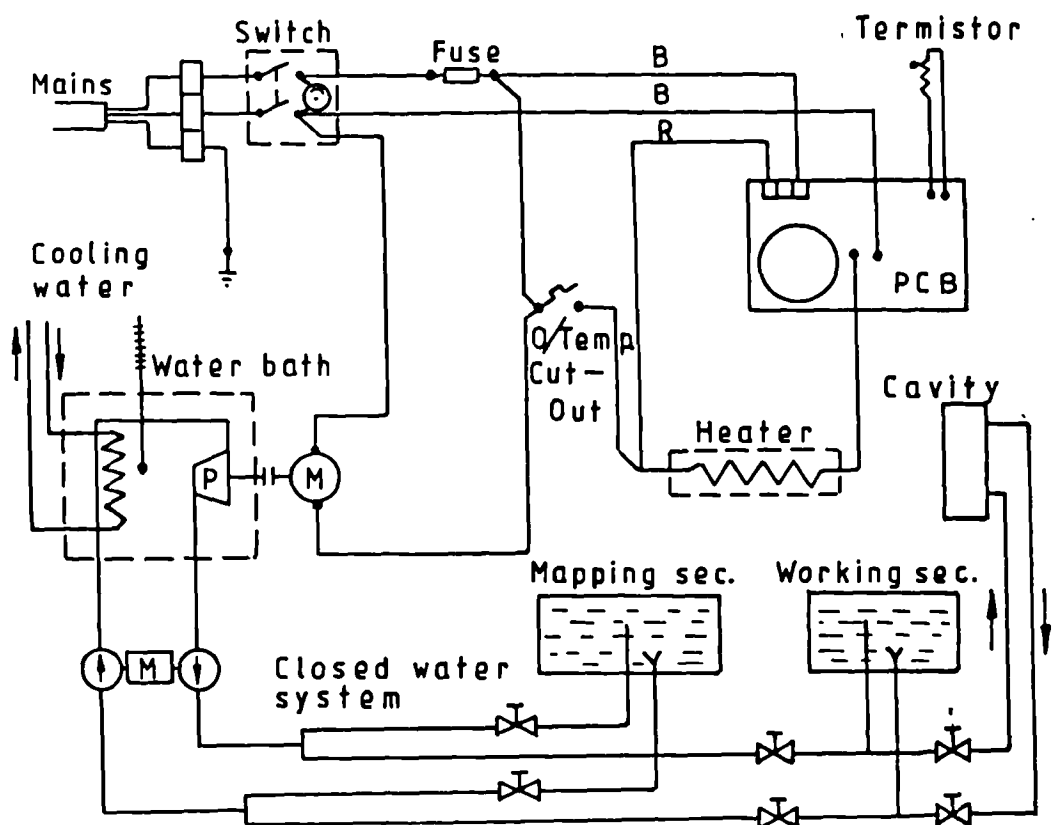


Fig. 50 Schematic drawing of the TE-8A water circuit diagram

## **6.2 Experimental Setup for Flow Visualisation in a Rectangular Cavity**

Natural convection phenomena in rectangular cavities with differentially heated walls have received considerable attention due to their many applications in energy-sensitive designs such as building systems with cavity walls and air gaps in unventilated spaces, double glazing, solar collectors and furnaces. There are numerous other examples. These complex phenomena have given rise to a very large number of numerical predictive studies. However, quantitative fundamental experiments are still necessary to lead to better understanding of both the physical phenomena and their numerical simulations.

The following experiment involves an application of liquid crystals for visualisation of both temperature and velocity fields in thermal convective flows. Such a visualisation leads not only to a global picture of flow configuration but also allows simultaneous and detailed quantitative measurements of temperature and velocity using liquid crystals as both flow and thermal tracer. This could be called PIVT (particle image velocimetry and thermometry). The concept of PIVT is introduced and some of its advantages and possibilities are discussed.

The thermal convective flow in this study was generated in a rectangular cavity of 180 mm long, 60 mm wide and 30 mm high. The cavity had isothermal hot & cold walls and was made from 8 mm perspex (apart from the lower copper plate), Figure 51. The temperatures of the heated (electrically) and cooled (by water) walls were continuously measured by thermocouples and registered by a multichannel recorder. The temperature fluctuations were below 0.1°C. The illumination of the flow field was done by a specially adapted 800 W photo-flash. A cylindrical lens and a diaphragm (slot) mounted in front of the discharge tube allowed the generation of a light sheet of 2-3 mm thickness and 200 mm width, Figure 52. The flash lamp was triggered

by a programmable impulse generator at a prescribed time sequence. Usually 4 to 12 flashes were used to take one photograph. The time interval between flashes varied from 1 to 15 seconds. To obtain information about the direction of the flow the last flash of a series was released at half the previous prescribed time interval. On the photograph the liquid crystal particles conveyed by the flow appear as a series of coloured and regularly spaced dots (see Figure 90). It can be seen that the general background colour is due to dispersion of much smaller particles. The photographs were made perpendicular to the line of the illumination and were taken with a 35 mm SLR camera with 90 mm lens. The angle of the inclination of the cavity was varied from the horizontal to the vertical (for YZ and YX planes).

Thermochromic BDH [118] liquid crystals were used to make visible the temperature and velocity fields in the glycerol-filled cavity. The glycerol, liquid-crystal mixture was prepared by dissolving unencapsulated chiral-nematic material (TM256 [118]) in ether and then spraying the mixture into the air above a free surface of glycerol. The ether evaporated in mid-air, leaving small drops of liquid crystal material which fell into the glycerol forming an "almost mono-dispersed" suspension of particles approximately 50-80 microns in diameter. The concentration was kept below 0.03% by weight.

In the present experiments interest centred on the shape of the isotherms (not in their absolute temperature values) and on the possibility of applying the True-colour image processing system for general observations of three-dimensional structures of heat and fluid flow in an enclosure.

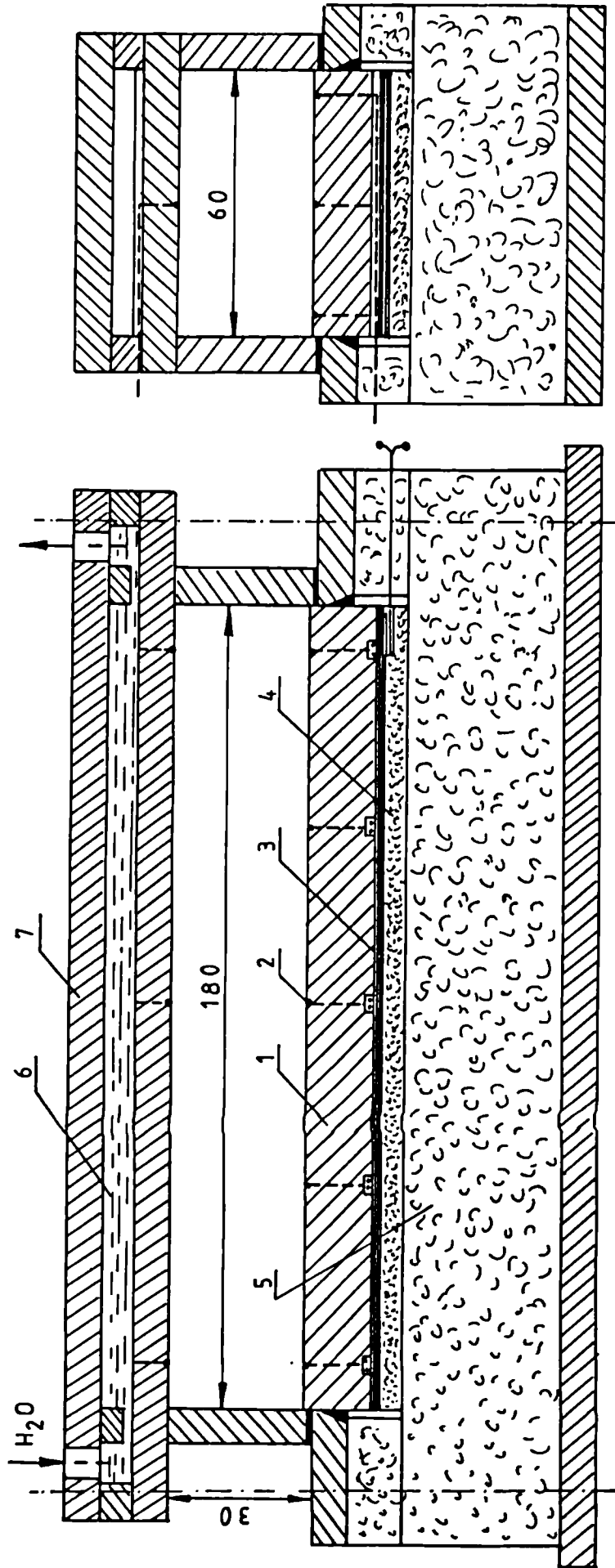
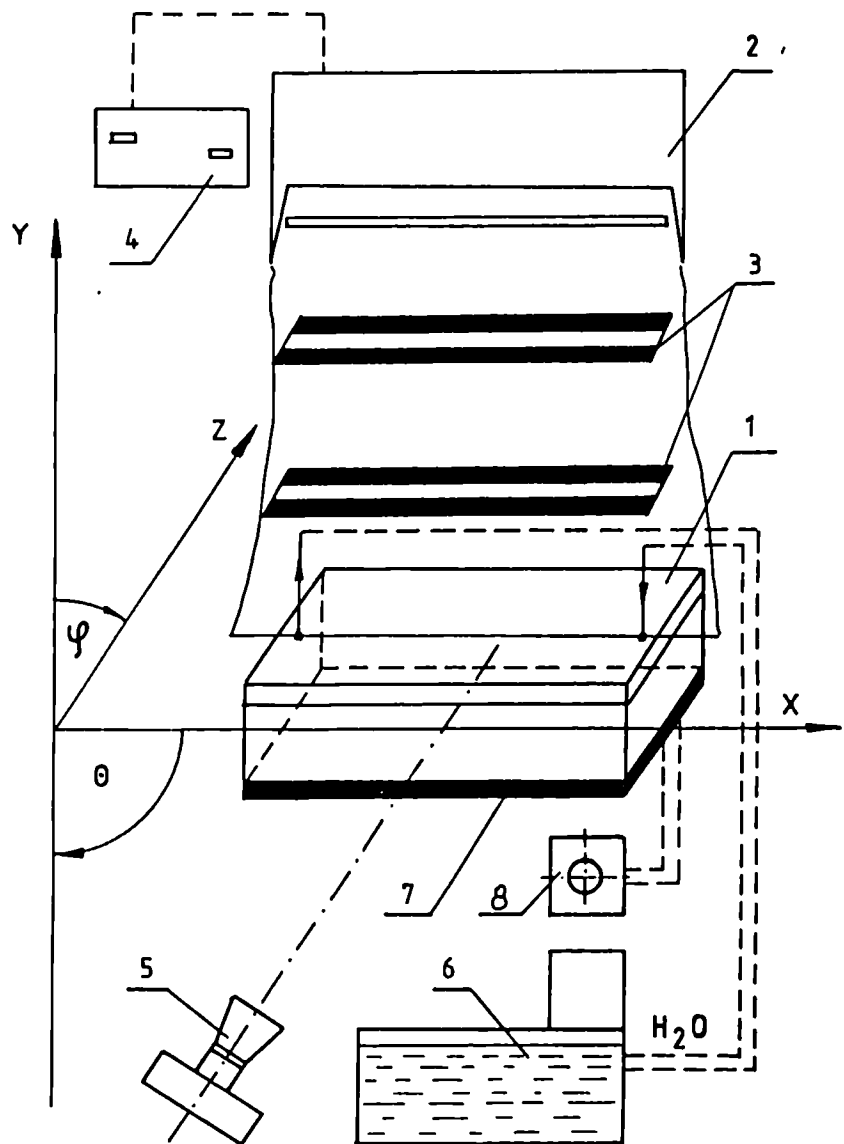


Fig. 51 Schematic of rectangular cavity  
 1. Copper plate 2. Thermocouples 3. Blanket 30 W heater 4. Wool  
 insulation 5. Polystyrene 6. Cooling water 7. Perspex top cover



**Fig. 52 Schematic of experimental facility**

1. Cavity 2. Power flash lamp 3. Light slots  
 4. Programmable generator trigger 5. Camera  
 6. Water bath 7. Blanket 30 W heater 8. Transformer

## 7. EXPERIMENTAL RESULTS

The heat transfer coefficient is a defined quantity, calculated from the surface heat flux and the difference between the surface temperature and some agreed reference temperature. This is usually the far field temperature, the mixed mean temperature or the adiabatic surface temperature. In the following experiments liquid crystals were used to determine the distribution of surface temperature and heat flux - this allows evaluation of the local heat transfer coefficient or Nusselt number.

The effect of a constant wall temperature and heat flux boundary conditions for the corrugated and flat plate working sections are obtained using a water bath while the temperature can be controlled with a thermostat (see Chapter 5.0). The temperature recorded from the liquid-crystal sheet is only at the red colour (yellow-green for image processing), this being a well defined colour for human viewing.

The local convective heat transfer coefficient  $h_\ell$  in "l" follows from the fact that the conductive heat flux  $q_k$  in either working section is equal to the convective heat flux from air to the surface in the stationary state:

$$h_\ell = \frac{k_t}{\delta_t} \frac{(t_\ell - t_b)}{(t_a - t_\ell)} \quad (8)$$

where:

- $k_t$  - mean conductivity of the liquid crystal package and plate
- $\delta_t$  - thickness of the liquid crystal package and plate
- $t_\ell$  - temperature of surface (liquid crystal isotherm temperature)
- $t_b$  - temperature of water
- $t_a$  - temperature of air

The experimental results are presented in terms of a local Nusselt number:

$$Nu_\ell = h_\ell D_h / k_a \quad (9)$$

where:  $D_h$  - hydraulic diameter  
 $k_a$  - conductivity of the air

With the temperature difference between the air and liquid crystal isotherms fixed, different heat transfer coefficient (Nusselt number) contours are determined by varying heat flux values.

### 7.1 Heat Transfer and Friction Factor

#### - Results for the Flat-Plate Working Section

As noted earlier, the contours of constant heat transfer coefficient are not directly equivalent to the isotherms, as measured from the photographs or images. They are determined after taking into account thermal conduction in the plate, radiation from the surface and other corrections, the key one being the lateral conduction. This correction is typically about 4% of the net flux [54].

The liquid crystal colour temperature used is  $27.7^\circ\text{C}$ , some  $17.6^\circ\text{C}$  below the air temperature ( $t_a = 45.3^\circ\text{C}$ ) for these experiments. Twelve to sixteen isotherms (each corresponding to a different heat flux) are photographed to record the local contours under an oblique Reynolds number (Figure 56a). The locations on each isotherm are digitized following a projection of the photographic image onto a digitizing pad.

Local heat transfer measurements have been carried out for Reynolds numbers based on the centreline inlet velocity along the main flow direction,  $V_i$  of 1796; 2390; 2850; 3394; 3900; 4540 & 5506. Only the bottom wall of a second single "diamond" was considered (as shown in Figure 44). Local heat transfer coefficient and Nusselt number

maps, derived from local wall-temperature distributions as indicated by TLC's, are reported in Figs. 53 to 59 for the Reynolds numbers examined. Average Nusselt numbers, obtained by numerical integration of these maps are also reported. An example of the three-dimensional Nusselt number distributions for  $Re = 1796$ ,  $2390$  and  $5506$  is shown in Figure 60.

Experimental results are summarised in Fig.61, together with experimental values of the maximum and minimum Nusselt number.

Outlet mean velocity profiles (for seven ducts and for both lower or trough, and upper or peak, corrugated plates) were measured using a Pitot pressure tube. Figure 62 shows a sample outlet mean velocity distribution for the flat-plate working section (the red and green colours corresponding to the upper and lower walls, respectively). It is evident from graphs that the flow is not everywhere strictly uniform. However, for the central ducts III and V respectively, the velocities agree, generally, to within  $\pm 1.5\%$  for Fig.62 and  $\pm 2.5\%$  for all experiments.

Figures 63 and 64 show the peak and trough wall static pressure variations along the flow ducts Nos. II and V together with centreline inlet velocity  $V_i$ . It is evident from the graph that there is a significant variation in mean pressure drop along the peak and trough. Due to turbulent flow streamwise and vertical velocity components the pressure drop distribution for the peak is higher than for the trough respectively, and is more non-linear in form. Also, by comparison of Figs.63 and 64 with Fig.48, it can be seen that the pressure gradient varies consistently with the channel expansion/contraction, Reynolds number and distance from entrance.

Figure 65 shows the corresponding friction factors of the same structures at the same Reynolds number. The diagram shows the friction factor  $f$  defined as:

$$f = \frac{2 \Delta P D_h}{\rho V_i^2 l} \quad (10)$$

where:  
 $D_h$  - hydraulic diameter  
 $V_i$  - centreline velocity in the main direction  
 $\Delta P$  - pressure drop  
 $l$  - length of the structure in the main flow direction  
 $\rho$  - density of air

In this part, the liquid crystal method has successfully been applied to obtain quantitative local and average heat transfer data for the initial corrugation geometry. For comprehensive quantitative local heat transfer data, the visibly sharp red line of the spectrum was obtained at different fluid temperatures for the same Reynolds number. These records were synthesised and then, using a semiautomatic procedure, the local heat transfer was displayed in three-dimensional manner and the average heat transfer calculated. Results are also presented for the local variation of pressure drop using micro-manometers. It is evident from the graph and photographs that there is a significant variation in mean pressure drop along the peak and trough and non-uniform local heat transfer distribution. Due to turbulent flow streamwise and vertical velocity components the pressure drop distribution for the peak is higher than for the trough respectively, and is more non-linear in form. A significant "entrance effect" was found in the experiment, together with the influence of Reynolds number on static pressure distribution along the peak. Also, by comparing Figs.63 and 64 with Fig.48, it can be seen that the pressure gradient varies consistently with the channel expansion/contraction and Reynolds number.

	$\alpha$	Nu	9
	$W/m^2 K$	—	
1	122.9	68.0	—
2	114.4	63.0	—
3	106.6	59.0	—
4	88.3	49.0	—
5	66.3	36.5	—
6	59.4	33.0	—
7	54.3	30.0	—
8	45.3	25.0	—
9	37.3	20.5	—
10	27.6	15.2	—
11	24.1	13.3	—
12	20.5	11.3	—

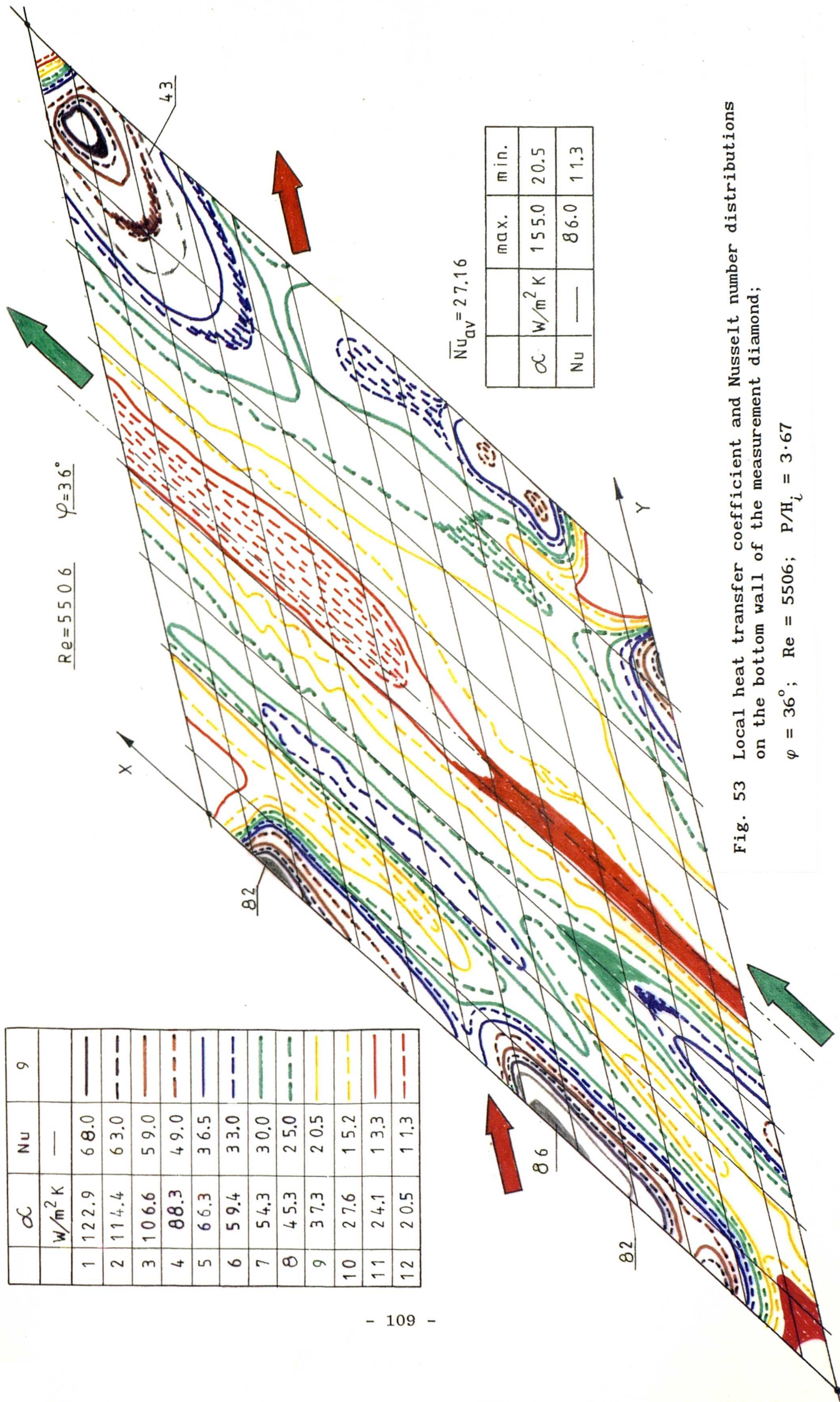
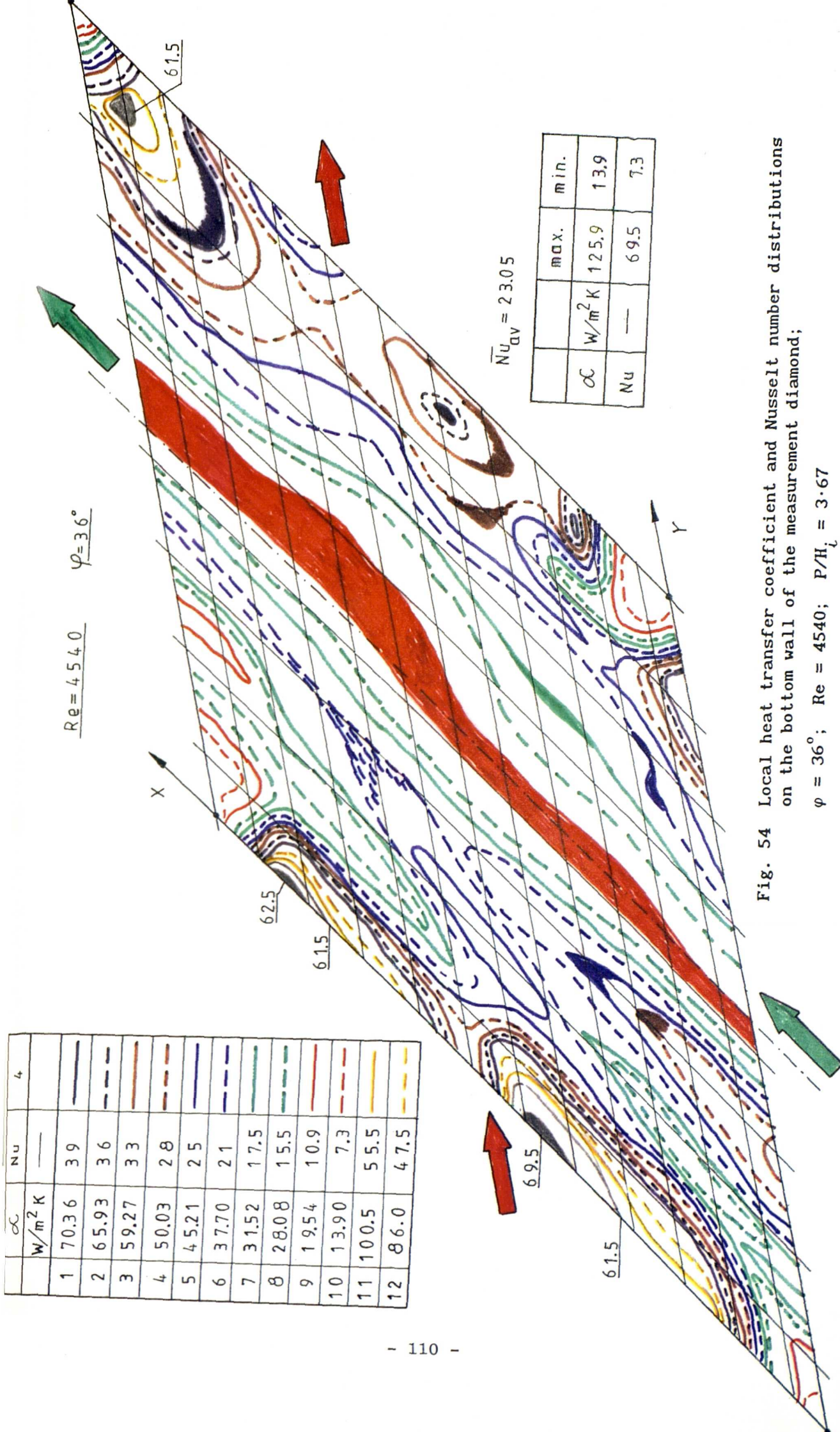


Fig. 53 Local heat transfer coefficient and Nusselt number distributions on the bottom wall of the measurement diamond;  
 $\varphi = 36^\circ$ ; Re = 5506;  $P/H_l = 3 \cdot 67$



Local heat transfer coefficient and Nusselt number distributions on the bottom wall of the measurement diamond;  
 $\varphi = 36^\circ$ ;  $Re = 4540$ ;  $P/H_L = 3.67$

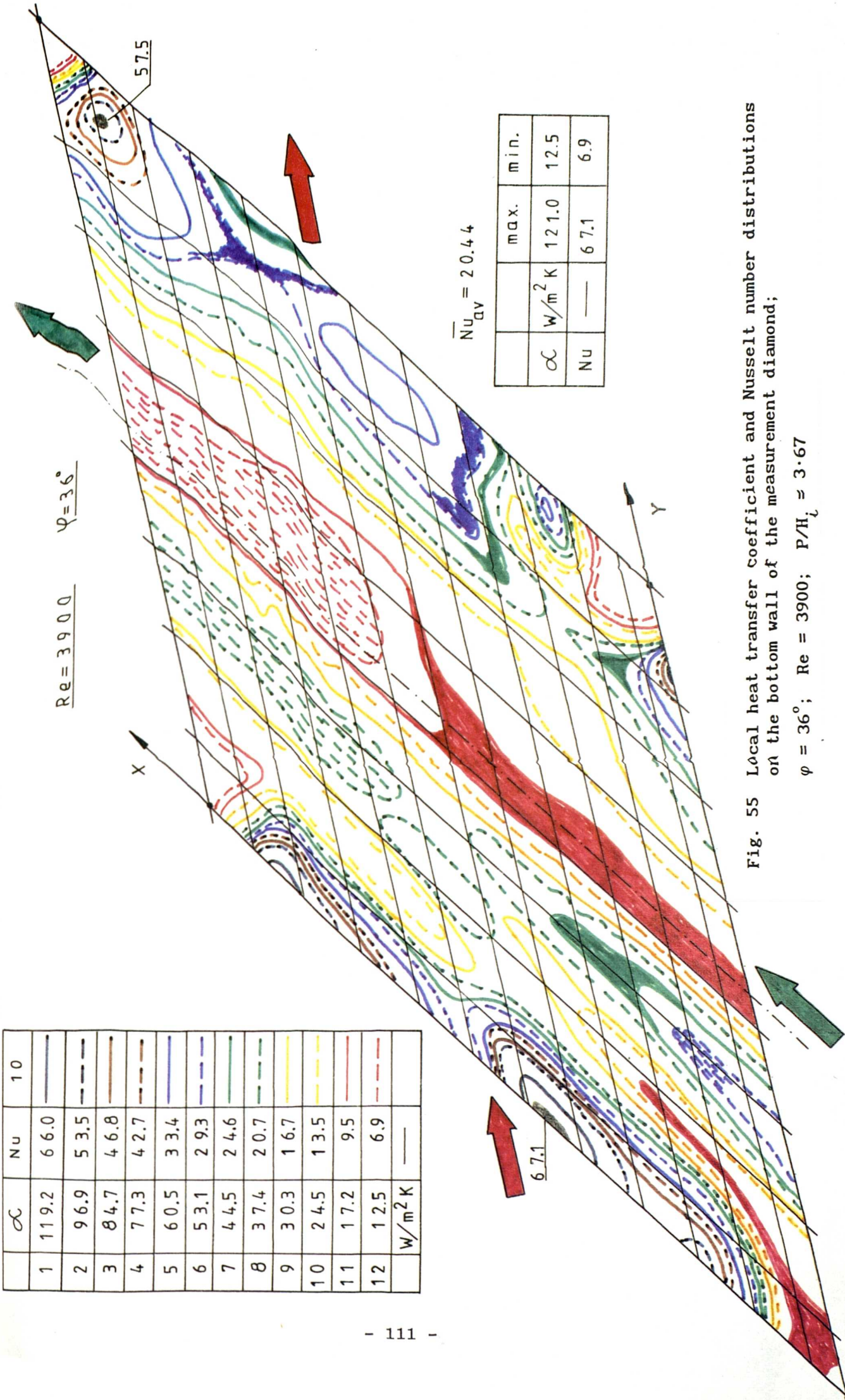


Fig. 55 Local heat transfer coefficient and Nusselt number distributions on the bottom wall of the measurement diamond;  
 $\varphi = 36^\circ$ ;  $R_e = 3900$ ;  $P/H_L = 3.67$

	$\alpha$	Nu	5
	$W/m^2 K$	—	
1	76.71	4.2	—
2	70.83	3.9	—
3	62.35	3.4	—
4	55.27	3.1	—
5	47.52	2.6	—
6	43.73	2.4	—
7	37.74	2.1	—
8	33.11	1.8	—
9	30.92	1.7	—
10	27.40	1.5	—
11	16.90	9.3	—
12	11.40	6.3	—

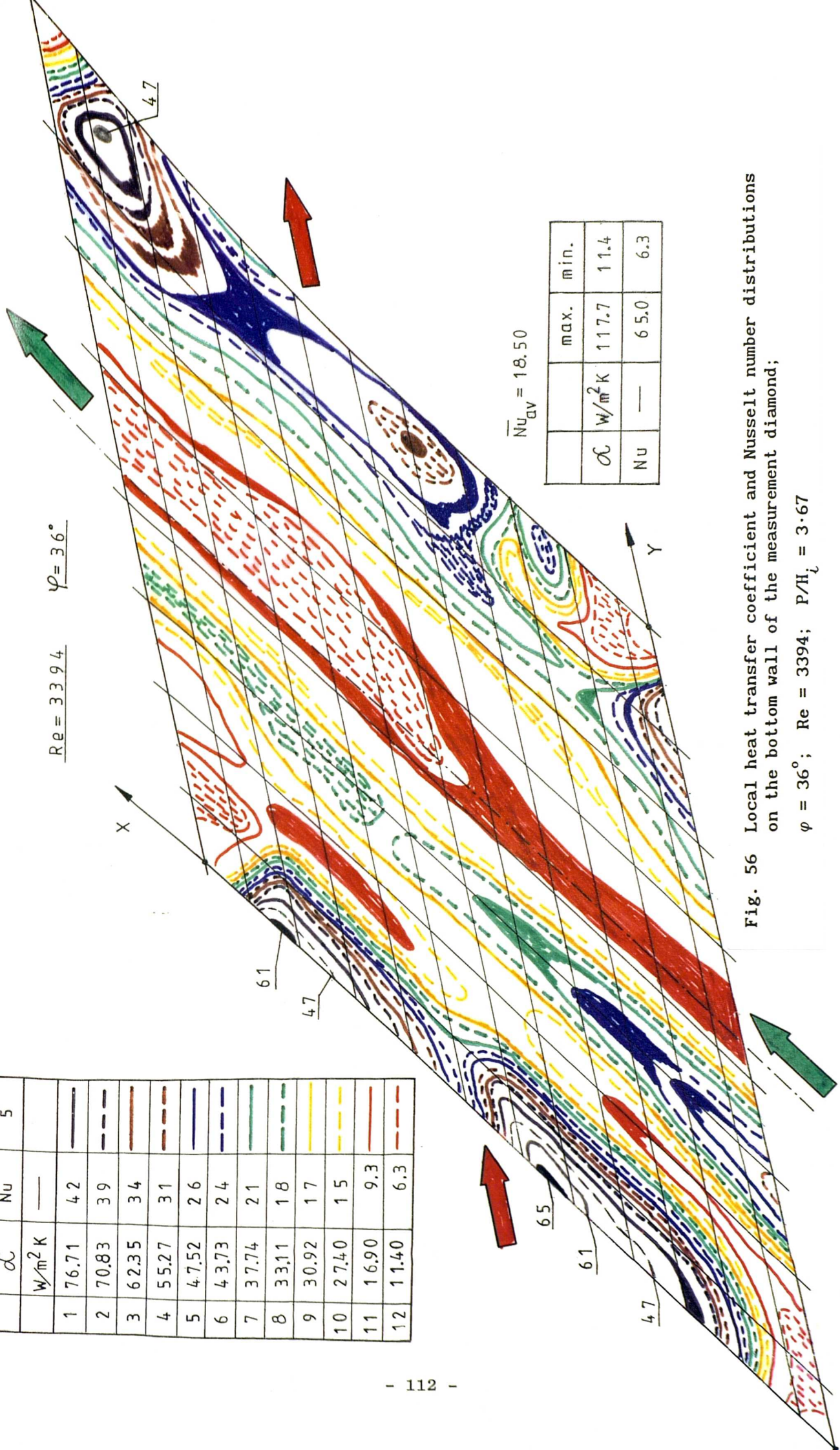


Fig. 56 Local heat transfer coefficient and Nusselt number distributions on the bottom wall of the measurement diamond;  
 $\varphi = 36^\circ; Re = 3394; P/H_i = 3 \cdot 67$

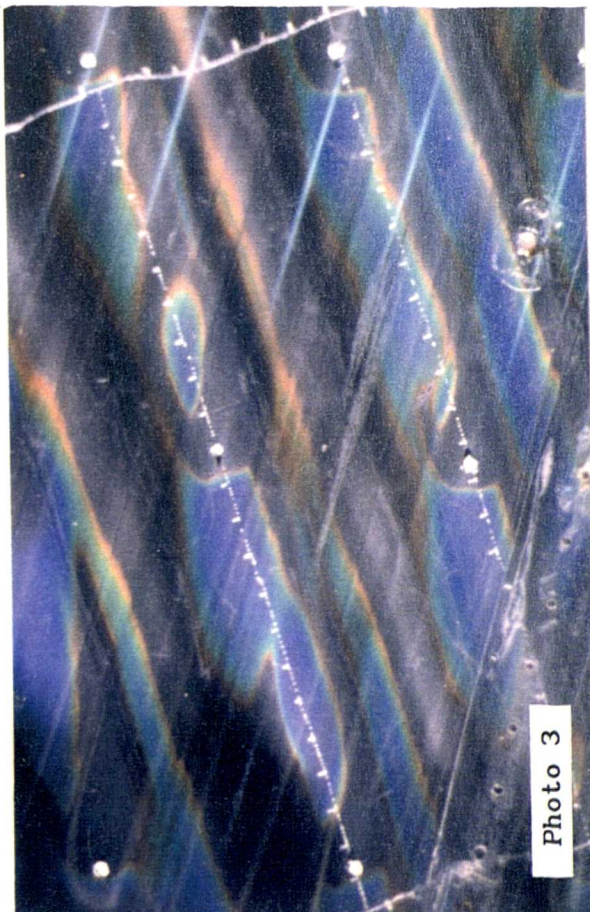
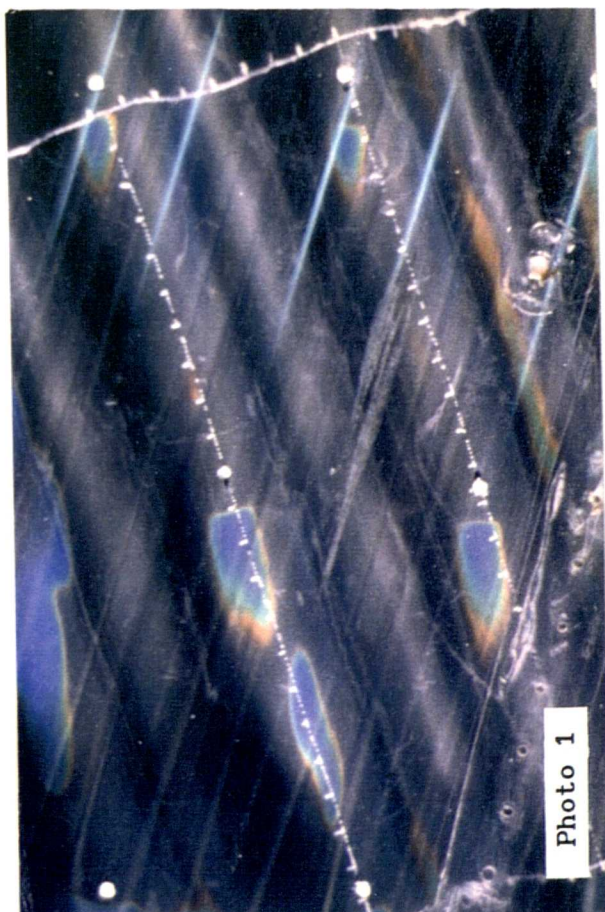
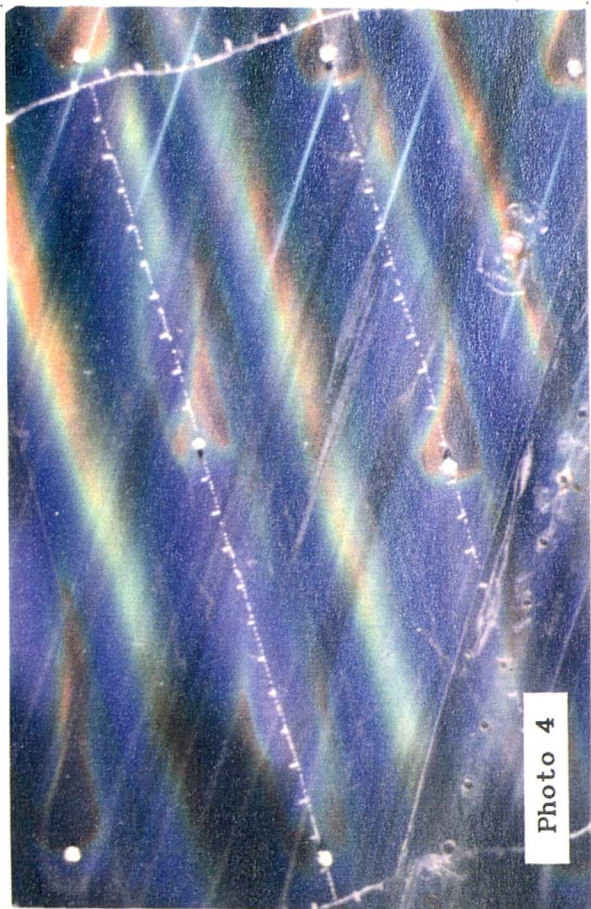
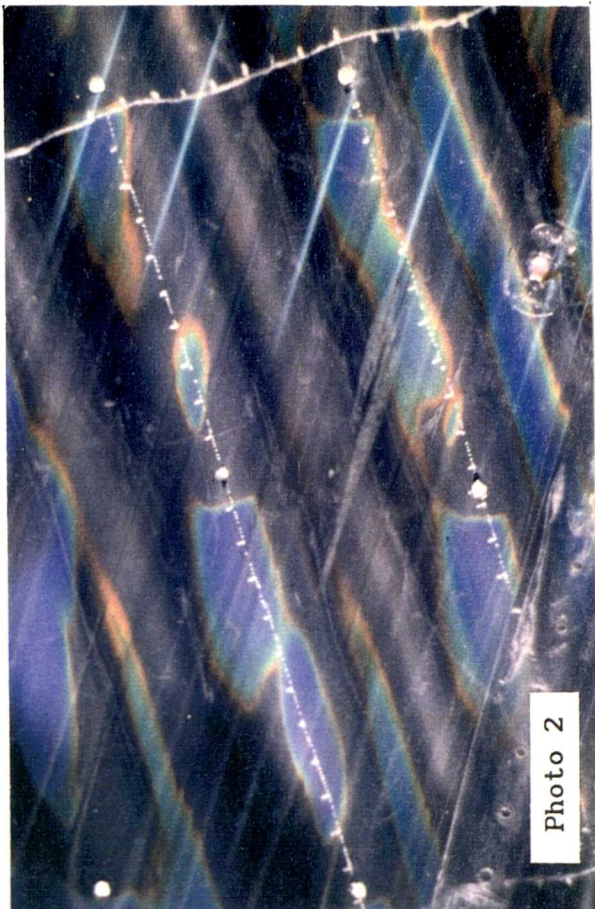


Fig. 56a Reproduction of colour transparency representing wall temperature contours at  $Re = 3394$  (Photo 1 - Exp.3; Photo 2 - Exp.7; Photo 3 - Exp.9; Photo 4 - Exp.12)

$\alpha$	Nu	11
$W/m^2 K$	—	—
1 8 4.4	4 6.6	—
2 7 5.9	4 2.0	—
3 6 9.5	3 8.3	—
4 5 4.1	2 9.9	—
5 4 2.9	2 3.7	—
6 3 5.6	1 9.7	—
7 3 1.3	1 7.3	—
8 2 6.6	1 4.7	—
9 2 2.4	1 2.4	—
10 1 7.5	9.7	—
11 1 1.7	6.5	—
12 9.2	5.1	—

$Re = 2850$        $\varphi = 36^\circ$

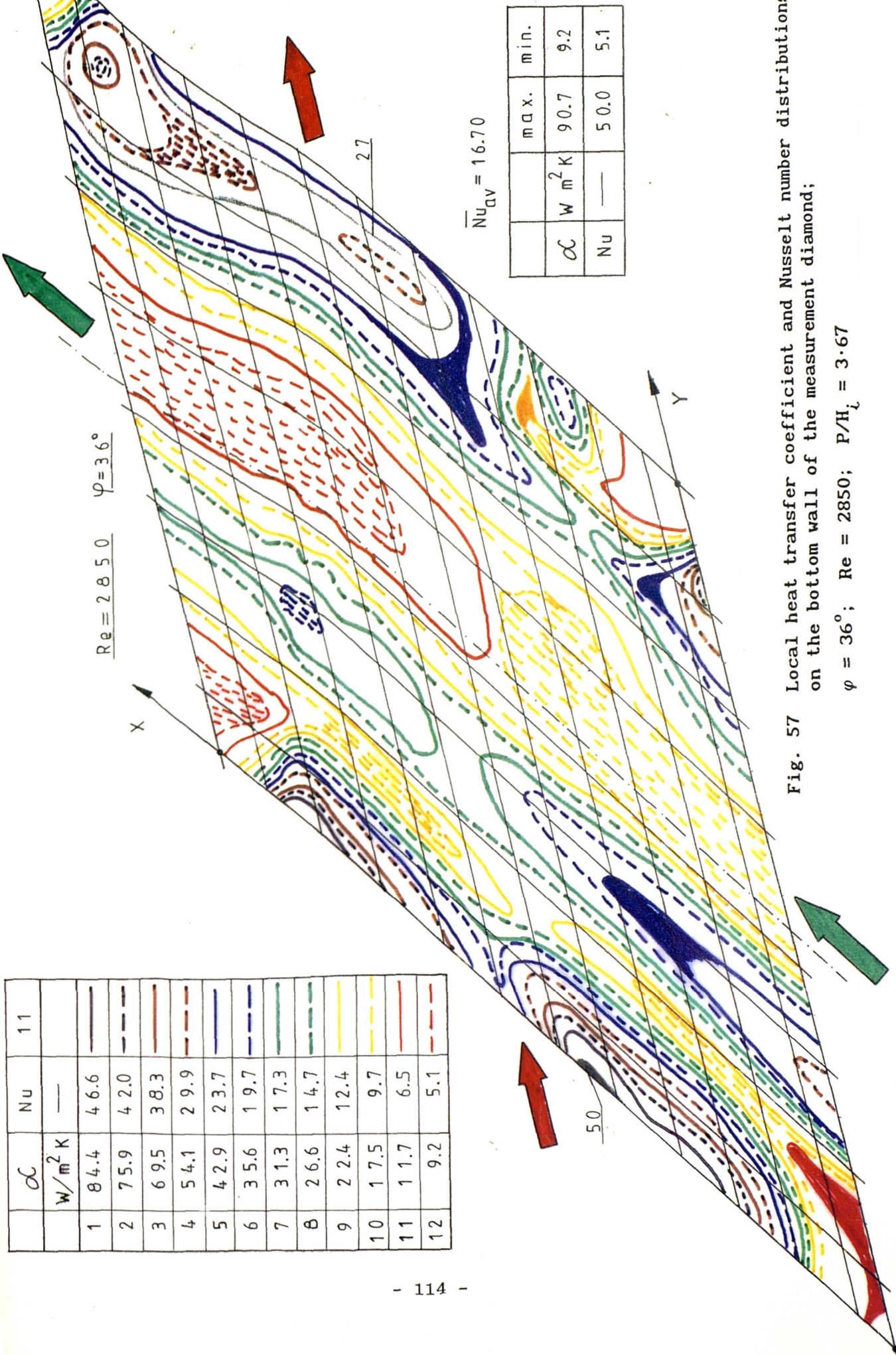
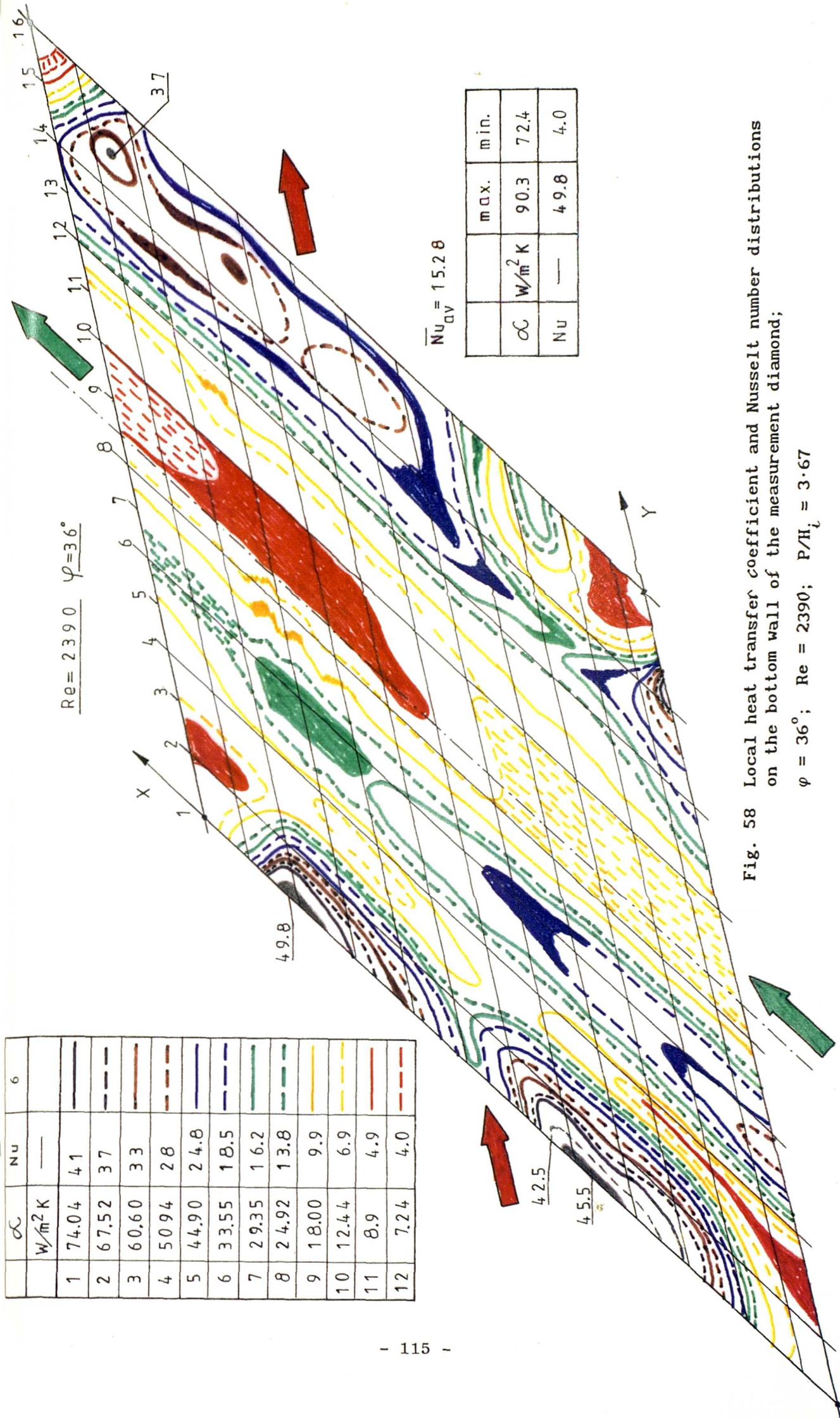


Fig. 57 Local heat transfer coefficient and Nusselt number distributions on the bottom wall of the measurement diamond;  
 $\varphi = 36^\circ$ ;  $Re = 2850$ ;  $P/H_L = 3 \cdot 67$



$\alpha$	Nu	7
$W/m^2 K$	—	
1	70.38	3.9
2	62.36	3.4
3	53.90	3.0
4	45.93	2.54
5	39.00	2.14
6	30.27	1.67
7	22.61	1.25
8	16.79	9.3
9	10.29	5.7
10	8.37	4.6
11	4.90	2.7

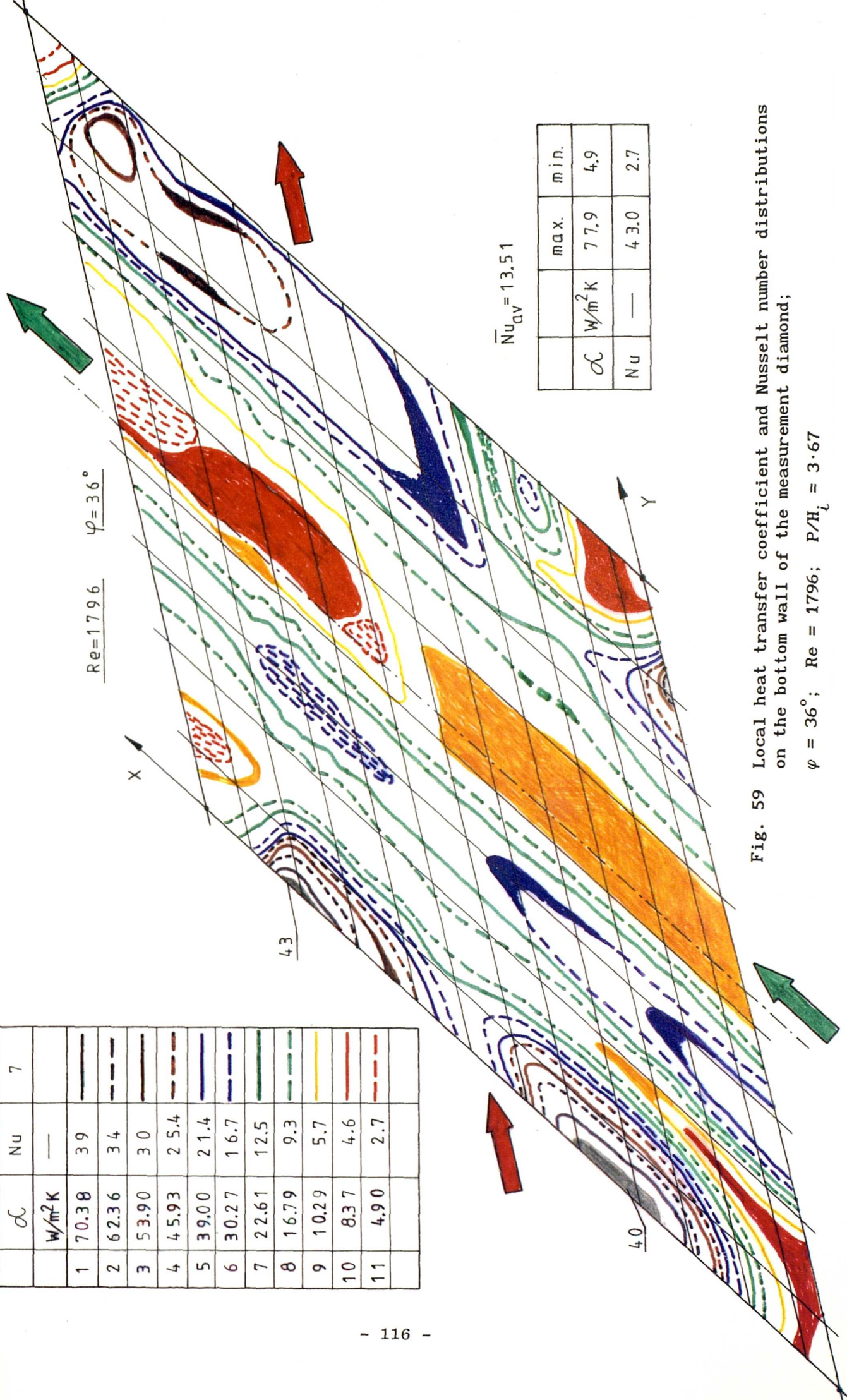


Fig. 59 Local heat transfer coefficient and Nusselt number distributions on the bottom wall of the measurement diamond;  
 $\varphi = 36^\circ$ ;  $Re = 1796$ ;  $P/H_t = 3 \cdot 67$

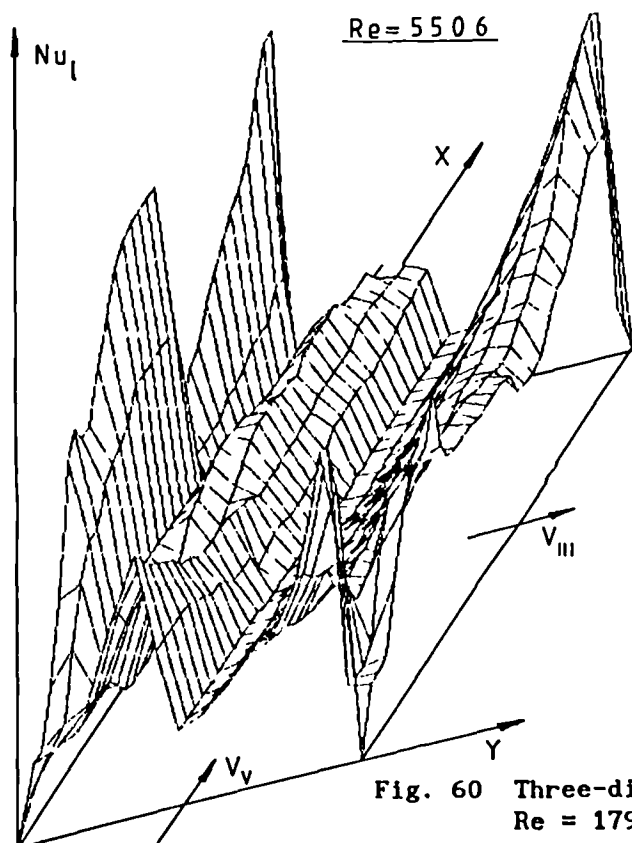
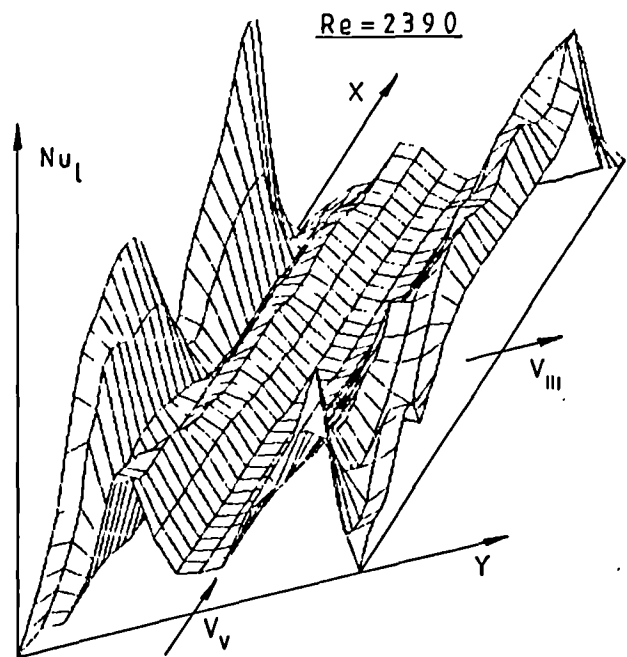
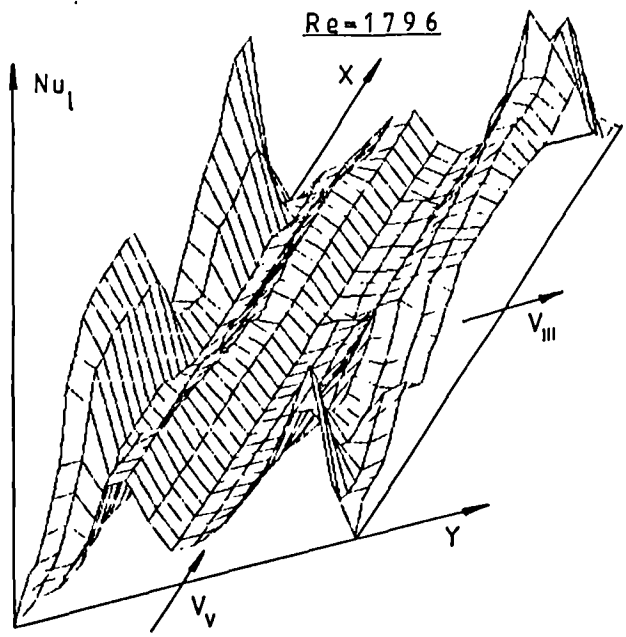


Fig. 60 Three-dimensional Nusselt number distributions for  
 $Re = 1796; 2390$  and  $5506$ ;  
 $\varphi = 36^\circ$ ;  $P/H_i = 3.67$

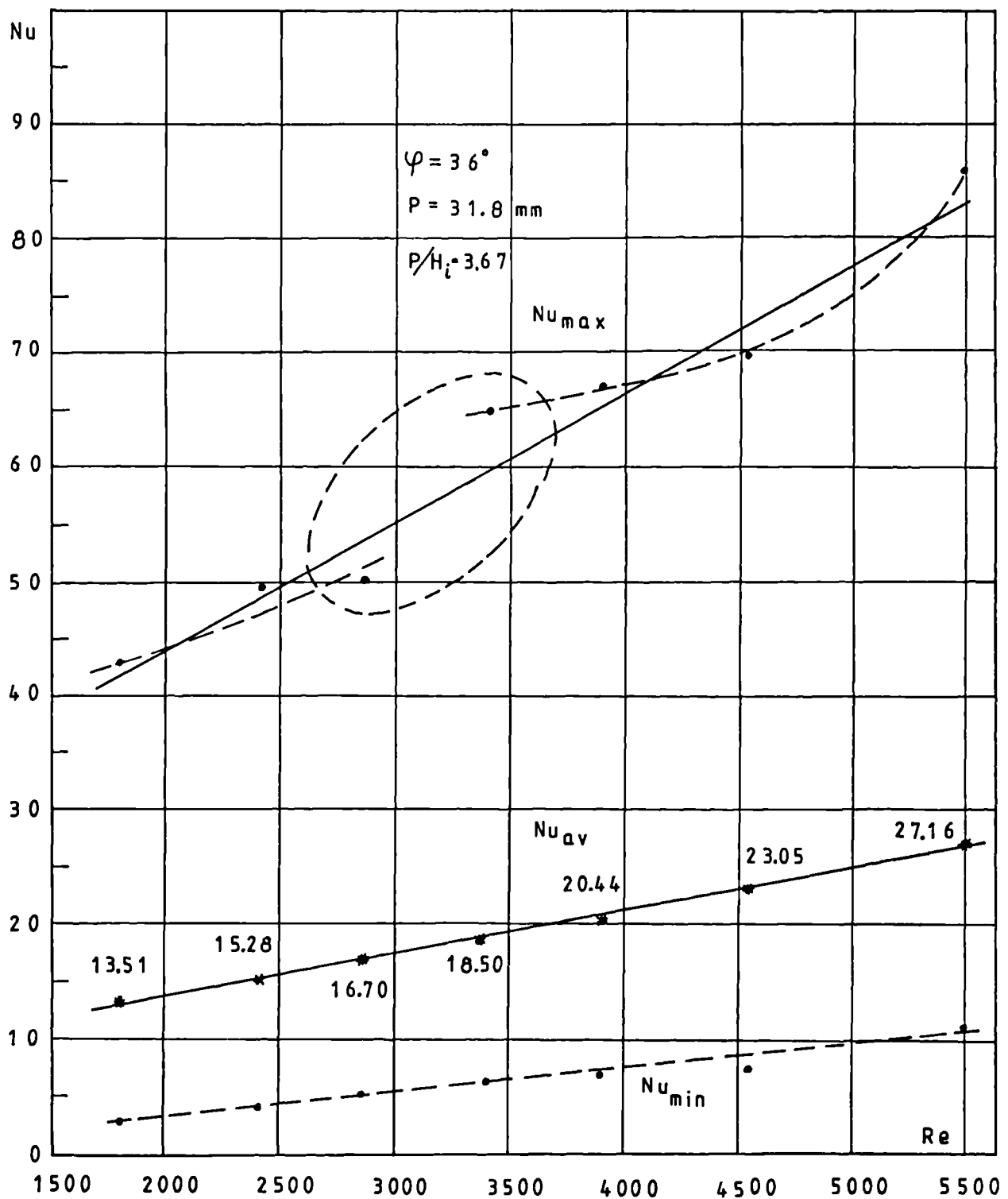


Fig. 61 Experimental; maximum, minimum and average Nusselt number distribution for uniform wall temperature  $t_w = 27.7^\circ\text{C}$ ;  
 $\varphi = 36^\circ$ ;  $P/H_i = 3.67$

$V_i$  m/s

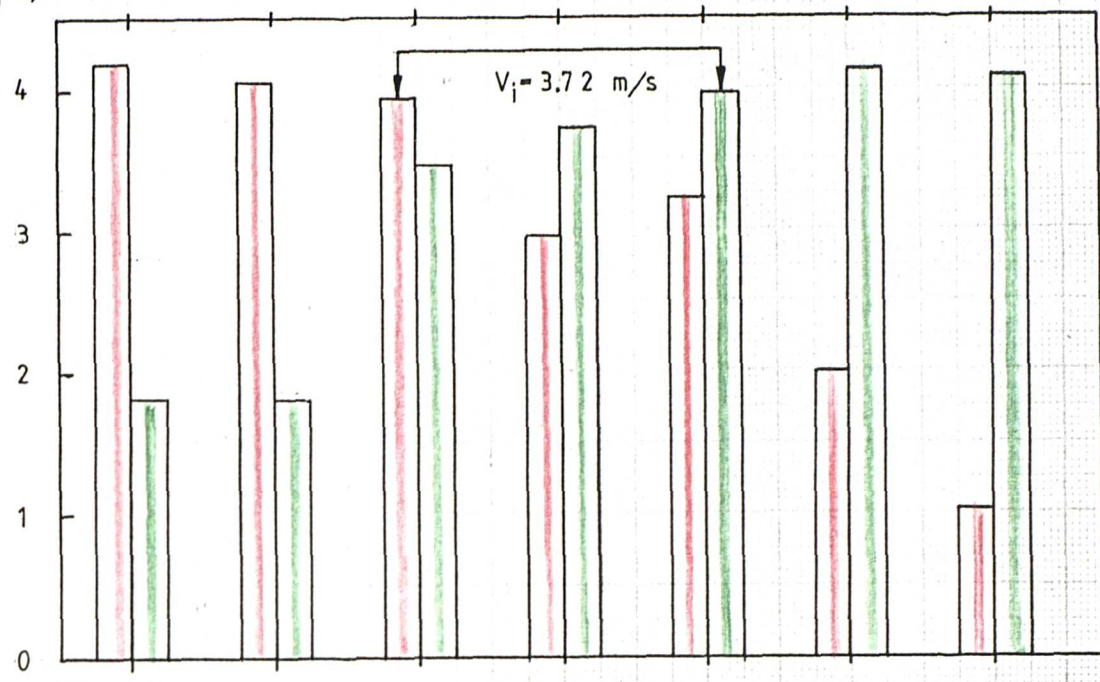


Fig. 17

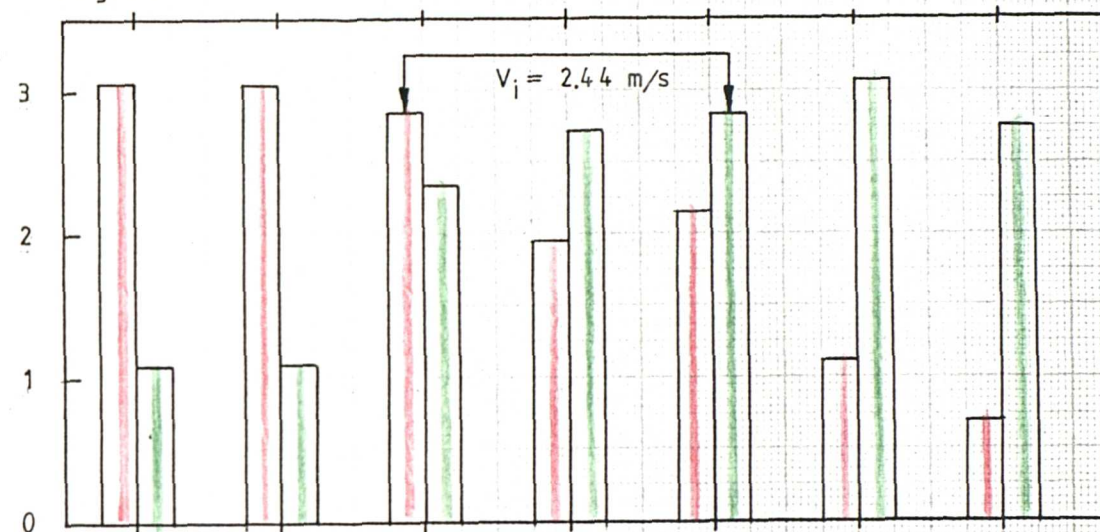


Fig. 18

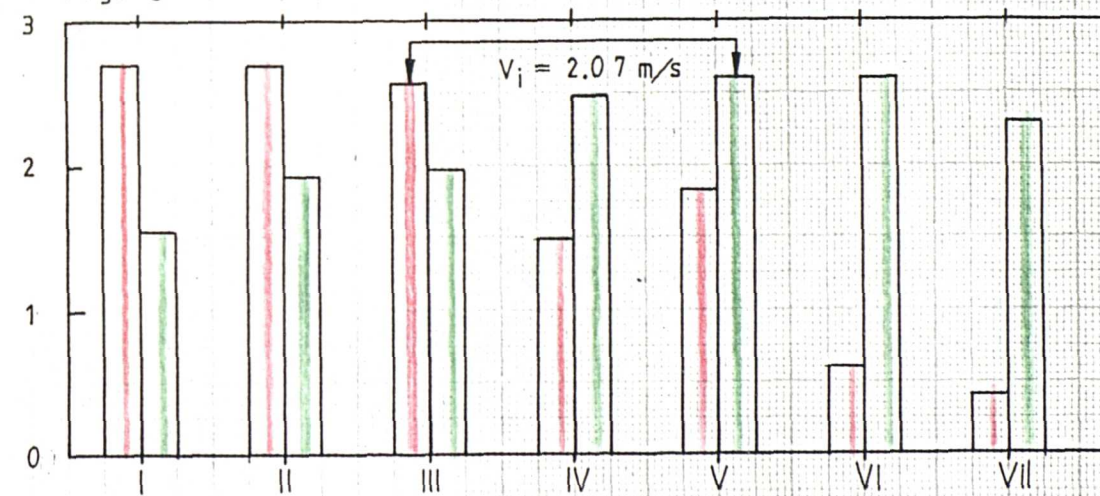


Fig. 62 Outlet velocity profiles (red colour - upper wall, green colour - lower wall).  $V_i = 3.72; 2.44$  and  $2.07 \text{ m/s}$

$$\varphi = 36^\circ; P/H_i = 3.67$$

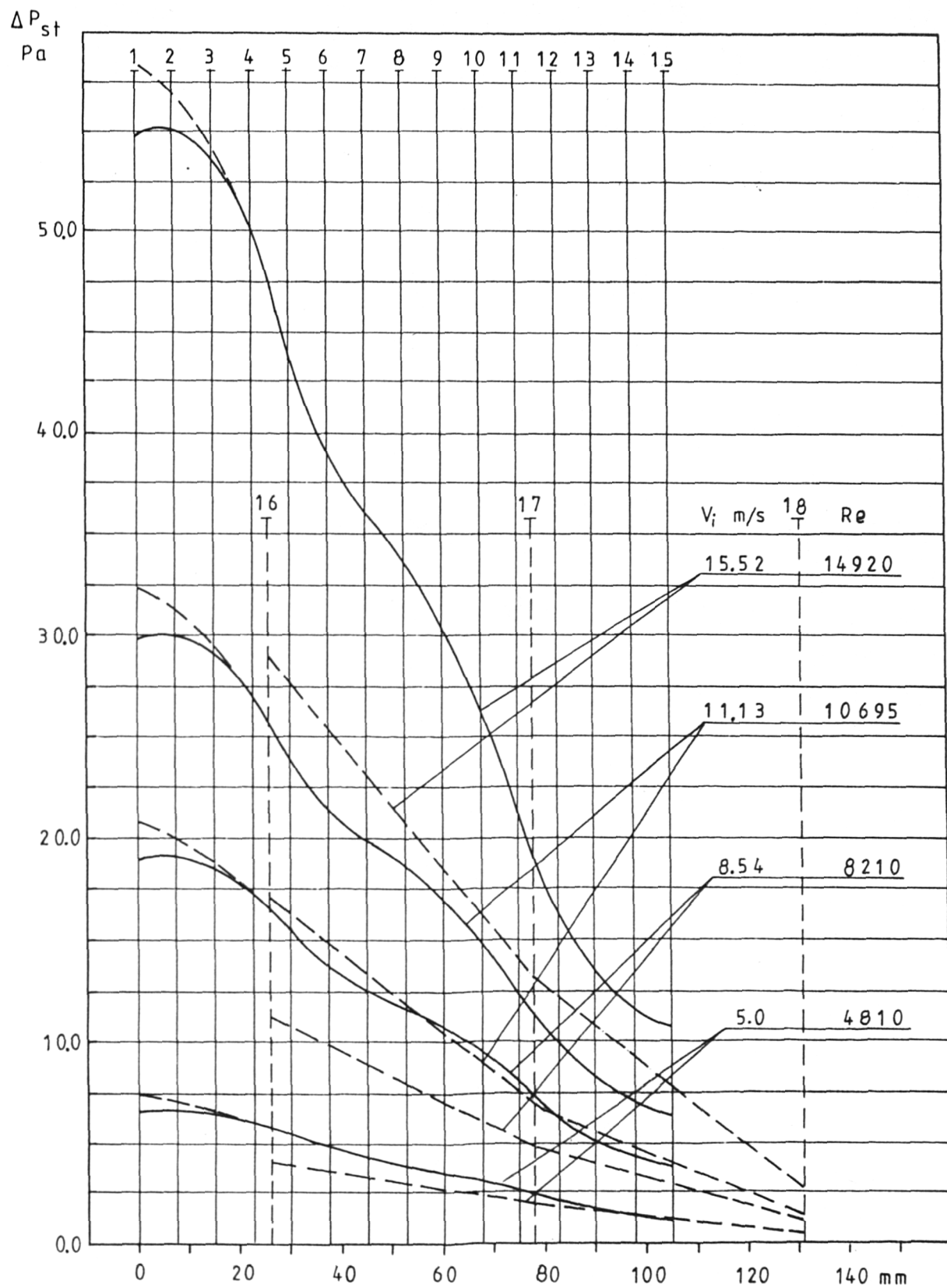


Fig. 63 Wall static pressure distribution along the flow ducts  
Nos. II and IV for  $V_i = 15.52, 11.13, 8.54$  and  $5.0 \text{ m/s}$   
 $\varphi = 36^\circ$ ;  $P/H_i = 3.67$

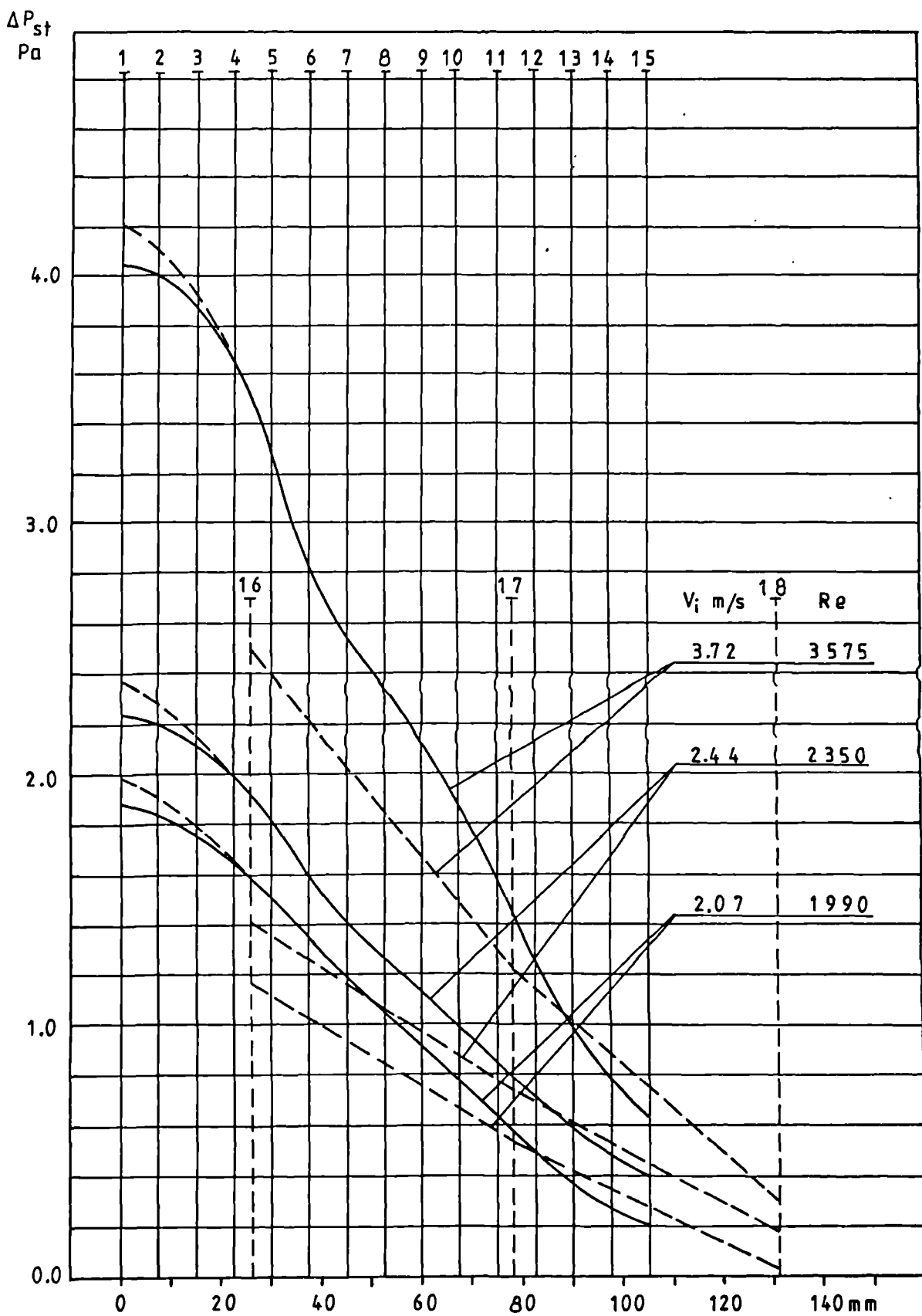


Fig. 64 Wall static pressure distribution along the flow ducts  
Nos. II and IV for  $V_i = 3.72, 2.44$ , and  $2.07 \text{ m/s}$   
 $\varphi = 36^\circ$ ;  $P/H_i = 3.67$

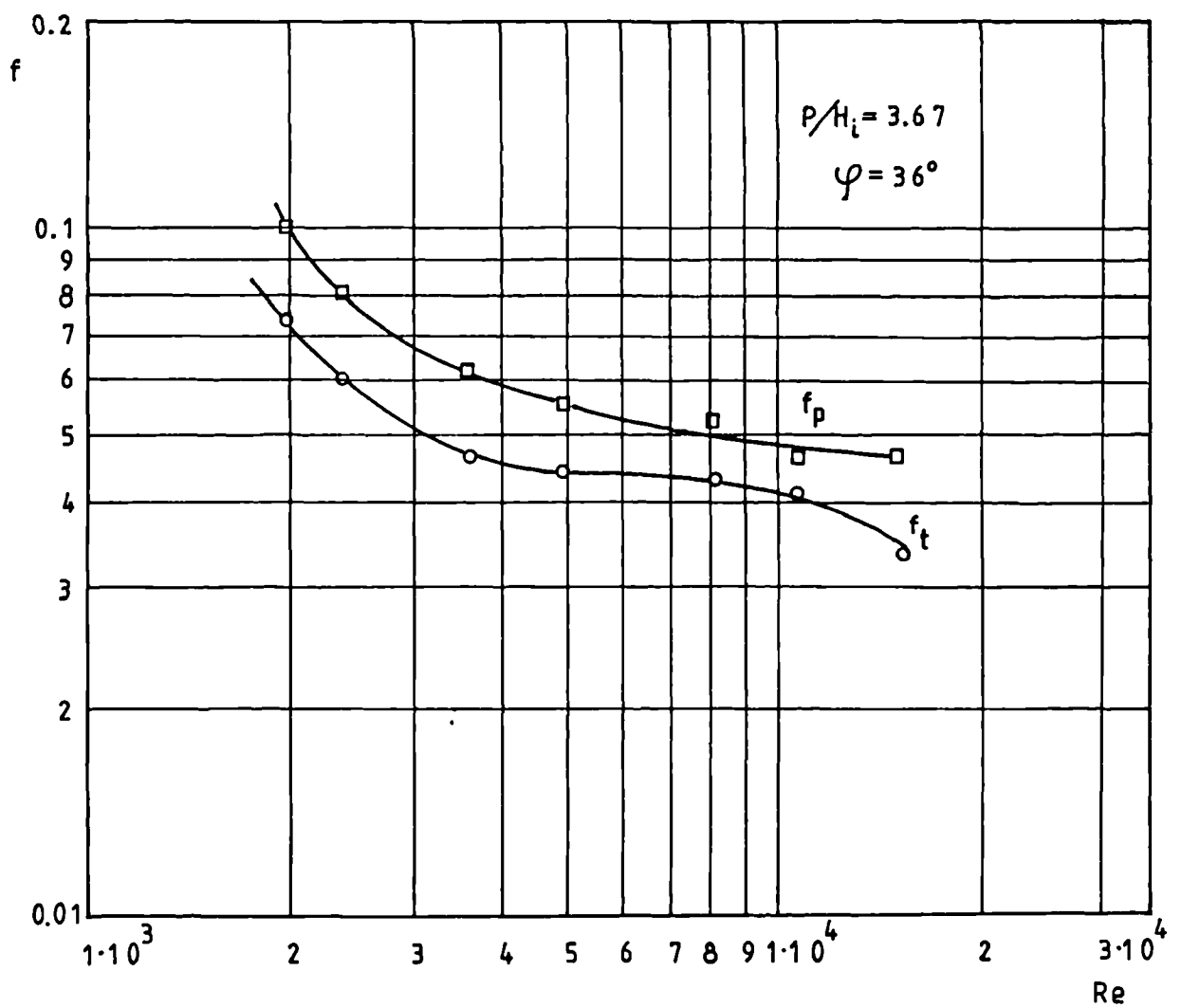


Fig. 65 Friction coefficient as functions of the Reynolds number in "cell 2" of corrugated upstream passages ( $f_p$  - the peak friction coefficient;  $f_t$  - the trough friction coefficient)

## **7.2 Heat Transfer and Friction Factor**

### **- Results for the Corrugated Working Section**

As described earlier, TLC's and True-Colour Image Processing were used here to determine the distribution of surface temperature and the heat flux - this allows evaluation of the local heat transfer coefficient and Nusselt number. The temperature recorded from the liquid-crystal sheet is only for the yellow-green colour resulting in a narrow isochromatic region after image processing and elimination of noise from the background. A single colour, giving narrow regions, enhanced the accuracy of the method [54][78].

The procedure in the selection of isothermal lines involves the following steps:

1. The image required for analysis is selected by operating the HSI segmentation.
2. A Hue range is specified corresponding to the temperature range, for example, 55 to 70 (Figs.66 and 67) gives the isothermal line of  $28.3 \pm 0.075^{\circ}\text{C}$ . This may be completed interactively to allow the operator to view the representation of the image during operation.
3. The segmentation area is selected for the field in which analysis is required.
4. To interpret the resulting Hue segmentation a Histogram is chosen to give data such as area of the Hue pixel values selected and total area of segmentation. From this the average Nusselt number can be estimated.

Average Nusselt numbers are calculated as weighted mean values of the local Nusselt numbers obtained from the relationship:

$$N_{av} = \frac{\sum_{i=1}^n N_{u\ell,i} r_i}{\sum_{i=1}^n r_i} \quad (11)$$

where:  $Nu_{\ell,i}$  - local Nusselt number obtained from Eqn. 9

$r_i$  - Hue ratio coefficient (ratio of number of pixels for Hue range being considered to total number of pixels)

$\ell$  - number of images

Local heat transfer and pressure drop measurements have been carried out for Reynolds numbers based on the centreline velocity of the air in the unitary cell,  $v_t$ . The corrugation angle tested ranged between  $30^\circ$  and  $75^\circ$  and the Reynolds number between 1200 and 5600.

Experimental results are summarised in Figs.66-70, together with experimental values of the friction factor for open and closed corrugated working section, and five values of inclination angle  $\varphi$ .

The experimental results of the friction factor are presented using Equation 12.

$$f = \frac{2 \Delta P D_h}{\rho (v_t \cos \varphi / 2)^2 \ell} \quad (12)$$

where:  $v_t$  - centreline velocity in the unitary cell

$\varphi$  - inclination angle of corrugated structures

Figures 66 and 67 show photographs of colour TV images of the liquid-crystal layer on the corrugated plate. The violet region corresponds to the higher heat transfer coefficient and brown-red to the lower, respectively. Also, colour-temperature visualisation demonstrates the distributions of temperatures and heat transfer coefficients on a test plate. High inclination angles lead to an inhomogeneous heat and fluid flow distribution. At the facing side flow impinges at the corrugation crests leading to an intensive heat transfer there. At the lee side, however, and within the valleys of

the structure (colour brown-red) there is reduced heat transfer. Looking at the corresponding sample in Figs.66-67 flow phenomena become evident. The major part of the flow follows the valleys, is reflected at the corresponding side walls and flows back in the valleys of the opposite plate. As this part of the flow is mainly characterised by boundary-layer effects, it leads to a lower heat transfer. A minor part of the flow follows the longitudinal direction, leading to the high heat transfer at the facing side of the corrugation crests. With decreasing inclination angle the flow following the valleys decreases leading to an improving mixing behaviour. The local heat transfer distributions become more homogeneous at smaller inclination angles. A relative high heat transfer occurs here between the rows of the contact points (violet colour).

Average values of the Nusselt number distributions are shown in Fig.68 as a function of the corrugation inclination angle  $\varphi$ , the Reynolds number and whether the sides of the corrugated working section are open or closed (dots represent experiments with open and crosses with closed sides of the working section, respectively). Figures 69 and 70 show the corresponding friction factor (pressure drop) of the same structures. The curve is fundamentally similar to the heat transfer, in that higher inclination angles result in increased friction factors. The effects of the inclination angle on the friction factor, however, are much more significant than for heat transfer.

Recently, three-dimensional, steady-state numerical simulations of fluid flow and heat transfer in the corrugated passages have been obtained by a finite-volume technique, allowing for general body-fitted grids and implemented in the computer code Harwell-FLOW3D, Release 2; Ciofalo et al [17][124] and Burns et al [121]. For example, Figs.71-72 compare the distribution of the average Nusselt number and friction factor obtained experimentally and numerically using FLOW3D.

The latter predictions used either (i) laminar flow assumptions or (ii) standard, or (iii) low-Reynolds number  $k-\epsilon$  turbulence model. The overall distributions of  $\text{Nu}$  and  $f$  are predicted quite well by low-Reynolds number  $k-\epsilon$  model.

The effect of the corrugation inclination angle on local and average heat transfer and thermohydraulic performance of plate heat exchangers was measured by Gaiser and Kottke [52] and Focke et al [51]. Average values of Nusselt number are shown in Fig.73 as a function of the corrugation inclination angle at a constant Reynolds number. Figure 74 also gives a comparison with data of Okada et al [128], Focke et al [51], Zogg [133] and Gaiser et al [52]. The general agreement is very good, although there is a slightly higher friction factor at larger values of  $\varphi$  - caused by the  $\cos\varphi/2$  in the denominator of Equation 12.

The corrugation inclination angle  $\varphi$ , is a major parameter influencing the performance of plate heat exchangers: this is because the angle  $\varphi$  determines the basic flow structure which in turn is the primary factor influencing both pressure drop and heat transfer.

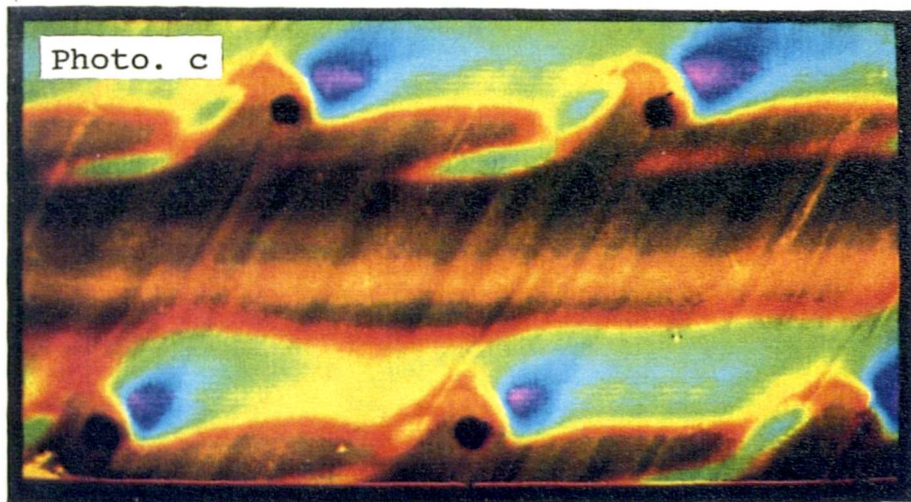
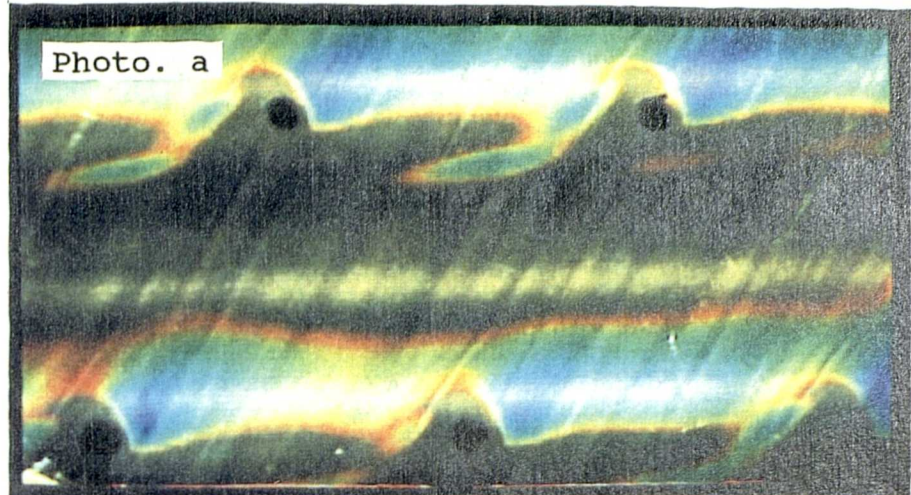


Fig. 66 a) Photographs of the colour distributions of the liquid crystal layer on a corrugated geometry

b) Images of the computer display after segmentation processing (Hue:55.70, Saturation:0.255, Intensity:0.255).  $t_g = 28.3^\circ\text{C}$

c) Images on the computer display after chromaticity processing (adjust saturation)

$$Re = 5100; \quad \varphi = 60^\circ; \quad P/H_i = 4.0; \quad t_a = 45.33^\circ\text{C}; \quad t_b = 22.2^\circ\text{C}$$

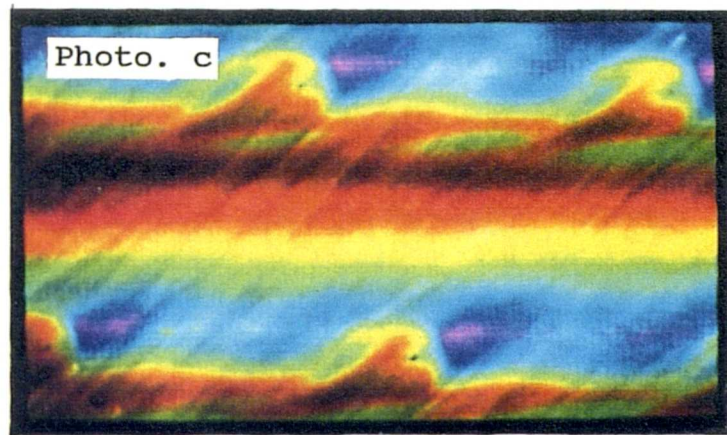
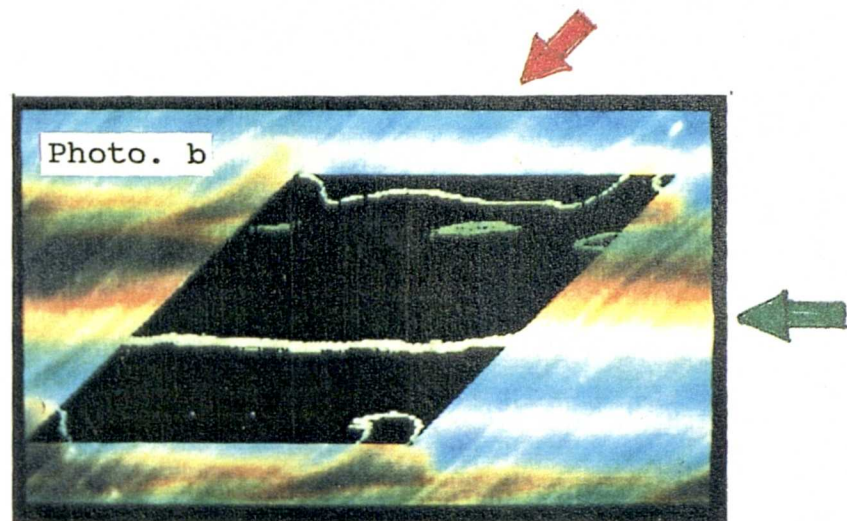
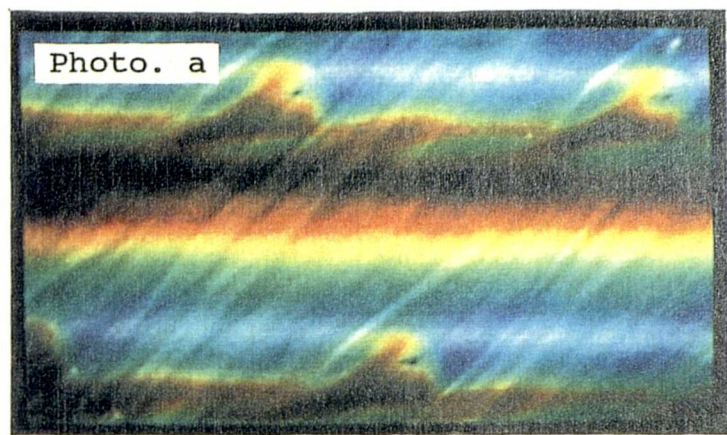


Fig. 67 a) Photographs of the colour distributions of the liquid crystal layer on a corrugated geometry  
 b) Images of the computer display after segmentation processing (Hue:55.70, Saturation:0.255, Intensity:0.255).  $t_g = 28.3^\circ\text{C}$   
 c) Images on the computer display after chromaticity processing (adjust saturation)

$$Re = 2670; \quad \varphi = 48^\circ; \quad P/H_i = 4.0; \quad t_a = 45.33^\circ\text{C}; \quad t_b = 26.29^\circ\text{C}$$

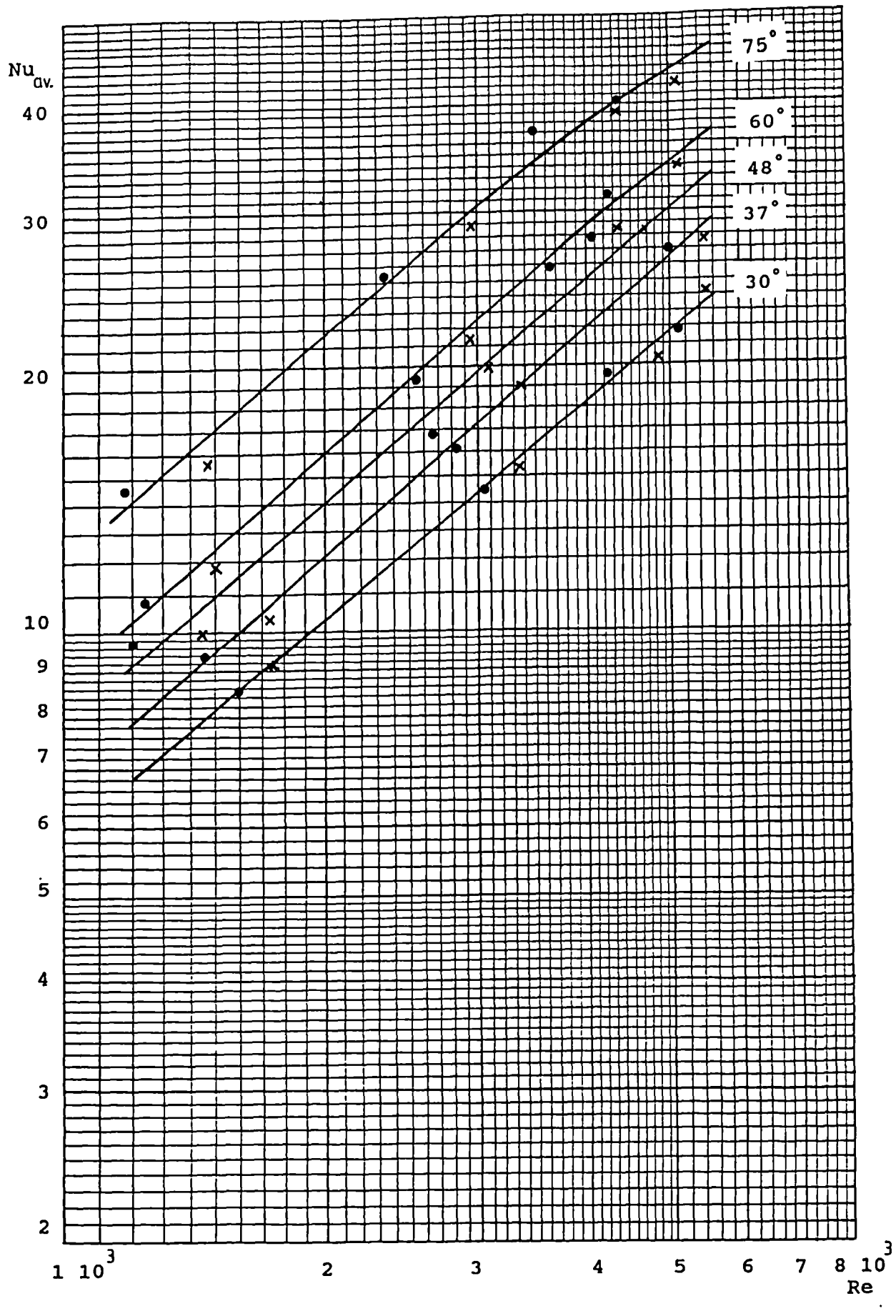


Fig. 68 Experimental; average Nusselt number distributions developed from True-colour image processing system for uniform wall temperature  $t_w = 28.3^\circ\text{C}$ .  $P/H_i = 4.0$  and  $\varphi = 30^\circ; 36^\circ; 48^\circ; 60^\circ$  and  $75^\circ$

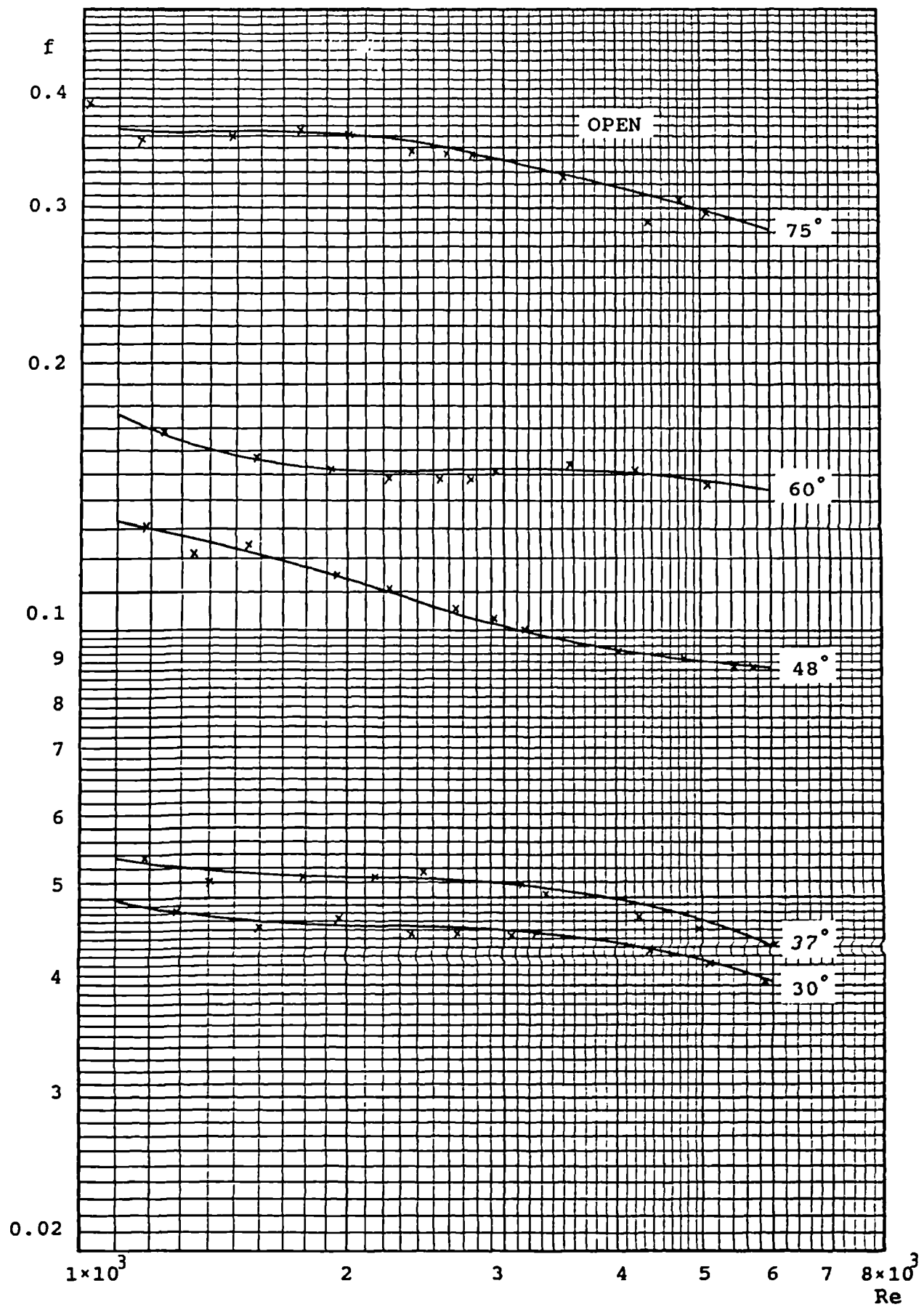


Fig. 69 Experimental friction coefficient of open downstream corrugated passages measured by the wall pressure tappings

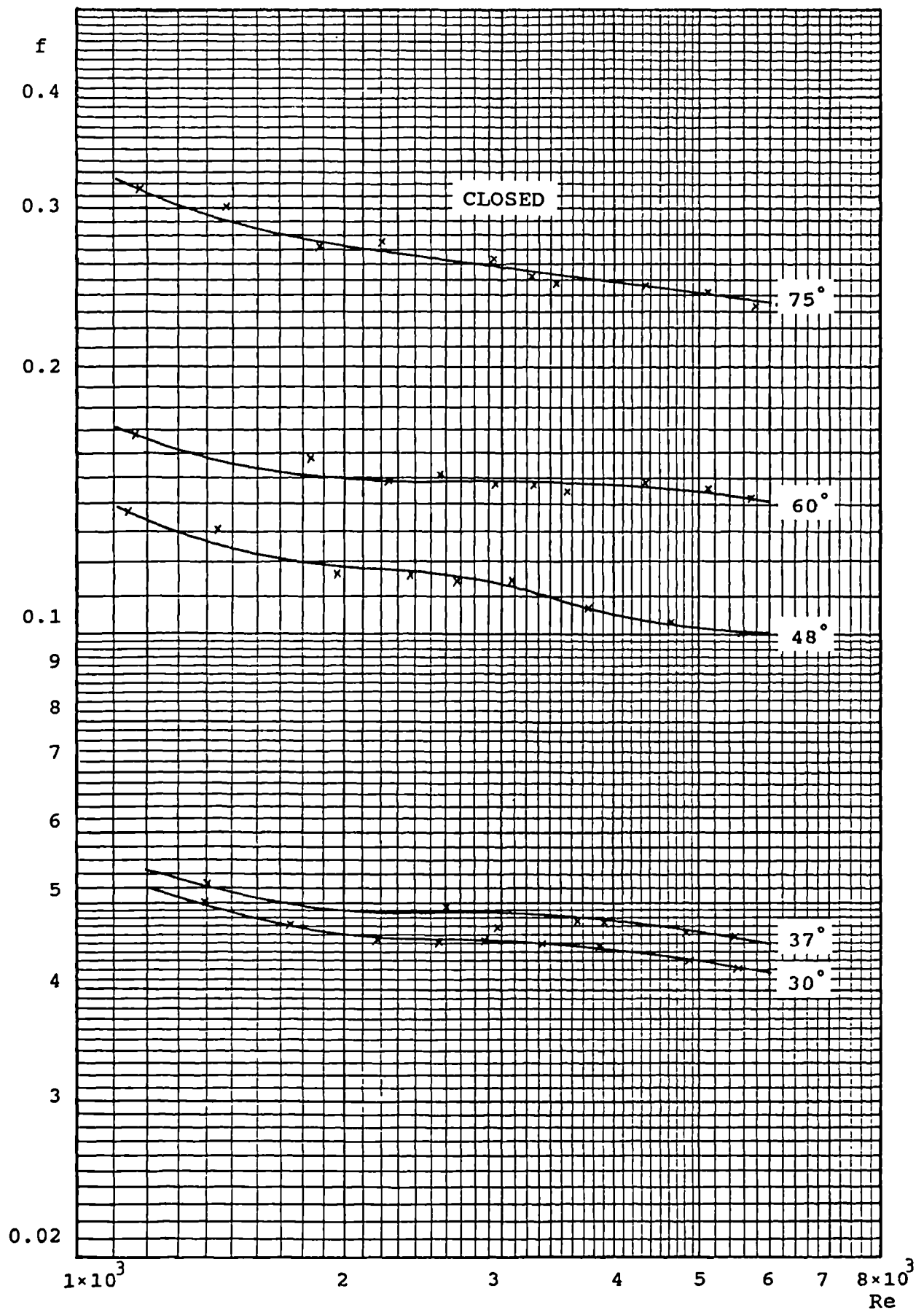


Fig. 70 Experimental friction coefficient of closed downstream corrugated passages measured by the wall pressure tappings

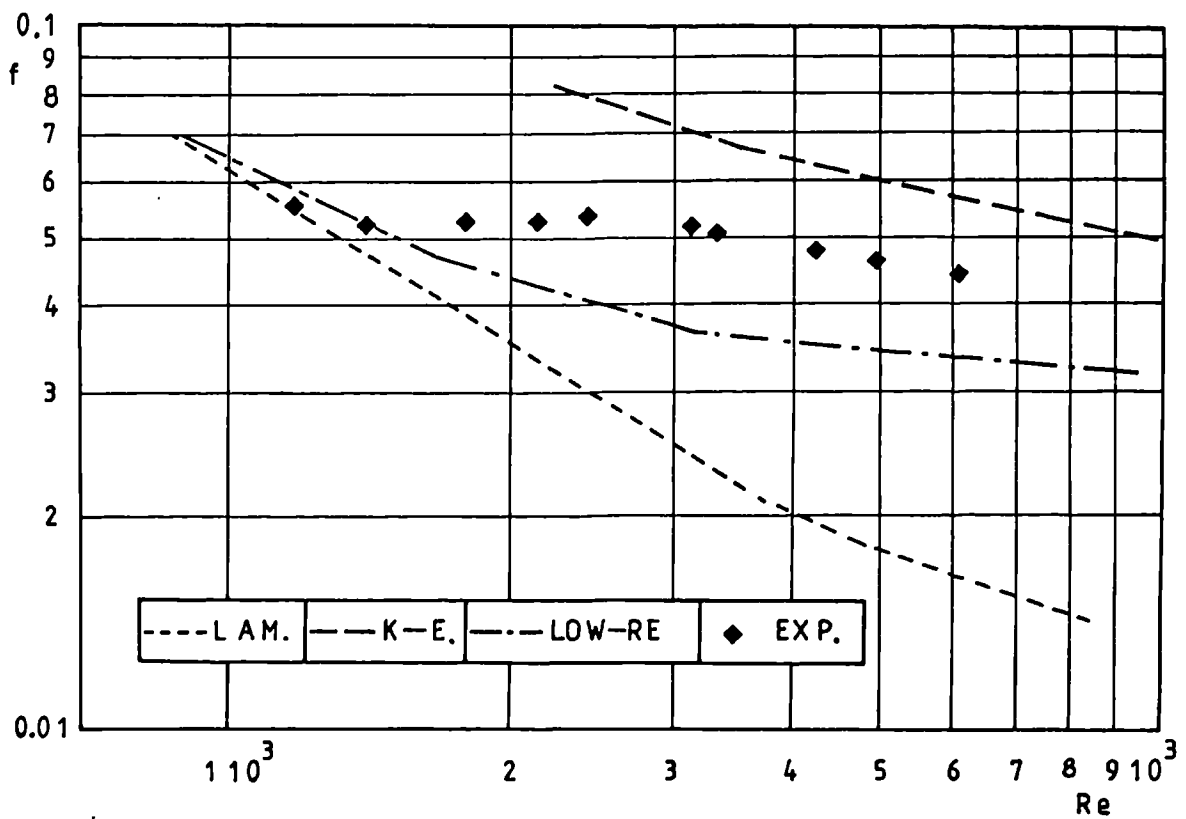


Fig. 72 Predicted vs. experimental friction factor for  
 $\varphi = 36^\circ$  and  $P/H_i = 4.0$

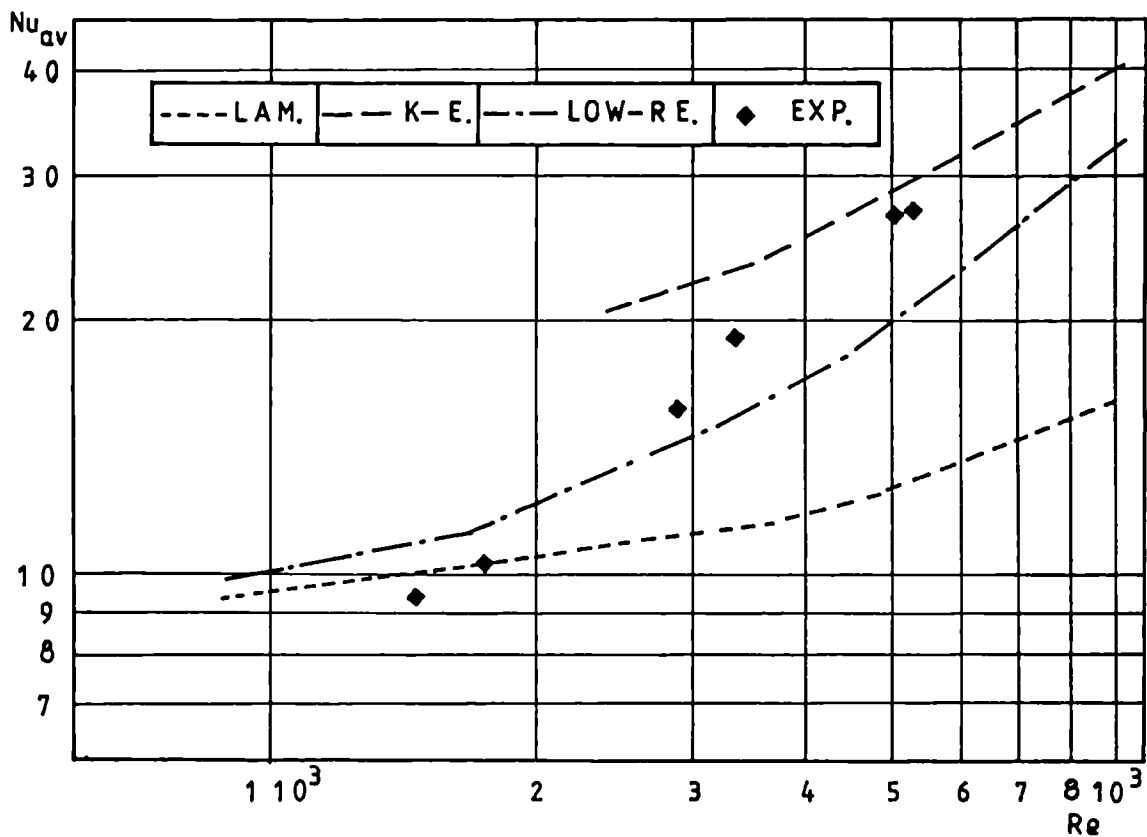


Fig. 71 Predicted vs. experimental average Nusselt number for  
 $\varphi = 36^\circ$  and  $P/H_i = 4.0$

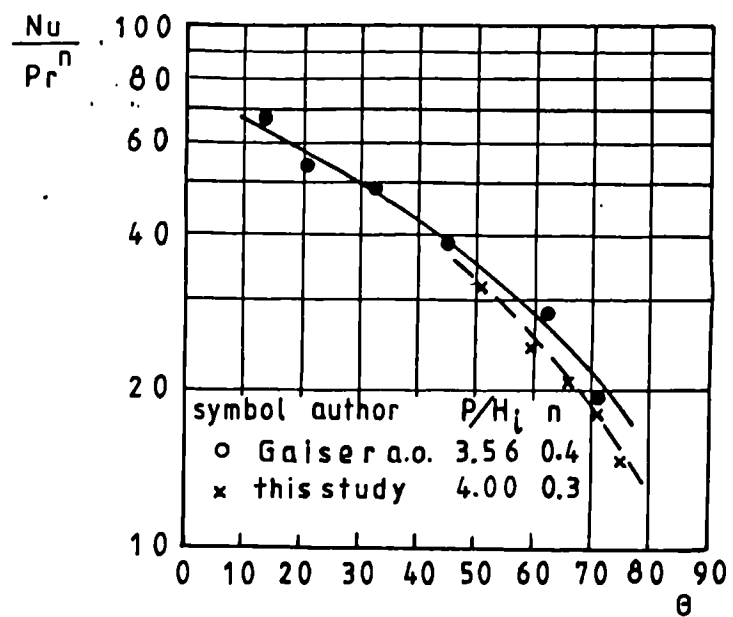


Fig. 73 Average Nusselt number of corrugated passages for  $Re_m = 2000$ ; where  $\theta = 90 - \varphi/2$

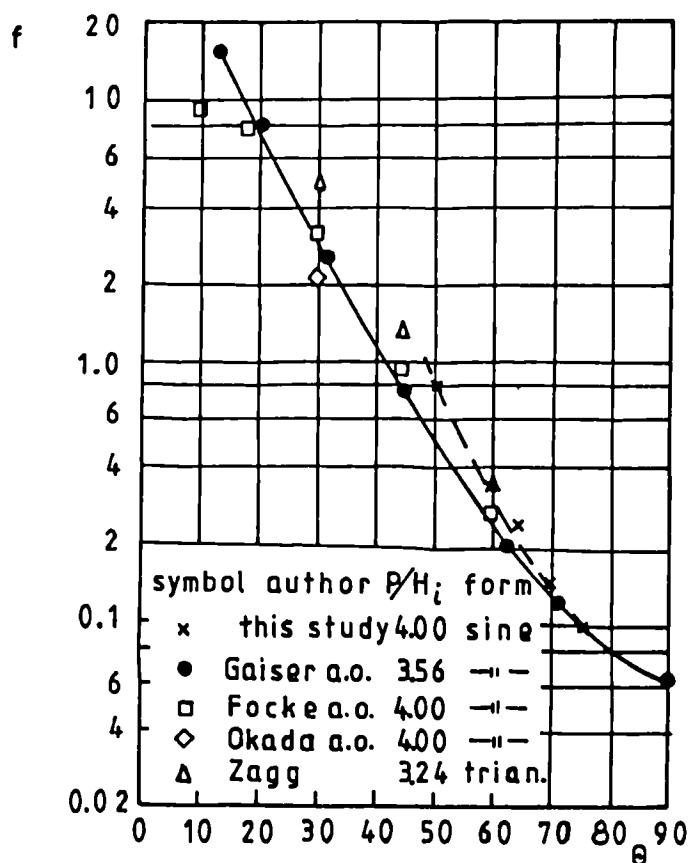


Fig. 74 Friction factors of corrugated passages for  $Re_m = 2000$ ; where  $\theta = 90 - \varphi/2$

### 7.3 Heat Transfer in a Parallel Plate Channel with Obstructions of Different Geometrical Shapes

The series of tests reported here examined heat transfer in a parallel plate channel disturbed by a number of complex geometrical configurations described in Chapter 6. Photographs were taken with a 35 mm SLR camera and RGB video camera using the procedure described in the previous chapter. However, co-ordinates of the contours of constant temperature obtained at constant heat flux are used to determine contours of constant convective heat transfer coefficient - different heat transfer coefficient (Nusselt number) contours are determined by varying the temperature of the air (temperature of water = const = 16°C).

Figures 75, 76, 79, 80 and 83 show results presented in terms of contours of constant Nusselt number for five different geometries and a Reynolds number of 10000. The channel Reynolds number, Re, based on channel hydraulic diameter and centreline properties. Also, Figures 77, 78, 81, 82 and 84 show photographs of the colour distributions of the liquid crystal on a plate disturbed by the various obstructions chosen.

The experimental results are presented in terms of local Nusselt number:

$$Nu_l = h_l D_h / k_a \quad (13)$$

The local heat transfer coefficient was evaluated by the following equation:

$$h_l = q(t_a - t_R) \quad (14)$$

where:  $q = 228 \text{ W/m}^2$  - constant heat flux

$t_R$  - liquid crystal isotherm temperature  
 $(t_R = 27.7 \pm 0.1^\circ\text{C})$

$t_a$  - temperature of air

$k_a$  - conductivity of air

$D_h$  - hydraulic diameter;  $D_h = 0.009 \text{ m}$

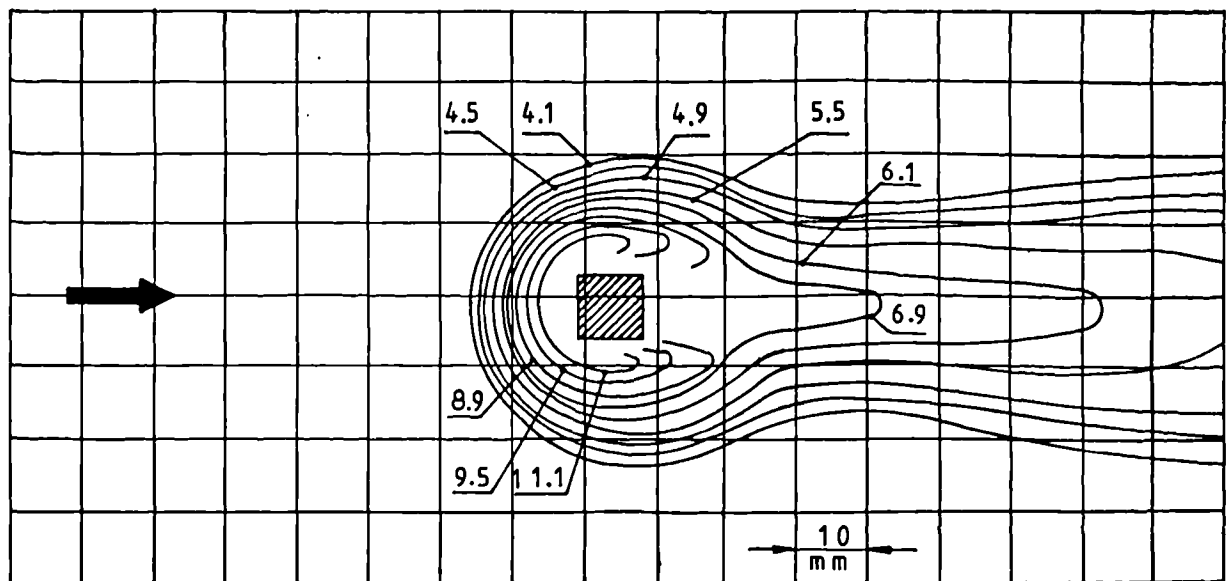
for square-section columns, square-section roughness elements and cylinders of  $D_h = 0.015$  m.

Figure 85 shows the Nusselt number distributions along the upstream and downstream side of the centreline of the cylinder, parallel to the flow direction at  $Re = 10000$ . In these figures the solid line shows results obtained using human colour sensation and dashed lines by the True-colour image processing system. The local Nusselt number y-axis profiles have the same general characteristic shape. However, the exact location of the local Nusselt number determined by the method employing human colour sensation is difficult near the cylinder due to compression of the isolines.

An example of the variation of Nusselt number perpendicular to the flow from the centre of the square double column is shown in Fig.87, a similar variation for one square column being shown in Figure 84. In these the dashed line represents the Nusselt number predicted by full numerical simulation using the Harwell code FLOW3D [100][121]. Also, Fig.89 shows the computational prediction of the isothermal map around the root of a single square obtained for the conditions of the experimental study (see the temperature contour at the same flow condition in Figure 77). The flow around the square column is characterised by separations at the trailing edges of the square and the wake flow which follows the separations. These separations at the trailing edge are forced. On the leeward side of the square, two counter-rotating vortices are formed [100]. From the observation of the turbulent flow field, one could probably envisage the enhancement of the so-called turbulent convective heat transfer due to the presence of the high level turbulent mixing around the square. This mechanism is a direct result of the flow separation and the subsequent turbulent wake developed downstream of the square. This type of heat transfer enhancement is passive, though, and there is a price to pay for it in the resulting pressure loss. This effect remains to be assessed after the establishment of the model.

The heat transfer enhancement is quite clearly shown in Fig.89 by consideration of the isotherm distribution of the flat plate. Figure 89, though, shows also the higher levels of heat transfer enhancement across the wake boundaries due to the higher levels of turbulent mixing. This phenomenon is indicated by the lobe-shaped Nusselt number distribution, the same type of distribution being also noted in experiment (Figure 77).

The correlation between the colour and temperature of the liquid crystal offers a chance to verify the numerical model quantitatively. This verification is quite difficult to carry out in the downstream direction. Both the numerical and the experimental studies indicate small changes in the temperature field over a large area downstream of the square (or cylinder), especially in the wake region. In fact, the 27.7°C temperature contour is diffused in the wake region, leaving an area with the same colour. This diffusion of colour downstream of the square presents a major difficulty in assessing the temperature distribution through manual processing, although somewhat less with digital image processing. The above discussion again demonstrates the advantage of a combined computational and experimental approach to considerations both of basic understanding, and engineering heat transfer and pressure drop performance.



**Fig. 75** Contours of constant Nusselt number distribution around single square column at  
 $Re = 10000$ ;  $q = 228 \text{ W/m}^2$ ;  $D_h = 0.009 \text{ m}$

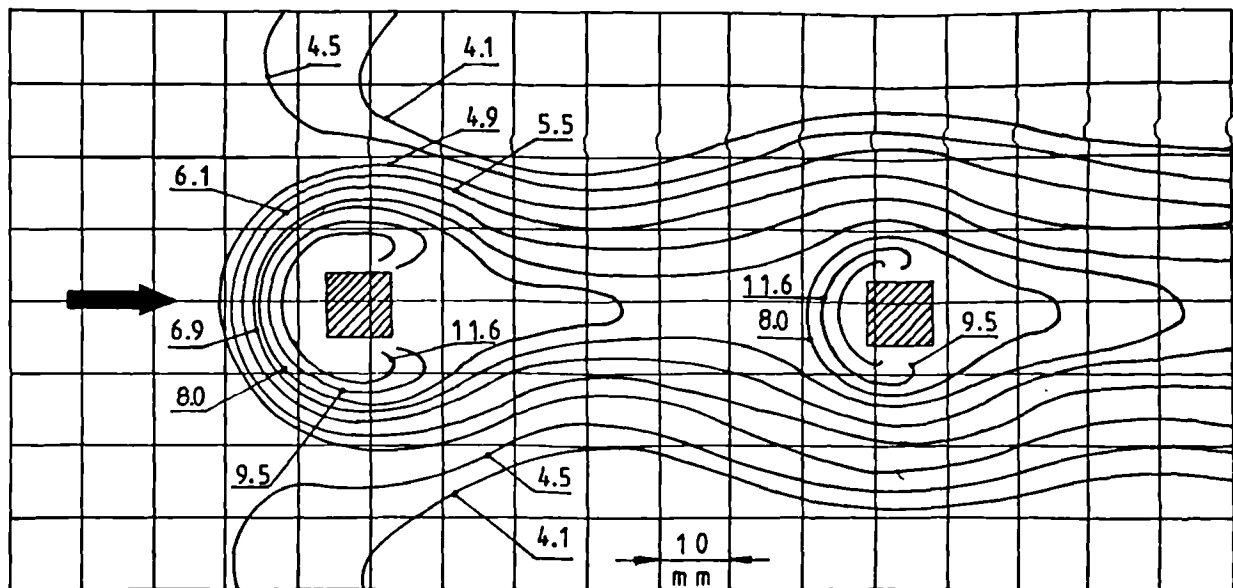


**Fig. 76** Contours of constant Nusselt number distribution around double square column at  
 $Re = 10000$ ;  $q = 228 \text{ W/m}^2$ ;  $D_h = 0.009 \text{ m}$

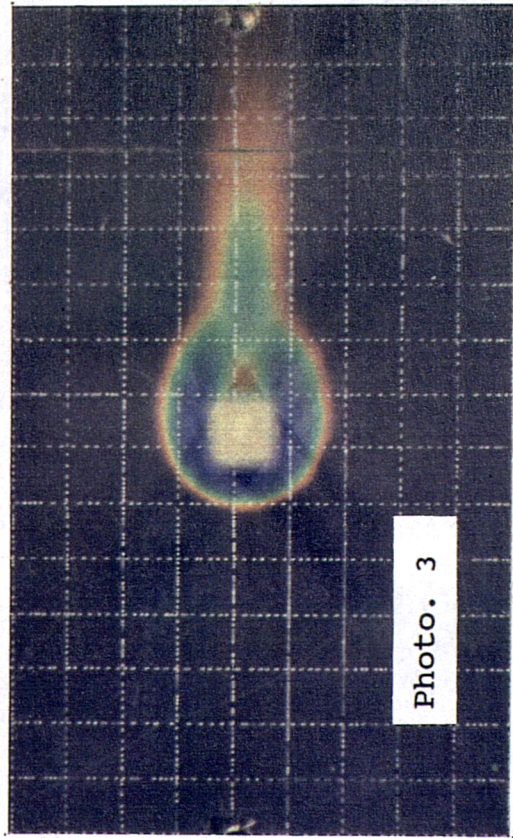
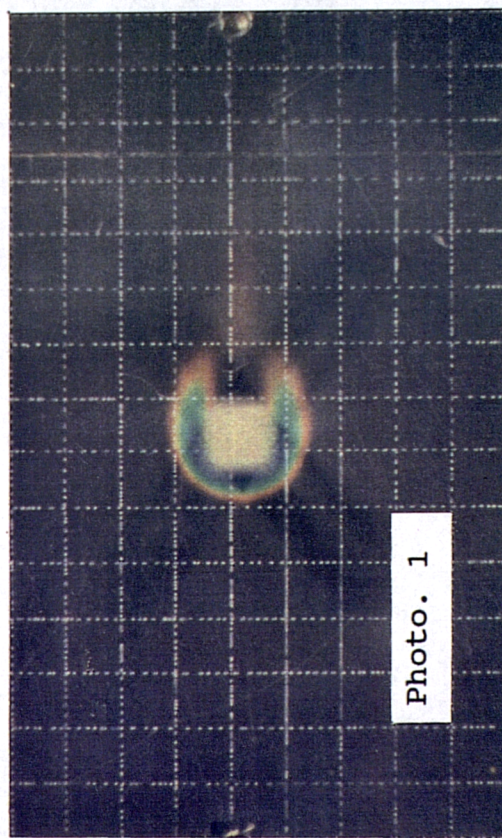
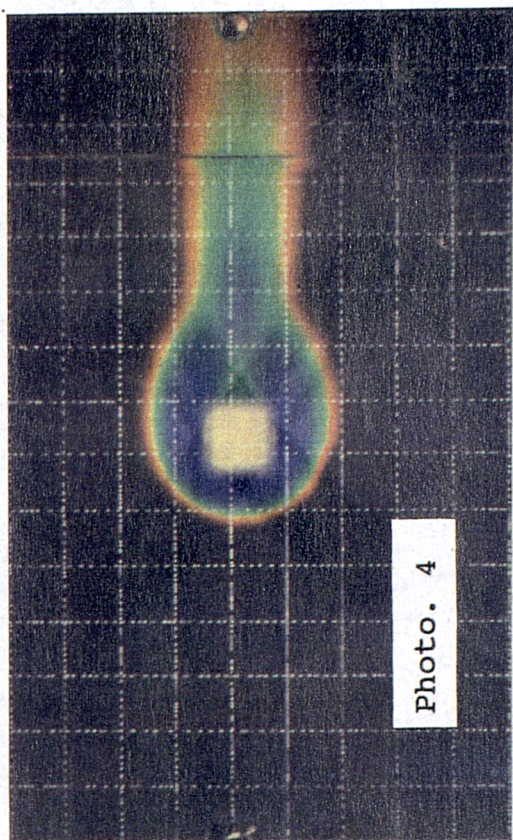
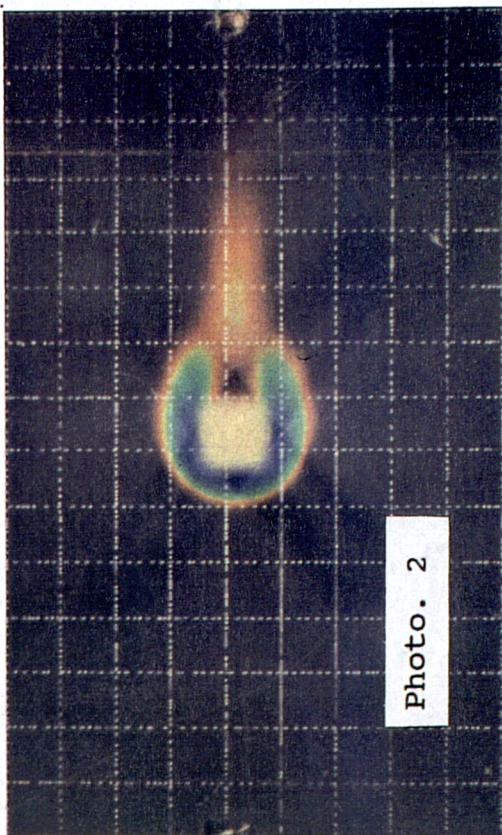


Fig. 77 Reproduction of colour transparency representing wall temperature contours at  $Re = 10000$ ;  $q = 228 \text{ W/m}^2$

Photo 1 -  $t_a = 37.1^\circ\text{C}$ , Photo 2 -  $t_a = 38.5^\circ\text{C}$ ,

Photo 3 -  $t_a = 40.0^\circ\text{C}$ , Photo 4 -  $t_a = 41.4^\circ\text{C}$ .

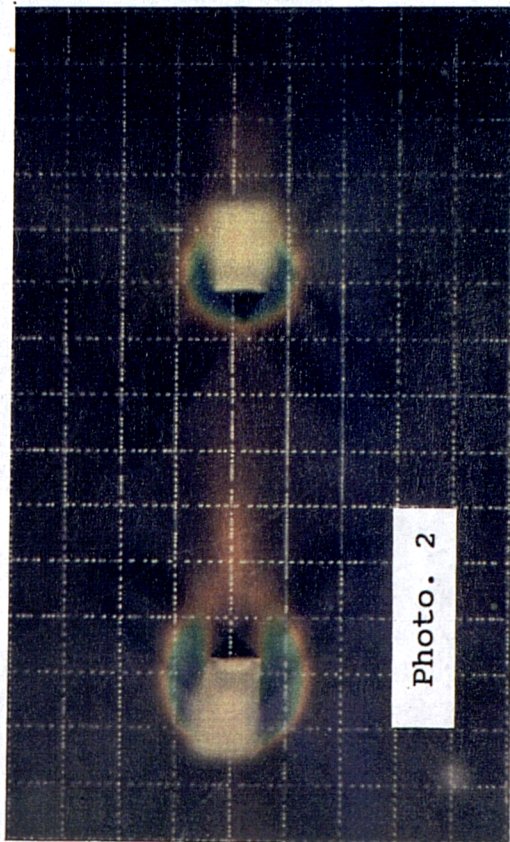


Photo. 2

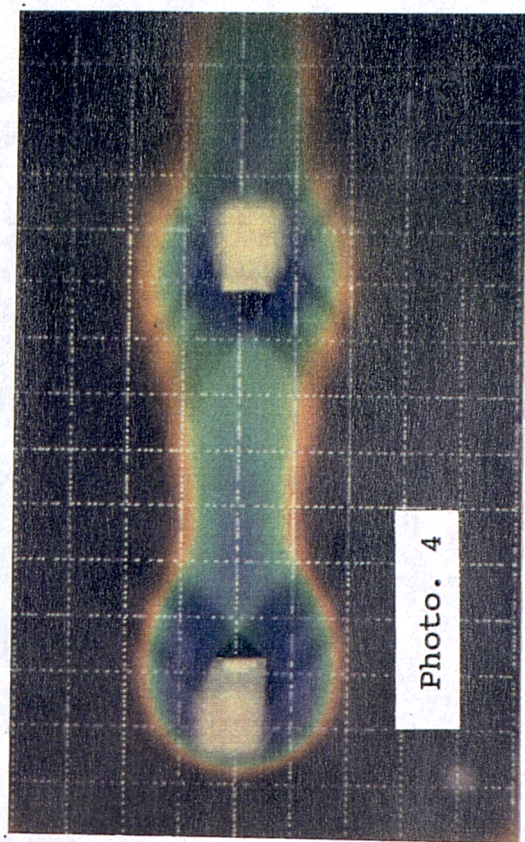


Photo. 4

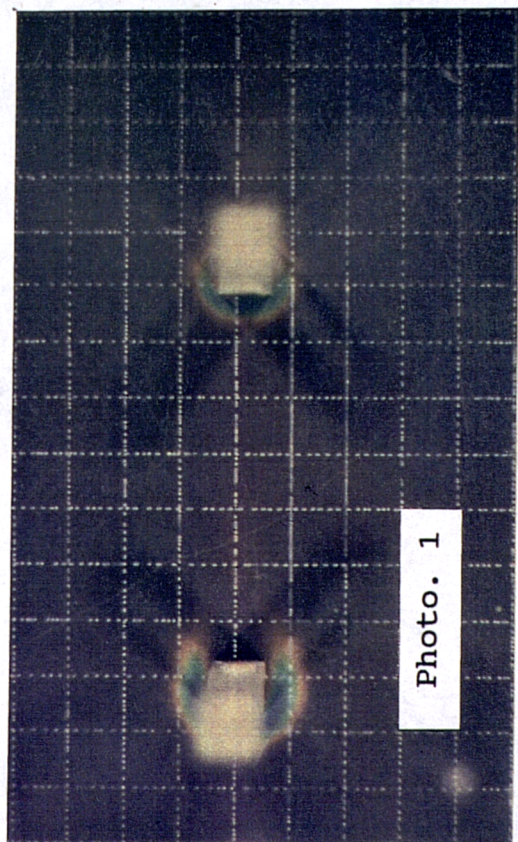


Photo. 1

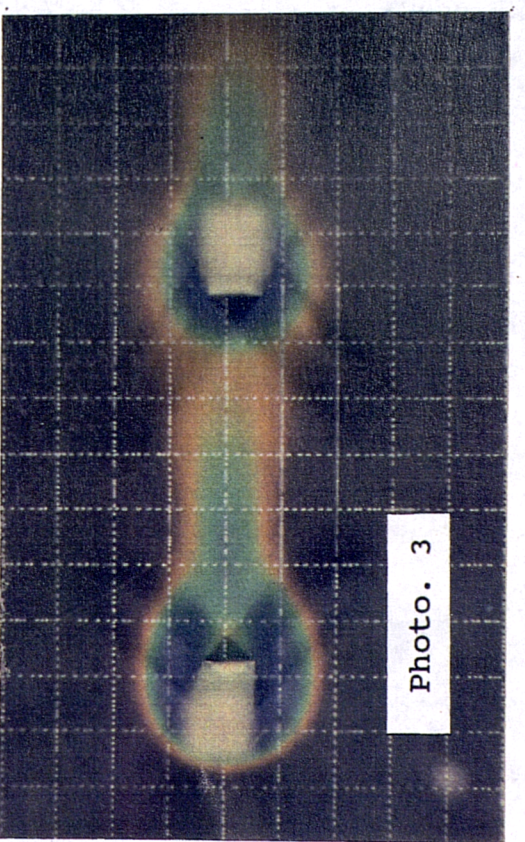
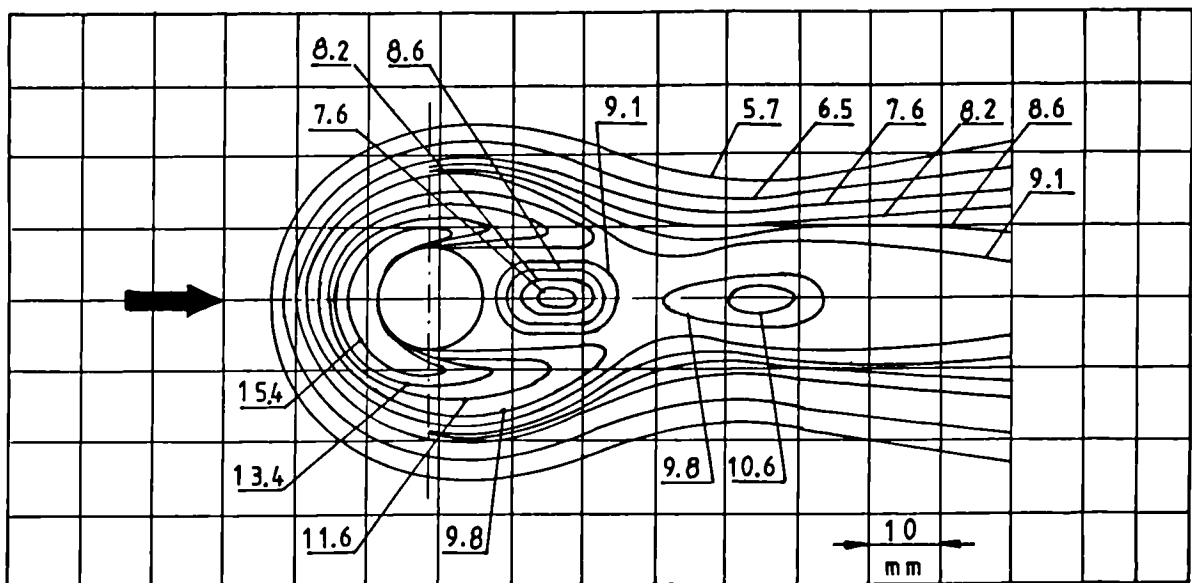


Photo. 3

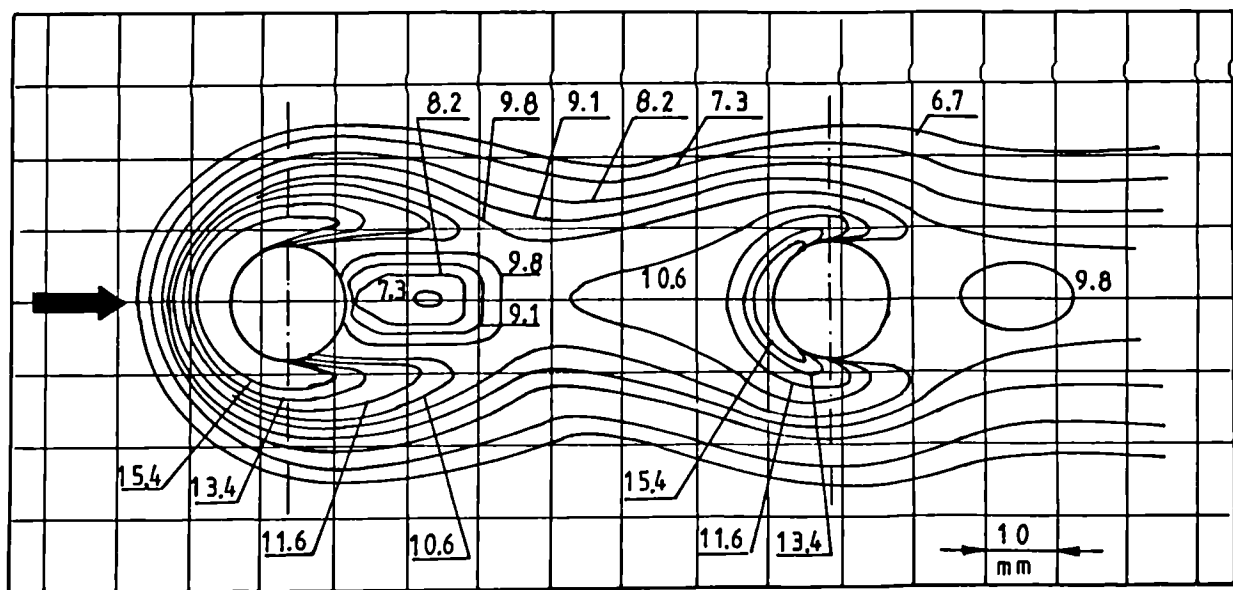
Fig. 78 Reproduction of colour transparency representing wall temperature contours at  $Re = 10000$ ;  $q = 228 \text{ W/m}^2$

Photo 1 -  $t_a = 35.7^\circ\text{C}$ , Photo 2 -  $t_a = 37.5^\circ\text{C}$ ,

Photo 3 -  $t_a = 40.0^\circ\text{C}$ , Photo 4 -  $t_a = 41.4^\circ\text{C}$ .



**Fig. 79** Contours of constant Nusselt number distribution around single cylinder at  $Re = 10000$ ;  $q = 228 \text{ W/m}^2$ ;  $D_h = 0.015 \text{ m}$



**Fig. 80** Contours of constant Nusselt number distribution around double cylinder at  $Re = 10000$ ;  $q = 228 \text{ W/m}^2$ ;  $D_h = 0.015 \text{ m}$

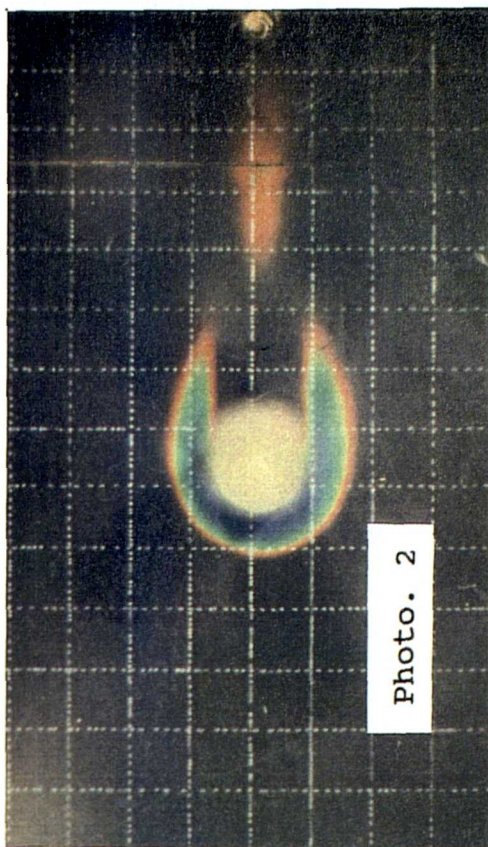


Photo. 2

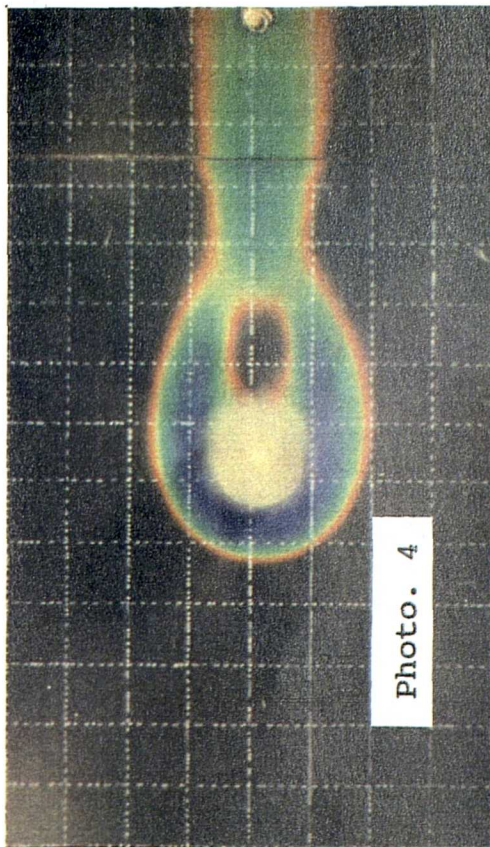


Photo. 4

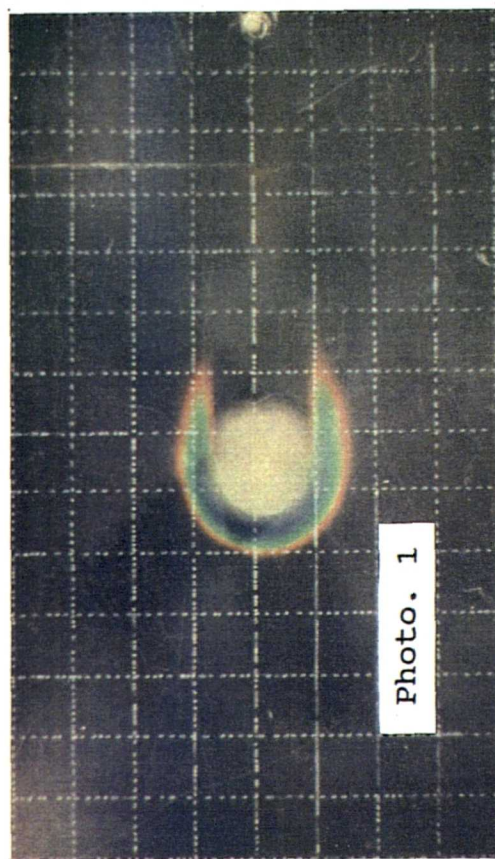


Photo. 1

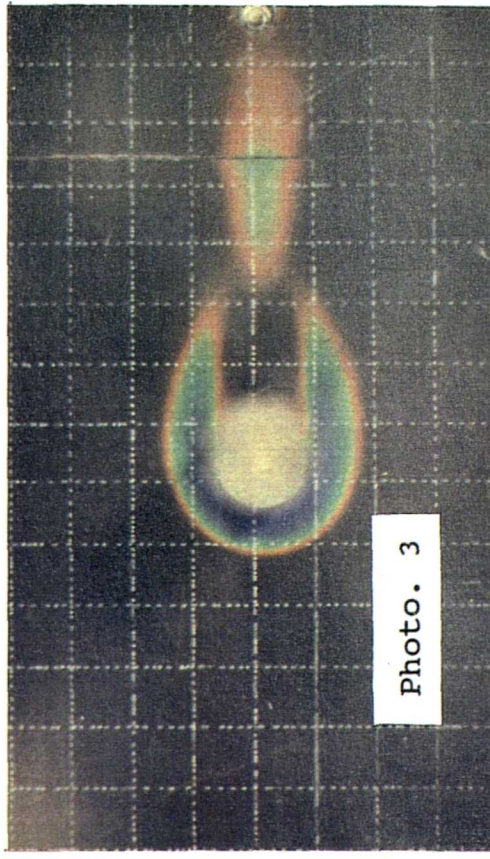


Photo. 3

Fig. 81 Reproduction of colour transparency representing wall temperature contours at  $Re = 10000$ ;  $q = 228 \text{ W/m}^2$   
Photo 1 -  $t_a = 38.3^\circ\text{C}$ , Photo 2 -  $t_a = 39.4^\circ\text{C}$ ,  
Photo 3 -  $t_a = 40.3^\circ\text{C}$ , Photo 4 -  $t_a = 42.0^\circ\text{C}$ .

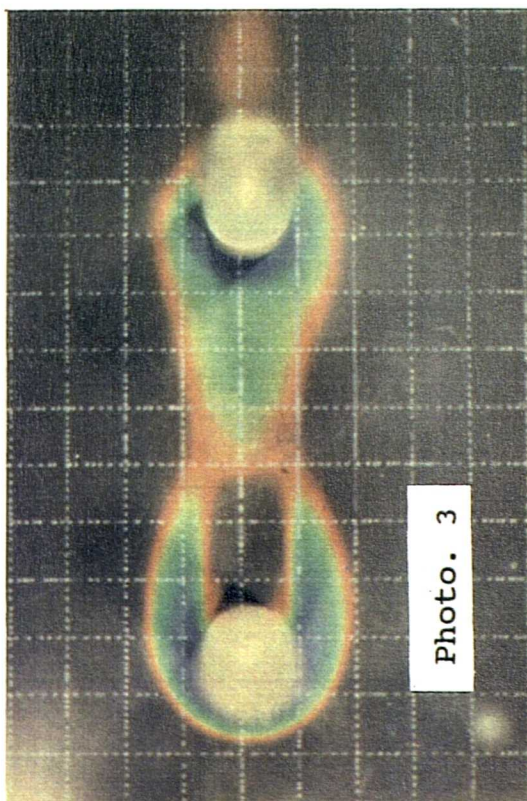
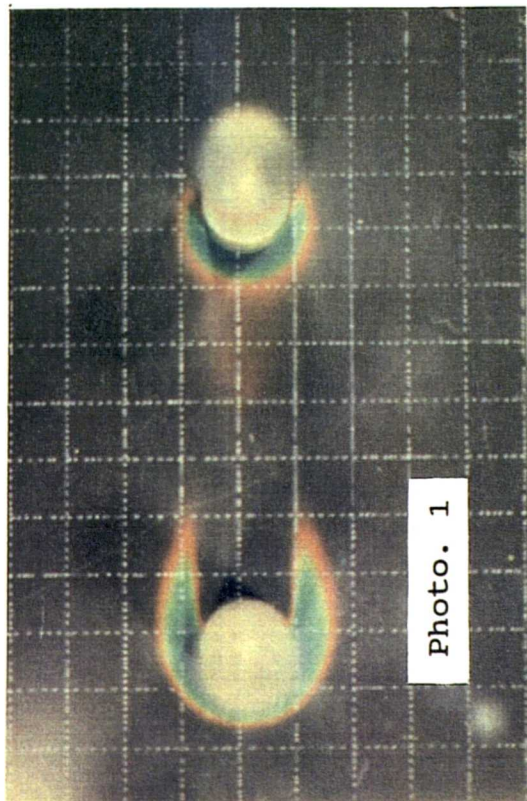
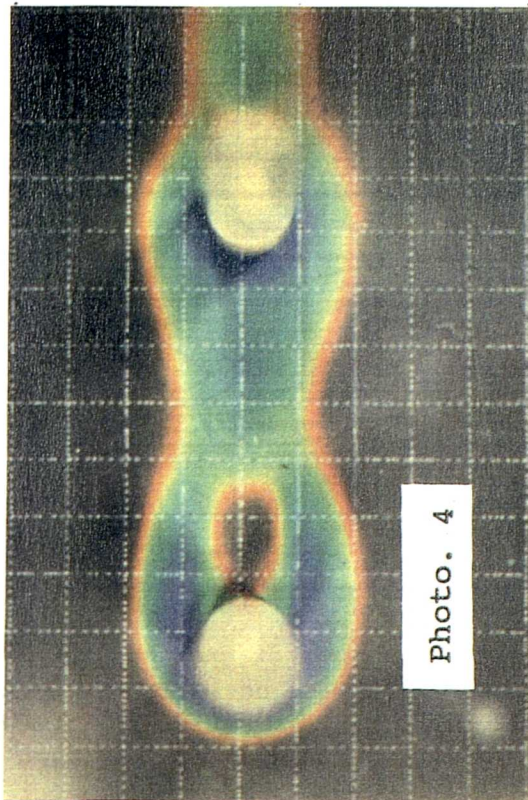
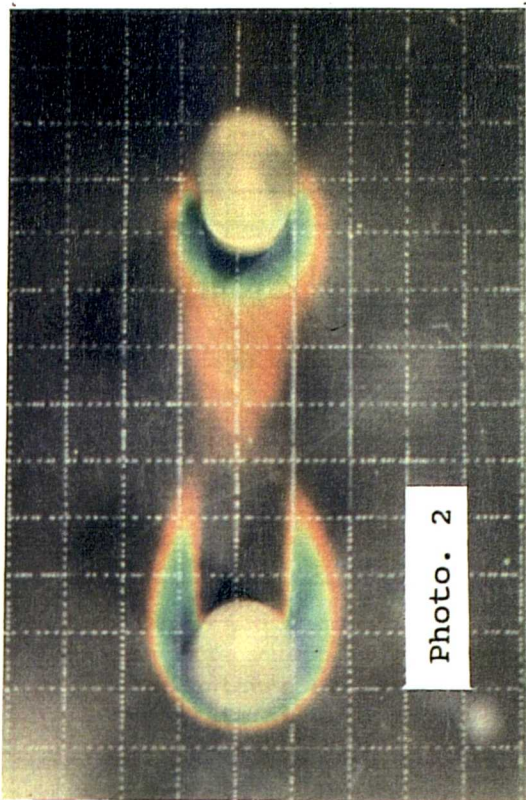


Fig. 82 Reproduction of colour transparency representing wall temperature contours at  $Re = 10000$ ;  $q = 228 \text{ W/m}^2$

Photo 1 -  $t_a = 38.3^\circ\text{C}$ , Photo 2 -  $t_a = 39.4^\circ\text{C}$ ,

Photo 3 -  $t_a = 40.3^\circ\text{C}$ , Photo 4 -  $t_a = 42.0^\circ\text{C}$ .

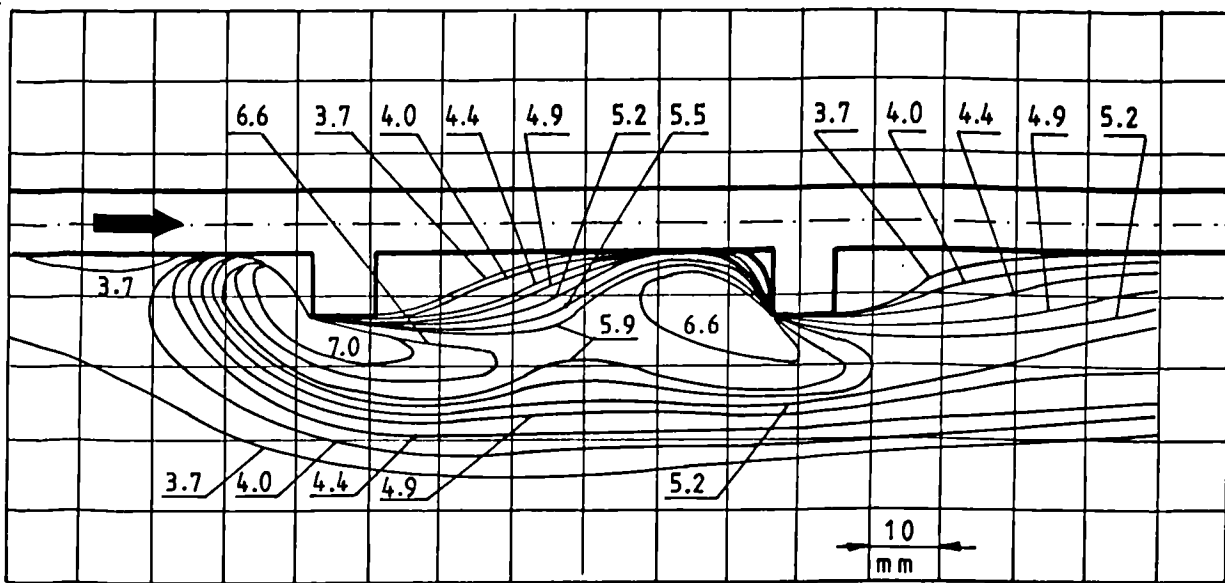


Fig. 83 Contours of constant Nusselt number distribution around roughness plate at  $Re = 10000$ ;  $q = 228 \text{ W/m}^2$ ;  $D_h = 0.009 \text{ m}$

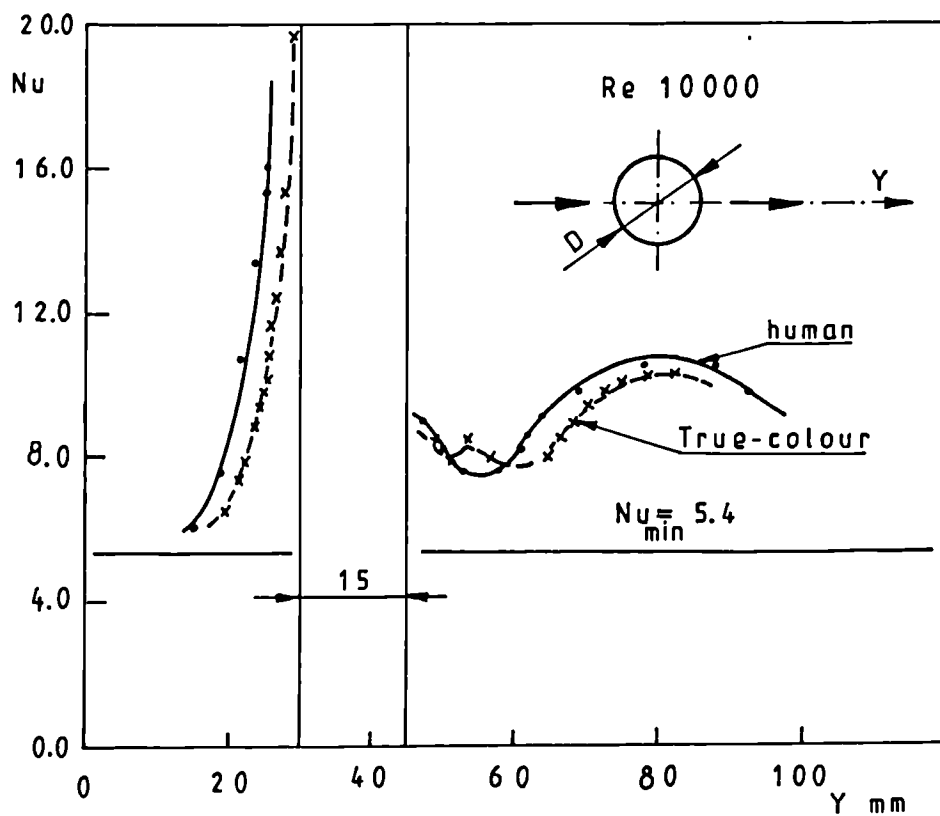


Fig. 85 Distribution of the local Nusselt number determined by the method employing human colour sensation and True-colour image processing, along a radius directly upstream and downstream of the cylinder (horizontal line represents channel base Nusselt number)

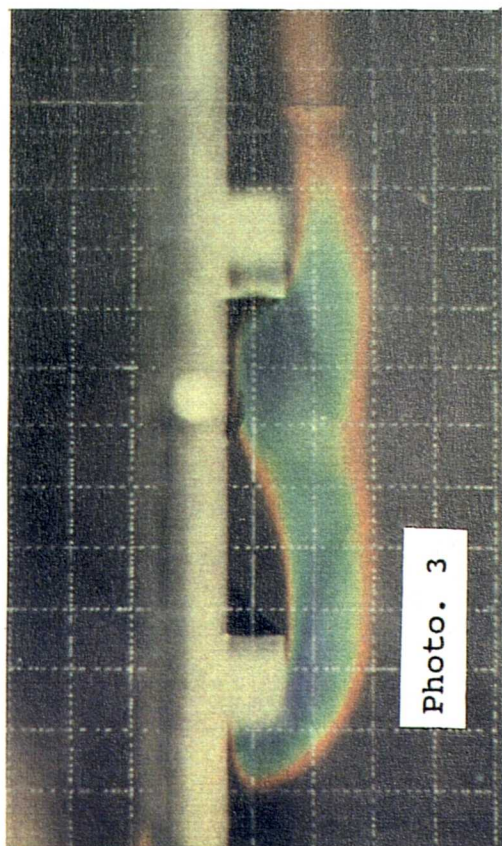
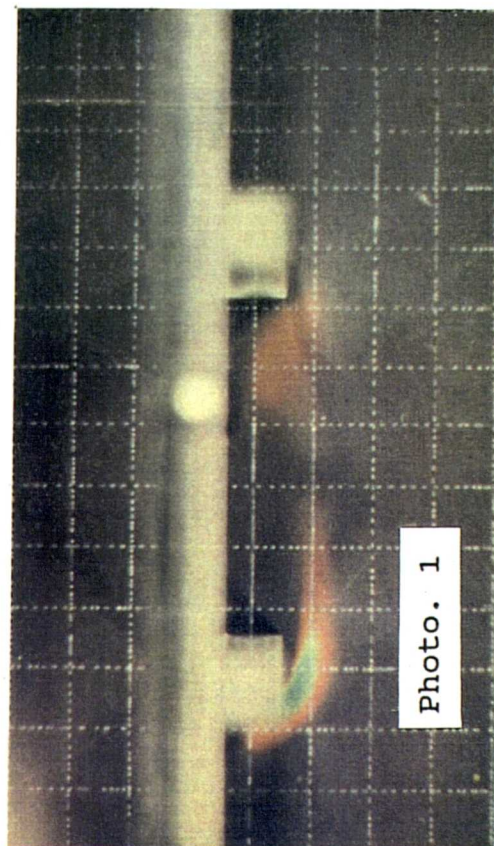
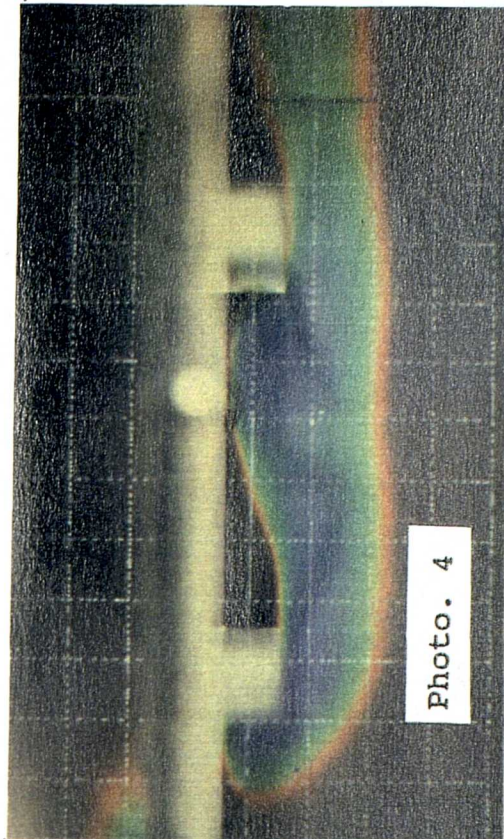
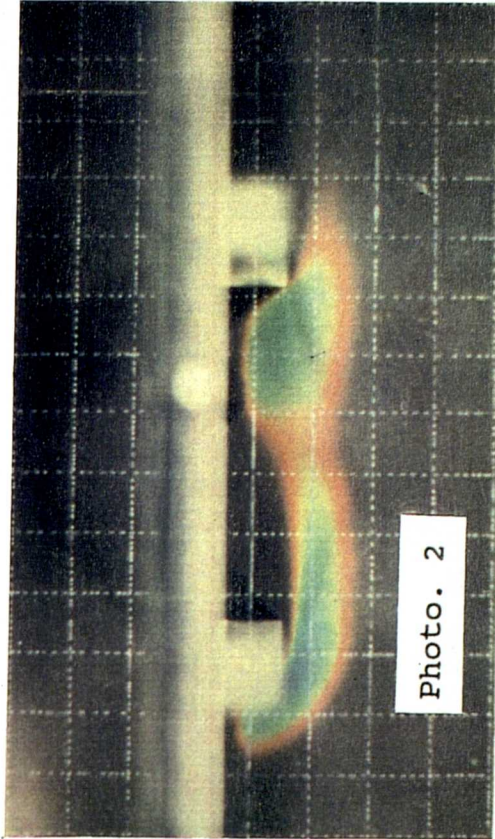


Fig. 84 Reproduction of colour transparency representing wall temperature contours at  $Re = 10000$ ;  $q = 228 \text{ W/m}^2$

Photo 1 -  $t_a = 38.3^\circ\text{C}$ , Photo 2 -  $t_a = 40.3^\circ\text{C}$ ,

Photo 3 -  $t_a = 42.0^\circ\text{C}$ , Photo 4 -  $t_a = 44.7^\circ\text{C}$ .

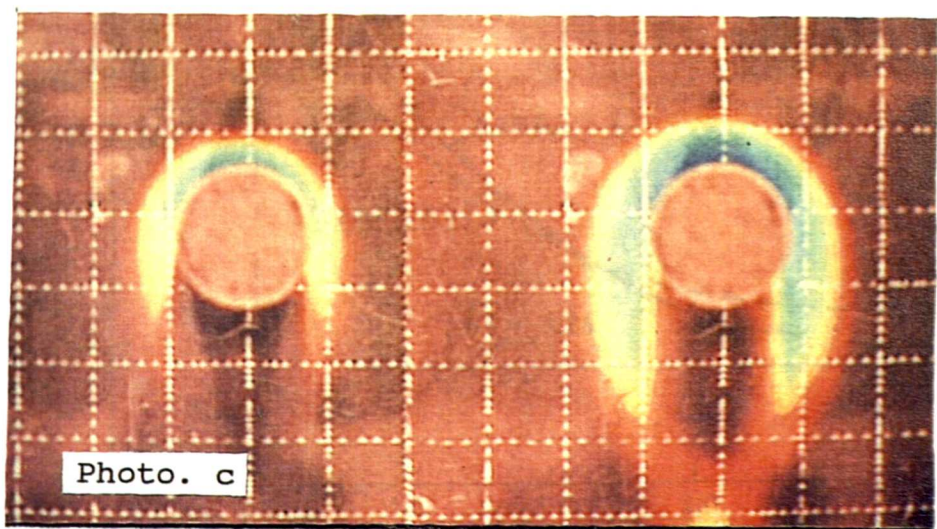
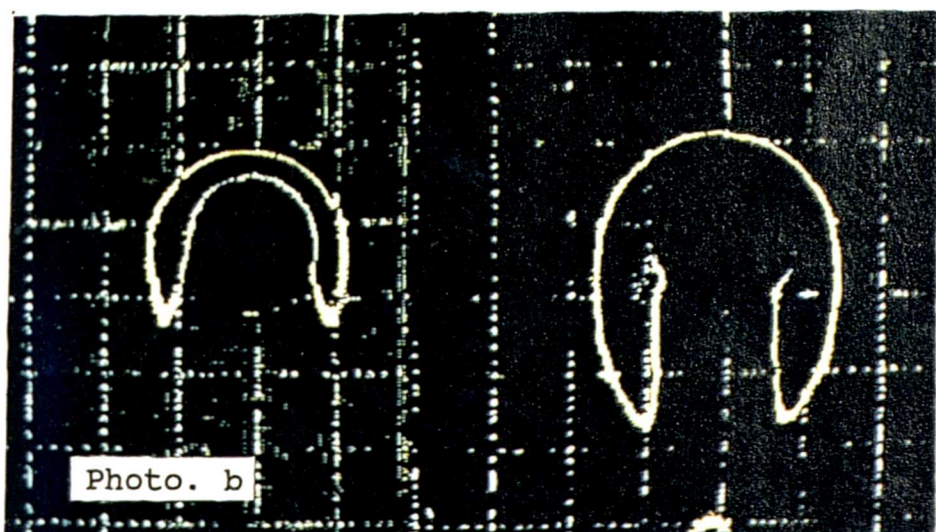
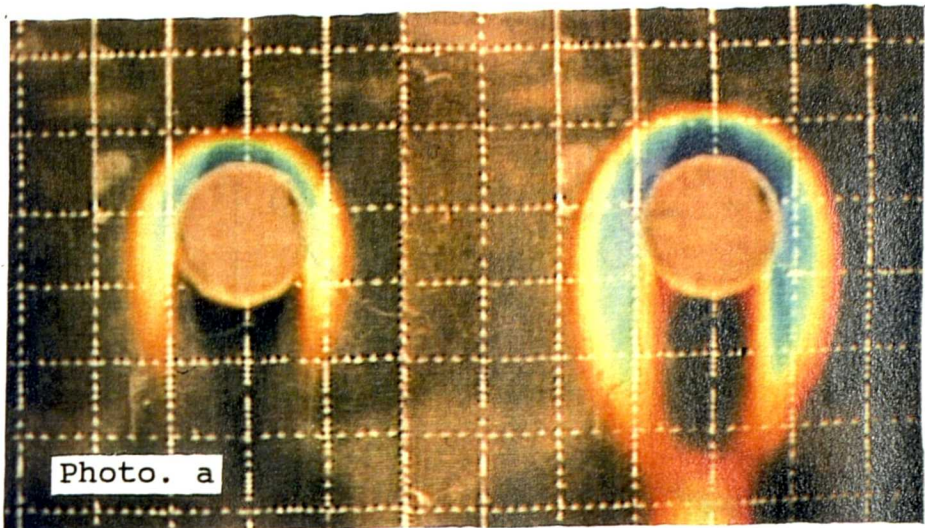


Fig. 86 Colour TV images of the liquid crystal layer on a cooled plate disturbed by a cylinder  
a) Image from RGB-camera  
b) Image through a segmentation-monochrome line show  $27.7^{\circ}\text{C}$  isochrome  
c) Image through chromaticity-adjust line hue map

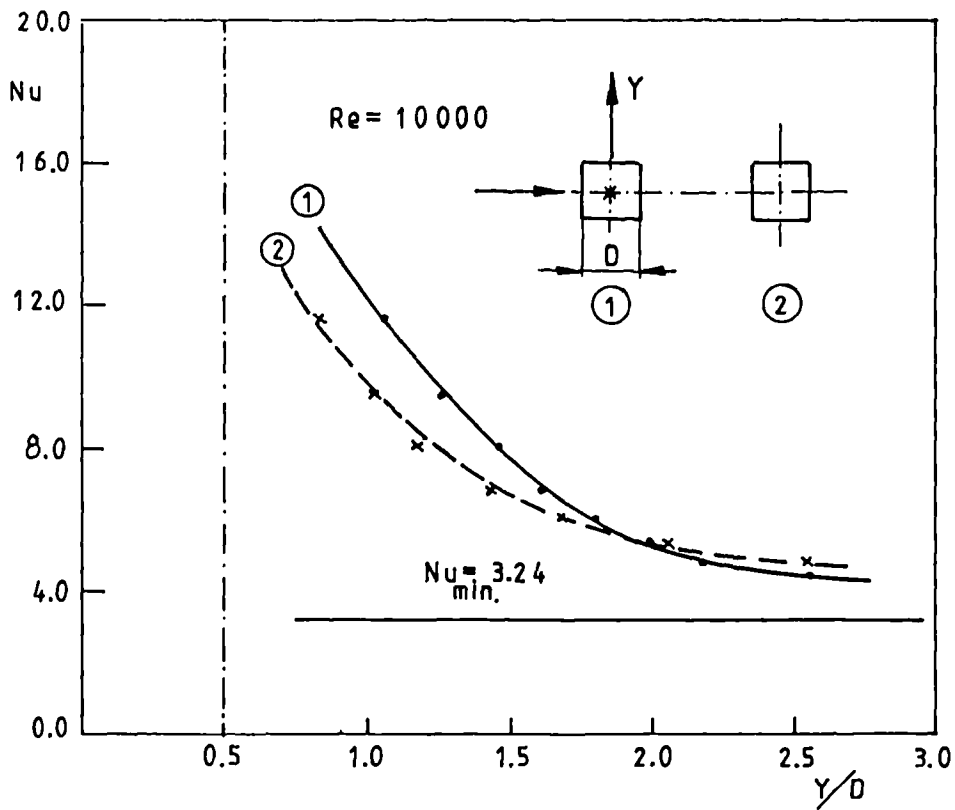


Fig. 87 Local Nusselt number around root of double square determined by human colour sensation (horizontal line represents channel base Nusselt number)

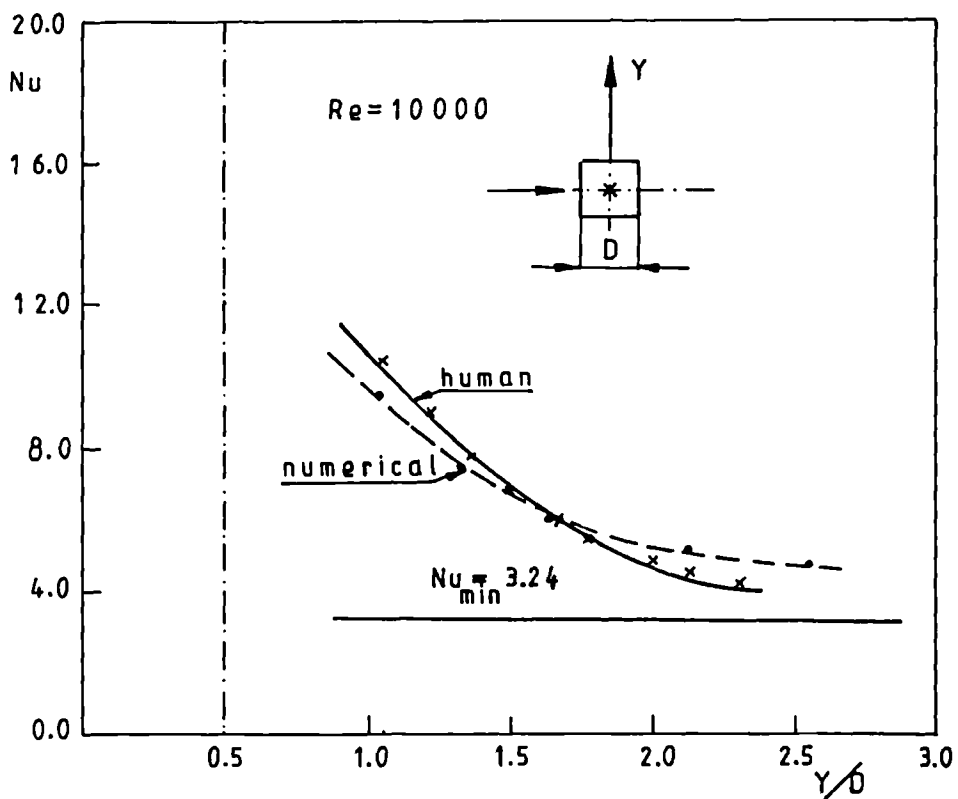


Fig. 88 Local Nusselt number around root of single square determined by human colour sensation and numerical simulation using Harwell-FLOW3D code

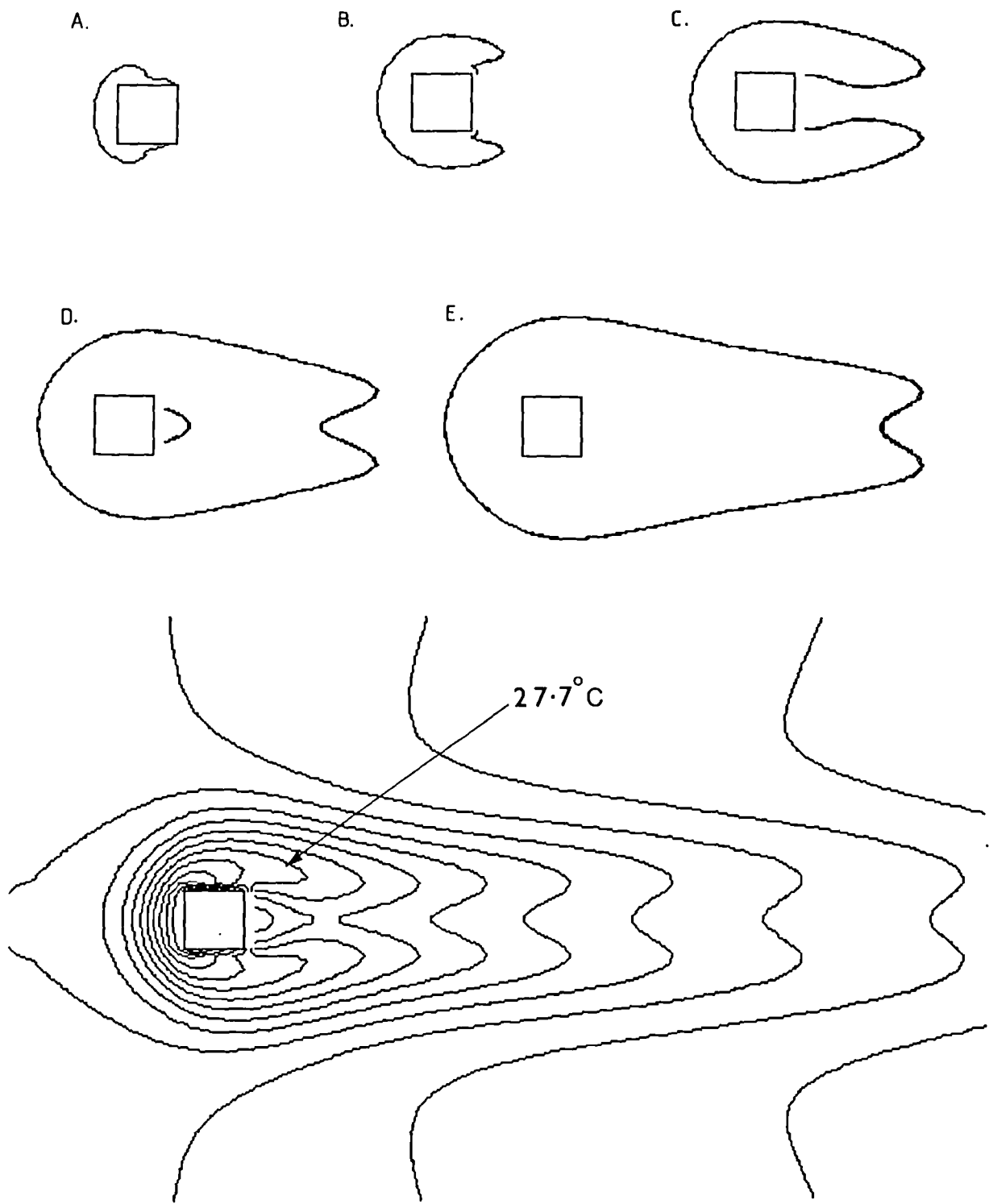


Fig. 89 Numerical simulation of isothermal map around root of single square using Harwell-FLOW3D code for Reynolds number of 10000 and constant heat flux  $q = \text{const} = 228 \text{ W/m}^2$

A)  $t_a = 38^{\circ}\text{C}$  B)  $t_a = 39^{\circ}\text{C}$  C)  $t_a = 40^{\circ}\text{C}$  D)  $t_a = 41^{\circ}\text{C}$  E)  $t_a = 42^{\circ}\text{C}$

#### 7.4 Temperature and Flow Visualisation in a Glycerol-Filled Cavity

The onset of free convection inside enclosed spaces involves an interesting but very complex flow phenomenon. Although the subject has been investigated experimentally, analytically and numerically and various predictions and correlations have been made, much work still remains to be done as the coupling between the flow field and temperature field has made these types of flows particularly hard to analyse and predict.

This present study is concerned with temperature and velocity visualisation within a rectangular enclosure using liquid crystals and True-colour image processing. These enclosures are geometrically simple but under certain conditions exhibit complex phenomena such as recirculation, stratification and turbulence, that correspond to such effects in more complex geometries.

In the case of free convection various flow regimes exist depending on two main dimensionless parameters, namely the Rayleigh number:

$$Ra = \frac{g \beta \delta^3 (t_h - t_c)}{\alpha \nu} \quad (15)$$

and the Prandtl number:  $Pr = \nu/\alpha$  (16)

together the geometry of the cavity.

In the above definitions,  $g$ ,  $\delta$ ,  $T_h$ ,  $T_c$ ,  $\alpha$ ,  $\beta$ ,  $\nu$  denote gravitational acceleration, cavity characteristic length (distance between two parallel walls), wall temperatures, thermal diffusivity, coefficient of thermal expansion and kinematic viscosity, respectively.

Since the physical problems in free convection are complex phenomena, experimental data are needed in order to develop reliable heat transfer correlations.

Suppose that the temperature difference ( $T_h - T_c$ ) between the plate walls is increased to such an extent that the buoyancy forces overcome the viscous forces resulting in a convective motion. From theoretical and experimental investigations for a horizontal enclosure the critical Rayleigh number is given by  $\underline{Ra}_c = 1708$ , which signifies the transition point where pure conduction heat transfer (i.e. molecular effects) is taken over by convection currents. The flow patterns caused by the convection currents are hexagonal cells called Bernard cells [88].

The above case concerns concepts of free convection when the fluid layer is horizontal but it may be extended to layers of fluid where the angle of inclination is varied from horizontal to vertical. In this case the onset of free convection in the fluid is also dependent on the angle of inclination  $\theta$ , the aspect ratio  $H/\delta$  where  $H$  is the height of the wall, as well as the Rayleigh and Prandtl numbers.

In the present experiments the angle of inclination of the cavity could be varied from horizontal through to vertical to observe how the free convection was affected. A temperature gradient of 10K ( $T_h = 297.6\text{K}$ ,  $T_c = 287.6\text{K}$ ) was used so as to obtain desired Rayleigh ( $Ra = 1.2 \cdot 10^4$ ) and Prandtl ( $Pr = 12.5 \cdot 10^3$ ) numbers and flow conditions in the particular cavity. A sequence of images was taken in the cavity under conditions of steady-state free convection. This sequence was for angles of inclination from horizontal to vertical in  $30^\circ$  steps. A liquid crystal with a colour-play range of  $3.8\text{ K}$  was used, the red colour band being  $19.6^\circ\text{C}$ . Figures 86 and 87 show images for the mid-plane of the cavity taken over angles from horizontal to vertical. On the photographs, the liquid crystals convected by the flow appear as a series of coloured, uniformly spaced dots. In this particular experiment 8 flashes at a time interval of 6 seconds were used to take one photograph. The displacements of the tracer particles, as recorded on the photographs, enable information to be obtained about

the velocity field in the cavity. This information is, of course, limited to components lying in the plane of observation. An example of the vertical velocity profiles in the mid-plane at various cross sections of the vertical cavity is given in Figure 92. The figure demonstrates that the vertical velocity profiles are slightly asymmetric; this results from the temperature dependence of the viscosity of glycerol.

As mentioned in Chapter 6, in the present experiments, we are interested only in the shape of the isotherms but not in their absolute temperature values. For such measurements, one needs another calibration procedure, for instance, a light source of discrete colour spectrum. The isotherms presented in Fig.94 are lines (white) of constant hue range bands for a picture taken under flow resulting from the horizontal configuration of the cavity. This was obtained by taking a photo-image using RGB video camera and then converting the RGB image to a HSI image. A hue range was selected thus eliminating all other pixels on the image with a different hue value to that selected. This information may be used to map isothermal contours, as hue has a direct relationship with temperature that is found by calibration.

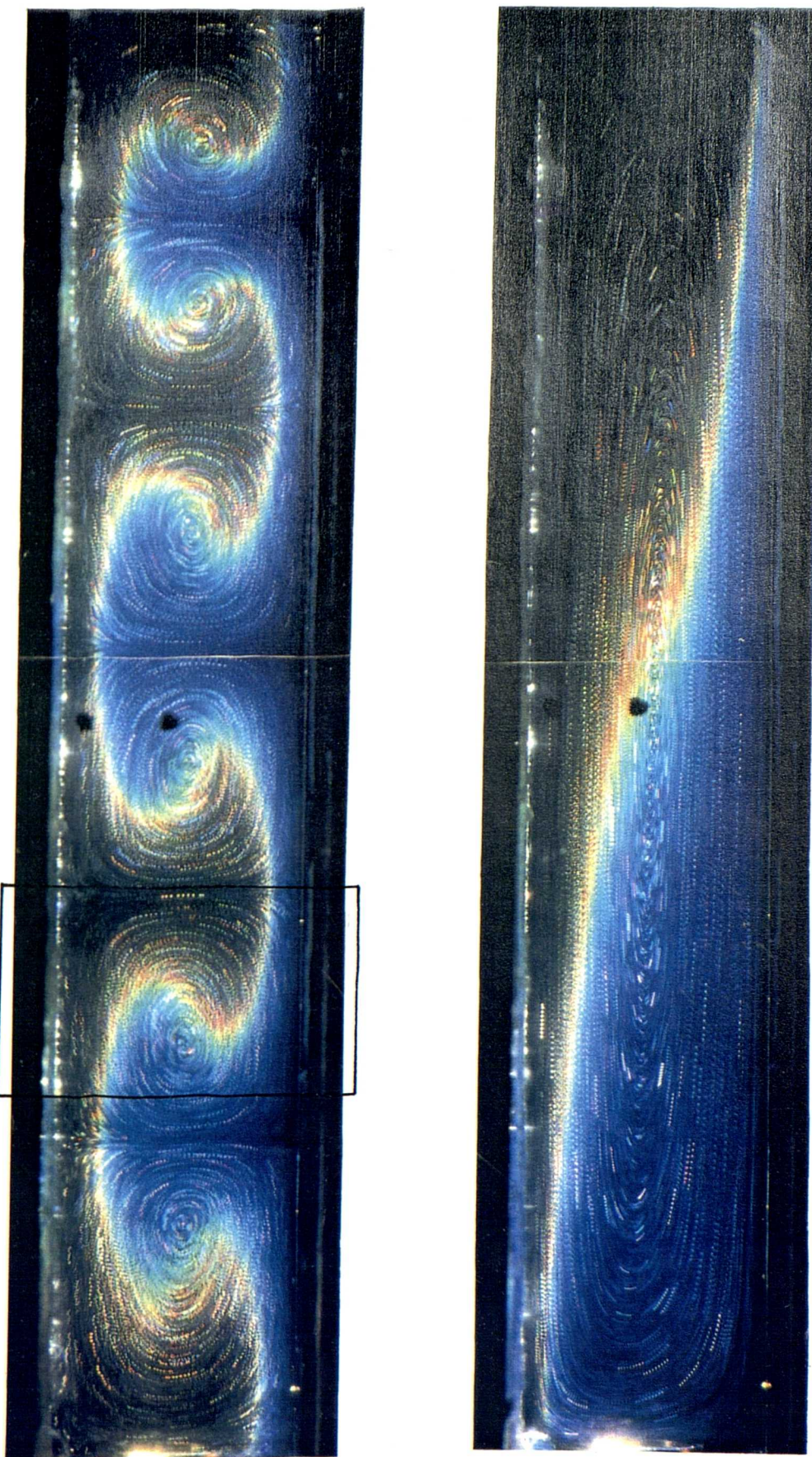


**Fig. 90** Temperature and velocity visualisation in a glycerol-filled cavity under free convection using neat chiral-nematic liquid crystal;  
 $\text{Ra} = 1.2 \cdot 10^4$  and  $\text{Pr} = 12.5 \cdot 10^3$   
 a) the horizontal position -  $\theta = 0^\circ$  showing the Bernard cells  
 b) the vertical position -  $\theta = 90^\circ$

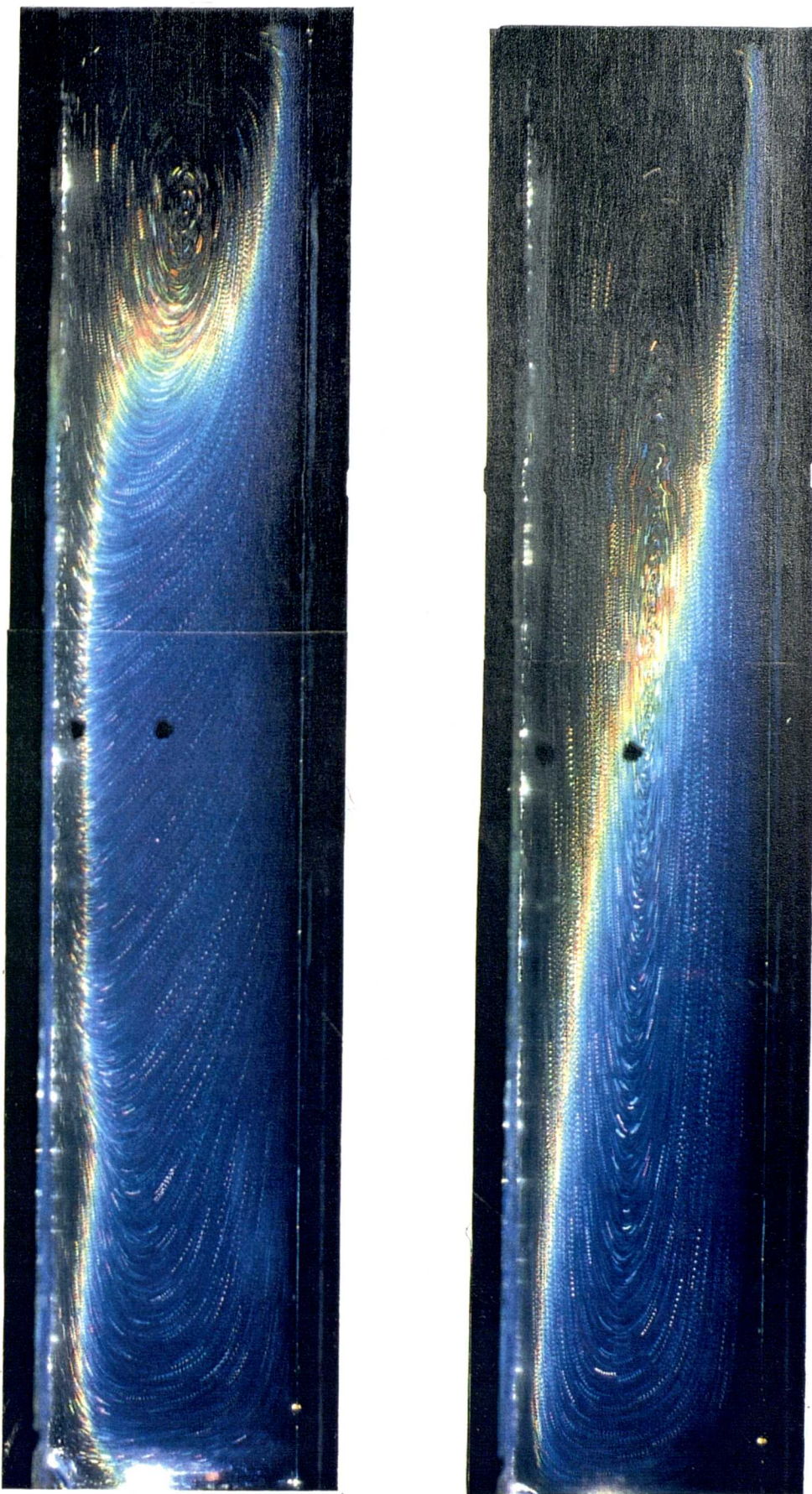
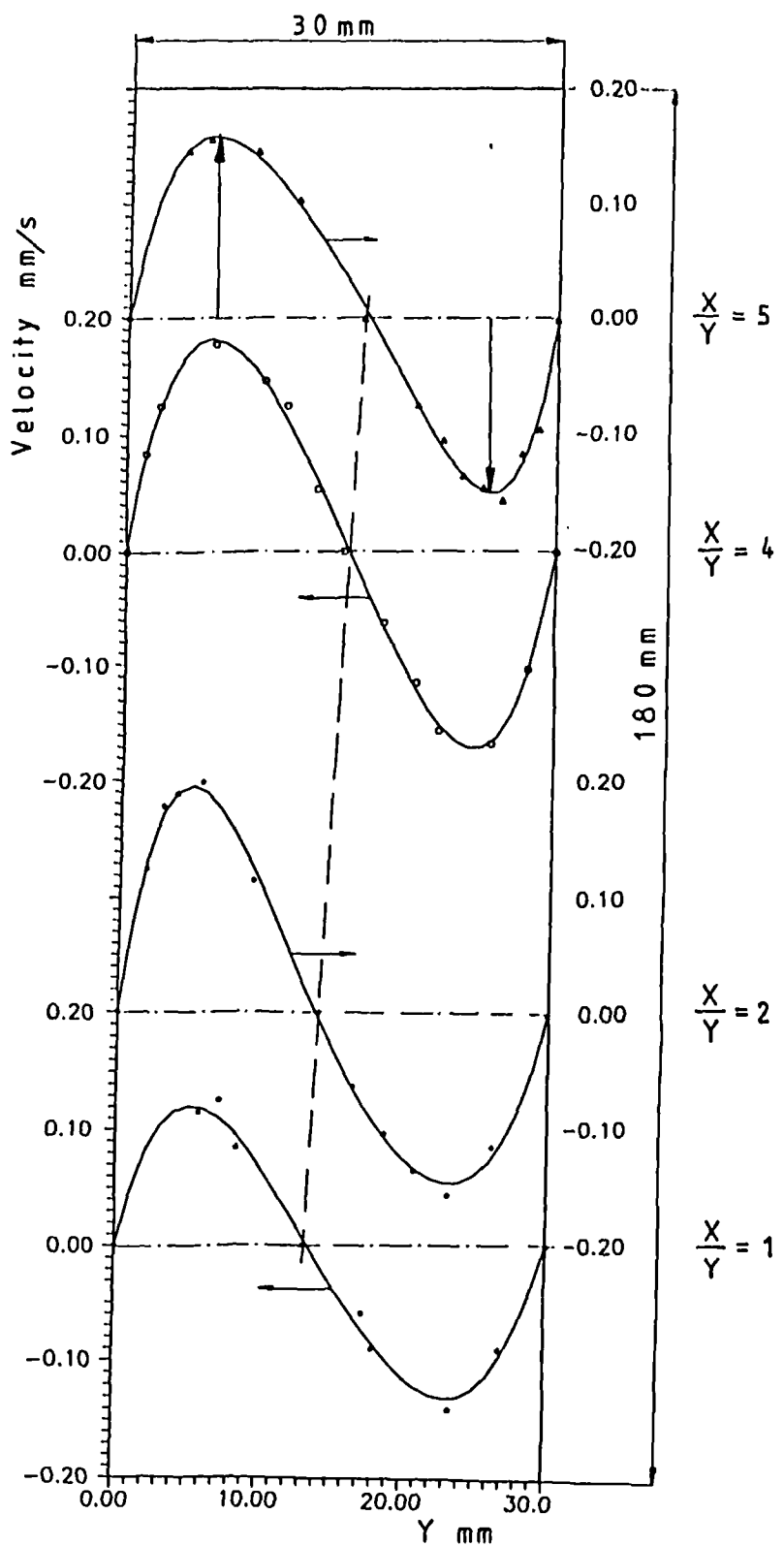


Fig. 91 Temperature and velocity visualisation in a glycerol-filled cavity under free convection using neat chiral-nematic liquid crystal;  
 $\text{Ra} = 1 \cdot 2 \cdot 10^4$  and  $\text{Pr} = 12 \cdot 5 \cdot 10^3$   
a) the inclination position -  $\theta = 30^\circ$   
b) the inclination position -  $\theta = 60^\circ$



**Fig. 92** Vertical velocity profiles at different heights in the vertical position of cavity;  
 $\text{Ra} = 1.2 \cdot 10^4$  and  $\text{Pr} = 12.5 \cdot 10^3$

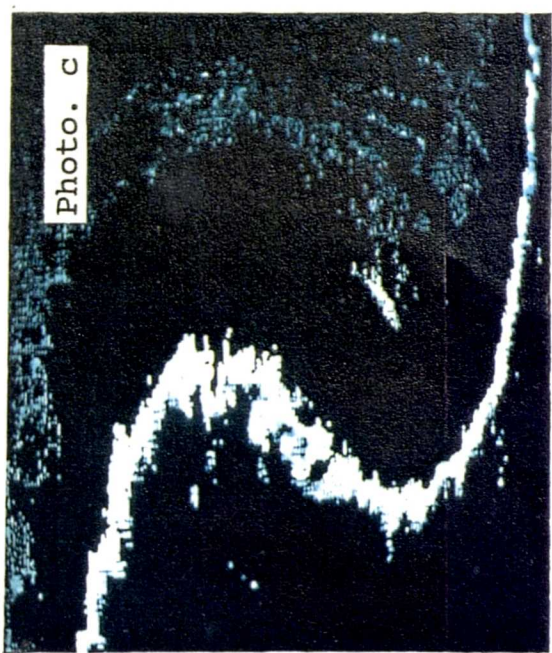
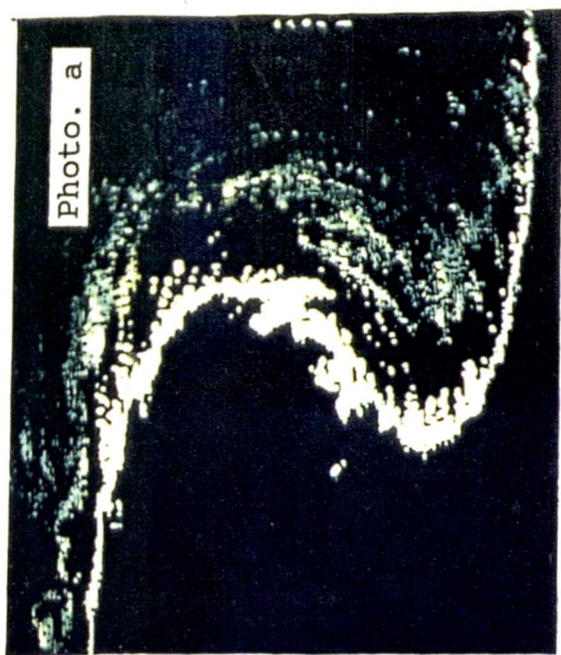
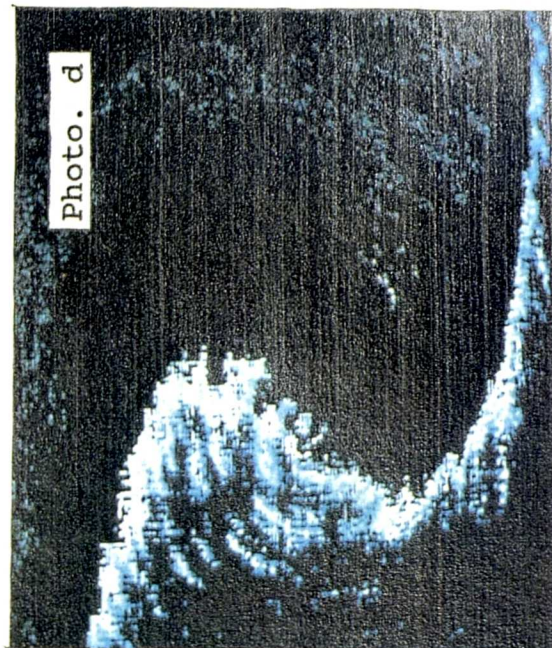
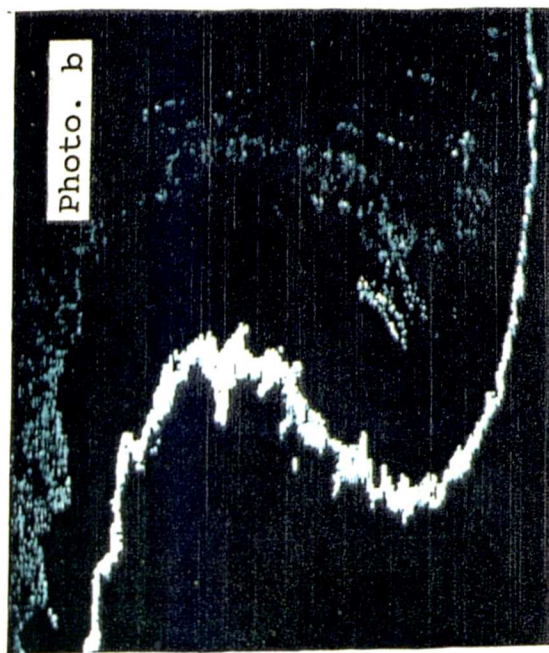


Fig. 93 Segmentation transform of the cavity image shown in framed region of Figure 90a

1. Photo a - Hue: 40-60
2. Photo b - Hue: 100-120
3. Photo c - Hue: 120-140
4. Photo d - Hue: 140-150

## 8. UNCERTAINTY ANALYSIS

Uncertainty analysis began as the statistical interpretation of the errors in well-replicated experimental results. It became apparent during the early 1950's that many important engineering experiments could not be repeated enough times to provide useful statistical information, for reasons of economy or pressure of time. A rational way to use the framework of statistical inference to estimate the uncertainty in these single-sample experiments was first presented by Kline and McClintock [127] and Holman [125] and still forms the basis for this branch of the art. More recently, Moffat [130,131,132] has presented a general description of the sources of errors in engineering measurements, the relationship between error and uncertainty, and how to use uncertainty analysis in the planning of an experiment.

In this experimental study the heat transfer coefficient (or Nusselt number) was determined using Equation (8) as a function of a few independent variables. When several independent variables are used in the function R, the uncertainty in a computed result could be estimated with good accuracy using a root-sum-square (RSS) combination,

$$\delta R = \left\{ \sum_{i=1}^N \left( \frac{\partial R}{\partial X_i} \varepsilon_i \right)^2 \right\}^{1/2} \quad (17)$$

This is the basic equation of uncertainty analysis. Each term represents the contribution made by the uncertainty in one variable,  $\varepsilon_i$ , to the overall uncertainty in the result,  $\delta R$ . Each term has the same form: the partial derivative of R with respect to  $X_i$  multiplied by the uncertainty interval for that variable [130].

\* The experimental uncertainty in "  $h_\ell$ " can be calculated using Equation (18):

$$\frac{\epsilon_h}{h_\ell} = \frac{1}{h_\ell} \left\{ \sum_{i=1}^N \left( \frac{\partial h_\ell}{\partial X_i} \epsilon_i \right)^2 \right\}^{1/2} \quad (18)$$

where:

$$\frac{\partial h_\ell}{\partial k_t} = (t_\ell - t_b) / \delta_t (t_a - t_\ell) = h_\ell / k_t \quad (19)$$

$$\frac{\partial h_\ell}{\partial \delta_t} = -k_t (t_\ell - t_b) / \delta_t^2 (t_a - t_\ell) = -h_\ell / \delta_t \quad (20)$$

$$\frac{\partial h_\ell}{\partial t_b} = -k_t t_b / \delta_t (t_a - t_\ell) = -h_\ell t_b / (t_\ell - t_b) \quad (21)$$

$$\begin{aligned} \frac{\partial h_\ell}{\partial t_\ell} &= k_t (t_\ell - t_b) \left[ \frac{1}{(t_a - t_\ell)} + \frac{1}{(t_\ell - t_b)} \right] / \delta_t (t_a - t_\ell) = \\ &= h_\ell \left[ \frac{1}{(t_a - t_\ell)} + \frac{1}{(t_\ell - t_b)} \right] \end{aligned} \quad (22)$$

$$\frac{\partial h_\ell}{\partial t_a} = -k_t (t_\ell - t_b) / \delta_t (t_a - t_\ell)^2 = -h_\ell (t_a - t_\ell) \quad (23)$$

As noted earlier, the contours of constant heat transfer coefficient are not directly equivalent to the isotherms, as measured from the photographs or video-images. They are determined after taking into account thermal conduction of the plate components for the TLC's two wall temperatures  $T_\ell$  and  $T_b$ , the mixed mean temperature of air  $T_a$ , radiation from the lamps and other corrections. The lateral heat conduction effects in the plexiglass plate is typically about 4% of the net flux and 0.4% on the corrugated plate, respectively for  $Re = 5500$  and the maximum film temperature differences of the TLC's, namely about  $14^\circ C$ .

The maximum error of wall temperature measurement by the present method is  $\pm 0.15^\circ\text{C}$  (for the flat-palte working section experiment) and  $\pm 0.075^\circ\text{C}$  (for the corrugated working section), as described in the previous section. The error of the bulk gas temperature is  $\pm 0.1^\circ\text{C}$  and  $\pm 0.025^\circ\text{C}$  for the constant-temperature water bath  $t_b$ . The uncertainty of thermal conduction is within  $\pm 0.005 \text{ W/m K}$ . Therefore, the maximum uncertainty of local heat transfer coefficient is within  $\pm 67\%$  at the lowest Reynolds number, decreasing to  $\pm 13\%$  at the highest Reynolds number of 5500. The average uncertainties of " $h_{av}$ " for the Reynolds number range of 1200-5500 are respectively 27% and 5%. Examples of the uncertainty analysis are given in Table 2. The largest measurement uncertainty occurs in the experimental run, where the temperature difference between the liquid crystals and water bath are smaller - any improvement in the current experimental result may be achieved by significantly increasing the thickness of corrugation plate  $\delta_t$ .

\* The experiments were carried out for the Reynolds number (Re) range of 1200-10000. Re was based on the hydraulic diameter of the corrugation structure, mapping section and the centreline velocity V. The uncertainty of the Reynolds number is within  $\pm 5\%$ , caused by errors of flow rate, channel spacing and air properties.

\* The experimental results of pressure drop are presented in Figs.65,69,70 in the form of friction factors vs Reynolds number and inclination angle  $\varphi$ . Wall static pressure drops were measured at the wall tappings by means of a micro-manometer model MDC FC002/Furness Controls Ltd., Bexhill. Because turbulent fluctuations fall to zero at the surface, the only error introduced is the fluctuation of flows into and out of the tapping. This falls to zero for a first order approximation, Bradshaw [12]. The only remaining error source is the difference between the pressure on a solid surface and the pressure in the hollow tapping. This has been assumed negligible for half a century for low speed flows where the tapping diameter is between

0.5-1.0 mm. Flow velocity (in the corrugated geometry) was measured using a Pitot tube. Bradshaw [12] also discusses errors of the Pitot tube and indicates that the accuracy is of the order of 0.25% provided the tube is aligned correctly, is not close to a wall, that the turbulence intensity is less than 5% and the total pressure does not change by more than 1% to 2%. Taking into account the above, and the temperature and velocity fluctuations of the air, the maximum uncertainty of the friction factor is less than 4%.

Re	Measured Quantity $x_i$	$k_t$ W/mK	$\delta_t$ m	$t_b$ °C	$t_e$ °C	$t_a$ °C	$c_h$ $\overline{h}_t$	$\left( \frac{c_h}{\overline{h}_t} \right)_{av}$	
<b>FLAT-PLATE WORKING SECTION</b>									
Re 5506 $\varphi = 36^\circ$	Uncertainty $c_i$	0.005	$0.025 \cdot 10^{-3}$	0.025	0.15	0.1	0.26 min $h_t$	0.10	
	$\left  \frac{\partial h_t}{\partial x_i} \right $	128.3	$19.0 \cdot 10^3$	212.5	9.58	1.2			
	Uncertainty $c_i$	0.005	$0.025 \cdot 10^{-3}$	0.025	0.15	0.1	0.04 max $h_t$		
	$\left  \frac{\partial h_t}{\partial x_i} \right $	925.0	$137. \cdot 10^3$	85.4	16.8	8.4			
Re 1796 $\varphi = 36^\circ$	Uncertainty $c_i$	0.005	$0.25 \cdot 10^{-3}$	0.025	0.15	0.1	0.68 min $h_t$	0.24	
	$\left  \frac{\partial h_t}{\partial x_i} \right $	52.3	$7.8 \cdot 10^3$	223.5	8.85	0.48			
	Uncertainty $c_i$	0.005	$0.025 \cdot 10^{-3}$	0.025	0.15	0.1	0.065 max $h_t$		
	$\left  \frac{\partial h_t}{\partial x_i} \right $	439.9	$65.2 \cdot 10^3$	162.8	12.4	4.0			
<b>CORRUGATED WORKING SECTION</b>									
Re 1170 $\varphi = 75^\circ$	Uncertainty $c_i$	0.005	$0.025 \cdot 10^{-3}$	0.025	0.075	0.1	0.53 min $h_t$	0.32	
	$\left  \frac{\partial h_t}{\partial x_i} \right $	81.8	$13.52 \cdot 10^3$	278.4	11.1	0.78			
	Uncertainty $c_i$	0.005	$0.025 \cdot 10^{-3}$	0.025	0.075	0.1	0.15 max $h_t$		
	$\left  \frac{\partial h_t}{\partial x_i} \right $	251.5	$43.8 \cdot 10^3$	247.7	40.4	2.51			
Re 5560 $\varphi = 30^\circ$	Uncertainty $c_i$	0.005	$0.025 \cdot 10^{-3}$	0.025	0.075	0.1	0.39 min $h_t$	0.17	
	$\left  \frac{\partial h_t}{\partial x_i} \right $	104.1	$18.15 \cdot 10^3$	272.6	11.3	1.04			
	Uncertainty $c_i$	0.005	$0.025 \cdot 10^{-3}$	0.025	0.075	0.1	0.07 max $h_t$		
	$\left  \frac{\partial h_t}{\partial x_i} \right $	509.4	$88.8 \cdot 10^3$	205.8	15.43	5.1			
Re 5100 $\varphi = 75^\circ$	Uncertainty $c_i$	0.005	$0.025 \cdot 10^{-3}$	0.025	0.075	0.1	0.19 min $h_t$	0.11	
	$\left  \frac{\partial h_t}{\partial x_i} \right $	209.0	$36.45 \cdot 10^3$	256.0	12.4	2.09			
	Uncertainty $c_i$	0.005	$0.25 \cdot 10^{-3}$	0.025	0.075	0.1	0.054 max $h_t$		
	$\left  \frac{\partial h_t}{\partial x_i} \right $	710.0	$124. \cdot 10^3$	170.8	17.4	7.1			
Re 1600 $\varphi = 30^\circ$	Uncertainty $c_i$	0.005	$0.025 \cdot 10^{-3}$	0.025	0.075	0.1	1.34 min $h_t$	0.54	
	$\left  \frac{\partial h_t}{\partial x_i} \right $	31.8	$5.54 \cdot 10^3$	288.5	10.7	0.32			
	Uncertainty $c_i$	0.005	$0.025 \cdot 10^{-3}$	0.025	0.075	0.1	0.21 max $h_t$		
	$\left  \frac{\partial h_t}{\partial x_i} \right $	183.5	$32. \cdot 10^3$	260.2	12.13	1.84			
<b>ENDWALL TEMPERATURE MEASUREMENTS</b>									
Re 10000	Uncertainty $c_i$	0.005	$0.025 \cdot 10^{-3}$	0.025	0.15	0.1	0.051	-	
	$\left  \frac{\partial h_t}{\partial x_i} \right $	195.0	$38 \cdot 10^3$	42.7	4.48	4.3			

Table 2 Uncertainty Analysis

## 9. CONCLUSIONS

In this thesis, the use of liquid crystals combined with image and data processing, have been applied to complex geometries of engineering significance, to provide quantitative heat transfer data suitable for performance purposes. The geometries are:

- (i) crossed-corrugated geometrical elements for air rotary heat exchangers,
- (ii) circular (both single and double) and a square section column, and
- (iii) square roughness elements.

The experience gained shows that this approach can shed new light on old problems and also open up new areas of research. The advent and development of liquid crystal techniques is an important part of the current development of optical measurement methods in heat and fluid flow situations in general. Image processed data makes available quantitative, full-field information about the distribution of temperature and heat transfer coefficient which will undoubtedly encourage the study of situations which have been, until now, too complex to consider. For example, the three-dimensional important cross-corrugated geometry has been studied for the first time. They can be used qualitatively and quantitatively in flow visualisation and measurement, respectively.

Finally, the concept of Data Thermography has been demonstrated, where the parameters of three-dimensional velocity and temperature space can be determined simultaneously. This method combines the use of liquid crystals in droplet form, colour image processing, data acquisition and analysis by computer. These are the main developments reported in this thesis.

## REFERENCES

1. AKINO, N., KUNUGI, T., UEDA, M. and KUROSAWA, A. "Liquid crystal thermometry based on automatic colour evaluation and applications to measure turbulent heat transfer". In: Transport Phenomena in Turbulent Flow Theory, Experiment and Numerical Simulation. Hirata, M. and Kasagai, N. (1988) (New York: Hemisphere Publishing Corp.) pp807-820.
2. AKINO, N., KUNUGI, T., ICHINUYA, K., MITSUSHIRO, K. and UEDA, M. (1989). Improved Liquid Crystal Thermometry Excluding Human Colour Sensation. Journal of Heat Transfer, Vol.III, pp558-565.
3. AKINO, N., KUNUGI, T., UEDA, M. and KUROSAWA, A. (1989) A Study of Thermo-Camera Using a Liquid Crystal. N.H.T.C., Philadelphia, U.S.A.
4. ANDREWS, H.C. (1978) Digital Image Processing. IEEE Computer Society, New York.
5. ASHFORTH-FROST, S., WANG, L.S., JAMBUNATHAN, K., GRAHAM, D.P. and RHINE, J.M. "Application of image processing techniques to liquid crystal thermography". Seminar: Optical Methods and Data Processing in Heat and Fluid Flow, 2-3 April (1992), City University, London, U.K.
6. BAYAZITOGLU, Y. and ÖZISIK, M.N. (1988) Elements of Heat Transfer. (New York: McGraw-Hill Book Co.).
7. BAUGHN, J.W., IRELAND, P.T., JONES, T.V. and SANIEL, N. (1989) A Comparison of the Transient and Heated-Coating Methods for the Measurement of Local Heat Transfer Coefficients on a Pin Fin. Journal of Heat Transfer, Vol.III, pp871-881.
8. BAUGHN, J.W., HOFFMAN, M.A. and MAKEL, D.B. (1986) Improvements in a New Technique for Measuring and Mapping Heat Transfer Coefficients. Rev.Sci.Instrum., Vol.57, pp650-654.
9. BONNETT, P., JONES, T.V. and McDONNELL, D.G. (1989) Shear-Stress Measurement in Aerodynamic Testing Using Cholesteric Liquid Crystals. Liquid Crystals, Vol.6, No.3, pp271-280.
10. BROWN, A. and SALUJA, C.L. (1978) The Use of Cholesteric Liquid Crystals for Surface Temperature Visualisation of Film-Cooling Processes. J.Phys.E.Sci.Instrum., Vol.II, pp1068-1-72.
11. BROWN, G.H. and SHAW, W.G. (1957) . The Mesomorphic State : Liquid Crystals. Chem.Rev., Vol.57, pp1049-1157.

12. BRADSHAW, P. (1970)  
Experimental Fluid Mechanics. (London: Pergamon Press).
13. CEBECI, T. and BRADSHAW, P. (1984)  
Physical and Computational Aspects of Convective Heat Transfer.  
(New York: Springer).
14. CHAMPA, R.A. (1972)  
USAF Applications of Liquid Crystal Materials. AFML-TR-72-77.
15. CHEW, P.E. "Rotary air preheaters on power station boilers".  
Proc. Institute of Energy Symposium "Waste Heat Recovery and  
Utilisation", Portsmouth, U.K., September 1985.
16. CHOJNOWSKI, B. and CHEW, P.E. (1978)  
Getting the Best out of Rotary Air Heaters.  
CEGB Research Journal, pp14-21.
17. CIOFALO, M., STASIEK, J. and COLLINS, M.W. "Flow and heat transfer  
in corrugated passages : Part 2 Direct and large-eddy simulation  
and comparison with experimental results". 2nd Int. Symposium on  
Engineering Turbulence Modelling and Measurements, Florence,  
Italy, 1993 (in preparation).
18. CIOFALO, M. and COLLINS, M.W. "Time-dependent numerical simulations  
of the starting flow of an incompressible fluid past a down-  
stream facing step". AGARD Conf. "Validation of Computational  
Fluid Dynamics", Lisbon, Portugal, 2-5 May, 1988.
19. CIOFALO, M., FODEMSKI, T.R. and COLLINS, M.W.  
"Large-eddy simulation of turbulent flow and heat transfer in  
plane channels". Proc. 6th Nat. Conf. on Heat Transfer, Italian  
Union of Thermofluid-dynamics (UIT), Bari, 9-11 June, 1988, p37.
20. CIOFALO, M. and COLLINS, M.W. (1989)  
k- $\epsilon$  Predictions of Heat Transfer in Turbulent Recirculating Flows  
Using an Improved Wall Treatment.  
Num. Heat Transfer, Part B, 15, pp21-47.
21. CIOFALO, M., COLLINS, M.W. and PERRONE, G. "Laminar flow and heat  
transfer predictions in cross-corrugated rotary regenerators".  
Proc. 8th Nat. Conf. UIT, Ancona, Italy, 28-30 June, 1990.
22. CIOFALO, M., PERRONE, G. and COLLINS, M.W. (1990)  
Predictions for Laminar Flows and Heat Transfer for a Cross-  
Corrugated Geometry. TFERC Report No.4, City University, London.
23. CIOFALO, M., PERRONE, G. and COLLINS, M.W. (1990)  
Predictions for Turbulent Flows and Heat Transfer for a Cross-  
Corrugated Geometry. TFERC Report No.5, City University, London.

24. CIOFALO, M., COLLINS, M.W. and PERRONE, G. "Turbulent flow and heat transfer predictions for cross-corrugated rotary regenerators". Proc. Eurotech Direct'91-ThermoFluids Engineering, 2-4 July, 1991, Birmingham, U.K.
25. CIOFALO, M., COLLINS, M.W. and HENRY, F.S. "Laminar and turbulent flow and heat transfer in cross-corrugated heat exchangers". Proc. 7th Int. Conf. "Numerical Methods for Thermal Problems", 8-12 July, 1991, Stanford, California, U.S.A.
26. COGHLAN, A. (1991)  
Clothes that Change Colour in the Heat of the Moment.  
New Scientist, 11 May.
27. COOPER, T.E. and GROFF, J.P. (1973)  
Thermal Mapping via Liquid Crystals of the Temperature Field Near a Heated Surgical Probe.  
Journal of Heat Transfer, Vol.5, pp250-256.
28. COOPER, T.E. and PETROVIC, W.K. (1974)  
An Experimental Investigation of the Temperature Field Produced by a Cryosurgical Cannula.  
Journal of Heat Transfer, Vol.96, pp415-420.
29. COOPER, T.E., FIELD, R.J. and MEYER, J.F. (1975)  
Liquid Crystal Thermography and its Applications to the Study of Convective Heat Transfer.  
Journal of Heat Transfer, Vol.97, pp442-450.
30. COLLINS, M.W., CIOFALO, M., PERRONE, G. and STASIEK, J.  
"Local heat transfer in corrugations for rotary regenerators: a combined predictive and experimental study - Part 1 : Problem description and predictions". Proc. Anglo-Soviet Seminar on Heat Transfer Modelling, 5-6 April, 1990, University of Manchester, Department of Engineering, U.K.
31. COLLINS, M.W. and STASIEK, J. (1991)  
"Local heat transfer in corrugations for rotary regenerators: a combined predictive and experimental study - Part 2 : Use of liquid crystals". Proc. Anglo-Soviet Seminar on Heat Transfer Modelling, 5-6 April, 1990, University of Manchester, Department of Engineering, U.K.
32. COLLINS, M.W. and CIOFALO, M. (1991)  
Computational Fluid Dynamics and its Application to Transport Processes. Journal of Chem.Tech.Biotechnol., pp5-47.
33. COLLINS, M.W. and STASIEK, J. "Temperature measurement and automatic data processing using thermochromic liquid crystals". Proc. 12th IMEKO World Congress, 5-10 September, 1991, Beijing, China.

34. CHAMBERLIN, G.J. and CHAMBERLIN, D.G. (1980)  
Colour, its Measurement, Computation and Application.  
(London: Heyden & Son Ltd.).
35. CRANE, R.J. and SABZVARI, J. "Liquid crystal mapping and laminar convective heat transfer in the presence of Görtler Vortices".  
Proc. 2nd U.K. Nat.Conf. on Heat Transfer, 14-16 September, 1988,  
Glasgow, pp687-700.
36. CRISSEY, R.J., GORDY, E., FERGASON, J.L. and LYMAN, R.B. (1964)  
A New Technique for the Determination of Skin Temperature Patterns.  
Journal of Investigative Dermatology, Vol.42, p89.
37. CRISSEY, J.T., FERGASON, J.L. and BETTENHAUSEN, J.M. (1965)  
Cutaneous Thermography with Liquid Crystals.  
Journal of Investigative Dermatology, Vol.45, p329.
38. DAWIS, F. (1967)  
A New Tool for NDT. Research/Development, Vol.18, pp24-27.
39. DEWIES, R.M., RHINES, J.M. and SIDHU, B.S. "The application of the liquid crystal technique to the experimental modelling of forced convective heat transfer in industrial heating processes".  
Proc. 1st U.K. Nat.Conf.on Heat Transfer, Leeds, 3-4 July, 1984,  
pp907-918.
40. DOWDEN, W.A. (1967)  
Cholesteric Liquid Crystals : A Review of Developments and Applications.  
Non-Destructive Testing, Vol.1, pp99-102.
41. DREHER, R., MEIER, G. and SAUPE, A. (1971)  
Selective Reflection by Cholesteric Liquid Crystals.  
Molecular Crystals and Liquid Crystals, Vol.13, pp17-26.
42. DE JEU, W.H. (1980)  
Physical Properties of Liquid Crystalline Materials.  
(New York: Gordon and Breach Science Publishers).
43. EDWARDS, R.J., JAMBUNATHAN, K. and BUTTON, B.L. (1988)  
Experimental Investigation of Turbulent Heat Transfer in Simultaneously Developing Flow in Finned Annuli.  
Experimental Heat Transfer, Fluid Mechanics and Thermodynamics.  
Eds. Shah,R.K.,Ganic,E.N. & Yang,K.T. (Elsevier Science Pub.Co.).
44. EDWARDS, R.J., JAMBUNATHAN, K. and BUTTON, B.L. "Heat transfer in annular ducts with freely decaying swirl flow". Proc. 9th Int. Heat Transfer Conference, 19-24 August, 1990, Jerusalem, Israel,  
Paper 16-TR-20.

45. FERGASON, J.L. (1964)  
Liquid Crystals. Scientific American, Vol.211, pp76-78.
46. FERGASON, J.L. and BROWN, G.H. (1968)  
Liquid Crystals and Living Systems.  
Journal of Am.Oil Chem.Soc, Vol.45, pp120-127.
47. FERGASON, J.L. (1968)  
Liquid Crystals in Non-destructive Testing.  
Appl. Optics, Vol.7, pp1729-1737.
48. FERGASON, J.L. (1970)  
Experiments and Cholesteric Liquid Crystals.  
American Journal of Physics., Vol.38, pp425-428.
49. FODEMSKI, T.R. and COLLINS, M.W. "Flow and heat transfer simulations for 2- and 3-dimensional smooth and ribbed channels". Proc. 2nd U.K. Nat. Conference on Heat Transfer, 14-16 September, 1988, Glasgow, pp845-860.
50. Fodemski, T.R. "Computer simulation study of thermohydraulic performance of corrugated ducts". Proc. 9th Int. Heat Transfer Conference, 19-24 August, 1990, Jerusalem, Israel, Paper 7-M-21.
51. FOCKE, W.W., ZACHARIADES, J. and OLIVIER, I. (1985)  
The Effect of the Corrugated Inclination Angle on the Thermo-hydraulic Performance of Plate Heat Exchangers".  
Int.J.Heat Mass Transfer, Vol.28, pp1469-1479.
52. GAISER, G. and KOTTKE, V. "Effect of corrugation parameters on local and integral heat transfer in plate heat exchangers and regenerators". Proc. 9th Int. Heat Transfer Conference, 19-24 August, 1990, Jerusalem, Israel, Paper 14-HX-15.
53. GOLDSTEIN, R.J. and TIMMERS, J.F. (1982)  
Visualisation of Heat Transfer from Arrays on Impinging Jets.  
Int.J.Heat Mass Transfer, Vol.25, pp1857-1868.
54. GOLDSTEIN, R.J. and FRANCHETT, M.E. (1988)  
Heat Transfer from a Flat Surface to an Oblique Impinging Jet.  
Journal of Heat Transfer, Vol.110, pp84-90.
55. GRAZIANI, R.A., BLAIR, M.F., TAYLOR, J.R. and MAYLE, R.E. (1980)  
An Experimental Study of Endwall and Airfoil Surface Heat Transfer in a Large Scale Turbine Blade Cascade.  
J.Eng.for Power, Vol.102, pp257-267.
56. GREEN, W.B. (1989)  
Digital Image Processing. A Systems Approach.  
(New York: Van Nostrand Reinhold).

57. HALL, E.L. (1979)  
Computer Image Processing and Recognition.  
(New York: Academic Press Inc.).
58. HENRION, C., BRIOTTET, X. and DINGUIRARD, M.  
"Automatic image processing of thermocolour paints for heat flow measurements in wind tunnel facilities". Int. Seminar: Optical Methods and Data Processing in Heat and Fluid Flow, 2-3 April, 1992, City University, London, U.K.
59. HEROLD, W. and WIEGEL, D. (1980)  
Problems of the Photographic Documentation of Liquid Crystalline Thermographs.  
Advances in Liquid Crystal Research and Applications.  
Edited by Lajos Bata, Budapest.
60. HILLER, W.J. and KOWALEWSKI, T.A. "Simultaneous measurement of temperature and velocity fields in thermal convective flows". Proc. 4th Int. Symposium on Flow Visualisation, 26-29 September, 1986, Paris.
61. HILLER, W.J., KOCH, St. and KOWALEWSKI, T.A. "Three-dimensional structures in laminar natural convection in a cube shaped enclosure". Proc. 1st World Conference on Experimental Heat Transfer, Fluid Mechanics and Thermodynamics, 4-9 September, 1988, Dubrovnik, pp722-729.
62. HIPPENSTEELE, S.A., RUSSELL, L.M. and STEPKA, F.S. (1983)  
Evaluation of a Method for Heat Transfer Measurements and Thermal Visualisation using a Composite of a Heater Element and Liquid Crystals.  
Journal of Heat Transfer, Vol.105, pp184-189.
63. HOLMES, B.J. and OBARA, C.J. (1987)  
Advances in Visualisation using Liquid Crystal Coatings.  
SAE Technical Report 87017.
64. HOLMES, B.J., CROOM, C.C., GALL, P.G., MANUEL, G.S. and CARRAWAY, D.L. (1986)  
Advanced Transition Measurement Method for Flight Applications.  
AIAA Report 86-9786.
65. HOOGENDOORN, C.J. (1977)  
The Effect of Turbulence on Heat Transfer at Stagnation Point.  
Int. Journal of Heat Mass Transfer, Vol.20, pp1333-1338.
66. IRELAND, P.T. and JONES, T.V.  
"Detailed measurements of heat transfer on and around a pedestal in fully developed passage flow". Proc. 8th Int. Heat Transfer Conference, San Francisco, 1986, pp975-980.

67. IRELAND, P.T. and JONES, T.V. (1987)  
The Response Time of a Surface Thermometer Employing  
Encapsulated Thermochromic Liquid Crystals.  
*J.Phys.E.*, Vol.20, pp1195-1199.
68. JONES, T.V. (1988)  
Gas Turbine Studies at Oxford 1969-1987.  
ASME Paper 88-GT-112.
69. JONES, T.V. and HIPPENSTEELE, S.A. (1988)  
High-Resolution Heat-Transfer-Coefficient Maps Applicable  
to Compound-Curve Surfaces using Liquid Crystals in a  
Transient Wind Tunnel.  
NASA Technical Memorandum 89855.
70. JUDD, D.B. and WYSZECKI, G. (1975)  
Colour in Business, Science and Industry.  
(New York: J. Wiley & Sons).
71. KASAGI, N., HIRATA, M. and KUMADA, M. (1981)  
Studies of Full-Coverage Film Cooling:  
Part 1, Cooling Effectiveness of Thermally Conductive Wall.  
ASME Paper 81-GT-37.
72. KASAGI, N., MOFFAT, R.J. and HIRATA, M. (1989)  
Liquid Crystals, Handbook of Flow Visualisation. Ed. W. Merzkirch.
73. KLEIN, E.J. (1968)  
Liquid Crystals in Aerodynamic Testing.  
*Astronautics and Aeronautics*, Vol.6, pp70-72.
74. KLEIN, E.J. (1968)  
Application of Liquid Crystals to Boundary Layer Flow  
Visualisation.  
AIAA 3rd Aerodynamic Testing Conference, AIAA Paper 68-376.
75. KLEIN, E.J. and MARGOZZI, A.P. (1969)  
Exploratory Investigation on the Measurement of Skin Friction  
by Means of Liquid Crystals.  
NASA TM-X-1774.
76. KOIDE, N. (1986)  
Synthesis, Characterisation and Some Aspects for Application of  
Polymer Liquid Crystals. Applied Liquid Crystals Research II.  
*Molecular Crystals & Liquid Crystals*, Vol.139, pp47-80.
77. MCELDERRY, E.D. (1970)  
Boundary Layer Transition at Supersonic Speeds Measured  
by Liquid Crystals.  
Air Force Flight Dynamics Laboratory, FDMG, TM-70-3.

78. MOFFATT, J.R. "Experimental heat transfer". Proc. 9th Int. Heat Transfer Conference, 19-24 August, Jerusalem, Israel, Paper KN-11.
79. MORIMOTO, Y., MINE, K., WAKABAYASHI, K. and SEKI, T. (1988) A Method of Hierarchical Diagnosis for Thermal Processes using Liquid Crystals. ACTA, IMEKO, pp263-270.
80. OGDEN, T.R. and HENDRICKS, E.W. (1984) Liquid Crystal Thermography in Water Tunnels. Experiments in Fluids, Vol.2, No.2, pp65-66.
81. den OUDEN, C. and HOOGENDOORN, C.J. "Local convective heat transfer coefficients for jets impinging on a plate : Experiments using a liquid crystal technique". Proc. 2nd U.K. Nat. Conference on Heat Transfer, 14-16 September, 1988, Glasgow, pp293-297.
82. PARKER, S.C. and HOLDEN, C.M.E. "Quantitative 3D holographic interferometry". Seminar: Optical Methods and Data Processing in Heat and Fluid Flow, 2-3 April, 1992, City University, London, U.K.
83. PARSLEY, M. "The use of thermochromic crystals in heat transfer and flow visualisation research". Proc. 2nd Int. Symposium on Fluid Control, Measurement, Mechanics and Flow Visualisation, 5-9 September, 1988, Sheffield, pp216-220.
84. PATANKAR, S.V. (1980) Numerical Heat Transfer and Fluid Flow. (New York: McGraw-Hill Book Co.).
85. PRATT, W.K. (1978) Digital Image Processing. (New York: J. Wiley & Sons).
86. RHEE, H.S., KOSEFF, J.R. and STREET, R.L. (1984) Flow Visualisation of a Recirculating Flow by Rheoscopic Liquid and Liquid Crystal Techniques. Experiments in Fluids, Vol.2, No.2, pp57-64.
87. ROJAS, J., WHITELAW, J.H. and YIANNESKIS, M. (1987) Forced Convective Heat Transfer in Curved Diffusers. Journal of Heat Transfer, Vol.109, pp866-871.
88. ROHSENOW, W.M. and HARTNETT, J.P. (1972) Handbook of Heat Transfer. (New York: McGraw-Hill Book Co.).
89. SAVOSTIN, A.F. and TIKHONOV, A.M. (1970) Investigation of the Characteristics of Plate-Type Heating Surfaces. Teploenergetika, Vol.17, pp75-78.

90. SIMONICH, J.C. and MOFFATT, R.J. (1982)  
New Technique for Mapping Heat Transfer Coefficient Contours.  
Rev.Sci.Instrum., Vol.53, pp678-683.
91. STASIEK, J. and GRYGIEL, P.  
"Visualisation study of laminar natural convection in horizontal cylindrical annuli". Proc. 5th Int. Symposium on Flow Visualisation, 21-25 August, 1989, Prague, Czechoslovakia, pp875-879.
92. STASIEK, J. and COLLINS, M.W.  
"Liquid crystal thermography applied to turbulent convective heat transfer in air heat exchangers using corrugated geometries". TEMPMEKO'90, 17-19 September, 1990, Helsinki, Finland, pp406-413.
93. STASIEK, J., COLLINS, M.W. and CHEW, P. "The application of liquid crystal thermography to the study of convective heat transfer and thermal visualisation". CANCAM'91, 2-6 June, 1991, University of Manitoba, Winnipeg, Canada, pp568-569.
94. STASIEK, J., COLLINS, M.W. and CHEW, P.  
"Liquid crystal mapping of local heat transfer in crossed-corrugated geometrical elements for air heat exchangers". Proc. Eurotech Direct'91-ThermoFluids Engineering, 2-4 July, 1991, Birmingham, U.K.
95. STASIEK, J. and COLLINS, M.W.  
"The use of liquid crystals in heat transfer experiments". V Summer School of Thermodynamics./ Experimental Methods in Heat Transfer. 9-13 September, 1991, Warsaw.
96. STASIEK, J. and COLLINS, M.W. (1989)  
Local Heat Transfer and Fluid Flow Fields in Crossed-Corrugated Geometrical Elements for Rotary Heat Exchangers.  
Report No.1: Design of Wind Tunnel and Review of Liquid Crystal Thermography. TFERC, October, City University, London, U.K.
97. STASIEK, J., SHAND, A., CIOFALO, M. and COLLINS, M.W. (1990)  
Local Heat Transfer and Fluid Flow Fields in Crossed-Corrugated Geometrical Elements for Rotary Heat Exchangers.  
Report No.2: Interim Report of work done to end of January 1990, TFERC, February, City University, London, U.K.
98. STASIEK, J. and COLLINS, M.W. (1990)  
Local Heat Transfer and Fluid Flow Fields in Crossed-Corrugated Geometrical Elements for Rotary Heat Exchangers.  
Report No.3: Initial Results of Liquid Crystal Measurements and Review of Automatic Processing. TFERC, June, City University, London, U.K.

99. STASIEK, J. and COLLINS, M.W. (1991)  
Local Heat Transfer and Fluid Flow Fields in Crossed-Corrugated  
Geometrical Elements for Rotary Heat Exchangers.  
Report No.8: Measurements using Liquid Crystals & Micro-  
manometers. TFERC, April, City University, London, U.K.
100. STASIEK, J., ZHANG, X. and COLLINS, M.W. "Surface flow visualisation using thermochromic liquid crystal and CFD". Int. Seminar: Optical Methods and Data Processing in Heat and Fluid Flow, 2-3 April, 1992, City University, London, U.K.
101. STASIEK, J., COLLINS, M.W. and CHEW, P.  
"Heat transfer measurements to corrugated surface using thermochromic liquid crystal and true-colour image processing". Int. Seminar: Optical Methods and Data Processing in Heat and Fluid Flow, 2-3 April, 1992, City University, London, U.K.
102. STASIEK, J., KARAYIANNIS, T.G., KACZYNISKI, J. and COLLINS, M.W.  
"A numerical and experimental study of natural convection in a cylindrical annulus". EUROTHERM SEMINAR No.16, 11-12 October, 1990, Pisa, Italy, pp35-42.
103. SHAND, A.M. (1988)  
An Image Processing System for Fluid Studies.  
AERE - R13283, July, U.K.
104. STEPHEN, M.J. and STRALEY, J.P. (1974)  
Physics of Liquid Crystals. Rev.Modern Physics, Vol.46, pp617-704.
105. SZYMCZYK, J., SIEKMANN, J. and CIESLINSKI, J. (1990)  
Experimental Study of Thermocapillary Convection at a Rotating  
Liquid-Gas Interface. AIAA 90-0410, 8-11 January, Nevada, U.S.A.
106. TANAKA, T. "Visualisation of the temperature field in thermal storage tanks by using the thermosensitive liquid crystal suspension method". Int. Symposium on Fluid Control, Measurement, Mechanics and Flow Visualisation, 5-9 September, 1988, Sheffield, pp212-215.
107. TOY, N. and SAVORY, E. "Quantitative assessment of surface temperatures using liquid crystals and digital imaging". Int. Seminar: Optical Methods and Data Processing in Heat and Fluid Flow, 2-3 April, 1992, City University, U.K.
108. TRAVIS, M. (1988)  
Image Processing Goes Colour. Computer Graphics World.
109. TRAVIS, M. (March 1991)  
True-colour Image Processing on the Desktop.  
Photonics Spectra, Laurin Publishing Co., Inc.

110. WANG, Z., IRELAND, P.T. and JONES, T.V.  
"Heat transfer measurements to rough surfaces using thermochromic liquid crystals". Proc. Anglo-Soviet Seminar on Heat Transfer Modelling, 5-6 April, 1990, University of Manchester, Department of Engineering, U.K.
111. WATTS, J. and WILLIAMS, F.  
"A technique for the measurement of local heat transfer coefficients using copper foil". 1st U.K.Nat. Conference on Heat Transfer, 3-5 July, 1984, Leeds, U.K.
112. WILSON, A. (1988)  
What Colour is Colour?  
Imaging and Graphics, Digital Design Publishing Company, 1/88.
113. WISNIEWSKI, S. (1988)  
Heat Transfer. P.W.N. Warszawa (in Polish).
114. WOODMANSEE, W.E. (1968)  
Aerospace Thermal Mapping Applications of Liquid Crystals.  
Appl. Optics, Vol.7, pp1721-1727.
115. YIANNEKIS, M.  
"Thermal monitoring by liquid crystals". Int. Conf. on Condition Monitoring, 21-23 May, 1986, Brighton, U.K., pp131-140.
116. YIANNEKIS, M.  
"Investigation of convective heat transfer in a ventilated chamber by liquid crystal thermography". 2nd U.K. Nat. Conference on Heat Transfer, 14-16 September, 1988, Glasgow, U.K.
117. ZHARKOVA, G.M.  
"Liquid crystals for aerodynamic investigations". Int. Seminar: Optical Methods and Data Processing in Heat and Fluid Flow, 2-3 April, 1992, City University, London, U.K.
118. B.D.H. LIMITED  
Advanced Materials Division, Broom, Road, Poole, BH24NN, U.K.
119. DATA TRANSLATION (1991). Image Processing Handbook.
120. Liquid Crystal Devices Limited  
Stonefield Way, Ruislip, Middlesex HA4 0YW, U.K.
121. BURNS, A.D., JONES, I.P., KIGHTLEY, J.R. and WILKES, N.S. (1987)  
FLOW3D, Release 2: User Manual. Laboratory Report, U.K.
122. COLLINS, M.W. (1991)  
Holographic Techniques for Whole-Field Thermal and Fluid Measurements. Aeronautical Journal, 95, 949, pp313-323.

123. COLLINS, M.W., STASIEK, J., CIOFALO, M. and CHEW, P.  
"The application of thermochromic liquid crystals to heat transfer problems in engineering - practical techniques and numerical predictions". 3rd U.K. and 1st European Heat Transfer Conference, 14-18 September, 1992, Birmingham, U.K.
124. CIOFALO, M., STASIEK, J. and COLLINS, M.W. (1992)  
Local Heat Transfer and Fluid Flow in Crossed-Corrugated Geometrical Elements for Rotary Heat Exchangers.  
Unpublished progress report, TFERC, City University, London, U.K.
125. HOLMAN, J.P. (1966)  
Experimental Methods for Engineers.  
(New York: McGraw-Hill Co.).
126. JONES, T.V., WANG, Z. and IRELAND, P.T.  
"The use of liquid crystals in aerodynamic and heat transfer experiments". Int. Seminar: Optical Methods and Data Processing in Heat and Fluid Flow, 2-3 April, 1992, City University, London.
127. KLINE, S.J. and McCLINTOCK, F.A. (1953)  
Describing Uncertainties in Single-Sample Experiments.  
Mechanical Engineering, 3-8 January.
128. OKADA, K., ONO, M., TOMIMARA, T., OKUMA, T., KONNO, H. and OHTANI, S. (1972)  
Design and Heat Transfer Characteristics of New Plate Heat Exchangers. Heat Transfer Jap. Res., Vol.1, pp90-95.
129. STASIEK, J. and COLLINS, M.W.  
"Particle image velocimetry and thermometry using liquid crystals and true-colour image processing". B.L.C.S. 7th Annual Conference, 6-8 April, 1992, University of Oxford, U.K.
130. MOFFATT, R.J. (1988)  
Describing the Uncertainties in Experimental Results.  
Experimental and Fluid Science, 1, pp3-17.
131. MOFFATT, R.J. (1985)  
Using Uncertainty Analysis in the Planning of an Experiment.  
Trans. ASME, J.Fluids Eng., 107, pp173-178.
132. MOFFATT, R.J. (1982)  
Contributions to the Theory of Single-Sample Uncertainty Analysis.  
Trans. ASME, J.Fluids Eng., 104, pp250-260.  
BRADSHAW, P. (1970)  
Experimental Fluid Mechanics (2nd edition: Pergamon Press).
133. ZOGG, M. (1972)  
Strömungs- und Stoffaustauschuntersuchungen an der Sulzer Gewebepackung. Dissertation 4886. Eidgenössische Technische Hochschule, Zürich.